

UNIVERSITY OF OKLAHOMA  
GRADUATE COLLEGE

MAGNETIC FABRICS AND PALEOMAGNETISM OF NORTH AMERICAN MUDROCKS:  
RELICS OF COMPLEX BURIAL HISTORIES

A DISSERTATION  
SUBMITTED TO THE GRADUATE FACULTY  
in partial fulfillment of the requirements for the  
Degree of  
DOCTOR OF PHILOSOPHY

By  
GERHARD HEIJ  
Norman, Oklahoma  
2018

MAGNETIC FABRICS AND PALEOMAGNETISM OF NORTH AMERICAN MUDROCKS:  
RELICS OF COMPLEX BURIAL HISTORIES

A DISSERTATION APPROVED FOR THE  
CONOCOPHILLIPS SCHOOL OF GEOLOGY AND GEOPHYSICS

BY

Dr. Richard Elmore, Chair

Dr. Roger Slatt

Dr. Shannon Dulin

Dr. Carl Sondergeld

Dr. Eric Ferré

© Copyright by GERHARD HEIJ 2018  
All Rights Reserved.

## Acknowledgements

First and foremost, I will be forever indebted to my advisor, Dr. Doug Elmore. Thank you for your guidance and allowing me the freedom to pursue ideas (both good and bad) during my graduate studies.

My committee members, Shannon Dulin, Roger Slatt, Eric Ferré and Carl Sondergeld provided invaluable feedback throughout the course of my PhD and I feel privileged to have learned from these scientists. Conversations, access to laboratory equipment and technical assistance from, Mike Engel, Josep Parés, John Pigott, Brett Carpenter, Lynn Soreghan, Mike Soreghan, Bill Heins and Andy Madden was greatly appreciated.

Eric Ferré, my master's advisor ignited my interest in research and I will always be grateful for the lessons I learned under his guidance. I am also deeply grateful for the high-field magnetic experiments he performed on my behalf.

I am thankful to Bryan Turner, Jeffrey Hardwick, Matthew Hamilton and Alyssa Wickard whose conversations and intellectual sparring shaped many of the ideas presented in this work. Several undergraduate students worked tirelessly in the paleomagnetic lab, in particular Brandon Maples and Samantha Johnston. I am also thankful for the musical workings of Duran Duran, George Michael, Toto and many others for drowning out the sounds of the magnetometer and other distractions.

I will always be appreciative of assistance from my uncle, Wim van der Plas. My parents, Leneke and Gerrit always provided constant love and support throughout this journey. Last, but not least, thanks to my wife, Amanda who supported me, managed my idiosyncrasies and kept me inspired throughout this journey.

## Table of Contents

Acknowledgements.....	iv
List of Figures.....	x
List of Tables.....	xxiii
ABSTRACT.....	xxiv
CHAPTER 1.....	1
INTRODUCTION.....	1
Chapter 1 Figures.....	4
REFERENCES.....	5
CHAPTER 2.....	6
THE MAGNETIC FABRIC OF THE WOLFCAMP FORMATION, MIDLAND BASIN, WEST TEXAS: UNDERSTANDING PETROFABRIC VARIABILITY, HYDROCARBON DISTRIBUTION AND IRON ENRICHMENT.....	6
ABSTRACT.....	6
INTRODUCTION.....	8
GEOLOGIC BACKGROUND.....	9
METHODS AND SAMPLING.....	12
Sampling and data provided.....	12
Magnetic Experiments.....	12
Hand-held X-Ray Fluorescence (HHXRF).....	14
Statistical clustering of variables.....	15
Image Analysis.....	16
RESULTS.....	16

DISCUSSION.....	20
Magnetic architecture.....	20
Diagenesis.....	21
Provenance and Iron-enrichment in the Wolfcamp .....	22
Mechanisms for fabric variability in mudrocks .....	24
Mechanisms for fabric variability in carbonates.....	25
Magnetic fabrics and TOC.....	26
CONCLUSIONS.....	28
Chapter 2 Figures.....	30
APPENDIX.....	42
REFERENCES .....	45
CHAPTER 3 .....	51
PALEOMAGNETISM AND MAGNETIC FABRIC OF THE WOLFCAMP FORMATION: DECIPHERING THE TIMING OF DIAGENETIC AND TECTONIC EVENTS IN THE MIDLAND BASIN.....	51
ABSTRACT.....	51
INTRODUCTION .....	53
GEOLOGIC BACKGROUND.....	55
METHODS AND SAMPLING .....	57
Experimental methods .....	58
Burial history and thermal modeling .....	60
Database and uncertainty .....	61
RESULTS.....	62

Core 1.....	62
Core 2.....	63
Core 3.....	65
Drilling induced remanent magnetizations (Core 1-3) .....	65
Triaxial thermal decay, IRM acquisition and Hysteresis data Core 1-3 .....	66
SEM and EDS of magnetic extracts Core 1-3 .....	67
Microtextural observations from thin sections Core 1-3 .....	68
1D Basin Modeling.....	69
DISCUSSION.....	70
Magnetic Fabrics and Fracture Orientations.....	70
Magnetic Remanence Carrier(s) and the Nature of CRMs.....	72
CONCLUSIONS.....	76
Chapter 3 Figures.....	78
Chapter 3 Tables .....	92
APPENDIX.....	93
REFERENCES .....	97
CHAPTER 4 .....	105
UNRAVELING THE COMPLEX BURIAL HISTORY OF THE ANTRIM FORMATION IN MICHIGAN BASIN USING PALEOMAGNETISM, ROCK MAGNETISM AND GEOCHEMISTRY .....	105
ABSTRACT.....	105
INTRODUCTION .....	107
GEOLOGIC BACKGROUND.....	109

Hydrothermal activity in the Michigan Basin.....	110
The Antrim Formation .....	110
METHODS .....	111
Magnetic experimental methods.....	112
Geochemistry and Petrography.....	114
RESULTS .....	115
Paleomagnetism .....	115
Rock Magnetism.....	118
Room Temperature AMS.....	119
Low Temperature AMS .....	120
Magnetic Susceptibility and XRF.....	121
Microscopy .....	121
Provenance.....	122
Stable Isotopes .....	122
DISCUSSION.....	123
Paleomagnetic interpretations, remanence-carrying minerals and petrography.....	123
Magnetic/Diagenetic differences owing to biogenic vs thermogenic gas production ...	126
Magnetic fabrics – Depositional or tectonically driven? .....	127
Origin of exotic minerals in the Antrim – hydrothermal or extrabasinal?.....	129
CONCLUSIONS.....	130
Chapter 4 Figures.....	133
Chapter 4 Tables .....	146
APPENDIX.....	148

REFERENCES .....	150
CHAPTER 5 .....	157
SUMMARY OF CHAPTERS .....	157
SYNTHESIS .....	158

## List of Figures

### Chapter 1

Figure 1. Schematic illustration of key variables involved in mudrock diagenesis..... 4

### Chapter 2

Figure 1. Map of Permian Basin in West Texas with major structural features and core locations.

Modified from Flawn et al. (1961). Green Star = Core 1 and 2; Red Star = Core 3; Diamond = Nellie #1 well; BA – Bend Arch; CBP – Central Basin Platform; DB – Delaware Basin; DRU – Devil Rivers Uplift; ES – East Shelf; FWB – Fort Worth Basin; LU – Llano Uplift; MA – Matador Arch; MB – Midland Basin; MU – Marathon Uplift; NM – New Mexico; NWS – North West Shelf; OA – Ozona Arch; PDB – Palo Duro Basin; VVB – Val Verde Basin. A generalized cross section (A-A') of the Permian Basin with stratigraphic boundaries of the Wolfcamp shown by dashed lines. Modified from Matchus and Jones (1984) and Engle et al. (2016)..... 30

Figure 2. (A) Example of massive siliceous mudrock facies from Core 3; (B) mud-supported carbonate debrite facies from Core 2; (C) clast-supported carbonate debrite facies from Core 1; (D) high frequency turbidites comprised mostly of Ta, Tb and Te sequences from Core 1..... 31

Figure 3. (A) Field-dependent magnetic susceptibility with 95% confidence intervals of specimens from Core 1 - 3. Note invariant behavior for both mudrock and carbonate facies. (B) Normalized reciprocal magnetic susceptibility ( $k_0/k$ ) vs. temperature for representative carbonate and mudrock facies from Core 2. Inset shows numerical model of ideal ferrimagnetic to ideal paramagnetic behavior from Richter and van der Pluijm (1994). (C) Cross plot of  $k_{lf}$  vs. Fe/S in Core 3. (D) Cross plot of  $k_{lf}$  vs. Al in Core 3... 32

Figure 4. (A)  $k_{lf}$  vs. Fe for siliceous mudrocks in Core 3. Note r-squared values for  $k_{lf}$  vs. Fe/S compared to  $k_{lf}$  vs. Fe in Figure 3C. (B) Cross plot of  $k_{lf}$  vs. Fe from Core 2. (C) Cross plot of  $k_{lf}$  vs. Mg for carbonate facies from Core 2 (with data points colored by corresponding T values). Insets show AMS stereonet (specimen coordinates) of representative specimens with predominately normal AMS fabric at Mg concentrations < 10,000ppm and mostly inverse AMS fabric at concentrations > 10,000ppm. (D) Fe/S for carbonate facies from Core 2. Note reduced r-squared value relative to Figure (B). ..... 33

Figure 5. (A) Representative siliceous mudrock facies showing euhedral/subhedral dolomite with ferroan rims (Fe-Dol), abundant authigenic chlorite (Chl), pyrite (Py) framboids and detrital micas (Mca) with interstitial pyrite forming within sheets. Inset shows example of multiple ferroan growth rims in dolomite found in siliceous mudrocks. (B) Warped clays along margins of corroded ferroan dolomite rim, interior of grain is Mg-rich dolomite (Mg-Dol). (C) Authigenic iron-rich chlorite adjacent to authigenic albite and surrounded by illite (Ill). (D) Pyrite framboids with overgrowths (OG) with sphalerite (Sp) encapsulating some pyrite framboids. White dashed circles represent original grain boundary of framboid prior to overgrowth (E) Cubic pyrite cluster in carbonate facies with sphalerite cement. (F) Marcasite (Mrc) replacing allochem with euhedral barite (Brt) in carbonate facies..... 34

Figure 6. (A) Zr vs. Ti/Nb cross plot (e.g. Bonjour and Dabard, 1991) with data colored by respective magnetic susceptibility data of mudrocks from Core 1-3. Note two major groupings emerge from the data: 1) Group 1 – Ti/Nb ratio  $\geq 430$ , lower Zr (mean = 89.7ppm) and with high  $k_{lf}$  (mean =  $2.78E-04$  SI) indicating more mafic provenance and 2) Group 2 – Ti/Nb  $\leq 430$ , higher Zr (mean = 123.5ppm) and lower  $k_{lf}$  (mean =  $2.18E-04$ )

suggesting more quartzofeldspathic (QL) provenance. Ungrouped data likely represents intrabasinal provenance. (B) Boxplot of  $k_{lf}$  data measured from mudrock facies in several sedimentary basins across North America (Steullet, 2014; Rose, 2015; Roberts, 2016). Note higher  $k_{lf}$  in the Wolfcamp relative to other mudrock units..... 35

Figure 7. (A - B) Cross plots of Pj vs. Al and log Pj/Al vs. Si/Al of siliceous mudrocks with data colored by Ca concentrations. (A) Pj has a clay concentration dependency in low Ca facies (<60,000 ppm) and no relationship with Pj in high Ca facies (>60,000 ppm). (B) A linear relationship for low and high-Ca siliceous mudrock facies shows quartz framework control on Pj. The change in regression slope likely reflects contribution from ferroan dolomite. .... 36

Figure 8. (A) Cross plot of Pj vs. Ca for carbonate facies with data colored by Al concentration. Anisotropy broadly decreases with Al (clay content) in carbonate facies. (B) log Pj/Al vs. Si/Al for carbonate facies colored by Ca concentration. Linear regressions with variable slopes coincide to individual carbonate facies and probably reflect the relative contribution of clay and ferroan dolomite on Pj. .... 37

Figure 9. Left images represent processed image maps where framework/cement is shown in black and matrix/TOC/porosity is displayed in white. Right images show unprocessed image maps. Note ferroan carbonate/quartz dominated mineralogy in high Ca-siliceous mudrock. Table with HHXRF data, scalar AMS data (T and Pj), average matrix to framework (M/F) per image set (n=9) and the standard deviation. Statistics in table for images above are labeled 1 and 2. .... 38

Figure 10. (A) Cross plot of TOC vs. Pj from Core 3(B- D) Cross plots of Ni vs. Pj, Cr vs. Pj and Ti/Nb vs. Pj with data points colored by TOC% from Core 3 (scale in B) ..... 39

Figure 11. (A) Contour plot of Pj vs. T modulated by TOC for siliceous mudrocks (n=35) and MTC facies (n=15) from Core 1 and 2 (B) Contour plot of Pj vs. T modulated by OSI for siliceous mudrocks (n=35) and MTC facies (n=15). Note fabric selective hydrocarbon associations in A and B. (C - D) Organoclay aggregates in siliceous mudrocks (Core 2) (Chl – chlorite; OM – Organic Matter; CBS – backscattered electron image) -. Other OM occurrences include (E) particulate organic matter with possible pores residing within carbonate facies (Core 1) (ETD – secondary electron image) and (F) wispy organic matter hosted within the matrix of siliceous mudrocks (Core 2). ..... 40

Figure 12. (Left) Simplified stratigraphic column of Core 3 – gray region represents siliceous mudrocks and light gray area represents a mass transport complex. (Middle) Lithomagneto-facies profile derived from FCM analysis with membership coefficient to each principal cluster where 1 represents complete membership and > 0 indicates partial membership. Cluster 1 is represented in black and Cluster 2 is displayed in white. (Right) Schematic petrofabric depicts relative concentration of framework grains and clay particle alignment. (Below) Table with centroid values for Clusters 1 and 2. .... 41

Burial history and thermal modeling ..... 60

Database and uncertainty ..... 61

### Chapter 3

Figure 1. (A) Map of Permian Basin in West Texas with major structural features and core locations. Modified from Flawn et al. (1961). Green Star = Core 1 and 2; Red Star = Core 3; BA – Bend Arch; CBP – Central Basin Platform; DB – Delaware Basin; DRU – Devil Rivers Uplift; ES – East Shelf; FWB – Fort Worth Basin; LU – Llano Uplift; MA – Matador Arch; MB – Midland Basin; MU – Marathon Uplift; NM – New Mexico; NWS

– North West Shelf; OA – Ozona Arch; PDB – Palo Duro Basin; VVB – Val Verde Basin.

A generalized cross section (A-A') of the Permian Basin with stratigraphic boundaries of the Wolfcamp shown by dashed lines. Modified from Matchus and Jones (1984) and Engle et al. (2016). ..... 78

Figure 2. (A-D) Workflow for applying geographical corrections to unoriented core. (A) Processed FMI log showing horizontal bedding and sub-vertical fracture that manifests as a sinusoidal feature. (B) Interpreted FMI image with arrows showing fracture trend. (C) Photograph of core slab with fracture (red) corresponding to FMI image in (B). (D) Schematic representation of drilled core slab. Solid black line represents sampling datum or specimen coordinate system and red line presents the sub-vertical fracture. Geographic coordinates for specimens were determined by measuring the angle between the fracture orientation and the plug site(s). ..... 79

Figure 3. (A-H) Zijdeveld diagrams (specimen coordinates) and demagnetization data for AF and thermal demagnetization experiments from Core 1 – 3. Note the presence of a DIRM in most specimens. Black squares = declinations, open squares = inclinations and red squares denote labeled demagnetization steps in mT or °C. (A-B) Zijdeveld diagrams and AF demagnetization data from Core 1 showing a representative (A) mudrock and (B) carbonate concretion specimen. (C-E) Zijdeveld diagrams and demagnetization data from Core 2 with representative (C) thermal decay of a mudrock specimen, (D) AF demagnetization of a carbonate and (E) diagenetically altered carbonate specimen. (F-H) Thermal and AF demagnetization of mudrock facies from Core 3. Note pronounced GRM development in (H) starting at 80mT. .... 80

Figure 4. (A) Rose plot of fracture orientations from FMI logs overlaid onto the equal-area projection of mean K1 and K3 AMS tensors with 95% confidence ellipses (geographically corrected) from Core 1. (B) Equal-area projection of corrected (Reoriented Core 1) ChRM directions with crosshair denoting VGP and uncorrected ChRM directions (Unoriented Core 1) (C) APWP for North America (Torsvik et al., 2012) from 190Ma through 0Ma. Black star indicates VGP for Core 1 with corresponding  $\alpha_{95}$  confidence ellipse in solid black. Dashed ellipses represent  $\alpha_{95}$  confidence ellipses for ages intersecting the VGP. (D-E) Expected inclination plots for North America. Red line = expected inclination (Torsvik et al., 2012); gray lines =  $\alpha_{95}$  confidence limits for expected inclinations (Torsvik et al., 2012); black line and translucent area = mean inclination with  $\alpha_{95}$  confidence limits. (D) Inclination only plot Core 2 (E) Inclination only plot Core 3. .... 81

Figure 5. Core 1: (left to right) Simplified stratigraphic column with mudrock facies displayed in dark gray, MTCs in light gray, carbonate nodules in green and diagenetically altered MTC in red. Equal-area stereonet for AMS data displayed in a geographic coordinate system (GCS). Dashed lines delineate boundaries in core from which the AMS data was collected whereas the adjacent data tracks correspond to depth. Data tracks show, from left to right ChRM inclinations ( $^{\circ}$ ), mass-normalized magnetic susceptibility ( $\chi$ ), SIRM/ $k_{If}$  values and  $\Delta GRM/\Delta NRM$  ratios. Shallow inclinations and their data are depicted by stars (green = carbonate concretions, red = diagenetically altered MTCs). Frequency distributions of each parameter is displayed directly below its corresponding track. Light yellow areas of the plot represent complete drilling overprint of the ChRM..... 82

Figure 6. Core 2: (left to right) Simplified stratigraphic column with mudrock facies displayed in dark gray, MTCs in light gray and diagenetically altered MTCs in red. Equal-area

stereonet for AMS data displayed in a geographic coordinate system (GCS). Dashed lines delineate boundaries of respective AMS data whereas the adjacent data tracks correspond to depth. Data tracks show, from left to right, ChRM inclinations ( $^{\circ}$ ), mass-normalized magnetic susceptibility ( $\chi$ ), SIRM/klf values and  $\Delta$ GRM/ $\Delta$ NRM ratios. Shallow inclinations and their data are depicted by stars. Frequency distributions of each parameter is displayed directly below its corresponding track. Light yellow areas of the plot represents total drilling overprint of the ChRM..... 83

Figure 7. Core 3: (left to right) Stratigraphic column with mudrock facies displayed in dark gray a single MTC in light gray. Equal-area plots for AMS data displayed in a specimen coordinate system (SCS). Dashed lines delineate boundaries of AMS data whereas the adjacent data tracks correspond to depth. Data tracks show, from left to right, ChRM inclinations ( $^{\circ}$ ), mass-normalized magnetic susceptibility ( $\chi$ ), SIRM/klf values and  $\Delta$ GRM/ $\Delta$ NRM ratios. Frequency distributions of each parameter is displayed directly below its corresponding track. Light yellow area of the plot represent complete drilling overprint of the ChRM. Note gradual inclination shallowing from 2950m to 2964m. ... 84

Figure 8. Core 1: (A-B) Concretions with septarian-like fissures that likely formed by shrinkage or dehydration owing to rapid burial. Note warped laminations underlying the concretion in (A). Fracture-fill is mainly comprised of barite and pyrite. Core 2 (C) Turbidite showing fining-up sequence with complex fracture arrays. Arrow indicates patchy chert replacement with pyrite “halo”. Horizontal fracture consistent with early overpressuring related to rapid burial. Sub-vertical tensile fractures appear to have formed later, perhaps during tectonic shortening? (D) Mud-supported debrite with abundant allochems and chert replaced clasts. .... 85

Figure 9. (A) Representative IRM acquisition curves from each core. Note single component, smooth concave down shape reaching saturation at 300-450mT. Inset shows a representative unmixed IRM acquisition curve and affirms that a single component best represents the coercivity spectrum. (B) Cross plot of  $k_{fd}$  vs.  $SIRM/k_{lf}$  suggests that SP grains influence  $SIRM/k_{lf}$  ratios in Core 2. Similar linear relationships are observed in Core 1 and 3. .... 86

Figure 10. (A-C) Representative triaxial thermal demagnetization plots from each core. Note incomplete decay of X and Y axis likely owing to oxidation of iron-sulfides. Rapid decay of the X and Y-axis does occur between 200°C and 300°C in several samples and may be indicative of ferrimagnetic iron sulfides. Unblocking temperatures for the Z axis range from 350°C to 400°C. .... 87

Figure 11. (A-I) Unprocessed, processed and fitted hysteresis loops with noise curves for both unprocessed and processed loops for one specimen from each core. Note strong paramagnetic component in all samples. Pole drift artifact present in all measurements. Overall, processed and fitted hysteresis loops display a single magnetic component (i.e. B, H) with the exception of Core 2 which shows a subtle wasp-waistedness (E) that may indicate SP/SD assemblages. .... 88

Figure 12. (A-D) Backscatter (CBS), secondary electron (ETD) and EDS spectra from magnetic extracts. (A) Predominately chlorite extract with some dispersed magnetite spherules showing both smoothed and textured surfaces. Black cross in top right represents EDS target. Its corresponding spectrum shows atomic percentages of Fe greater than that of chlorite alone, suggesting that magnetite resides within chlorite. (B) Example of textured, stoichiometric magnetite spherule, crystal shapes are consistent with pyrite framboids or

spinel crystal habits. (C) Amorphous magnetite mass with some organic material. (D) Organic-rich extract with magnetite showing possible spinel crystal habit and fine grained chlorite/Fe-rich smectite. EDS scan shows trace amount of Cr in magnetite. (E) Rare ferrimagnetic sulfide that corresponds to either greigite or pyrrhotite. .... 89

Figure 13. Backscatter images from siliceous mudrocks (A-E) and MTC (F). (A) Detrital rutile and mica with iron sulfide growth within sheets (pyrite (Py) or greigite (G)?). (B) Large barite (Brt) crystal with “fish-tail” habit rimmed with chlorite and replaced by pyrite overgrowths (OG) on framboids (Fram). Note replacement of ferroan dolomite (Fe-dol) by pyrite overgrowths. Isolated sphalerite cement. (C) Authigenic chlorite with increased concentration of iron (high electron density) and ultrafine-grained intergrown chlorite along with authigenic albite (Ab) with tabular habit. (D) Polyframboid within an allochem showing a variety of textures. (E) Cubic pyrite crystal hosting inclusions of sphalerite (barite is also commonly observed) and possible inclusions of ferrimagnetic sulfides. EDS scans on areas with higher electron densities (circled top left) show elemental concentrations other than pyrite (circled middle left). (F) Textural transition from cubic pyrite to bladed crystal habit may correspond to a compositional change to pyrrhotite (Po) and/or marcasite (Mrc). .... 90

Figure 14. (A) 1D basin model with isotherms for Irion County. The approximate boundaries of major tectonic phases are denoted by dashed lines. The absolute and relative timing of burial events are depicted as a paragenetic sequence and are premised on AMS, paleomagnetic and textural relationships observed through SEM analysis. Solid bars in the sequence are considered to be well constrained events, faded bars of the CRMs correspond to the  $\alpha_{95}$  range of paleomagnetic ages and faded bars with question marks

represent that the start or end of an event is poorly constrained. (B) Thermal profile predicted by the model for three iterations of Cenozoic uplift (2000m, 800m, 300m) plotted along with  $R_o$  data. Note the best fit solution obtained using 800m of Cenozoic uplift and erosion. .... 91

## Chapter 4

- Figure 1. Geologic Map of Michigan modified from Dicken et al. (2004) and East et al. (2005). Schematic cross-section modified from Ma et al. (2009). Core locations denoted by stars. MCRS = Midcontinent rift system..... 133
- Figure 2. Representative lithofacies from each member in the Krocker core (A) – Norwood (B) – Paxton and (C) – Lachine. Similar facies characteristics are observed in the St. Chester core. (D) Carbonate concretion with pyritized margin in the St. Chester core..... 134
- Figure 3. Representative Zijderveld diagrams and associated demagnetization curves from the Lachine, Paxton, Norwood and Squaw Bay. Note HC components only residing with Paxton and Norwood members. Stable LC components reside in the Lachine and Squaw Bay with the exception of one stable thermal demagnetization experiment from a Lachine specimen. .... 135
- Figure 4 . Inclination only plots derived from the North American apparent polar wander path (Torsvik et al., 2012). (A) Mean inclinations with  $\alpha_{95}$  for various components – Krocker core. (B) Mean inclinations with  $\alpha_{95}$  for various components – St. Chester core. Solid black line indicates mean inclination and light-gray lines denote its  $\alpha_{95}$ . .... 136
- Figure 5. From left to right. AMS equal-area stereonet in specimen coordinate system and confidence ellipses for K1 and K3 tensors. LC and HC coercivity data with range of values per sampling depth indicated by error bars and mean inclination depicted by solid red line

with  $\alpha_{95}$ . If no error bars are present, error bars were too small to plot. NRM and SIRM values, error bars are too small to be depicted. Bottom – from left to right, frequency distribution histograms for K1, K3, LC and HC components. Bottom left – legend. ... 137

Figure 6. From left to right. LC coercivity and HC coercivity data with range of values per sampling depth indicated by error bars. If no error bars are present, only one specimen was measured or error bars were too small to plot. Mean inclination depicted by solid red line with  $\alpha_{95}$  in gray for LC components. For mean NRM and SIRM values, error bars are too small to be depicted. Far right – AMS Equal-area stereonet. Note streaked K3 tensors. .... 138

Figure 7. Representative triaxial thermal decay plots with low coercivity in blue, medium coercivity in black and high coercivity in red. Norwood and Paxton exhibit similar decay patterns in both cores. Similarly, Lachine and Squaw Bay display similar decay with magnetization residing mostly in low-coercivity minerals. Note sharp increase occurring at 300-350°C owing to oxidation of pyrite. .... 139

Figure 8. Representative processed hysteresis loops of Antrim and Squaw Bay specimens. Note wasp-waisted shapes among Norwood and Paxton specimens in the Krockner well. Pole drift artifacts occur in certain specimens however, loop closure is achieved in all specimens. .... 140

Figure 9. (A) Day plot of Antrim and Squaw Bay specimens. The horizontal and vertical lines delimitate the theoretical area for single (SD), pseudo-single (PSD) and multi domain (MD) magnetite grains. These lines and the mixing reference curves are from Dunlop (2002a, 2002b). (B) and (C) Representative coercivity spectrum modeling. Gray curve = spline fit of data. Blue line – high coercivity component with  $\alpha_{95}$ , purple line – low

coercivity component, orange line – cumulative Gaussian curves (high + low coercivity components)..... 141

Figure 10. A, C, E, G: Room temperature (RT) and low temperature (LT) AMS data of representative specimens from each member with corresponding  $K_{lf}$  (bulk susceptibility) vs.  $P_j$  (corrected degree of magnetic anisotropy) and  $P_j$  vs  $T$ (shape factor). B, D, F, H: Normalized reciprocal magnetic susceptibility ( $k_0/k$ ) vs. temperature of corresponding specimens..... 142

Figure 11. (A) Magnetic susceptibility ( $k_{lf}$ ) vs. Fe cross plot with data points colored by sulfur (ppm). Magnetic susceptibility controlled by iron-bearing minerals when sulfur concentrations are low. With increasing sulfur no relationship is observed particularly in the Lachine member. Perhaps iron in the Lachine is mostly bound to pyrite and chalcopyrite which have lower magnetic susceptibilities than illite. (B) Positive correlation between Al and  $k_{lf}$  suggests clays control the magnetic susceptibility and its anisotropy..... 143

Figure 12. (A) Reflected light image of pyritized bed in the Paxton – Krockner core. (Py – pyrite) Note preferential oxidation of iron sulfides. (B) Cubic pyrite with oxidized intergrown marcasite in the Lachine – Krockner Core (See Appendix 1 for EDS spectra). (C) Pyrite and sphalerite (Sp) in the Paxton the note relic framboids at the nucleus of several pyrite grains – Krockner core. (D) Nickel-bearing pyrite surrounded by calcite (Ca) in the Paxton – St. Chester Core. (E) Siliceous mudrock with chlorite (Chl) in the Norwood – St. Chester. (F) Patch of barite (Brt) and celestine (Cls) cement with euhedral and double terminated quartz (Qtz) in the Paxton – Krockner core. (G) Monazite and chalcopyrite

(Ccp) in the Lachine member – Krockner core. (H) Euhedral chalcopyrite grain within calcite in the Lachine member – Krockner core. ....	144
Figure 13. Ti/Nb vs Zr plot with data points colored by their copper concentration. Group 1 - 4 delimited by ellipses.....	145
Figure 14. (A) Carbon and oxygen stable isotope data from this study and from Budai et al. (2002). Vein specimens display depleted $\delta^{18}\text{O}$ whereas matrix specimens show more standard values. Budai et al. (2002) attributes high $\delta^{13}\text{C}$ values to bacterial methanogenesis whereas data from this study indicate abiotic methane oxidation (Budai et al., 2002). (B) Sampling sites for isotopic analysis. (C) Vuggy porosity in fracture with curved crystal habit indicative of baroque dolomite. Cross polar photomicrograph of vein fill with calcite (Cal) and coarsely crystalline mosaics of anhedral to subhedral baroque dolomite with undulose extinction .....	146

## List of Tables

### Chapter 3

Table 1. Hysteresis data from processed and fitted loops. Corresponding SIRM/ $k_{lf}$ ratios and S-ratios also shown.....	92
--	----

### Chapter 4

Table 1. Statistics for magnetic components. SB – Squaw Bay, LC – lower coercivity component, HC – higher coercivity component.....	147
Table 2. Results from coercivity spectrum modeling or “unmixing”. Component 1 = HC; Component 2 = LC; $B_h$ = mean coercivity; DP = dispersion parameter; OC = observed contribution; EC = extrapolated contribution. ....	147

## ABSTRACT

Paleomagnetism and rock magnetism are valuable tools to characterize the spatial and temporal aspects of mudrock burial histories. This dissertation utilizes magnetic fabrics, paleomagnetism, geochemistry and electron microscopy to document the burial histories of the Wolfcamp and Antrim mudrocks residing in the Midland and Michigan basins, respectively. The main findings of this study may be summarized as follows:

- Both normal and inverse magnetic fabrics record far-field Laramide tectonic shortening in the Wolfcamp Shale. Normal fabrics are carried by Fe-bearing clays whereas inverse fabrics result from high concentrations of ferroan dolomite.
- A Jurassic chemical remanent magnetization (CRM) in the Wolfcamp is related to clay diagenesis, specifically illitization and chloritization.
- Integrated paleomagnetic dating coupled with burial history and petrographic examination provides a more robust means to construct paragenetic sequences.
- Total organic carbon and redox sensitive elements correlate with scalar magnetic parameters which suggests a genetic relationship between clays and organic carbon that stems from adsorption processes during deposition.
- Released hydrocarbon concentrations are fabric selective and favor low magnetic anisotropy, prolate to triaxial magnetic fabrics. This finding suggests a petrofabric control on hydrocarbon migration in fine-grained sediments.
- Fe-enrichment in the Wolfcamp shale evidenced by trace element geochemistry and anomalously high magnetic susceptibility are consistent with a mafic provenance sourced from the Central Basin Uplift in the Permian Basin.

- Late Paleozoic CRMs in the Antrim are associated with hydrothermal activity resulting from reactivation of the Midcontinent Rift System.
- Magnetic fabrics in the Antrim Formation indicate either depositional long-lived paleocurrents or far-field shortening from the Alleghenian orogeny.
- Exotic minerals assemblages in the Antrim (i.e. Monazite and Chalcopyrite) are consistent with hydrothermal activity, however, some fraction of these minerals could be detrital which may provide additional insight regarding the structural evolution of the Michigan Peninsula.

# CHAPTER 1

## INTRODUCTION

Mudrocks comprise approximately two thirds of the sedimentary rock record, yet, our understanding of diagenetic processes operating in these rocks remains disproportional to that of sandstones and carbonates (e.g. Schieber et al., 1998). Mudrocks (or shales) represent fine-grained sedimentary rocks consisting of clay- and silt-size particles ( $<62.5\mu\text{m}$ ) (Blatt et al., 1980). Diagenesis in mudrocks includes all of the physical, chemical and biological processes involved after deposition and during burial until metamorphic conditions are reached. The variables influencing diagenesis can be divided into two main categories, predepositional and post-depositional (Elmore et al., 2016) (Figure 1). An accounting of these variables paints a complex picture of mudrock diagenesis especially when one considers that variables within each category operate across non-discrete spatiotemporal boundaries and the magnitude of their influence on diagenesis can vary across time. Despite the inherently complex nature of mudrock diagenesis, the timing of fluid activity and temperature dependent diagenetic reactions can be recorded using paleomagnetism by way of chemical remanent magnetizations (CRMs) (e.g. Elmore et al., 2012). Paleomagnetic studies of Paleozoic sedimentary rocks in North America reveal CRMs related to illitization of smectite, migration of orogenic fluids, hydrothermal fluids, hydrocarbon migration and other diagenetic processes (McCabe and Elmore, 1989; Hirt et al., 1993; Katz et al., 2000; Dennie et al., 2012; Jackson and Swanson-Hysell, 2012; Roberts and Elmore, 2017). A common theme among these processes is some combination of elevated temperatures, fluid migration and chemical activity that facilitate neoformation of ferrimagnetic minerals. Understanding the timing of these processes can provide valuable insights regarding the evolution of sedimentary basins and

provide temporal constraints on key petroleum systems elements such as hydrocarbon migration (e.g. Magoon and Dow, 1994).

An additional, often overlooked component of diagenesis is a quantitative evaluation of how mudrock fabrics are shaped from deposition through burial. Mudrock textural analysis is usually a qualitative exercise where rocks are described by a bewildering set of nomenclature in service of inferring depositional environments and processes. These analyses are valuable, however, petrofabric analysis can offer an additional dimension to traditional textural analysis by adding information about particle alignment, intensity and preferred orientations. Anisotropy of magnetic susceptibility (AMS) is a high resolution tool that can provide such information which can be used to quantify processes such as compaction and tectonism (e.g. Borradaile, 1988; Schwehr et al., 2006). This tool is especially useful for mudrocks because clay, a major constituent of mudrocks, often dominates the magnetic susceptibility and therefore the magnetic fabric of mudrocks can reflect its overall rock fabric.

Chapter 2 develops this concept and explores the relationship between scalar AMS parameters and geochemistry using data collected from the Wolfcamp Shale in the Midland Basin. Novel relationships are developed to determine the contribution of paramagnetic minerals to magnetic susceptibility and delineate the control of clay alignment vs clay-concentration on scalar AMS parameters. After establishing the underlying controls on magnetic susceptibility, the degree of anisotropy ( $P_j$ ) and shape ( $T$ ) of the AMS ellipsoid across different lithofacies, I explore how these parameters, in conjunction with organic and inorganic geochemistry, can be used to interpret organic matter delivery, establish provenance lithotypes and describe pathways and barriers to hydrocarbon migration in the Wolfcamp Formation. Evidence of magnetic carrier minerals and proof of concept for the nature of  $P_j$  and  $T$  are provided through scanning electron microscopy

(SEM) and image analysis. SEM observations also provide the basis for a diagenetic paragenetic sequence which compliments the results in Chapter 3. A manuscript of Chapter 2 has been accepted by AAPG Bulletin earlier this year.

In Chapter 3, paleomagnetism is used to infer the absolute timing of illitization/chloritization in three Wolfcamp Formation cores. Through establishing the timing of this process, the timing of authigenic minerals which share textural relationships with chlorite can also be inferred. These findings are evaluated with respect to a burial history model for one core which provides additional context about evolving thermal conditions during subsidence/uplift. AMS in this study is used to determine the presence of tectonism in the Midland Basin and additionally, constrain the timing of ferroan dolomite formation. The work in Chapter 3 illustrates the potential of integrating several methods which operate at varying scales of observation along with basin modeling to reconstruct the sequence of diagenetic events and burial history of a given basin. A manuscript for this chapter has been submitted to AGU's G<sup>3</sup> journal.

Chapter 4 presents the first paleomagnetic and rock magnetic study of the Devonian Antrim Shale in the Michigan Basin. Stable isotope data, petrographic observations and paleomagnetic results point to hydrothermal fluids altering the Antrim, which until now, has only been successfully documented in underlying rocks in the Michigan Basin. The Antrim shale also represents an ideal case study to evaluate whether there are significant diagenetic differences between thermogenic and biogenically dominated natural gas formation. AMS data from the Antrim Formation indicate non-unique results suggesting that either long-lived paleocurrents or subtle tectonic shorting was active in the Michigan Basin. A detailed investigation of the origin of exotic minerals suggests that some of these minerals could be detrital in origin which can have implications for the structural evolution of the Michigan Peninsula.

Lastly, in Chapter 5, I summarize the findings from the preceding chapters and discuss how these findings illuminate which variable(s) represent first-order controls on mudrock diagenesis in their respective basins.

### Chapter 1 Figures

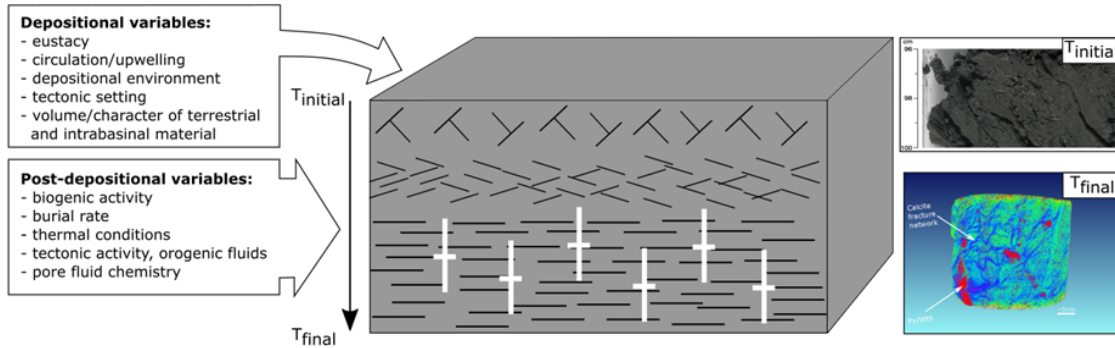


**Figure 1.** Schematic illustration of key variables involved in mudrock diagenesis. Model shows early ( $T_{initial}$ ) face-to-edge clay microstructures evolving to face-to-face contacts during progressive burial ( $T_{final}$ ). Mineralized fractures shown by white symbols form during burial. (top right) Organic rich hemipelagic sediment from modern environment represents initial diagenetic conditions. (bottom right) XRCT scan of complex mineralogy and fracture network in ancient mudrock represents a complex diagenetic end-member.

## REFERENCES

- Blatt, H., G. V. Middleton, and R. C. Murray, 1980, *Origin of Sedimentary Rocks*: 2nd edition: Englewood Cliffs, NJ, Prentice Hall Inc., 782 p.
- Borradaile, G.J., 1988, Magnetic susceptibility, petrofabrics and strain. *Tectonophysics*, 156(1), pp.1-20.
- Dennie, D., Elmore, R.D., Deng, J., Manning, E. B., and Pannalal, J., 2012, Paleomagnetism of the Mississippian Barnett Shale, Fort Worth Basin, Texas. Remagnetization and chemical alteration of sedimentary rocks: Geological Society of London, 371, 89–106, doi: 10.1144/SP371.10.
- Elmore, R.D., Muxworthy, A.R. and Aldana, M., 2012, Remagnetization and chemical alteration of sedimentary rocks. Geological Society, London, Special Publications, 371, pp.SP371-15.
- Elmore R. D., Heij, G.W. and Wickard, A.K, 2016, Paragenesis of mineralized fractures and diagenesis of prominent North American shales. *SEPM Sedimentary Record*, Vol 14, 4, 4-9.
- Hirt, A., A. Banin and A. Gehring, 1993, Thermal generation of ferromagnetic minerals from iron-enriched smectites. *Geophys. J. Int.*, 115: 1161–1168.
- Jackson, M. and Swanson-Hysell, N.L., 2012, Remagnetization and chemical alteration of sedimentary rocks: Geological Society of London Special Publication 371, 229 – 2551.
- Katz, B., Elmore, R.D., Cogoini, M., Engel, M.H. and Ferry, S., 2000, Associations between burial diagenesis of smectite, chemical remagnetization, and magnetite authigenesis in the Vocontian trough, SE France. *Journal of Geophysical Research: Solid Earth*, 105(B1), pp.851-868.
- Magoon, L.B. and Dow, W.G., 1994, *The petroleum system: chapter 1: Part I. Introduction*. AAPG Memoir 60, p. 3-24.
- McCabe, C. and Elmore, R.D., 1989, The occurrence and origin of late Paleozoic remagnetization in the sedimentary rocks of North America. *Reviews of Geophysics*, 27(4), pp.471-494.
- Schieber, J., Zimmerle, W. and Sethi, P.S., 1998, *Shales and mudstones (Volume I, Basin studies, sedimentology, and paleontology)*. Schweizerbart'sche Verlagsbuchhandlung, Stuttgart, E, 384 p.
- Schwehr, K., Tauxe, L., Driscoll, N. and Lee, H., 2006, Detecting compaction disequilibrium with anisotropy of magnetic susceptibility. *Geochemistry, Geophysics, Geosystems*, 7(11), doi:10.1029/2006GC001378.
- Roberts, J.M. and Elmore, R.D., 2017, A diagenetic study of the Woodford Shale in the southeastern Anadarko Basin, Oklahoma, USA: Evidence for hydrothermal alteration in mineralized fractures. *Interpretation*, 6(1), pp.SC1-SC1

## CHAPTER 2

# THE MAGNETIC FABRIC OF THE WOLFCAMP FORMATION, MIDLAND BASIN, WEST TEXAS: UNDERSTANDING PETROFABRIC VARIABILITY, HYDROCARBON DISTRIBUTION AND IRON ENRICHMENT

### ABSTRACT

Rock fabrics have long been recognized as a key variable influencing unconventional reservoir properties and yet, petrofabric analysis is rarely incorporated in reservoir characterization in a quantitative and scalable manner. This work introduces anisotropy of magnetic susceptibility (AMS) coupled with hand-held x-ray fluorescence (HHXRF) to define the origin of petrofabrics in the Wolfcamp Formation and examine their relationship with total organic carbon (TOC) and oil saturation indices (OSI). Standard paleomagnetic plugs were drilled from three vertical cores spanning the entire Wolfcamp Formation in the Midland Basin, West Texas. Low temperature magnetic experiments suggest paramagnetic minerals contribute between 93.4-98.6% of the low-field bulk magnetic susceptibility ( $k_{lf}$ ) across all lithotypes. Scanning electron microscopy revealed frequent occurrences of paramagnetic minerals such as chlorite, illite, ferroan dolomite, marcasite and pyrite. Fe-rich clays such as chlorite carry the AMS signal in mudrocks with a minor contribution from ferroan dolomite. Conversely, ferroan dolomite carries the AMS signal in most carbonate facies with a minor influence from Fe-rich clays. The degree of magnetic anisotropy ( $P_j$ ) and shape factor ( $T$ ) in mudrocks are compositionally dependent and respond to changes in both clay and framework grain concentration. For carbonate facies,  $P_j$  and  $T$  vary widely due to changes in depositional facies and the concentration of ferroan dolomite.

TOC strongly correlates with  $P_j$  and strongly oblate magnetic fabrics. This relationship likely stems from the adsorption of organic matter (OM) to clays during deposition and may

indicate that organoclay composites were responsible for delivering OM to the sediment-water interface. Elevated OSI are fabric selective, favoring low Pj and T fabrics suggesting that such fabrics facilitate hydrocarbon migration more so than high Pj and T fabrics. Fuzzy-c means clustering provides a framework to describe AMS and geochemical transitions at the core scale and could serve as a tool to map barriers and pathways to hydrocarbon migration.

Finally, Ti/Nb and  $k_{if}$  data points to a mafic provenance lithotype and suggests layered-intrusive complexes in the Central Basin Uplift were exposed and eroded during deposition of the Wolfcamp Formation. Mafic source rocks likely increased the supply of micronutrients such as dissolved iron and may have enhanced productivity in the Midland Basin.

## INTRODUCTION

The Wolfcamp Formation in the Midland Basin, West Texas, is a major unconventional resource with combined oil-bearing pay zones that span hundreds of meters (Friedrich and Milliken, 2013). According to estimates by the U.S geological survey, the Wolfcamp Formation contains an estimated average of 20 billion barrels of oil, 450 billion m<sup>3</sup> of associated natural gas, and 1.6 billion barrels of natural gas liquids (Gaswirth et al., 2016). Optimizing production from the Wolfcamp requires detailed reservoir characterization in order to identify zones that yield economic volumes of hydrocarbons. Reservoir characterization typically involves a battery of analyses such as visual core description, X-ray diffraction (XRD), source rock analysis (SRA), optical/electron microscopy, porosity and permeability measurements all in service to defining the petrophysical properties, depositional and diagenetic framework of unconventional reservoir rocks (e.g. Milliken et al., 2012). Despite the wealth of data obtained from these analyses, quantitative petrofabric data is rarely incorporated.

Magnetic petrofabrics are measured using anisotropy of magnetic susceptibility (AMS), a highly sensitive tool that rapidly measures the preferred alignment, degree of anisotropy, and shape of the AMS ellipsoid in a rock (e.g. Borradaile, 1988). In mudrocks, the dominant magnetic carriers are paramagnetic clays (e.g. illite, chlorite) which may constitute ~30 to ~60% of mudrock mineralogy (e.g. Parés, 2015) and therefore, the magnetic susceptibility and petrofabric is largely controlled by clays. Despite this, the presence of ferromagnetic (*sensu lato*) minerals (e.g. magnetite) must be constrained as their magnetic susceptibility is orders of magnitude greater than that of paramagnetic clays and can complicate petrofabric interpretations (e.g. McCabe et al., 1985; Richter and van der Pluijm, 1994; Martín-Hernández and Hirt, 2001; Martín-Hernández and Ferré,

2007). Previous AMS studies on mudrocks have primarily focused on tectonically formed fabrics, paleocurrent directions, and paleomagnetic investigations (e.g. Rochette, 1988; Aubourg et al., 1991; Schieber and Ellwood, 1993; Winkler et al., 1996; Chadima et al., 2006). These studies rely on oriented specimens in order to evaluate lineations related to stress fields or hydrodynamic forces. Specimens for this study were obtained from unoriented vertical cores which limits the applicability of tectonic or paleocurrent inferences from the orientation of AMS tensors. As a result, this study focuses primarily on the scalar parameters computed from AMS, specifically, the corrected degree of magnetic anisotropy ( $P_j$ ) and the shape factor ( $T$ ) (Jelinék, 1981). The interpretation of these parameters require no a priori knowledge of the geographical orientation of the specimen. Previous studies have shown that scalar AMS parameters can assess the degree of clay particle alignment and arrangement of clay aggregates (i.e. edge-to-face versus face-to-face clay domains) (Parés and van der Pluijm, 2004; Schwehr et al., 2006). This work explores the relationships between geochemistry and AMS parameters to develop a framework to describe clay microstructures and identify paramagnetic minerals. A simple model is proposed where clay microstructures and alignment inferred from AMS control the distribution and migration of hydrocarbons in unconventional reservoirs. Finally, integration of magnetic susceptibility with trace-element geochemistry offers a genetic-based solution to understanding iron-enrichment in the Wolfcamp Formation.

## **GEOLOGIC BACKGROUND**

The Permian Basin covers an area of  $\sim 190,000\text{km}^2$  and occupies most of West Texas and the Southeastern corner of New Mexico. A map and W-E cross section of the Permian Basin is shown in Figure 1 (modified from Flawn et al, 1961; Matchus and Jones, 1984; Engle et al., 2016). The Midland Basin represents one of several sub-basins within the foreland of the Marathon-

Ouachita fold-and-thrust belt (Figure 1). This basin is bordered by carbonate platforms along the north, east and western margins and is separated from the Val Verde Basin by the Ozona Arch to the south (Figure 1).

During the early Paleozoic through the Mississippian, the ancestral Tobosa Basin occupied the region and presumably formed a regional sag along a passive continental margin (Frenzel et al., 1988). Paleozoic sediments were deposited during this time and are comprised of shallow water carbonates and fine-grained siliciclastic rocks capped by organic-rich Devonian shales (Engle et al., 2016). In the late Mississippian, collision of North and South America resulted in the formation of the Marathon Ouachita fold-and-thrust belt. In response to this collision, the Tobosa Basin was segmented by intrabasinal uplifts (e.g. Central Basin Uplift) and sub-basins, most notably, the Midland and Delaware Basin (Ross, 1986; Yang and Dorobek, 1995). The fault bound Central Basin Uplift (CBU), which is now known as the Central Basin Platform (CBP) experienced differential uplift during the middle through late Pennsylvanian which caused the asymmetric basin geometries observed in the Midland and Delaware Basins (Yang and Dorobek, 1995) (Figure 1). The CBP hosts a large igneous body evidenced by aeromagnetic and gravity anomalies extending over an area of  $\sim 15,000\text{km}^2$  (Adams and Keller, 1994). Gabbroic rocks were recovered from the Nellie No.1 well at 1402m and were continuously encountered until a depth of 5822m (Kargi and Barnes, 1995 and references within) (Figure 1). Models developed by Adams (1995) and Keller et al., (1989) suggest four lobes of a laterally continuous intrusive complex, the largest of which is named the Nellie layered intrusive complex and, based on U-Pb dating, formed during the Proterozoic between 1073-1163Ma (Keller et al., 1989).

During the Pennsylvanian and Early Permian, carbonates were deposited onto the shelves (e.g., Northwest Shelf, Eastern Shelf, and Central Basin Platform) and fine-grained siliciclastic

sediments filled both the Midland and Delaware Basins (Engle et al., 2016). Deposition of the Wolfcamp Formation occurred within these rapidly subsiding depocenters and is broadly characterized by progradational and erosionally backstepping platform to basin sequences (Mazzullo and Reid, 1989). Following foreland development, the region experienced tectonic quiescence and gradual subsidence continued through the Mesozoic (Yang and Dorobek, 1995). The Marathon-Ouachita thrust belt has since been buried by Mesozoic and Cenozoic sediments, most of which have been removed due to Cenozoic uplift related to Laramide and Basin and Range tectonics (Sinclair, 2007). Additional noteworthy structural features in west Texas include a crystalline structural dome of Grenville affinity exposed at the Llano uplift and Paleozoic sedimentary/metasedimentary uplifts occurring further west along the fold-and-thrust belt (i.e. Marathon Uplift, Devils River Uplift) (Figure 1).

Cores for this study capture the entire Wolfcamp Formation spanning >300m and contain carbonate mass transport complexes (MTCs) of variable thickness and frequency, punctuated by siliceous mudrock facies. The depositional environment ranges from proximal shelf to distal slope. Siliceous mudrocks range from finely laminated to massive (Figure 2A). Carbonate MTCs are comprised of mud-supported and clast-supported debrites and turbidites some of which show evidence of slumping (Figure 2B, 2C). Following the turbidite classification scheme of Bouma (1962) turbidite facies occur as amalgamated  $T_a$  and  $T_b$  with occasional accompanying  $T_c$  sequences (Figure 2D). MTCs are dominated by allochthonous carbonate material (allochems and lithoclasts) and are broadly referred to as carbonate facies in this paper. Diagenetic facies include chert and pyrite replaced turbidites (primarily within the  $T_a$  sequence), carbonate concretions and phosphate nodule-rich siliceous mudrocks.

## METHODS AND SAMPLING

### *Sampling and data provided*

Three vertical cores were utilized for this study, two adjacent cores near the southeastern margin (Core 1 and 2) (Appendix 1) and one from the south central part of the Midland Basin (Core 3) (Figure 1). Full length plugs were extracted from slabs from each core and cut to standard paleomagnetic plugs (25 mm diameter x 22 mm height) (Core 1: 1783m - 1948.9m, n = 115; Core 2: 1954.7m - 2122m, n = 185 and Core 3: 2949.9m - 3010.2m, n = 64). Plugs were sampled at intervals of 3.0m – 5.0m for both Core 1 and 2 whereas for Core 3, a denser sampling scheme was employed (0.5m - 1.0m). This sampling scheme was chosen to capture lithofacies variability within each core. Thin sections were made from representative specimens for SEM and energy dispersive spectroscopy (EDS). Devon Energy and Pioneer Natural Resources provided Rock-Eval™ and total organic content (TOC) data. Oil saturation indices (OSI) were calculated from the Rock-Eval™ data using the formulation developed by Jarvie (2012) in order to evaluate the amount of producible oil.

### *Magnetic Experiments*

Magnetic experiments were performed using a KLY-4S Kappabridge magnetic susceptimeter and data were processed using Anisoft 4.2 (Chadima and Jeliněk, 2009). Low-field magnetic susceptibility ( $k_{lf}$ ) represents the degree of magnetization (M) of a material in response to an applied magnetic field (H) and is represented by volume normalized ( $k_{lf}$ ) or mass normalized ( $\chi$ ) units (e.g. Tarling and Hrouda, 1993). Magnetic susceptibility of diamagnetic and paramagnetic minerals is field-independent whereas for many ferromagnetic (*sensu lato*) minerals the magnetic susceptibility is a function of the applied field following a non-linear relationship between magnetization and the applied field (Hrouda et al., 2006). Multi-domain (MD) pyrrhotite, hematite

and titanomagnetite exhibit clear field-dependent susceptibility that follow the Rayleigh Law at fields  $< 300 \text{ A/m}$  (Worm et al, 1993; Hrouda, 2002; Hrouda, 2009), whereas, magnetite shows field-independent susceptibility (Jackson et al., 1998) and thus cannot be distinguished from paramagnetic behavior in this analysis. Consecutive magnetic susceptibility measurements from  $2 \text{ A/m}$  to  $700 \text{ A/m}$  were performed to evaluate the presence of field-dependent magnetic minerals. To test for the presence of magnetite, low temperature susceptibility measurements were performed using a modified experimental approach similar to that of Parés and van der Pluijm (2002) where samples are cooled to  $77 \text{ K}$  and subsequently measured until the sample reaches ambient temperature ( $\sim 297 \text{ K}$ ). Magnetite undergoes a change from a cubic to monoclinic crystal symmetry at temperatures below  $110\text{-}120 \text{ K}$  (known as the Verwey transition) and as a result its magnetic susceptibility is greatly reduced at low temperatures (e.g. Moskowitz et al., 1998). Low-field AMS was performed to measure the magnetic petrofabric. AMS is represented by a symmetric second rank tensor and may be plotted as a magnitude ellipsoid with three mutually perpendicular principal axes  $K_1$ ,  $K_2$  and  $K_3$  where  $K_1 > K_2 > K_3$ . Six independent matrix elements are required to describe the anisotropy tensor, however, more orientations provide over determinacy of the matrix diagonal which allows calculation of tensor fits by least squares methods (see Girder, 1961). The degree of anisotropy of the magnitude ellipsoid is described by the corrected degree of anisotropy ( $P_j$ ) and the shape of the ellipsoid can be described by the shape parameter ( $T$ ) (Jeliněk, 1981). An oblate magnetic fabric is observed when  $0 \leq T \leq 1$  and prolate when  $-1 \leq T \leq 0$ . Magnetic fabrics are considered normal when the principal magnetic axes ( $K_1$ ,  $K_3$ ) coincide with crystal shape axes (e.g. phyllosilicates) or inverse, where the  $K_1$  parallels the foliation and  $K_3$  parallels the lineation (e.g. ferroan dolomite) (Rochette, 1988). A combination of inverse and normal magnetic fabrics are known as mixed/intermediate fabrics (Ferré, 2002).

### ***Hand-held X-Ray Fluorescence (HHXRF)***

HHXRF analysis was undertaken on all plugs using a Bruker Tracer III-V HH-ED-XRF Spectrometer. Plugs were analyzed for major (Mg, Al, Si, S, K, Ca, Ti, Mn, and Fe) and trace (Ba, Cr, Ni, Zn, Zr, and Nb) elements for 90 seconds at 15kV and 60 seconds at 40kV, respectively. Raw X-ray spectra were calibrated using well-defined mudrock calibration reference materials (Rowe et al., 2012) and are reported in parts per million (ppm). Elemental abundances and ratios were used as proxies to infer both magnetic and bulk mineralogy, redox conditions and provenance lithotypes. Fe/S and Fe were used to evaluate the approximate contribution of non-iron-sulfides and total iron-bearing minerals to the magnetic susceptibility, Al were used as a proxy for clay concentration, Ni and Cr as redox indicators, Ca for carbonate concentration, Zr as a terrestrial source and textural maturity indicator, Si/Al for quartz concentration and Ti/Nb as a provenance lithotype indicator (i.e. basic vs. quartzofeldspathic) (e.g. Bonjour and Dabard, 1991; Tribovillard et al., 2006). Ti and Nb are not prone to remobilization during diagenesis making Ti/Nb a robust proxy for provenance analysis (Bonjour and Dabard, 1991). The Fe/S ratio serves as an *ad hoc*, first-order approximation of non-iron-sulfide minerals in the XRF scanning volume. Of course, this ratio is susceptible to the contribution of sulfur from other sources such as barite, sphalerite, gypsum and celestine. With the exception of a few samples (which were omitted from this calculation) most specimens from this study have concentrations of barium and zinc ranging from 0 to 100 ppm. Low concentrations of these elements are unlikely to completely invalidate the Fe/S ratio considering that sulfur concentrations typically fall between 10,000 and 20,000 ppm. The influence of celestine and gypsum are also considered to be insignificant because Sr covaries with Ca, suggesting that most of the Sr resides with carbonate minerals and neither celestine nor gypsum were detected after extensive electron microscopy. The weight % ratio for Fe and S in

pyrite/marcasite is  $\sim 0.87$ , therefore values exceeding 0.87 should reflect the presence of non-sulfurous iron-bearing minerals such as chlorite and ferroan carbonates. Ferrimagnetic sulfides such as greigite and pyrrhotite have higher ratios ( $\sim 1.3-1.5$ ) than pyrite but, constitute an extremely minor portion of the total iron-sulfide fraction in most sedimentary rocks and are therefore not likely to impact this ratio.

### ***Statistical clustering of variables***

Magnetic and geochemical data were organized into a lithomagneto-facies (LM) scheme using fuzzy c-means (FCM) clustering (concept first introduced by Zadeh (1996)) in order to evaluate chemical and fabric transitions in siliceous mudrocks from the densely sampled Core 3. Unlike “hard” clustering techniques (e.g. K-means), this style of multivariate statistical treatment allows for each data point to belong to more than one cluster and therefore describe transitions by way of assigning a membership coefficient to each observation based on fuzzy set theory (e.g. Dekkers et al., 1994; Everitt et al., 2011). FCM clustering and evaluation of its principal components via non-linear principal component mapping (Sammon, 1969) were performed in RStudio version 1.1.456. Prior to FCM clustering, the data were transformed to their natural log and standardized in order to achieve symmetric or normal distributions. Clustering was performed using a Euclidian dissimilarity measure and a membership coefficient of 2 (Gan et al., 2007). Mapping the principal components of the clustered data was used to aid in discriminating different clusters within the mudrock facies (Appendix). Cluster algorithms can perform poorly when there are outliers in the data, high degrees of collinearity among variables, or high skewness of the clustering variables (e.g. Everitt et al., 2011). To mitigate irregularities with clustering, both carbonate and visibly diagenetically altered facies were omitted from the analysis. Similarly, only one elemental proxy (e.g. Al = clay proxy, instead of both Al and K) was selected for clustering

to avoid issues with collinearity. The variables chosen for this FCM clustering included Si/Al (quartz proxy), Ca (carbonate proxy), Al (clay proxy), Ni (TOC proxy), Pj, T, and  $k_{lf}$ .

### ***Image Analysis***

Backscatter electron images were obtained with a FEI Scanning Electron Microscope (SEM) using FEI's Maps 2.0 software which automatically acquires high resolution images across defined areas and stitches them together to form image maps. Nine 200 $\mu\text{m}$  x 200 $\mu\text{m}$  maps were acquired for representative thin sections using a consistent 3 x 3 grid. Images were processed using ImageJ in order to separate matrix from framework/cement. Edge-filters and Gaussian smoothing were used to enhance grain boundaries and reduce image noise. Processed images were compared to unprocessed images to ensure valid segmentation of matrix from cement/framework grains. Ultra-fine grains (<5 $\mu\text{m}$ ), porosity and organic matter were designated as matrix and grains >5 $\mu\text{m}$  were designated as framework/cement. Error from this analysis would likely stem from an overestimation of the matrix however, the overall accuracy of this approach is sufficient to evaluate the role of matrix to framework/cement (M/F) ratios on magnetic anisotropy.

## **RESULTS**

Field-dependent susceptibility measurements indicate invariant behavior in both carbonate and siliceous mudrock facies (Figure 3A). Representative temperature-dependent susceptibility measurements broadly follow the Curie-Weiss law (no evidence for Verwey transitions) between ~100K and 297K in both siliceous mudrock and carbonate facies (Figure 3B). Following the numerical model established by Richter and van der Pluijm (1994), paramagnetic minerals contribute between 98.6 to 95.3% of the total susceptibility in mudrock facies and likewise with carbonate facies (93.4 to 96.9%). Bulk magnetic susceptibility ( $\chi$ ) values range from 1.98E-08 to

1.59E-07 m<sup>3</sup>/kg<sup>-1</sup> (mean = 5.81E-08 m<sup>3</sup>/kg<sup>-1</sup>) in mudrocks and from 1.44E-08 m<sup>3</sup>/kg<sup>-1</sup> to 1.05E-07 m<sup>3</sup>/kg<sup>-1</sup> (mean = 4.56E-08 m<sup>3</sup>/kg<sup>-1</sup>) in carbonate facies. A positive linear regression is observed for Fe/S vs.  $k_{lf}$  ( $r^2 = 0.85$ ) and Al vs.  $k_{lf}$  ( $r^2 = 0.55$ ) for mudrock facies in Core 3 (Figure 3C, 3D). Similar relationships exist for the Core 1 and 2 as well. Conversely, a poor correlation exists between Fe and  $k_{lf}$  ( $r^2 = 0.36$ ) in mudrock facies (Figure 4A). For carbonate facies, a positive linear regression is observed for both Fe vs.  $k_{lf}$  ( $r^2 = 0.53$ ) and Mg vs.  $k_{lf}$  ( $r^2 = 0.51$ ) (Figure 4B, 4C). T values represented by a color gradient in Figure 4C indicate that magnetic fabrics are dominantly oblate at Mg <10000 ppm and mostly prolate at Mg >10000 ppm. This threshold also broadly characterizes the change from predominately normal to inverse AMS fabrics (Figure 4C). Contrary to mudrock facies a poor relationship exists between Fe/S and  $k_{lf}$  ( $r^2 = 0.34$ ) for the carbonate facies (Figure 4D).

SEM and EDS analysis revealed the presence of authigenic iron-bearing minerals including chlorite, cubic pyrite, marcasite, framboidal pyrite and ferroan dolomite (Figure 5A-F and Appendix). Noteworthy textural features include multiple ferroan rims on euhedral/subhedral dolomite (Figure 5A-inset), corroded ferroan dolomite rims with warped clays along crystal margins (Figure 5B), overgrowths on framboids with trace amounts of Mn within the overgrowth (Figure 5D), widespread cubic pyritization in carbonate facies and “spearhead” crystal habits in certain iron sulfides (Figure 5E, 5F).

Ti/Nb ratios were plotted against Zr and with each data point colored by their magnetic susceptibility in order to elucidate provenance lithotypes (Figure 6A). This analysis was limited to mudrock facies because MTC facies would subject trace-elements to sorting artifacts during deposition (e.g. Condie et al., 1995). Two distinct groups emerge within siliceous mudrock facies across all Cores: 1) high Ti/Nb ( $\geq 430$ ) and lower Zr (mean = 89.7ppm) with increased magnetic

susceptibility (mean  $k_{lf} = 2.78E-04$  SI and 2) low Ti/Nb ( $\geq 430$ ) and higher Zr (mean = 123.5 ppm) with decreased magnetic susceptibility (mean  $k_{lf} = 2.18E-04$  SI) A third, less defined grouping occurs in the lower left domain of Figure 6A and corresponds to specimens with allochthonous carbonates and/or significant chert replacement.

Group 1 occurs more frequently in the lower Wolfcamp whereas Group 2 typically occurs in the Upper Wolfcamp (see Appendix for stratigraphic boundaries). Comparison of magnetic susceptibility of the Wolfcamp to other mudrock units in North America, specifically the Haynesville, Marcellus, Antrim and Woodford (Anadarko and Ardmore Basins) indicates that magnetic susceptibility is significantly greater (24.8% to 82.8%) than mudrocks from these basins (Steullet, 2014; Rose, 2015; Roberts; 2016) (Figure 6B).

P<sub>j</sub> values were compared to Al, Ca and Si/Al ratios to examine the role of clay concentration and framework minerals (carbonate and quartz) on magnetic anisotropy in siliceous mudrocks (Figure 7A, 7B). In low-Ca (<60,000 ppm) siliceous mudrocks, Al has a linear relationship with P<sub>j</sub> whereas high-Ca (>60,000 ppm) siliceous mudrocks have no obvious relationship with Al (Figure 7A). To test the role of framework grains (specifically quartz) on magnetic anisotropy, P<sub>j</sub> was normalized with Al and plotted against Si/Al (Figure 7B). Linear trends emerge in both Ca-poor (<60,000 ppm) and Ca-rich (>60,000 ppm) siliceous mudrocks. Outliers in Figure 7B usually correspond to prolate, low anisotropy facies with excessive chert replacement and/or widespread pyritization. In carbonate facies, P<sub>j</sub> broadly decreases with increasing Ca and higher P<sub>j</sub> specimens typically have increased Al concentration (Figure 8A). P<sub>j</sub>/Al vs. Si/Al shows three distinct trends with increasing Ca that also correspond to facies type (Figure 8B). The slope of regression lines for each facies coincides with the relative concentration of clay and ferroan dolomite observed in each facies.

Representative image analysis outputs, unprocessed backscattered images and statistics are shown in Figure 9. In low-Ca siliceous mudrocks, high matrix to framework/cement ratios correspond to elevated magnetic anisotropy and strongly oblate AMS ellipsoids. Conversely, in high-Ca siliceous mudrocks, low matrix to framework/cement ratios exhibit lower magnetic anisotropy and moderately oblate to weakly prolate AMS ellipsoids.

P<sub>j</sub> also has positive correlations with TOC, Ni, Cr and Ti/Nb ratios in mudrock facies (Figure 10A-D). Contour plots of P<sub>j</sub> and T modulated by TOC and OSI respectively for all lithotypes are shown in Figure 11A and 11B. Dominantly oblate and strongly anisotropic samples are associated with elevated TOC (Figure 11A). In contrast, low anisotropy, dominantly prolate samples exhibit higher OSI although, there are exceptions (Figure 11B). SEM observations provide evidence of organoclay composites occurring more frequently in strongly oblate, high magnetic anisotropy samples (Figure 11C, 11D). Although less frequently observed, organic matter unassociated with clays does occur in the Wolfcamp such as organic matter occupying intergranular pores in carbonates and wispy organic matter microtextures in siliceous mudrocks (Figure 11E, 11F).

Using the variables outlined in the Methods section, FCM revealed two principal clusters for siliceous mudrock facies in Core 3 (Figure 12). Visualization of the clustered data using its principal components suggest that the variation in the data is best explained by two clusters (Appendix). The membership coefficient for each cluster is displayed by the LM profile and a schematic representation of each cluster was drawn to illustrate fabric transitions. Cluster 1 is characterized by increased values of Ni, T, k<sub>if</sub>, P<sub>j</sub>, Al and decreased values of Si/Al and Ca whereas Cluster 2 is characterized by the inverse (Figure 12). The LM profile displays several sections (e.g. 2950m – 2954m) dominated by one facies as well as sections with rapid facies shifts (e.g. 2978m

- 2982m) (Figure 12). A prominent gradation occurs from mixed Cluster 1 and 2 at the terminus of the MTC (2975m) until a membership coefficient of 1 in Cluster 1 is reached (2966m). This gradation also occurs in reverse (i.e. from dominantly Cluster 2 to Cluster 1) directly above this interval.

## DISCUSSION

### *Magnetic architecture*

Invariant field-dependence and the absence of Verwey transitions in low temperature experiments suggests little to no contribution from stoichiometric magnetite or MD grains of titanomagnetite, pyrrhotite and hematite to the magnetic susceptibility in both carbonate and mudrock facies (Figure 3A, 3B). However, a suppressed Verwey transition owing to the presence of SD titanomagnetite or maghemite cannot be completely discounted (Özdemir et al., 1993; Moscovitz et al., 1998). The presence of superparamagnetic (SP) or single-domain (SD) pyrrhotite could not be precisely determined, however, examination of temperature-dependent susceptibility data indicates that samples approach near ideal paramagnetic behavior following the scheme developed by Richter and van der Pluijm (1994). This suggests that if SP/SD pyrrhotite is indeed present, it constitutes a volumetrically insignificant fraction and therefore, its impact on the magnetic susceptibility and its anisotropy is minor.

Among siliceous mudrocks,  $k_{lf}$  values and their correlation with Fe/S and Al, along with petrographic observations, affirm that paramagnetic iron-rich clays control the magnetic susceptibility. A significantly improved correlation coefficient for Fe/S vs.  $k_{lf}$  compared to Fe vs.  $k_{lf}$  suggests that iron-sulfides have little effect on the magnetic susceptibility in mudrocks (Figure 3C, 4A). Similar correlation coefficient improvements are observed in both Core 1 and 2

suggesting that this ratio appears to constrain, at least as a first-order approximation, whether or not iron-sulfides (e.g. pyrite) contribute to the magnetic susceptibility especially when other sulfur-bearing minerals are in low abundance (e.g. gypsum).

For carbonates, the relationship between Fe and  $k_{lf}$  (Figure 4B) is better defined than Fe/S vs.  $k_{lf}$  (Figure 4D). This suggests that normalization of iron-sulfides using the Fe/S ratio is not appropriate for these rocks and iron sulfides contribute to the magnetic susceptibility to some extent. Aside from Fe, Mg exhibits a reasonable correlation with  $k_{lf}$  (Figure 4B). Among major rock forming minerals in sedimentary rocks, Mg resides within carbonate minerals and clay. No correlation exists between Al (clay) and  $k_{lf}$  in carbonates therefore, the Mg vs.  $k_{lf}$  correlation observed in Figure 4C likely indicates the concentration of ferroan carbonates, specifically ferroan dolomite which is frequently observed via SEM. Ferroan dolomite exhibits inverse AMS tensors with prolate shapes (Rochette, 1988). An apparent threshold of 10,000ppm Mg represents the transition from prolate to oblate dominated magnetic fabrics (Figure 4C). This threshold also broadly characterizes the boundary from predominantly mixed/inverse AMS fabrics to chiefly normal AMS fabrics (Rochette et al., 1992; Ferré, 2002). Overall, the combination of inorganic chemistry, AMS tensor orientations and scalar AMS data all suggest that magnetic susceptibility in carbonates is controlled by ferroan dolomite specifically ferroan dolomite with lesser contributions from iron sulfides and Fe-rich clays.

### ***Diagenesis***

SEM observations indicate complex paragenesis among iron-bearing minerals. Ferroan dolomite likely formed during early diagenesis given its euhedral/subhedral habit and clay fabrics conforming around many rhombs (Figure 5A, 5B). Multiple ferroan rims are observed in several

grains and several pyrite framboids have overgrowths (Figure 5A-inset, 5D). Framboids form due to bacterial sulfate reduction (BSR) and are a hallmark of early diagenesis in marine sediments (e.g. Berner, 1970; Sweeney and Kaplan, 1973). Trace amounts of Mn suggests that Mn-reduction occurred coeval with or immediately following BSR (Canfield and Thamdrup, 2009). The relative timing of overgrowths on framboids is uncertain, however, considering the encapsulation of framboids by sphalerite (Figure 5D), framboids rims formed prior to authigenic sphalerite. Pyrite overgrowths and abundant ferroan dolomite are consistent with a protracted iron supply, particularly during early diagenesis.

Authigenic chlorite, marcasite, sphalerite and cubic pyrite likely formed during late diagenesis (Figure 5C, 5E, 5F). Chlorite forms between 40-120°C and generally undergoes a solid-state transformation from montmorillonite to chlorite (e.g. Beaufort et al., 2015). Cubic pyrite tends to form during late diagenesis as a result of thermal sulfate reduction (TSR) (Machel et al., 1995). Figure 5F shows marcasite evidenced by the “spearhead” crystal habit. Marcasite generally forms from precursor pyrite and precipitates at low pH (Taylor and Macquaker, 2000; Schieber, 2011). Low pH conditions during burial may have developed during the maturation of organic matter which releases carboxylic acid into pore fluids (e.g. Jaffe et al., 1988). Acidic pore fluids could have caused partial corrosion of iron-carbonates (e.g. Figure 5B) and thereby provide a source of iron for authigenic chlorite precipitation (Hiller, 1993).

### ***Provenance and Iron-enrichment in the Wolfcamp***

A first order compositional control on sedimentary rocks is the type of provenance material delivered to the basin (Heins and Kairo, 2007). In most foreland systems, fold-and-thrust belts (FTB) often serve as the primary source of material eroded and deposited into the basin (DeCelles,

2003). Examination of trace-element geochemistry and magnetic susceptibility reveals two main provenance lithotypes (Figure 6A). Group 1 represents dominantly mafic provenance material broadly confined to the Lower Wolfcamp whereas Group 2 indicates more quartzofeldspathic source material supplied to the Upper Wolfcamp. Possible origins of mafic material to the Midland Basin are not immediately apparent because regionally, modern exposures of pre-Permian mafic rocks are virtually absent, with the exception of minor serpentinite outcrops at the Llano uplift (Figure 1). Apatite fission track (AFT) data collected at the Llano exposure suggests that it was buried during the Marathon-Ouachita orogeny (Corrigan et al., 1998) and therefore represents an unlikely source of ferromagnesium material to the Midland Basin. Elevated Ti/Nb ratios from Group 1 are probably a result of uplifted and eroded layered intrusive complexes from the CBU. This claim is consistent with the kinematic history of the CBU which can be summarized by three main phases: 1) the CBU existed as a low-relief feature during the middle Paleozoic evidenced by stratigraphic geometries (Schumaker, 1992); 2) mild, followed by intense uplift started during the middle Pennsylvanian based on sudden changes in thickness of Pennsylvanian through Lower Permian rocks (Yang and Dorobek, 1995) and 3) seismic evidence suggests that the CBU is comprised of several asymmetric blocks, that were differentially uplifted and eroded during the late Pennsylvanian to form a relatively flat surface (Yang and Dorobek, 1995). This third phase is likely responsible for erosion of some fraction of the layered intrusive complex to the Midland Basin. Mafic material was probably delivered to the neighboring Delaware basin simultaneously and perhaps, in greater quantities based on the differential uplift of the CBU, however, further studies are required to validate this hypothesis. In addition to iron derived from the CBU, intrabasinal iron mobilization during diagenesis or transport from the shelf via MTCs likely contributed to iron enrichment in the Wolfcamp as well (Raiswell and Anderson, 2005). Alongside

other factors such as paleoclimate, increased iron (a key micronutrient for benthic organisms) delivered to the basin could have enhanced organic productivity leading to more organic material reaching the basin floor during the deposition of the lower Wolfcamp. This may be a significant contributing factor to why such vast quantities of hydrocarbons occur in the Delaware and Midland Basins.

The apparent transition from a mafic influenced (Group 1) to quartzofeldspathic provenance (Group 2) in the Midland Basin could be a result one or some combination of processes such as: 1) increased sediment contributions from the Marathon-Ouachita fold-and-thrust belt or 2) a shift in provenance lithotype(s) from the CBU. Magnetic susceptibility data from other mudrocks in North American basins (including foreland basins) further supports an iron-enrichment mechanism specific to the Midland Basin (Figure 6B). An appreciable population of mudrocks have both low Ti/Nb and low Zr concentrations with variable magnetic susceptibility across the entire Wolfcamp (Figure 6A). This population likely represents dominantly intrabasinal provenance material (e.g. biogenic silica and redeposited carbonate material).

### ***Mechanisms for fabric variability in mudrocks***

P<sub>j</sub> has a strong clay-concentration dependency among low-Ca siliceous mudrocks and no obvious relationship with high-Ca siliceous mudrocks (Figure 7A). Clay normalized P<sub>j</sub> (log P<sub>j</sub>/Al) shows a positive linear correlation among both low and high-Ca siliceous mudrocks (Figure 7B). A linear relationship for low-Ca siliceous mudrocks is expected considering that as quartz framework grains increase, clay concentration decreases proportionally and vice-versa. From a textural standpoint, this means that in low-Ca siliceous mudrocks, clay particle alignment stands a function of both framework (quartz) and clay concentration (Kawamura and Ogawa, 2002;

Schwehr et al., 2006; Parés, 2015). The role of framework grains on  $P_j$  is also confirmed petrographically, with higher M/F ratios coinciding with increased  $P_j$  (Figure 9). Interestingly,  $P_j$  for high-Ca siliceous mudrocks also have a clear relationship with quartz concentration (Figure 7B) but no relationship with clay concentration (Figure 7A). Perhaps at  $Al < 55000\text{ppm}$ , clays no longer dominate the magnetic susceptibility and ferroan carbonates begin to exert a greater influence on the clay concentration-dependent component of magnetic anisotropy in siliceous mudrocks. The introduction of more ferroan dolomite will however, further impact clay alignment (e.g. clay warping in Figure 5B) and therefore, the linear relationship observed among high-Ca siliceous mudrocks will remain. The change in regression line slope in Figure 5B probably results from the introduction of more ferroan dolomite. By eliminating the clay concentration dependency of  $P_j$  through normalization with Al, it may be possible discriminate fabrics controlled purely by clay alignment from fabrics controlled by both clay concentration and their overall alignment.

### ***Mechanisms for fabric variability in carbonates***

Magnetic fabric variability in carbonates is largely controlled by depositional facies (Figure 8A). Mud-supported debrites show higher  $P_j$  values which indicate that clays exert some control on the magnetic fabric. Turbidites show both low and high anisotropy signatures, with higher anisotropy in  $T_e$  sequences and lower anisotropy in  $T_a$  and  $T_b$  sequences. Such trends likely reflect hydrodynamic partitioning from carbonate clast-supported ( $T_a$  and  $T_b$ ) to more clay-rich facies ( $T_e$ ). Clast-supported debrites exhibit low anisotropy which probably indicate a ferroan dolomite controlled susceptibility. As a first order approximation, carbonate facies (with the exception of mud-supported debrites) are primarily composed of quartz and carbonate material of which some fraction is ferroan dolomite. The change in slope between low-Ca to high-Ca trends in Figure 8B

may represent the relative concentration of ferroan dolomite to clay as a function of quartz. Examination of the low-Ca slope in Figure 8B relative to the high-Ca slope in Figure 8B shows a significant difference in gradient. Among carbonate facies, these cross plots may also prove useful to discriminate clay-dominated from ferroan carbonates controlled magnetic fabrics which often are the dominant paramagnetic carriers in carbonates (Tarling and Hrouda, 1993).

Rock magnetic methods are generally performed in order to define the ferromagnetic mineralogy and granulometry (e.g. IRM unmixing, magnetic hysteresis, thermomagnetic experiments), however, these experiments can be destructive, time consuming and offer little means to extract which specific paramagnetic minerals contribute to the magnetic fabric of sedimentary rocks. Simple geochemical relationships with magnetic properties such as those presented here can provide valuable constraints on the contribution of different paramagnetic minerals to magnetic susceptibility and evaluate whether magnetic fabrics are shaped by the concentration of clays, their alignment or both.

### ***Magnetic fabrics and TOC***

The linear relationship between P<sub>j</sub> vs. TOC likely stems from adsorption of organic matter (OM) to iron-rich clays. Adsorption of OM with clays occurs primarily due to van der Waals interactions, ligand exchange and cation bridging (Arnarson and Keil, 2000). Experimental work by Satterberg et al. (2003) suggest that montmorillonite has the greatest affinity for organic matter owing to its high cation exchange capacity. In addition to pelagic fall-out, iron-rich montmorillonite could have played a vital role in delivering organic matter to the sediment-water interface and later, during diagenesis transformed to chlorite and illite. The correlations observed with P<sub>j</sub> vs. Ni and P<sub>j</sub> vs. Cr (Figure 10B, 10C) further support this claim, as both Ni and Cr can

reside in the octahedral sites of chlorite (e.g. DeCaritat et al., 1993). Ni and Cr also have good correlations with TOC and suggests that anoxic conditions were present during deposition (Tribovillard et al., 2006). Lastly, the Pj vs. Ti/Nb ratio further affirms that mafic source material played a vital role in organic matter production by providing nutrients to drive productivity in the Midland Basin.

SEM observations provide evidence of the association between organic matter and chlorite (Figure 11C, 11D). In addition to organoclay composites shown in figure 11C and 11D, organic matter also occurs independently of clays (Figure 11E, 11F) although such features are less frequently observed. Contour plots of Pj vs. T modulated by TOC shows that in addition to increasing Pj, TOC tends to be associated with strongly oblate fabrics (Figure 11A). Kennedy et al. (2002) demonstrated that up to 85% of TOC variation in black shales can be explained by the surface area of clays. Strongly oblate magnetic fabrics potentially represent the optimal mineral surface area for TOC adsorption. Pj vs. T contour plots modulated by OSI show essentially the opposite behavior suggesting that released hydrocarbons favor low anisotropy, triaxial to prolate fabrics which often result from high concentrations of ferroan dolomite (Figure 11B). Such fabrics are generally framework dominated and are more likely to behave as conduits for hydrocarbon migration. A key factor controlling permeability pathways in mudrocks is clay petrofabric (Daigle and Dugan, 2011). The underlying mechanism for OSI favoring certain fabric types could result from less tortuous permeability pathways owing to lower degrees of clay particle alignment (Backeberg et al., 2017). This is most likely the case in low anisotropy, prolate/triaxial fabrics. However, increased OSI does not exclusively reside in low anisotropy, prolate magnetic fabrics. Isolated high OSI in oblate domains in Figure 11B could represent released hydrocarbons residing in pores occurring in organic matter intercalated with clays (Figure 11C). This highlights the

importance of performing detailed SEM analysis to ascertain the microstructural associations of OM with AMS fabric types.

An outstanding issue for those working at the core scale is effectively upscaling core data to an entire reservoir. Construction of LM profiles, such as the one in this study, could be a useful means to scale high resolution petrofabric data and perhaps, correlate this data to adjacent cores in a given basin (Figure 12). If the distribution of hydrocarbons does show a petrofabric control, such profiles could be useful in determining the relative propensity for petrofabrics to inhibit or facilitate hydrocarbon migration (Figure 12). For example, sections dominated by Cluster 1 are likely to inhibit hydrocarbon migration relative to Cluster 2. Aside from mapping potential migration pathways, LM profiles may reflect depositional processes such as the apparent fining-up sequence immediately following the MTC (Figure 12). Once the magnetic architecture is established, integration of LM profiles with other standard core analysis techniques may provide a more holistic approach to understanding sedimentological processes operating in fine-grained rocks.

## CONCLUSIONS

1. The AMS carriers in the Wolfcamp include iron-rich clays and ferroan dolomite with iron-rich clays dominating magnetic susceptibility in mudrock facies and ferroan dolomite controlling magnetic susceptibility in carbonate facies. The use of non-destructive low-temperature magnetic methods and inorganic geochemistry can establish the total contribution of paramagnetic minerals and delineate the types of paramagnetic minerals contributing to the magnetic susceptibility.
2. Pj in mudrocks stands a function of clay concentration and framework minerals. The Pj/Al ratio plotted against the dominant framework mineral (i.e. quartz) could be a useful means

to assess the degree to which  $P_j$  results from the alignment of clays in mudrocks. The slope of such plots may also indicate the relative abundance of clay and ferroan dolomite in sedimentary rocks.

3.  $P_j$  variability in carbonates is largely facies dependent with “cleaner” carbonates dominated by ferroan dolomite and mud-rich carbonates dominated by clays.
4. Abundant iron-rich authigenic minerals, high magnetic susceptibility (relative to many other North American mudrocks) and Ti/Nb ratios suggest mafic source material was delivered to the Midland Basin. The most likely source would be uplifted layered intrusive complexes that form part of the Central Basin Uplift.
5. The  $P_j$ /TOC relationship probably stems from organic matter adsorption to iron-rich clays. This relationship could be useful in other fine-grained rocks to establish whether or not clays are responsible for delivering OM to the sediment water interface in marine settings. Additionally, the association of TOC with strongly oblate fabrics affirms that mineral surface area of clays represent a key control on adsorption of OM to clays.
6. TOC and OSI in the Wolfcamp is fabric selective and suggests that petrofabrics exert a significant control migration pathways.

The integration of AMS with XRF and existing analysis performed on unconventional reservoir rocks can provide both petrophysical and geological insights that can add an additional dimension to unconventional reservoir characterization. These methods are rapid, cost effective, require little sample preparation and could address the problem of connecting scales of observation in unconventional reservoir characterization.

## Chapter 2 Figures

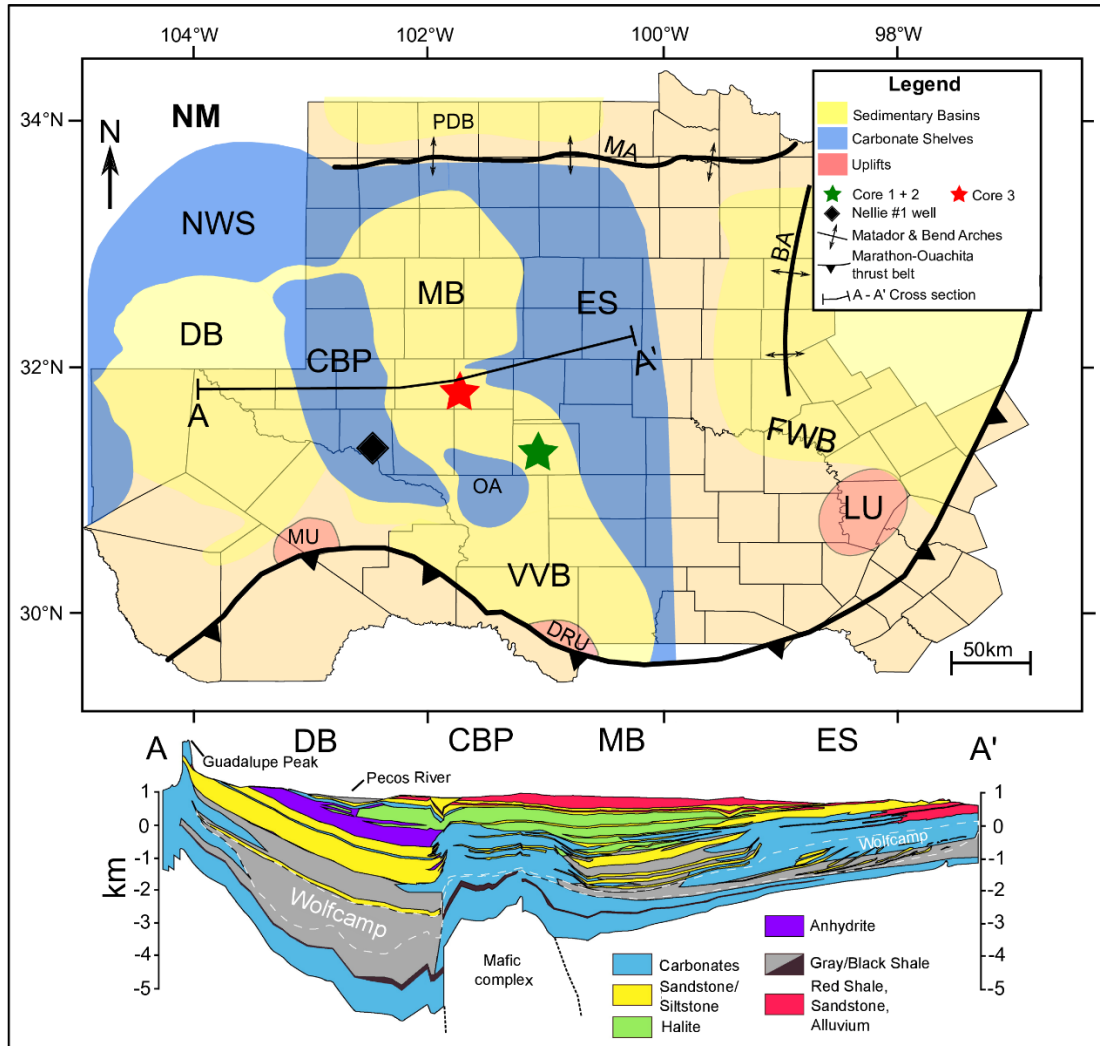


**Figure 1.** Map of Permian Basin in West Texas with major structural features and core locations. Modified from Flawn et al. (1961). Green Star = Core 1 and 2; Red Star = Core 3; Diamond = Nellie #1 well; BA – Bend Arch; CBP – Central Basin Platform; DB – Delaware Basin; DRU – Devil Rivers Uplift; ES – East Shelf; FWB – Fort Worth Basin; LU – Llano Uplift; MA – Matador Arch; MB – Midland Basin; MU – Marathon Uplift; NM – New Mexico; NWS – North West Shelf; OA – Ozona Arch; PDB – Palo Duro Basin; VVB – Val Verde Basin. A generalized cross section (A-A') of the Permian Basin with stratigraphic boundaries of the Wolfcamp shown by dashed lines. Modified from Matchus and Jones (1984) and Engle et al. (2016).

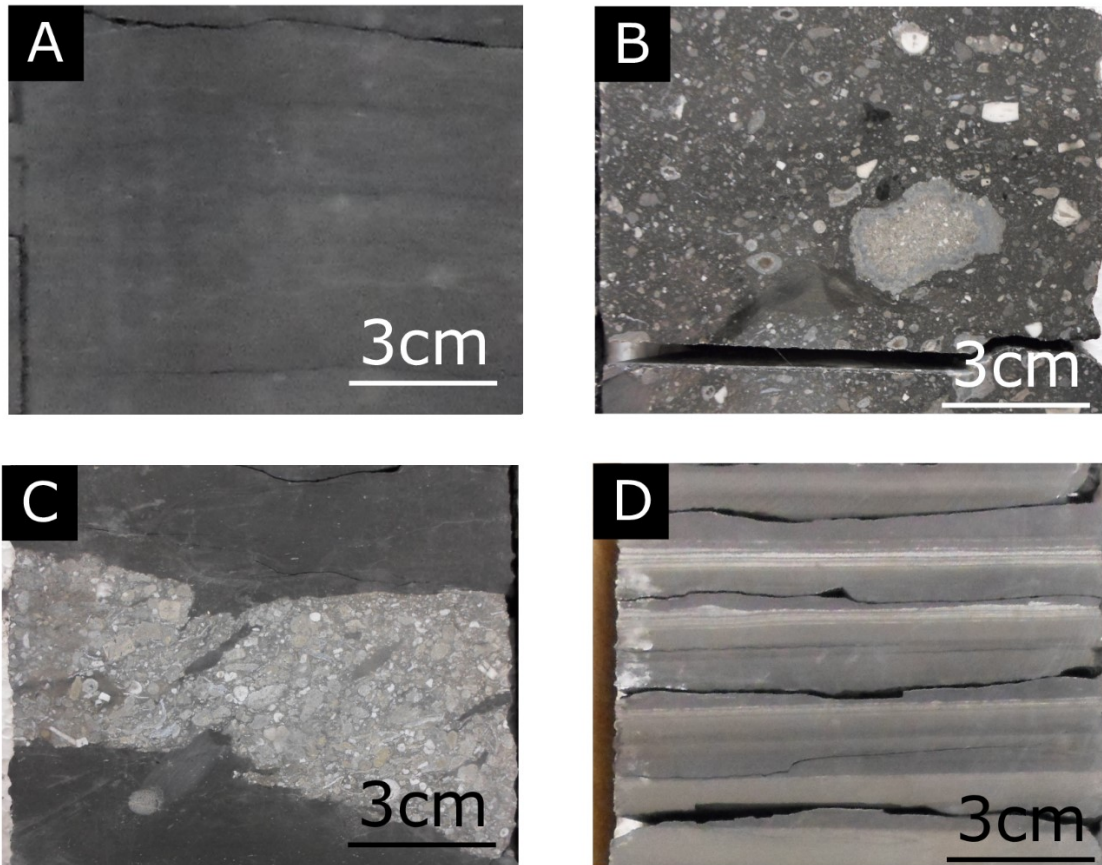


**Figure 2.** (A) Example of massive siliceous mudrock facies from Core 3; (B) mud-supported carbonate debris facies from Core 2; (C) clast-supported carbonate debris facies from Core 1; (D) high frequency turbidites comprised mostly of Ta, Tb and Te sequences from Core 1.

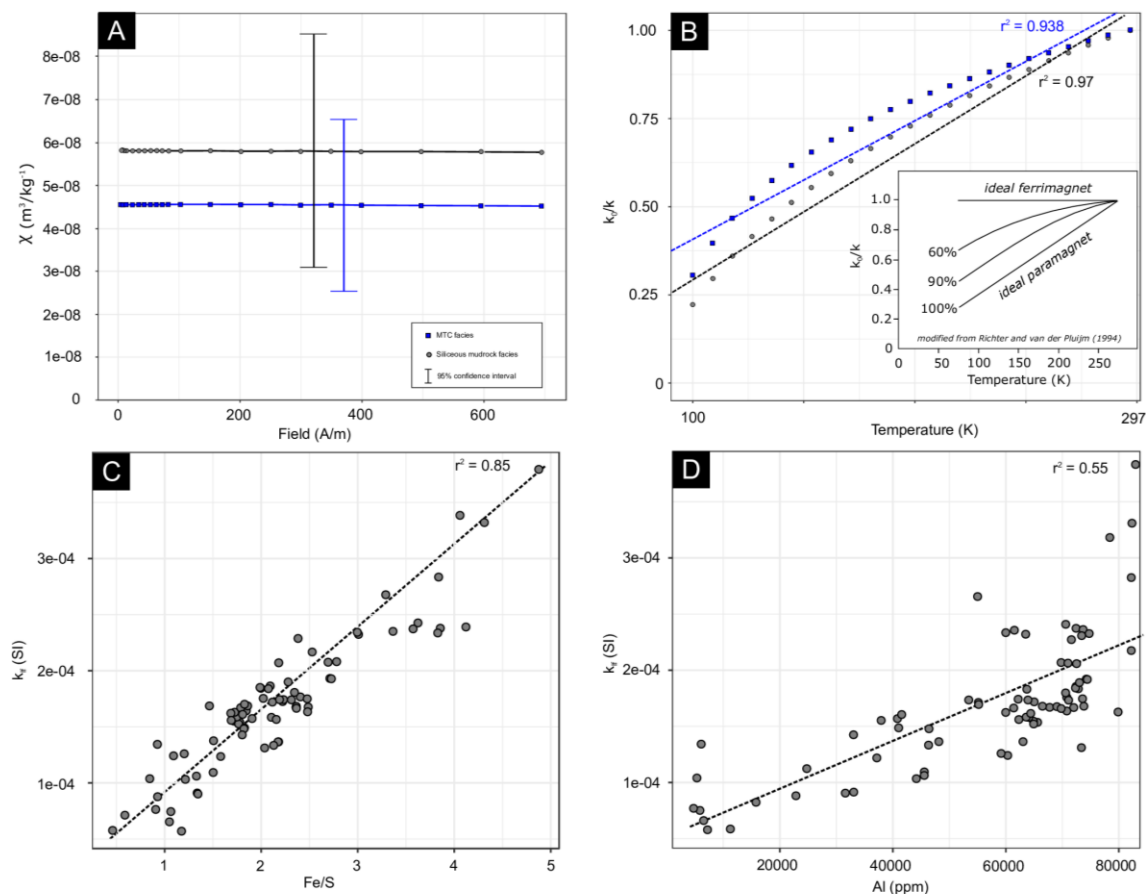


**Figure 3.** (A) Field-dependent magnetic susceptibility with 95% confidence intervals of specimens from Core 1 - 3. Note invariant behavior for both mudrock and carbonate facies. (B) Normalized reciprocal magnetic susceptibility ( $k_0/k$ ) vs. temperature for representative carbonate and mudrock facies from Core 2. Inset shows numerical model of ideal ferrimagnetic to ideal paramagnetic behavior from Richter and van der Pluijm (1994). (C) Cross plot of  $k_{if}$  vs. Fe/S in Core 3. (D) Cross plot of  $k_{if}$  vs. Al in Core 3.

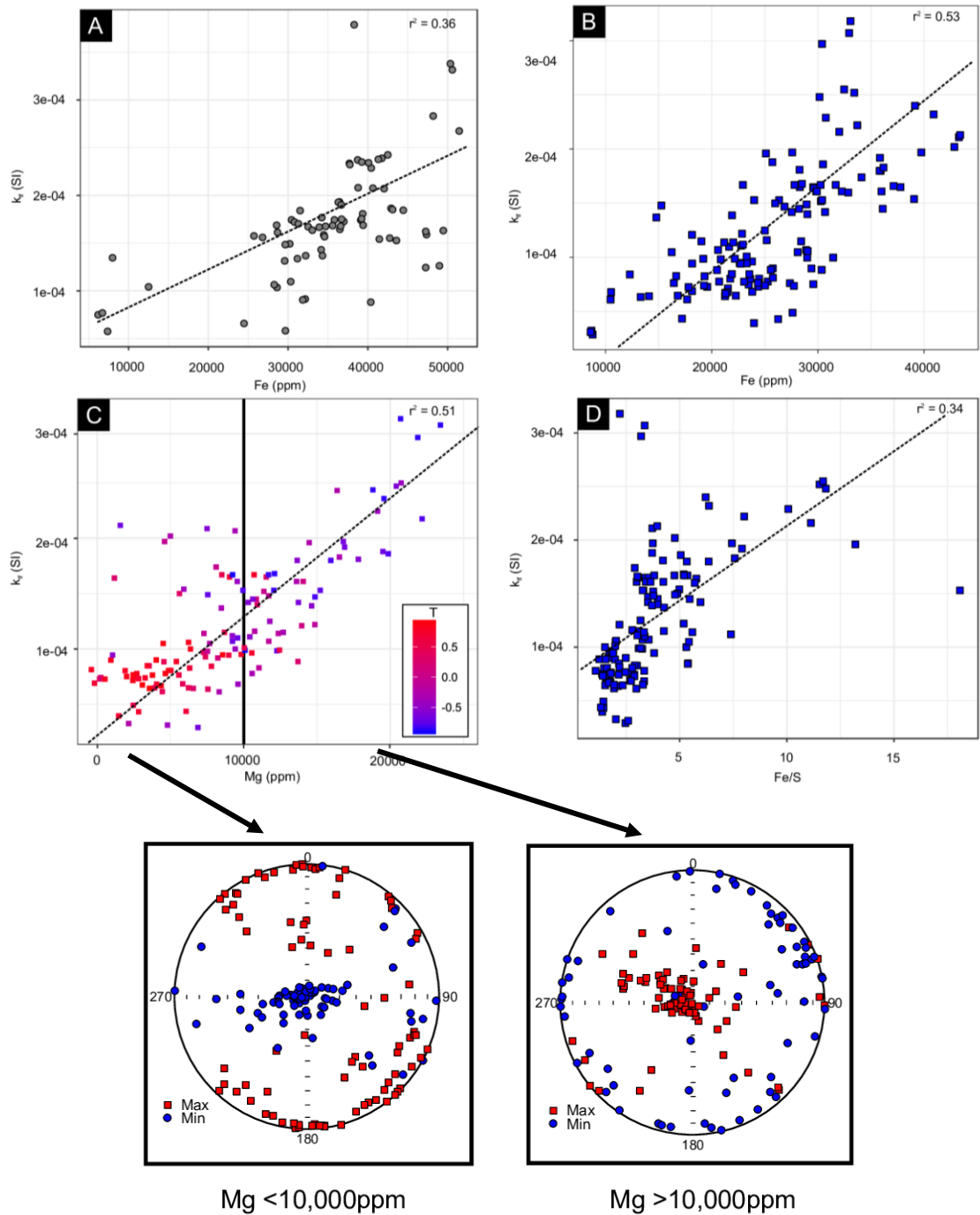


**Figure 4.** (A)  $k_{If}$  vs. Fe for siliceous mudrocks in Core 3. Note r-squared values for  $k_{If}$  vs. Fe/S compared to  $k_{If}$  vs. Fe in Figure 3C. (B) Cross plot of  $k_{If}$  vs. Fe from Core 2. (C) Cross plot of  $k_{If}$  vs. Mg for carbonate facies from Core 2 (with data points colored by corresponding T values). Insets show AMS stereonets (specimen coordinates) of representative specimens with predominately normal AMS fabric at Mg concentrations < 10,000ppm and mostly inverse AMS fabric at concentrations > 10,000ppm. (D) Fe/S for carbonate facies from Core 2. Note reduced r-squared value relative to Figure (B).

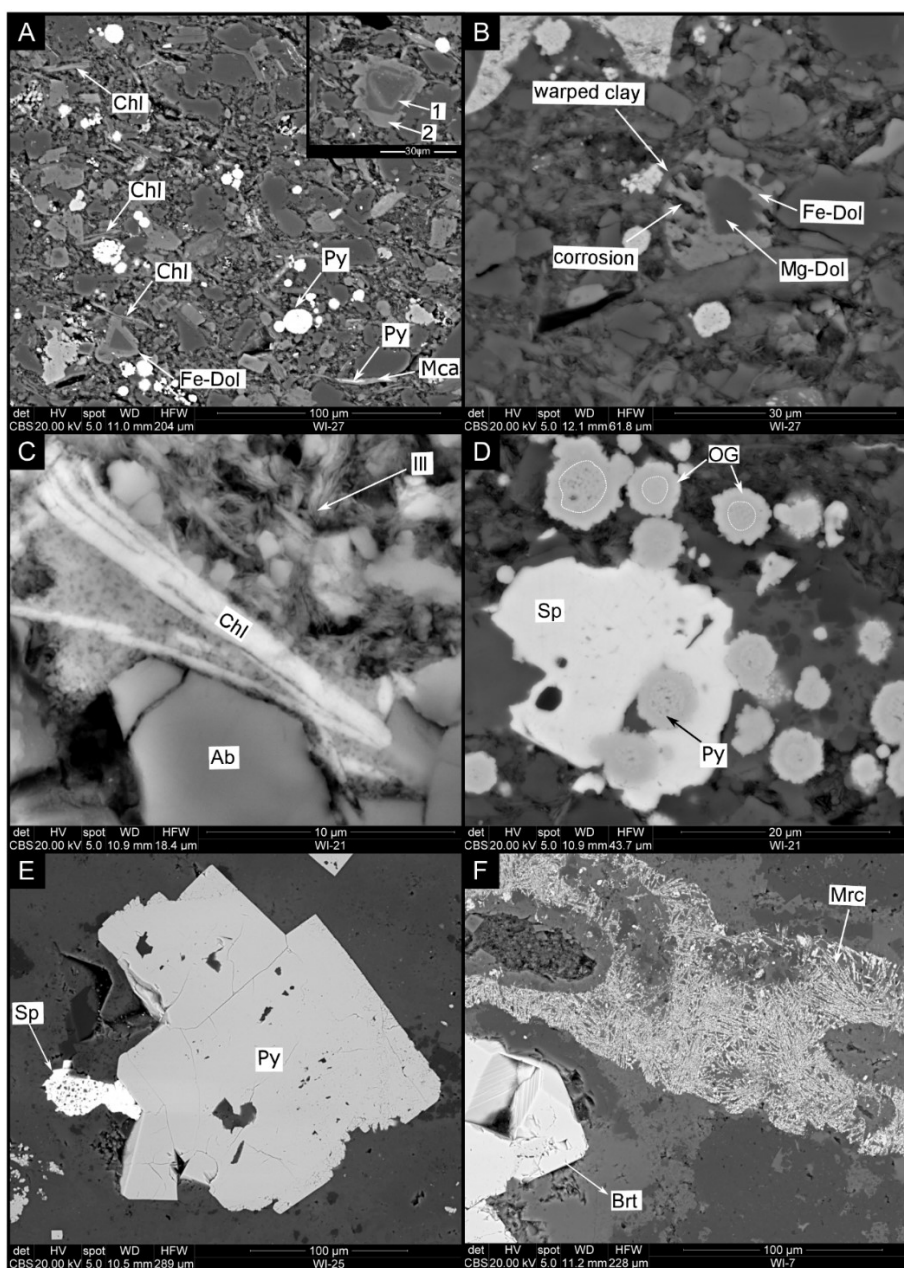


**Figure 5.** (A) Representative siliceous mudrock facies showing euhedral/subhedral dolomite with ferroan rims (Fe-Dol), abundant authigenic chlorite (Chl), pyrite (Py) framboids and detrital micas (Mca) with interstitial pyrite forming within sheets. Inset shows example of multiple ferroan growth rims in dolomite found in siliceous mudrocks. (B) Warped clays along margins of corroded ferroan dolomite rim, interior of grain is Mg-rich dolomite (Mg-Dol). (C) Authigenic iron-rich chlorite adjacent to authigenic albite and surrounded by illite (Ill). (D) Pyrite framboids with overgrowths (OG) with sphalerite (Sp) encapsulating some pyrite framboids. White dashed circles represent original grain boundary of framboid prior to overgrowth (E) Cubic pyrite cluster in carbonate facies with sphalerite cement. (F) Marcasite (Mrc) replacing allochem with euhedral barite (Brt) in carbonate facies

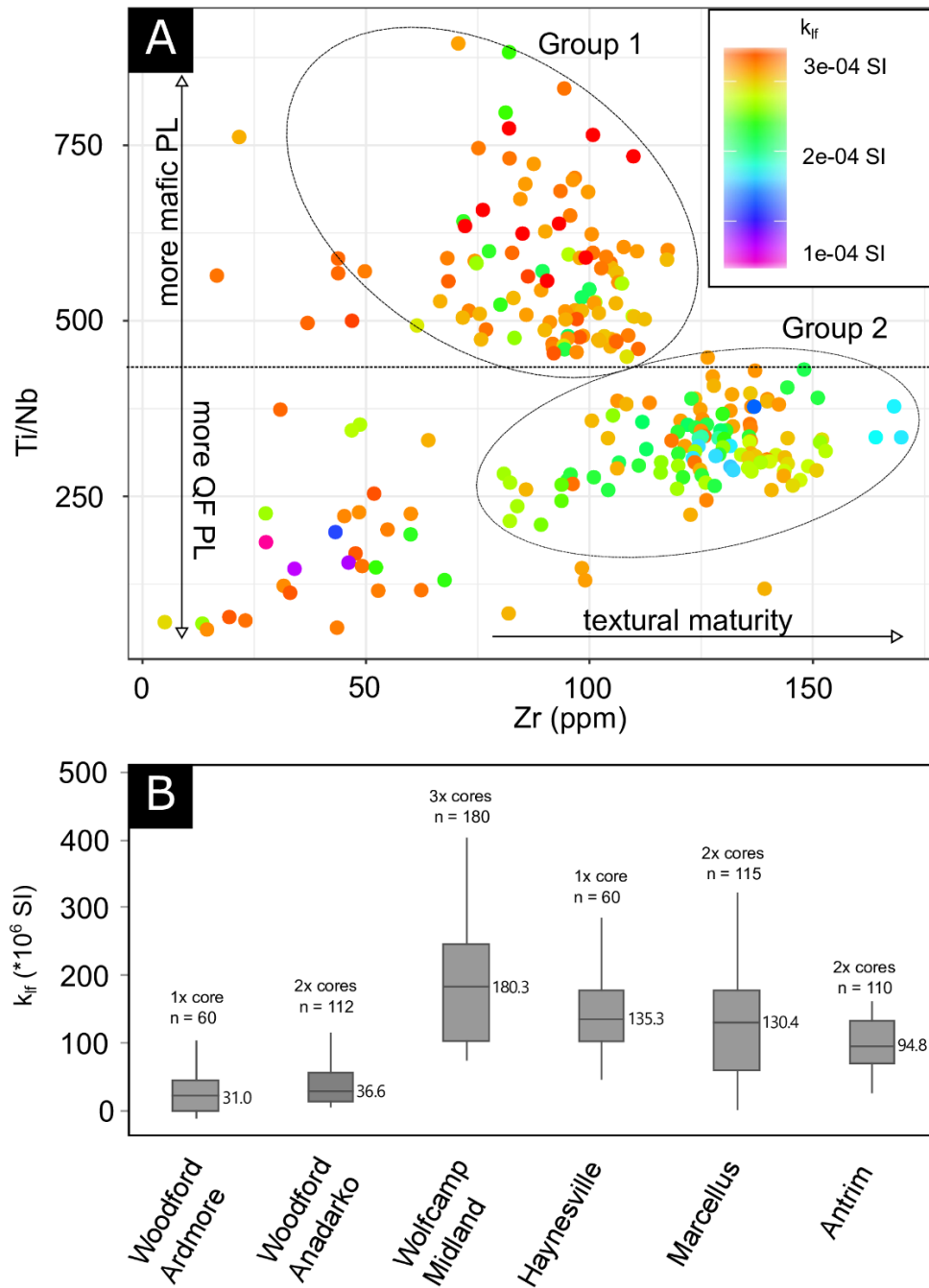


**Figure 6.** (A) Zr vs. Ti/Nb cross plot (e.g. Bonjour and Dabard, 1991) with data colored by respective magnetic susceptibility data of mudrocks from Core 1-3. Note two major groupings emerge from the data: 1) Group 1 – Ti/Nb ratio  $\geq 430$ , lower Zr (mean = 89.7ppm) and with high  $k_{If}$  (mean =  $2.78E-04$  SI) indicating more mafic provenance and 2) Group 2 – Ti/Nb  $\leq 430$ , higher Zr (mean = 123.5ppm) and lower  $k_{If}$  (mean =  $2.18E-04$ ) suggesting more quartzofeldspathic (QL) provenance. Ungrouped data likely represents intrabasinal provenance. (B) Boxplot of  $k_{If}$  data measured from mudrock facies in several sedimentary basins across North America (Stullet, 2014; Rose, 2015; Roberts, 2016). Note higher  $k_{If}$  in the Wolfcamp relative to other mudrock units.

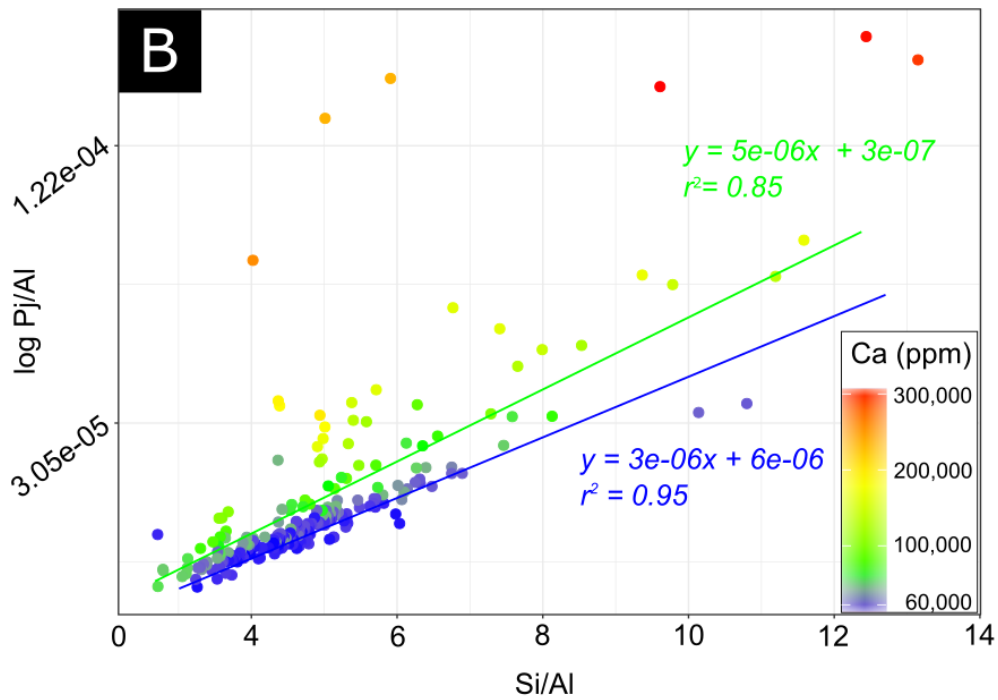
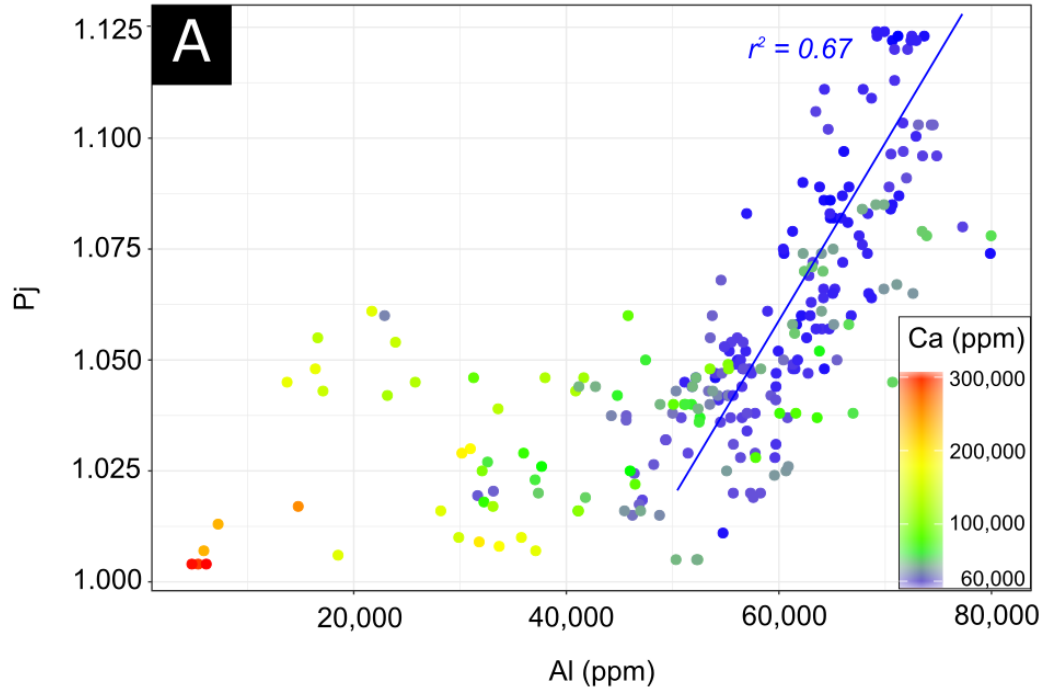


**Figure 7.** (A - B) Cross plots of Pj vs. Al and  $\log Pj/Al$  vs. Si/Al of siliceous mudrocks with data colored by Ca concentrations. (A) Pj has a clay concentration dependency in low Ca facies (<60,000 ppm) and no relationship with Pj in high Ca facies (>60,000 ppm). (B) A linear relationship for low and high-Ca siliceous mudrock facies shows quartz framework control on Pj. The change in regression slope likely reflects contribution from ferroan dolomite.

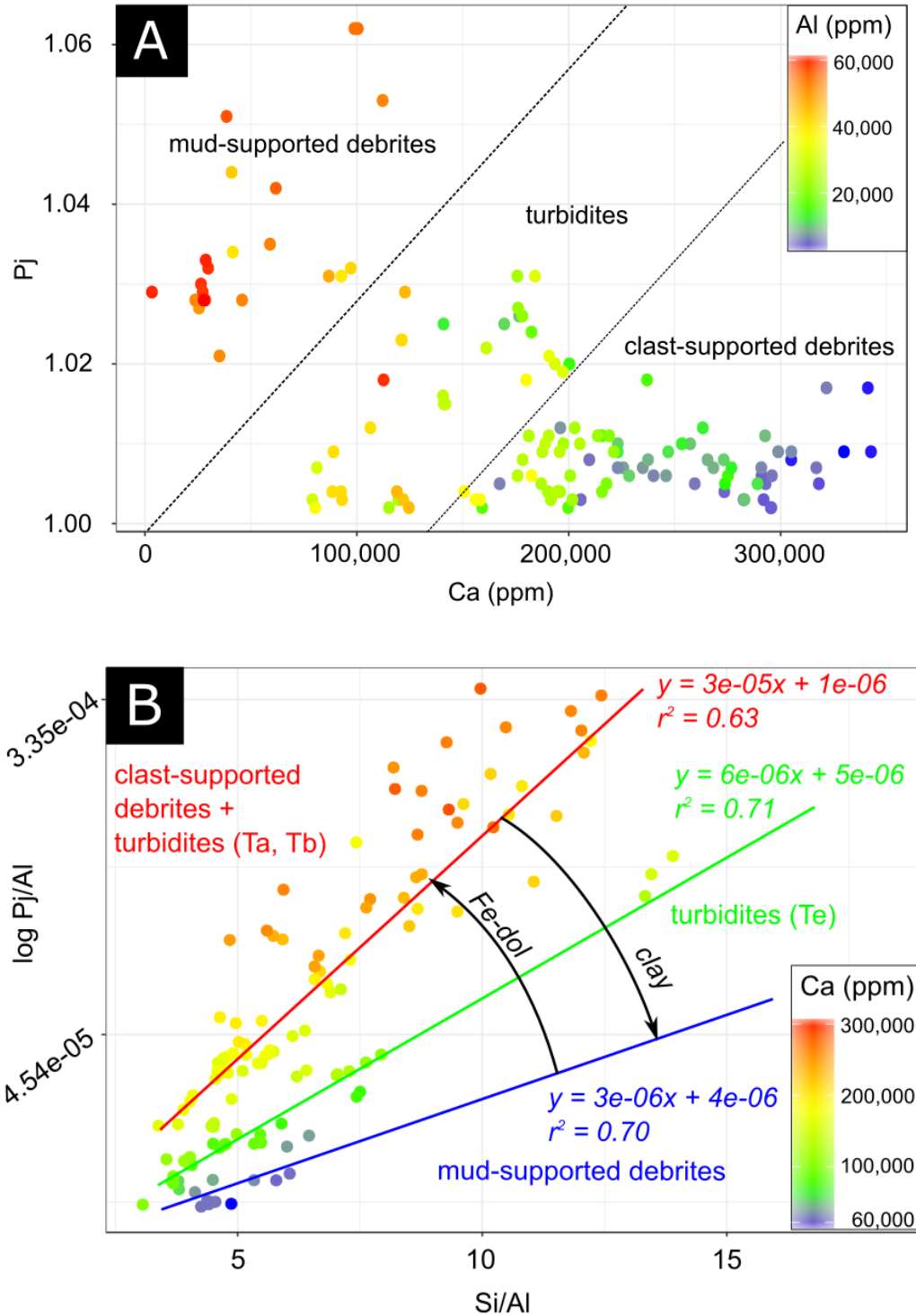
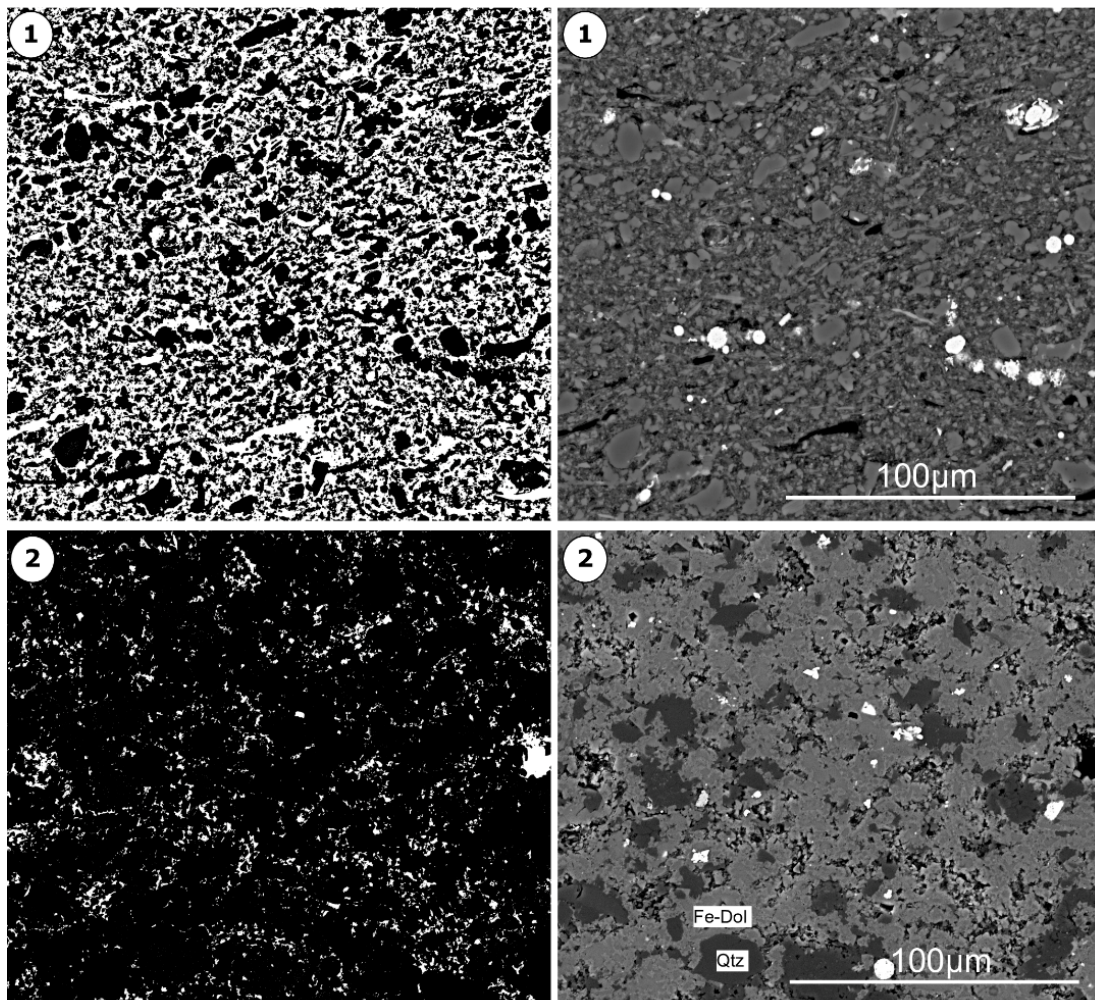


**Figure 8.** (A) Cross plot of Pj vs. Ca for carbonate facies with data colored by Al concentration. Anisotropy broadly decreases with Al (clay content) in carbonate facies. (B)  $\log Pj/Al$  vs. Si/Al for carbonate facies colored by Ca concentration. Linear regressions with variable slopes coincide to individual carbonate facies and probably reflect the relative contribution of clay and ferroan dolomite on Pj.



	Al (ppm)	Si/Al	Ca (ppm)	Avg. M/F	Std. M/F	T	Pj
low Ca siliceous mudrock ①	72,100	3.89	10,000	0.42	0.09	0.98	1.100
	69,800	3.91	36,700	0.40	0.12	0.97	1.089
	62,200	3.99	33,900	0.36	0.13	0.97	1.078
	55,200	4.37	42,200	0.30	0.05	0.94	1.048
high Ca siliceous mudrock ②	41,200	5.46	92,600	0.09	0.04	0.45	1.030
	37,500	5.89	99,100	0.08	0.06	-0.28	1.002
	14,800	8.67	273,400	0.05	0.02	-0.54	1.004

**Figure 9.** Left images represent processed image maps where framework/cement is shown in black and matrix/TOC/porosity is displayed in white. Right images show unprocessed image maps. Note ferroan carbonate/quartz dominated mineralogy in high Ca-siliceous mudrock. Table with HXRF data, scalar AMS data (T and Pj), average matrix to framework (M/F) per image set (n=9) and the standard deviation. Statistics in table for images above are labeled 1 and 2.

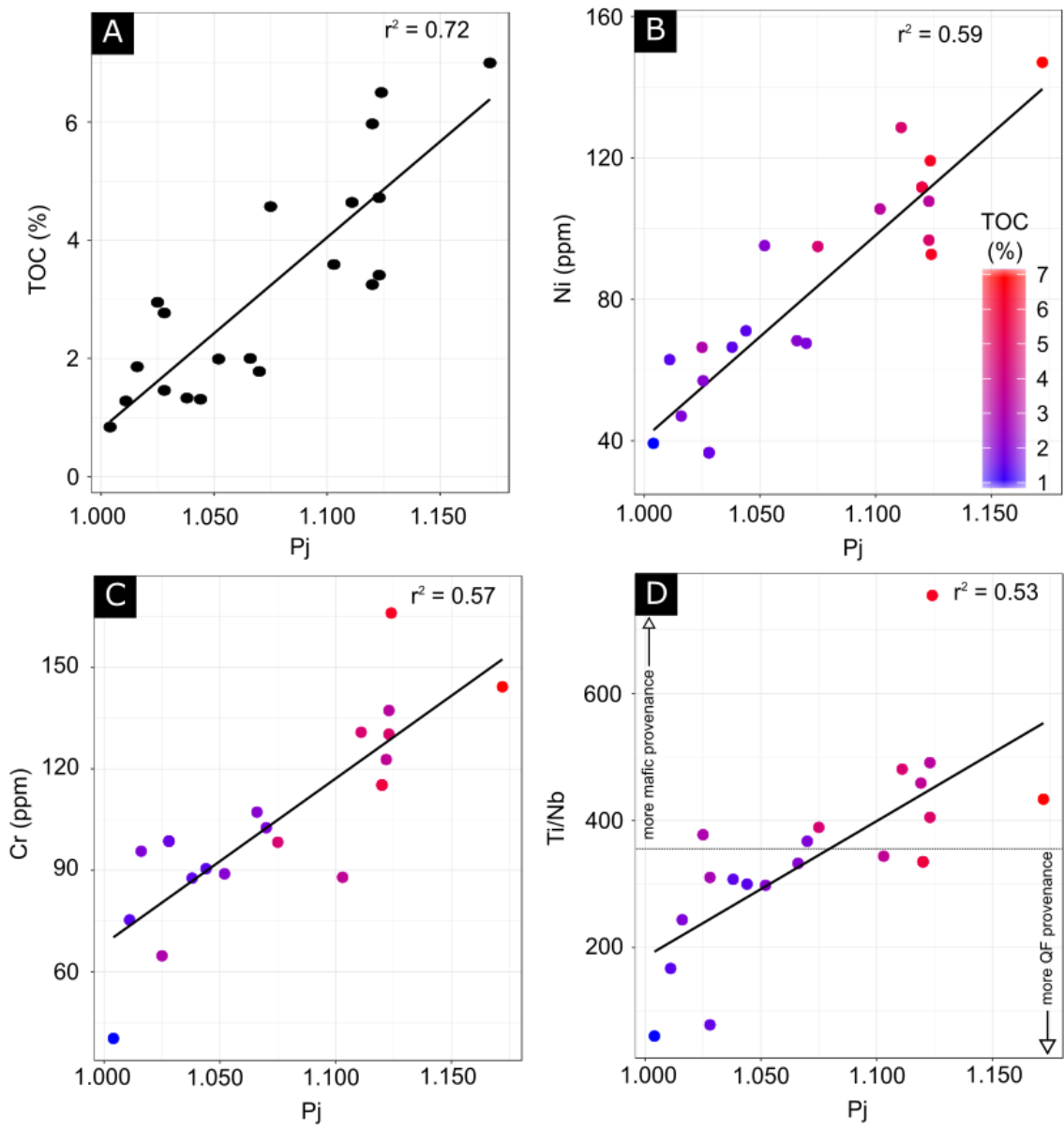


**Figure 10.** (A) Cross plot of TOC vs. Pj from Core 3(B- D) Cross plots of Ni vs. Pj, Cr vs. Pj and Ti/Nb vs. Pj with data points colored by TOC% from Core 3 (scale in B)

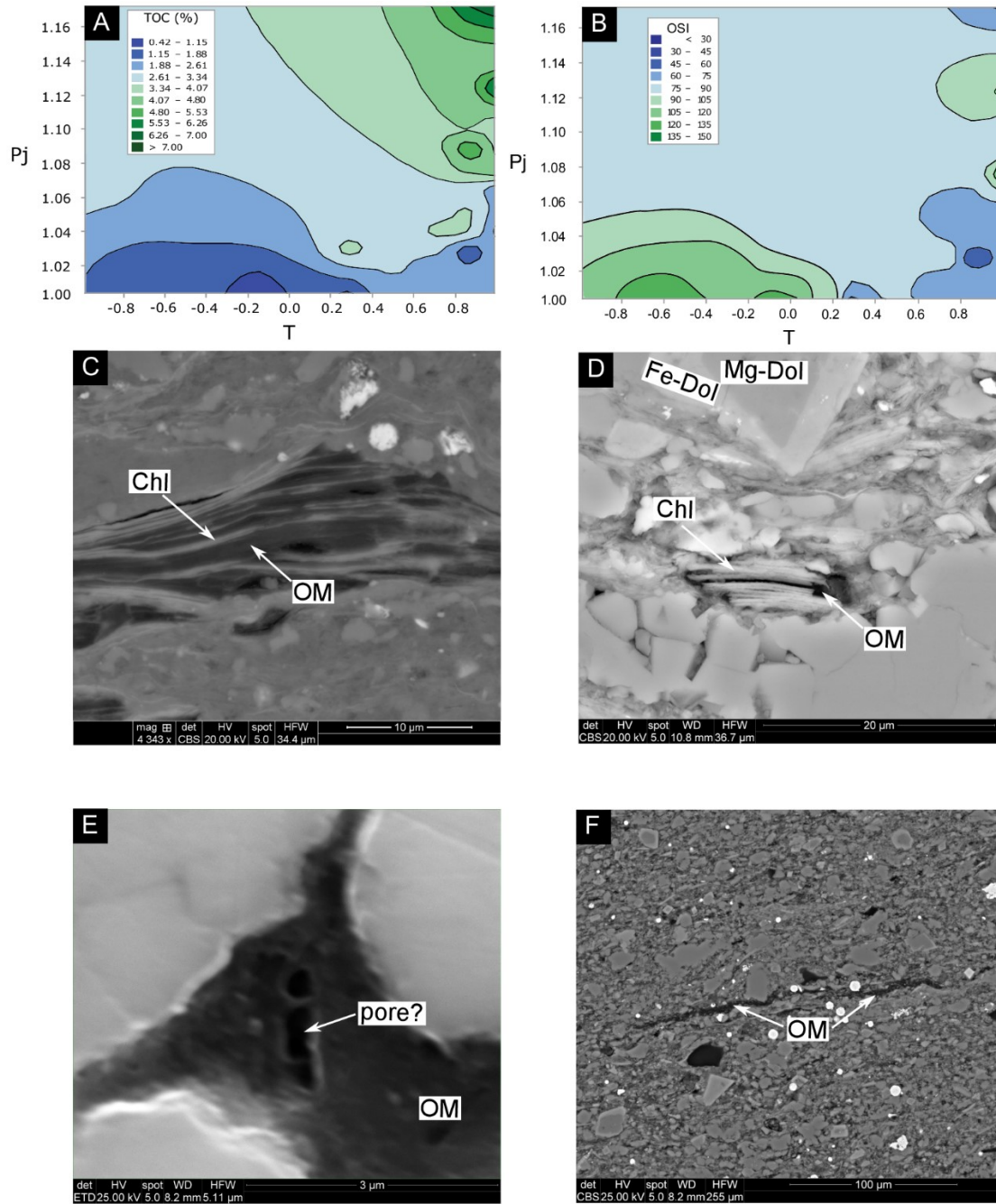


**Figure 11.** (A) Contour plot of Pj vs. T modulated by TOC for siliceous mudrocks (n=35) and MTC facies (n=15) from Core 1 and 2 (B) Contour plot of Pj vs. T modulated by OSI for siliceous mudrocks (n=35) and MTC facies (n=15). Note fabric selective hydrocarbon associations in A and B. (C - D) Organoclay aggregates in siliceous mudrocks (Core 2) (Chl – chlorite; OM – Organic Matter; CBS – backscattered electron image) -. Other OM occurrences include (E) particulate organic matter with possible pores residing within carbonate facies (Core 1) (ETD – secondary electron image) and (F) wispy organic matter hosted within the matrix of siliceous mudrocks (Core 2).

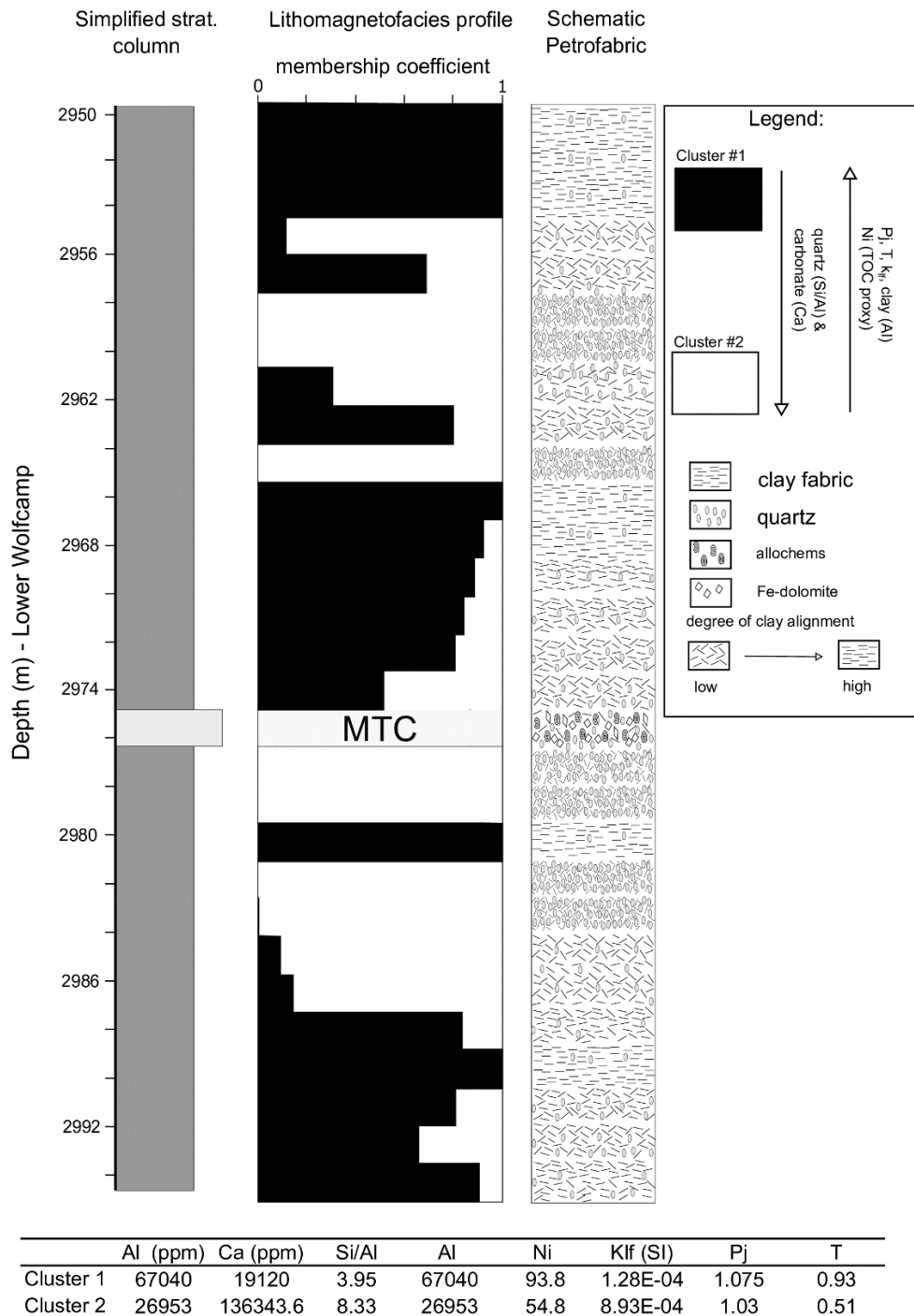
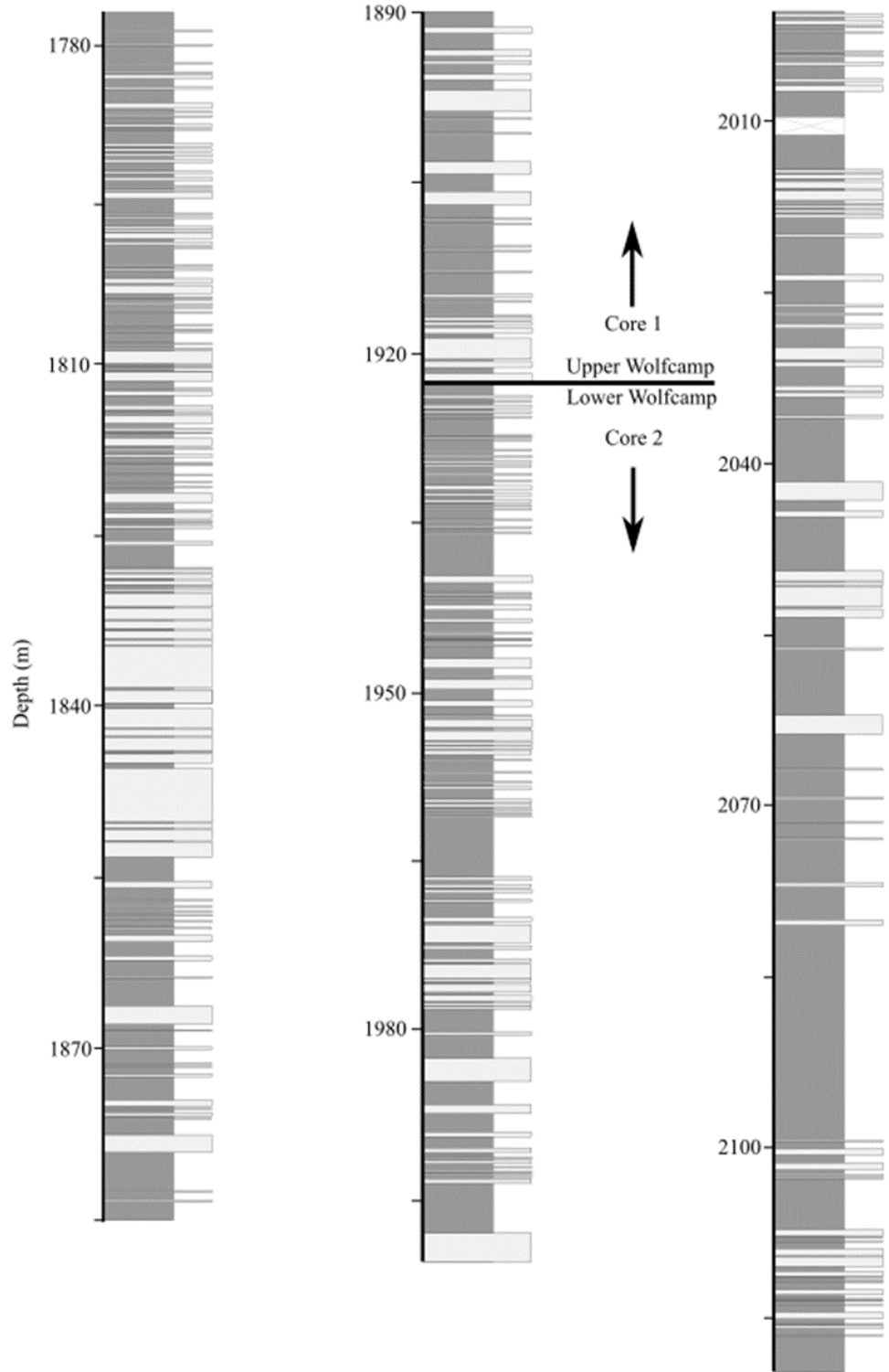
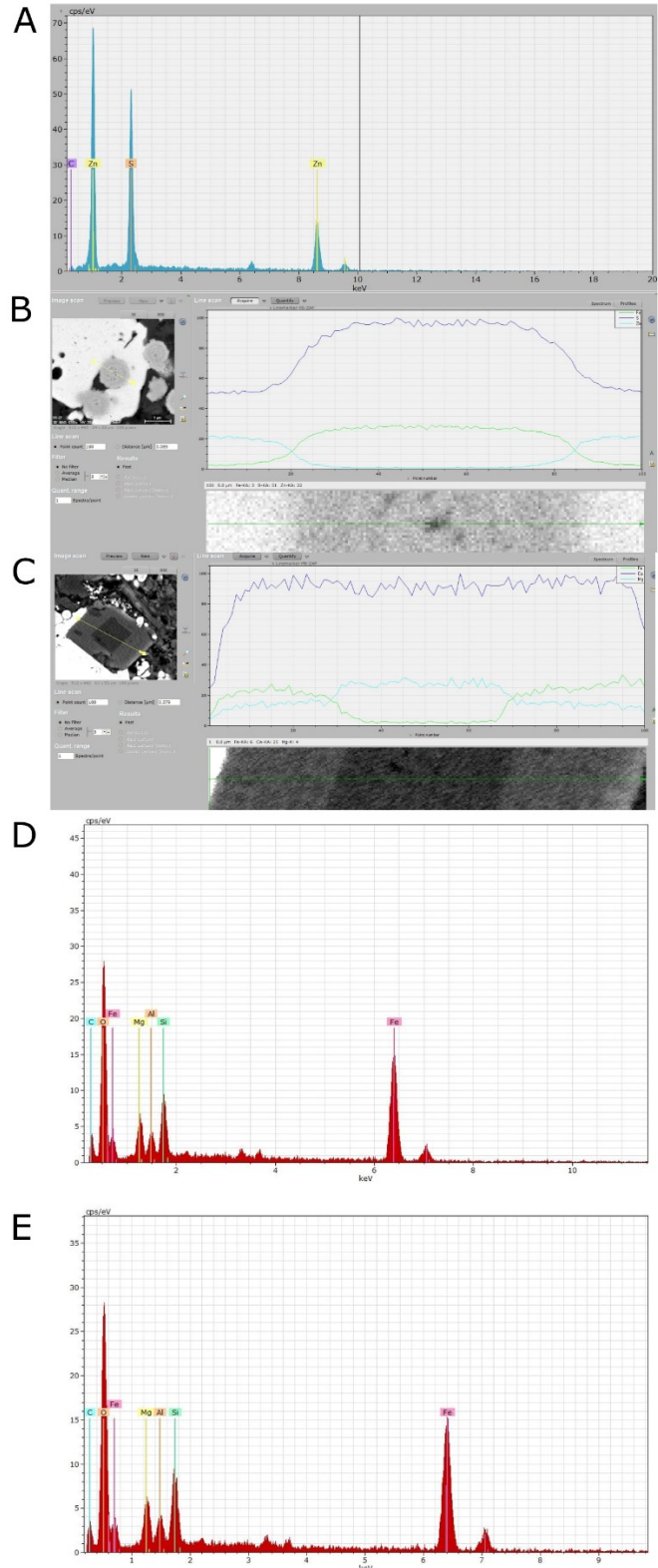


**Figure 12.** (Left) Simplified stratigraphic column of Core 3 – gray region represents siliceous mudrocks and light gray area represents a mass transport complex. (Middle) Lithomagneto-facies profile derived from FCM analysis with membership coefficient to each principal cluster where 1 represents complete membership and > 0 indicates partial membership. Cluster 1 is represented in black and Cluster 2 is displayed in white. (Right) Schematic petrofabric depicts relative concentration of framework grains and clay particle alignment. (Below) Table with centroid values for Clusters 1 and 2.

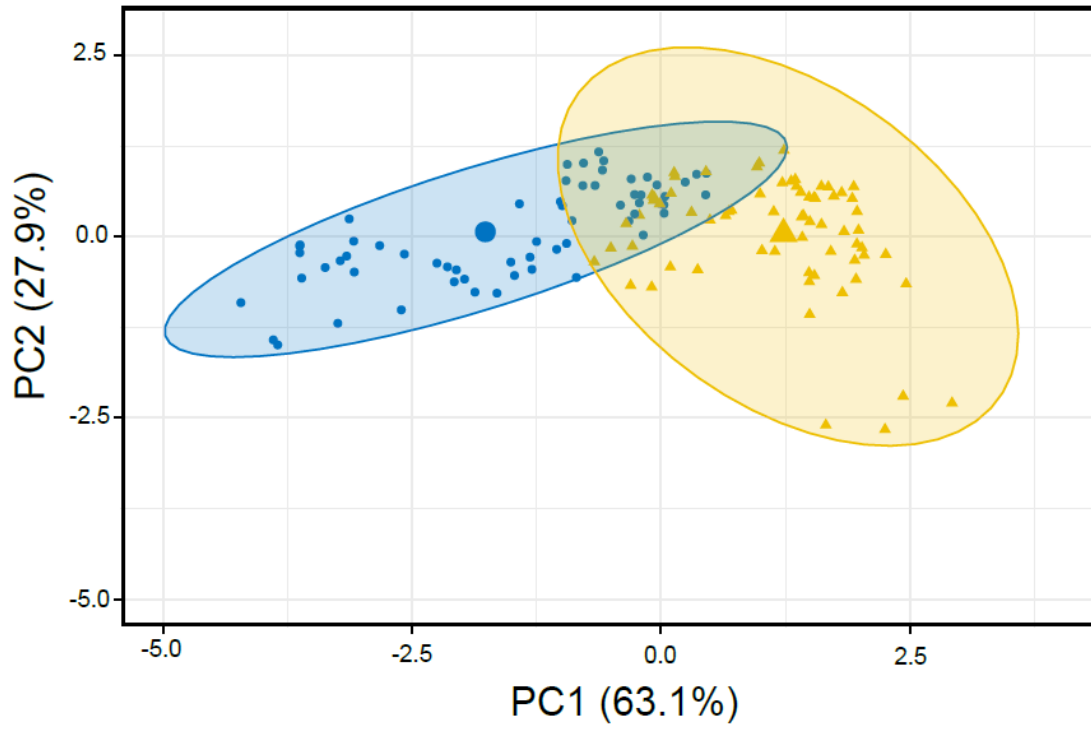
# APPENDIX



Simplified core descriptions of Core 1 and 2. Dark gray – mudstone facies; light gray – carbonate facies.



(A) EDS spectra for sphalerite in Fig. 5D (B) EDS line scan in Fig. 5D (C) Example of line scan of dolomite with ferroan rim (D) + (E) examples of EDS spectra of chlorite.



Principal components diagram showing two principal clusters.

## REFERENCES

- Adams, D.C. and Keller, G.R., 1994, Possible extension of the Midcontinent Rift in west Texas and eastern New Mexico. *Canadian Journal of Earth Sciences*, 31(4), pp.709-720.
- Adams, D.C. and Miller, K.C., 1995, Evidence for late Middle Proterozoic extension in the Precambrian basement beneath the Permian basin. *Tectonics*, 14(6), pp.1263-1272.
- Arnarson, T. S., and Keil, R. G., 2000, Mechanisms of pore water organic matter adsorption to montmorillonite. *Marine chemistry*, 71(3-4), 309-320.
- Aubourg, C., Rochette, P., and Vialon, P., 1991, Subtle stretching lineation revealed by magnetic fabric of Callovian-Oxfordian black shales (French Alps). *Tectonophysics*, 185(3-4), 211-223.
- Backeberg, N. R., Iacoviello, F., Rittner, M., Mitchell, T. M., Jones, A. P., Day, R. and Striolo, A., 2017, Quantifying the anisotropy and tortuosity of permeable pathways in clay-rich mudstones using models based on X-ray tomography. *Scientific Reports*, 7(1), 14838.
- Beaufort, D., Rigault, C., Billon, S., Billault, V., Inoue, A., Inoue, S., and Patrier, P., 2015, Chlorite and chloritization processes through mixed-layer mineral series in low-temperature geological systems—a review. *Clay Minerals*, 50(4), 497-523.
- Berner, R.A., 1970, Sedimentary pyrite formation. *American journal of science*, 268(1), pp.1-23.
- Bonjour, J. L., and Dabard, M. P., 1991, Ti/Nb ratios of clastic terrigenous sediments used as an indicator of provenance. *Chemical Geology*, 91(3), 257-267.
- Borradaile, G. J., 1988, Magnetic susceptibility, petrofabrics and strain. *Tectonophysics*, 156(1-2), 1-20.
- Canfield, D.E. and Thamdrup, B., 2009, Towards a consistent classification scheme for geochemical environments, or, why we wish the term ‘suboxic’ would go away. *Geobiology*, 7(4), pp.385-392.
- Condie, K. C., Dengate, J., and Cullers, R. L., 1995, Behavior of rare earth elements in a paleoweathering profile on granodiorite in the Front Range, Colorado, USA. *Geochimica et Cosmochimica Acta*, 59(2), 279-294.
- Corrigan, J., Cervany, P. F., Donelick, R., and Bergman, S. C., 1998, Postorogenic denudation along the late Paleozoic Ouachita trend, south central United States of America: magnitude and timing constraints from apatite fission track data. *Tectonics*, 17(4), 587-603.
- Chadima, M., and Jeliněk, V., 2009, Anisoft 4.2: anisotropy data browser for windows. Agico. Inc, Brno. <https://www.agico.com/text/software/anisoft/anisoft.php>
- Chadima, M., Pruner, P., Šlechta, S., Grygar, T., and Hirt, A. M., 2006, Magnetic fabric variations

- in Mesozoic black shales, Northern Siberia, Russia: Possible paleomagnetic implications. *Tectonophysics*, 418(1-2), 145-162.
- Daigle, H., and Dugan, B., 2011, Permeability anisotropy and fabric development: A mechanistic explanation. *Water Resources Research*, 47(12).
- DeCaritat, P., Hutcheon, I. and Walshe, L., 1993, Chlorite geothermometry: a review. *Clays and Clay Minerals*, 41. p. 219–239
- DeCelles, P. G., and Horton, B. K., 2003, Early to middle Tertiary foreland basin development and the history of Andean crustal shortening in Bolivia. *Geological Society of America Bulletin*, 115(1), 58-77.
- Dekkers, M. J., Langereis, C. G., Vriend, S. P., Van Santvoort, P. J. M., and De Lange, G. J., 1994, Fuzzy c-means cluster analysis of early diagenetic effects on natural remanent magnetisation acquisition in a 1.1 Myr piston core from the Central Mediterranean. *Physics of the Earth and Planetary Interiors*, 85(1-2), 155-171.
- Engle, M.A., Reyes, F.R., Varonka, M.S., Orem, W.H., Ma, L., Ianno, A.J., Schell, T.M., Xu, P. and Carroll, K.C., 2016, Geochemistry of formation waters from the Wolfcamp and “Cline” shales: Insights into brine origin, reservoir connectivity, and fluid flow in the Permian Basin, USA. *Chemical Geology*, 425, pp.76-92.
- Everitt, B.S., Landau, S., Leese, M. and Stahl, D., 2011, Cluster analysis: Wiley series in probability and statistics. John Wiley and Sons.
- Ferré, E.C., 2002, Theoretical models of intermediate and inverse AMS fabrics. *Geophysical Research Letters*, 29(7), pp.31-1.
- Flawn, P. T., Goldstein, A. J., King, P. B., and Weaver, C. E., 1961, The Ouachita System: University of Texas, Austin, Bureau of Economic Geology, Publications 6120, 401 p.
- Frenzel, H. N., Bloomer, R. R., Cline, R. B., Cys, J. M., Galley, J. E., Gibson, W. R., ... and Thompson III, S., 1988, The Permian basin region. Sedimentary cover—North American craton: US: Boulder, Colorado, Geological Society of America, *The Geology of North America*, 2, 261-306.
- Friedrich, M. and Milliken, M., 2013, August. Determining the contributing reservoir volume from hydraulically fractured horizontal wells in the Wolfcamp formation in the Midland Basin. In *Unconventional resources technology conference* (pp. 1461-1468). Society of Exploration Geophysicists, American Association of Petroleum Geologists, Society of Petroleum Engineers
- Gan, G., Ma, C. and Wu, J., 2007, *Data Clustering: Theory, Algorithms and Applications*. Washington, D.C.: American Statistical Association/Society for Industrial and Applied Mathematics (Vol. 20). Siam.
- Gaswirth, S.B., Marra, K.R., Lillis, P.G., Mercier, T.J., Leathers-Miller, H.M., Schenk, C.J., Klett,

- T.R., Le, P.A., Tennyson, M.E., Hawkins, S.J. and Brownfield, M.E., 2016, Assessment of undiscovered continuous oil resources in the Wolfcamp shale of the Midland Basin, Permian Basin Province, Texas, 2016 (No. 2016-3092). US Geological Survey.
- Girdler, R. W., 1961, The measurement and computation of anisotropy of magnetic susceptibility of rocks. *Geophysical Journal International*, 5(1), 34-44.
- Heins, W. A., and Kairo, S., 2007, Predicting sand character with integrated genetic analysis. *Special Papers-Geological Society of America*, 420, 345.
- Hillier, S., 1993, Origin, diagenesis, and mineralogy of chlorite minerals in Devonian lacustrine mudrocks, Orcadian Basin, Scotland. *Clays and Clay Minerals*, 41, 240-240.
- Hrouda, F., 2002, Low-field variation of magnetic susceptibility and its effect on the anisotropy of magnetic susceptibility of rocks. *Geophysical Journal International*, 150(3), 715-723.
- Hrouda, F., Chlupáčová, M., and Mrázová, Š., 2006, Low-field variation of magnetic susceptibility as a tool for magnetic mineralogy of rocks. *Physics of the Earth and Planetary Interiors*, 154(3-4), 323-336.
- Jackson, M., Moskowitz, B., Rosenbaum, J., and Kissel, C., 1998, Field-dependence of AC susceptibility in titanomagnetites. *Earth and Planetary Science Letters*, 157(3), 129-139.
- Jaffe, R., Albrecht, P., and Oudin, J. L., 1988, Carboxylic acids as indicators of oil migration—I. Occurrence and geochemical significance of C-22 diastereoisomers of the (17 $\beta$ , H, 21 $\beta$ H) C 30 hopanoic acid in geological samples. In *Organic Geochemistry In Petroleum Exploration* (pp. 483-488).
- Jarvie, D. M., 2012, Shale resource systems for oil and gas: Part 2—Shale-oil resource systems. *American Association of Petroleum Geologists Memoir* 97, 69–87.
- Jelinek, V., 1981, Characterization of the magnetic fabric of rocks. *Tectonophysics*, 79(3-4), pp.T63-T67.
- Kargi, H. and Barnes, C.G., 1995, A Grenville-age layered intrusion in the subsurface of west Texas: Petrology, petrography, and possible tectonic setting. *Canadian Journal of Earth Sciences*, 32(12), pp.2159-2166.
- Kawamura, K., and Ogawa, Y., 2002, Progressive microfabric changes in unconsolidated pelagic and hemipelagic sediments down to 180 mbsf, northwest Pacific, ODP Leg 185, Site 1149. In *Proceedings of the Ocean Drilling Program, Scientific Results* (Vol. 185, pp. 1-29). College Station, TX: Ocean Drilling Program.
- Keller, G.R., Hills, J.M., Baker, M.R. and Wallin, E.T., 1989, Geophysical and geochronological constraints on the extent and age of mafic intrusions in the basement of west Texas and eastern New Mexico. *Geology*, 17(11), pp.1049-1052.
- Kennedy, M. J., Pevear, D. R., and Hill, R. J., 2002, Mineral surface control of organic carbon in

- black shale. *Science*, 295(5555), 657-660.
- Machel, H. G., Krouse, H. R., and Sassen, R., 1995, Products and distinguishing criteria of bacterial and thermochemical sulfate reduction. *Applied geochemistry*, 10(4), 373-389.
- Martín-Hernández, F., and Hirt, A. M., 2001, Separation of ferrimagnetic and paramagnetic anisotropies using a high-field torsion magnetometer. *Tectonophysics*, 337(3-4), 209-221.
- Martín-Hernández, F. and Ferré, E.C., 2007, Separation of paramagnetic and ferrimagnetic anisotropies: A review. *Journal of Geophysical Research: Solid Earth*, 112(B3).
- McCabe, C., Jackson, M. and Ellwood, B.B., 1985. Magnetic anisotropy in the Trenton limestone: results of a new technique, anisotropy of anhysteretic susceptibility. *Geophysical Research Letters*, 12(6), pp.333-336.
- Moskowitz, B.M., Jackson, M. and Kissel, C., 1998, Low-temperature magnetic behavior of titanomagnetites. *Earth and Planetary Science Letters*, 157(3-4), pp.141-149.
- Mazzullo, S. J., and Reid, A. M., 1989, Lower Permian platform and basin depositional systems, northern Midland Basin, Texas. In: P.D. Crevello, J.L. Wilson, J.F. Sarg and J.F. Read (Editors), *Controls on Carbonate Platform and Basin Development*. Soc. Econ. Paleontol. Mineral., Spec. Publ., 44: 305—320.
- McCabe, C., Jackson, M. and Ellwood, B.B., 1985, Magnetic anisotropy in the Trenton limestone: results of a new technique, anisotropy of anhysteretic susceptibility. *Geophysical Research Letters*, 12(6), pp.333-336.
- Milliken, K.L., Esch, W.L., Reed, R.M. and Zhang, T., 2012. Grain assemblages and strong diagenetic overprinting in siliceous mudrocks, Barnett Shale (Mississippian), Fort Worth Basin, Texas. *Aapg Bulletin*, 96(8), pp.1553-1578.
- Özdemir, Ö., Dunlop, D. J., and Moskowitz, B. M., 1993, The effect of oxidation on the Verwey transition in magnetite. *Geophysical Research Letters*, 20(16), 1671-1674.
- Parés, J.M., 2015, Sixty years of anisotropy of magnetic susceptibility in deformed sedimentary rocks. *Frontiers in Earth Science*, 3, p.4.
- Parés, J. M., and van der Pluijm, B. A., 2002, Phyllosilicate fabric characterization by low-temperature anisotropy of magnetic susceptibility (LT-AMS). *Geophysical Research Letters*, 29(24).
- Parés, J. M., and Van der Pluijm, B. A., 2004, Correlating magnetic fabrics with finite strain: Comparing results from mudrocks in the Variscan and Appalachian Orogens. *Geologica Acta: an international earth science journal*, 2(3).
- Raiswell, R., and Anderson, T. F., 2005, Reactive iron enrichment in sediments deposited beneath euxinic bottom waters: constraints on supply by shelf recycling. *Geological Society, London, Special Publications*, 248(1), 179-194.

- Richter, C. and van der Pluijm, B.A., 1994, Separation of paramagnetic and ferrimagnetic susceptibilities using low temperature magnetic susceptibilities and comparison with high field methods. *Physics of the Earth and Planetary Interiors*, 82(2), pp.113-123.
- Roberts, M. J., 2017, A diagenetic and paleomagnetic study of the Woodford Shale, Oklahoma, U.S.A. , Master's thesis, University of Oklahoma, Norman, Oklahoma, 63p.
- Rochette, P., 1988, Inverse magnetic fabric in carbonate-bearing rocks. *Earth and Planetary Science Letters*, 90(2), pp.229-237.
- Rochette, P., Jackson, M. and Aubourg, C., 1992. Rock magnetism and the interpretation of anisotropy of magnetic susceptibility. *Reviews of Geophysics*, 30(3), pp.209-226.
- Rose, D. D., 2015, A diagenetic study of the Haynesville Shale, Bossier Parish and Red River Parish, Louisiana, Master's thesis, University of Oklahoma, Norman, Oklahoma, 80p.
- Ross, C. A., 1986, Paleozoic evolution of southern margin of Permian basin. *Geological Society of America Bulletin*, 97(5), 536-554.
- Rowe, H., Hughes, N., and Robinson, K., 2012, The quantification and application of handheld energy-dispersive x-ray fluorescence (ED-XRF) in mudrock chemostratigraphy and geochemistry. *Chemical Geology*, 324, 122-131.
- Sammon, J.W., 1969, A nonlinear mapping for data structure analysis. *IEEE Transactions on computers*, 100(5), pp.401-409.
- Satterberg, J., Arnarson, T. S., Lessard, E. J., and Keil, R. G., 2003, Sorption of organic matter from four phytoplankton species to montmorillonite, chlorite and kaolinite in seawater. *Marine Chemistry*, 81(1-2), 11-18.
- Schieber, J., 2011, Marcasite in black shales—a mineral proxy for oxygenated bottom waters and intermittent oxidation of carbonaceous muds. *Journal of Sedimentary Research*, 81(7), 447-458.
- Schieber, J., and Ellwood, B. B., 1993, Determination of basinwide paleocurrent patterns in a shale succession from anisotropy of magnetic susceptibility (AMS): a case study of the mid-Proterozoic Newland formation, Montana. *Journal of Sedimentary Research*, 63(5).
- Schwehr, K., Tauxe, L., Driscoll, N. and Lee, H., 2006, Detecting compaction disequilibrium with anisotropy of magnetic susceptibility. *Geochemistry, Geophysics, Geosystems*, 7(11).
- Shumaker, R.C., 1992, Paleozoic Structure of the Central Basin Uplift and Adjacent Delaware Basin, West Texas (1). *AAPG Bulletin*, 76(11), pp.1804-1824.
- Sinclair, T. D., 2007, The generation and continued existence of overpressure in the Delaware Basin, Texas. [Doctoral dissertation]: Durham University, 302 p.
- Steullet, A. K., 2014, An integrated paleomagnetic and diagenetic study of the Marcellus Shale

- within the Plateau Province of the Appalachian Basin, Master's thesis, University of Oklahoma, Norman, Oklahoma, 80p.
- Sweeney, R.E. and Kaplan, I.R., 1973, Pyrite framboid formation; laboratory synthesis and marine sediments. *Economic Geology*, 68(5), pp.618-634.
- Tarling, D., and Hrouda, F. (Eds.), 1993, *Magnetic anisotropy of rocks*. Chapman and Hall, London, 217 pp.
- Taylor, K. G., and Macquaker, J. H. S., 2000, Early diagenetic pyrite morphology in a mudstone-dominated succession: the Lower Jurassic Cleveland Ironstone Formation, eastern England. *Sedimentary Geology*, 131(1-2), 77-86.
- Tribovillard, N., Algeo, T.J., Lyons, T. and Riboulleau, A., 2006, Trace metals as paleoredox and paleoproductivity proxies: an update. *Chemical Geology*, 232(1), pp.12-32.
- West Texas Geological Society. Stratigraphic Committee, Matchus, E.J. and Jones, T.S., 1984. *East-west cross section through Permian Basin of West Texas*. The Society.
- Winkler, A., Florindo, F., Sagnotti, L. and Sarti, G., 1996. Inverse to normal magnetic fabric transition in an upper Miocene marly sequence from Tuscany, Italy. *Geophysical Research Letters*, 23(9), pp.909-912.
- Worm, H. U., Clark, D., and Dekkers, M. J., 1993, Magnetic susceptibility of pyrrhotite: grain size, field and frequency dependence. *Geophysical Journal International*, 114(1), 127-137.
- Yang, K. M., and Dorobek, S. L., 1995, The Permian basin of west Texas and New Mexico: tectonic history of a " composite" foreland basin and its effects on stratigraphic development. *Stratigraphic evolution of foreland basins: SEPM Special Publication*, 52, 149-174.
- Zadeh, L.A., 1996, Fuzzy sets. In *Fuzzy Sets, Fuzzy Logic, And Fuzzy Systems: Selected Papers by Lotfi A Zadeh* (pp. 394-432). Alves, T., K. Omosanya, and P. Gowling, 2015, Volume rendering of enigmatic high-amplitude anomalies in southeast Brazil: A workflow to distinguish lithologic features from fluid accumulations: *Interpretation*, 3, A1-A14.

## CHAPTER 3

# PALEOMAGNETISM AND MAGNETIC FABRIC OF THE WOLFCAMP FORMATION: DECIPHERING THE TIMING OF DIAGENETIC AND TECTONIC EVENTS IN THE MIDLAND BASIN

### ABSTRACT

An integrated rock magnetic, paleomagnetic, basin modeling and electron microscopy study was performed on three cores covering the entire Wolfcamp Formation in the Midland Basin, West Texas. This work contributes new insights regarding the diagenetic history of the Wolfcamp Shale and refines our understanding of tectonic influences in the Midland Basin. Chemical remanent magnetizations (CRMs) developed during the Jurassic in all three cores under investigation. These magnetizations are attributed to chloritization/illitization of Fe-rich smectite. Isothermal remanent magnetization (IRM) acquisition, triaxial IRM thermal decay, saturation isothermal remanent magnetization (SIRM)/magnetic susceptibility ( $k_{lf}$ ) ratios, magnetic hysteresis and electron microscopy of magnetic extracts indicate that the magnetization resides primarily in SD-PSD magnetite. Gyroremanent magnetizations (GRM) and intervals with elevated SIRM/ $k_{lf}$  ratios suggest possible contributions from greigite and/or pyrrhotite. Geographic orientation of one core was achieved through correlating sub-vertical fractures detected in formation image logs to its corresponding fractures in core slabs. Consistent anisotropy of magnetic susceptibility (AMS) lineations carried by paramagnetic clays are observed in all cores. Geographically corrected AMS data shows a NE-SW lineation which stands consistent with observed fracture trends. Similarly, inverse AMS fabrics, resulting from ferroan dolomite display a streaked distribution toward the NW-SE shortening direction. These fabrics likely developed in response to Laramide-aged layer parallel shortening (LPS). 1D Basin modeling suggests

temperatures consistent with chloritization/illitization (100°C-120°C) for the Jurassic CRM. Basin modeling also provides new estimates of Cenozoic uplift in the Eastern Midland Basin.

## INTRODUCTION

Understanding the burial history of sedimentary rocks is necessary in order to unravel the post-depositional evolution of sedimentary basins and establish boundary conditions for hydrocarbon exploration. The burial history of the Greater Permian basin has been well documented (Frenzel et al., 1988; Sinclair, 2007; Rose, 2016), however, key questions regarding the nature and timing of tectonic and thermochemical processes operating in the Midland Basin remain unresolved. This study seeks to resolve the spatiotemporal boundaries of such processes in the Midland Basin by integrating paleomagnetic, rock magnetic, basin modeling, petrographic and electron microscopy data. The specific unit under investigation is the Wolfcamp Formation which can be broadly characterized as oil-bearing siliceous and calcareous mudrocks punctuated by carbonate-rich mass transport complexes (MTCs) (Hamlin and Baumgardner, 2012). The Wolfcamp is a crucial economic resource which according to estimates by the U.S geological survey, contains an estimated average of 20 billion barrels of oil, 16 trillion cubic feet of associated natural gas, and 1.6 billion barrels of natural gas liquids (Gaswirth et al., 2016). This work represents the first paleomagnetic and rock magnetic study of the Wolfcamp formation in the Midland Basin.

Previous paleomagnetic studies of other Paleozoic sedimentary rocks in North America have documented chemical remanent magnetizations (CRM) related to illitization of smectite, migration of orogenic fluids, hydrothermal fluids, hydrocarbon migration and other late diagenetic processes (McCabe and Elmore, 1989; Hirt et al., 1993; Katz et al., 2000; Dennie et al., 2012; Jackson and Swanson-Hysell, 2012; Roberts and Elmore, 2017). A common theme among these processes is some combination of elevated temperatures, fluids and chemical activity that facilitate the growth of ferrimagnetic minerals. Textural evidence suggests that the formation of

ferrimagnetic minerals occurs either through the replacement of preexisting minerals such as oxidation of iron sulfides (e.g. Brothers et al., 1996) or neoformation of minerals from solution (Elmore et al., 2012; Roberts, 2015). Importantly, conditions must allow for ferromagnetic mineral authigenesis to proceed through the blocking volume in order to acquire a stable magnetic remanence (e.g. Butler, 1998).

Dating of burial diagenetic events are invaluable in establishing the timing of processes that can adversely impact hydrocarbon reservoirs (e.g. hydrothermal alteration) or provide the timing of key petroleum systems elements (as outlined by Magoon and Dow, 1994) such as hydrocarbon migration. In addition to obtaining the timing of burial events, the chemical and physical processes shaping rock fabrics are key to understanding the evolution of sedimentary basins. Anisotropy of magnetic susceptibility (AMS) has been effectively utilized in this capacity and can document incipient compression, fingerprint tectonic domains in foreland systems, measure paleocurrent directions and mechanical compaction (Aubourg et al., 1991; Schieber and Ellwood, 1993; Pares and van der Pluijm, 2004; Schwehr et al., 2006; Weil and Yonkee, 2009; Almqvist and Koyi, 2018). Effective interpretation of both AMS and paleomagnetic data hinge upon precisely oriented samples in order to determine paleomagnetic pole positions and evaluate stress fields or paleocurrents. Precise orientation of specimens has proven challenging in previous core-based studies (e.g. Dennie et al., 2012). Efforts to reorient ancient characteristic remanent magnetizations (ChRM) using a modern viscous remanent magnetization (VRM) has proven successful (e.g. Rolph et al. 1995; Dennie et al., 2012), however, during the coring processes a drilling-induced remanent magnetization (DIRM) can obscure or reset both VRMs and ChRMs. Despite these issues, many core based studies can utilize an inclination only method (e.g. Arason and Levi, 2010) to determine the age of ChRMs if borehole deviation angles are known. A

limitation of this method is the non-unique nature of inclination-only ages, particularly for Cenozoic and Late Paleozoic magnetizations. With the advent of borehole imaging, specifically the resistivity based formation image logging tool, it is now possible to reorient paleomagnetic specimens relative to sub-vertical natural fractures that can be traced from the image log to its corresponding fractures in core slabs (e.g. MacLeod et al., 1994). Implementation of this method relies on numerous, interpretable sub-vertical fractures across an entire core to minimize the effect of mechanical rotation between specimen sites.

### **GEOLOGIC BACKGROUND**

The Greater Permian Basin occupies the southwestern portion of the midcontinent craton in West Texas and southern New Mexico. The Permian Basin is described as a foreland basin comprised of sub-basins which are segmented by intrabasinal uplifts such as the Central Basin Platform (CBP) and bordered by carbonate shelves (Figure 1) (e.g. Flawn, 1961; Frenzel et al., 1988; Yang and Dorobek, 1995). The Midland Basin represents one of several sub-basins within the foreland of the Marathon-Ouachita Fold-and-Thrust belt and is structurally bounded by several prominent subsurface features, including carbonate platforms along the east, north and western margins with the Val Verde Basin and Ozona Arch delineating the southern margin of the basin (Figure 1).

During the early Paleozoic through the Mississippian, the ancestral Tobosa Basin occupied the region (Galley, 1958). The Tobosa Basin likely represented a regional down warped feature along a passive continental margin located south of the Matador Uplift and is predominately filled with carbonate and fine-grained siliciclastic material (e.g. Ellenberger, Wilberns Formations) (Galley, 1958; Frenzel et al., 1988). Structural uplifts bordering and within the Tobosa Basin began to develop in the Late Mississippian due to the collision of North and South America which

resulted in the formation of the Marathon-Ouachita fold-and-thrust belt (Ross, 1986; Yang and Dorobek, 1995). One of the most prominent uplifts, the Central Basin Uplift, (later becoming the CBP) formed early during the Marathon-Ouachita orogeny. Gravimetric studies on the CBP suggest a substantial mafic body underlying the CBP and which was confirmed by the discovery of mafic and ultramafic rocks recovered from the Nellie#1 well starting at 1402m (Keller et al., 1989, Kargi and Barnes, 1995).

Thick fine-grained siliciclastic sediments and limestones (Wolfcampian, Leonardian, and Guadalupian) filled the Midland Basin until the late Permian when Ochoan evaporitic sequences were deposited in the remaining accommodation space (Frenzel et al., 1988). The Wolfcamp Formation forms part of this massive sedimentary sequence and was deposited during the Wolfcampian stage (299-280Ma). The environment of deposition for the Wolfcamp is characterized as progradational and erosionally backstepping platform to basin sequences (Mazzullo and Reid, 1989) deposited within a rapidly subsiding depocenter. Following the Permian, tectonic quiescence continued through most of the Mesozoic with continental style sedimentation during the Triassic (Yang and Dorobek, 1995, McGowen et al., 1977). Early Cretaceous (Comanchean) sediments unconformably overlay Triassic and Paleozoic units and are comprised of shallow marine and peritidal sediments (Rose, 2016). Cenozoic sediments are sparse in the Midland Basin owing to regional erosion that is likely related to Laramide and later, Basin and Range tectonics (Horak, 1985). Laramide structures are present in west Texas along the Rio Grande and Guadalupe Mountains, however, surficial evidence of tectonic activity in the eastern Permian Basin associated with either event are non-existent (Frenzel et al., 1988). Apatite fission track analysis (AFTA) performed by Sinclair (2007) in the neighboring Delaware Basin suggests >2000m of uplift and erosion from the Early Cretaceous to the Late Miocene. In contrast, Rose

(2016) estimates  $\sim 34000 \text{ km}^3$  of Cenozoic erosion across most of the Midland Basin based on stratigraphic extrapolation of Cretaceous sediments further south. If one assumes uniform erosion across the region, this equates to  $\sim 300\text{m}$  of missing sediments in our study area. Overall, the nature and degree of Cenozoic uplift/erosion in the Midland Basin remains unclear. Considering this uncertainty and its impact on the burial history of the Midland basin, this study also addresses the magnitude of Cenozoic uplift using 1D Basin modeling.

Cores for this study capture the entire Wolfcamp Formation in the southeastern Midland basin and part of the lower Wolfcamp formation located in the central part of the basin. Facies observed across all cores include carbonate mass transport complexes (MTCs) of variable thickness and frequency, siliceous/calcareous mudrocks and diagenetically altered facies.

## **METHODS AND SAMPLING**

Full length plugs were extracted from slabs using a drill press from three vertical cores: Core 1 (1783-1948.9m,  $n = 175$ ) and Core 2 (1954.7-2122m,  $n = 285$ ) located in southern Irion County and Core 3 (2949.9-3010.2m,  $n = 64$ ) located in Glasscock County (Figure 1). Samples were cut to standard paleomagnetic plugs (25 mm diameter x 22 mm height) with each sampling interval yielding 2-4 specimens. Specimens from all cores were oriented with respect to stratigraphic up and drilled with respect to a fixed datum (specimen coordinate system) in each core. FMI logs of the entire length of Core 1 and 2 were provided by Devon Energy (sample shown in Figure 2A). Orientations of sub-vertical fractures imaged by the FMI logs were measured and matched to the corresponding fractures in the core (Figure 2B, 2C). Specimen coordinates were then converted to geographic coordinates by determining the angle between the fracture orientation and the plug site(s) (Figure 2D). Dip meter data and FMI logs indicated horizontal bedding in Core 1 and 2 therefore no dip-correction was applied to the data.

### ***Experimental methods***

Natural remanent magnetization (NRM) measurements were performed using a 2G Enterprise cryogenic magnetometer fitted with DC superconducting quantum interference devices (SQUIDS) housed in a magnetically shielded room at the University of Oklahoma. Specimens were subjected to alternating field (AF) demagnetization at field increments of 10mT from 0mT to 120mT. Following AF demagnetization, specimens underwent stepwise thermal demagnetization from 0°C to 450°C at 50°C increments. Principal components of the demagnetization data was evaluated with Zijderveld diagrams to determine the characteristic remanent magnetization (ChRM) (Ziderveld, 1967; Kirschvink, 1980; Torsvick et al., 2000). A threshold maximum angular deviation (MAD) value of  $<10^\circ$  was employed for determining magnetization components and mean paleomagnetic directions for the oriented core were computed using Fisher (1953) statistics. For oriented specimens, the virtual geomagnetic pole (VGP) was determined from mean paleomagnetic directions of the entire core and plotted on the North American apparent polar wander path (APWP) compiled by Torsvik et al. (2012). For unoriented specimens, inclination only data was processed using the statistical routine proposed by Arason and Levi (2010) in order to correct for shallow-inclination bias and plotted against the expected inclinations obtained from the North American APWP (Torsvik et al., 2012). Specimens with an inclination component greater than those observed on an expected inclination plot for a given locality (.i.e.  $< 80^\circ$ ) are deemed to have formed from an isothermal remanent magnetization related to drilling or DIRM.

High-field magnetic hysteresis measurements were performed on one specimen from each core using a Princeton Measurements vibrating sample magnetometer (VSM) 3900-04 at Southern Illinois University Carbondale. Each specimen underwent an applied field of 1 Tesla (T) at a field

step of 5.0 mT and averaging time of 1s. This configuration optimized signal to noise ratios, however, due to an extremely weak ferromagnetic signal, the raw data required additional processing to elucidate hysteresis properties from each specimen. Data conditioning was performed using HystLab, a MATLAB based software written by Paterson et al. (2018). Each hysteresis dataset underwent identical treatment which included linear high-field slope corrections, loop centering and paramagnetic drift corrections (Jackson and Solheid, 2010; Paterson et al., 2018). Hysteresis parameters (remanent magnetization ( $M_{rs}$ ), saturation magnetization ( $M_s$ ) and coercivity ( $B_c$ )) were computed from both processed and fitted loops. Raw and processed hysteresis loop fidelity was assessed using a Q-factor which represents the linear correlation between the upper and inverted lower branches (Jackson and Solheid, 2010). S-ratios, which are given by  $-IRM_{300mT}/IRM_{1000mT}$  were calculated to determine the proportion of ferrimagnetic to canted antiferromagnetic minerals (e.g. Liu et al., 2007). Back-field demagnetization curves were measured in order to obtain remanent coercivity ( $B_{cr}$ ) and isothermal remanent magnetizations (IRM) were measured and processed using the Max Unmix program (Maxbauer et al., 2016) to reveal the coercivity spectrums of representative specimens from each core. Saturation isothermal remanent magnetization (SIRM) were measured after applying a field of 1.2T on specimens following AF demagnetization. Bulk magnetic susceptibility ( $k_{lf}$ ), frequency-dependent susceptibility ( $\chi_{FD}$ ) and anisotropy of magnetic susceptibility (AMS) measurements were performed at 200A/m using a MFK1-FA Kappabridge magnetic susceptimeter. Frequency-dependent susceptibility ( $\chi_{FD}$ ) was measured to detect the presence of superparamagnetic (SP) grains and AMS measurements were performed to determine the magnetic petrofabric (e.g. Dearing et al., 1996; Borradaile, 1988; Tarling and Hrouda, 1993). Anisoft V4.2 was used to process AMS data and calculate the orientation of principal magnetic axes (K1, K2, K3) and scalar

parameters including the degree of magnetic anisotropy ( $P_j$ ) and shape of the AMS ellipsoid ( $T$ ) (Jelinek, 1981; Chadima, 2009). The SIRM/ $k_{lf}$  ratio was used to detect changes in magnetic mineralogy. For example, magnetite-bearing rocks exhibit SIRM/ $k_{lf}$  values of  $\leq 20\text{kAm}^{-1}$  whereas pyrrhotite and greigite are  $\geq 20\text{kAm}^{-1}$ ; however, this ratio is also influenced by paramagnetic and superparamagnetic (SP) contributions (e.g. Stoner et al., 1996; Peters and Dekers, 2003; Maher, 2007). Magnetic minerals were separated from bulk specimens by slowly pumping a slurry of micronized specimens past a stationary neodymium magnet (e.g. Reynolds et al., 2001).

Laboratory induced gyroremanent magnetizations (GRM) were computed from AF demagnetization data using the equation developed by Fu et al. (2008). The presence of a GRM coupled with curving demagnetization vectors has been attributed to the presence of greigite (e.g. Snowball, 1997). Thermal demagnetization of triaxial IRMs ( $x = 120\text{mT}$   $y = 500\text{mT}$   $z = 1200\text{mT}$ ) were also performed to fingerprint magnetic carrier minerals based on their unblocking temperatures.

Visual core description was performed using the facies scheme of Hamlin and Baumgardner (2012) with additional emphasis on diagenetically altered features (Wickard et al., in press). Microscale observations were made using a FEI Field emission scanning electron microscope (SEM) fitted with a Bruker XFlash 6I100 EDS (energy dispersive spectroscopy) system operated at 20 keV. These analyses were performed on polished thin sections from representative lithofacies and magnetic extracts derived from magnetic slurry separations.

### ***Burial history and thermal modeling***

A 1-D burial and thermal model was developed for Irion county (Core 1 and 2) using Basin Mod1D (Platte River Associates, 2002) in order to determine whether the timing of a ChRM

corresponds to specific thermal/tectonic events in the eastern Midland Basin. Several inputs are necessary in order to construct a geologically valid model. These inputs include lithospheric heat flow history, thermal conductivity and heat capacity of the lithologies, surface temperature history and burial history (Metwalli and Pigott, 2005). Modeling involves perturbing the crustal stretching factor (or beta) until the calculated present-day temperature profile matches the observed thermal profile from well-log temperature readings (e.g. Metwalli and Pigott, 2005). Modelled maturities and paleotemperatures are iterated against thermal maturity data to obtain a least-squares best fit.

### ***Database and uncertainty***

Data inputs and assumptions used for the model are provided in the Appendices. Lithospheric heat flow was obtained from modern-day data compiled by Blackwell et al. (2011). Surface temperatures were constrained by: 1) determining the paleolatitudes across geologic time using paleogeographic reconstructions by Blakey (2008), 2) estimating modern-day mean annual surface temperatures (MAST) (e.g. Deconto, 2009) for the respective paleolatitudes and 3) modulate MASTs by temperature variations from 542Ma until present as determined by Frakes et al. (1992). Burial history inputs such as unit thicknesses, age and their lithological compositions were determined from a composite electric type log (San Angelo Geological Society Stratigraphic committee, 1957), isopach maps (Barnes and Bell, 1977; Craig et al., 1979; Rose, 2016) and well logs provided by Devon Energy. Default software values for initial porosity and compaction (e.g. Baldwin and Butler, 1985) were adopted for lithological compositions. Additionally, the porosity–depth relationship for decompaction correction of Falvey and Middleton (1981) was applied to lithologies. Limited paleobathymetric estimates were obtained from Brown et al. (1990) and sea-level changes were incorporated from Haq and Schutter (2008). Finally, vitrinite reflectance ( $R_o$ )

and borehole temperature readings were provided by the works of Pawlewicz et al. (2005) and Devon Energy, respectively.

Estimates of eroded thickness in the Midland Basin, particularly during the Cenozoic, represents the most significant uncertainty in the model. Therefore, basin modeling was performed using two end member thicknesses that are derived from the aforementioned works of Sinclair (2007) and Rose (2016) and iterated until a best-fit thermal profile was achieved.

## RESULTS

### *Core 1*

Fracture orientations from FMI logs and mean AMS tensors with 95% confidence ellipses (geographically corrected) are shown in Figure 4A. The predominant fracture and AMS trend is NE-SW, with a lesser population in a NW-SE fracture trend. Vertical to sub-vertical AMS fabrics with a subtle NW-SE trend predominate at depths less than 1816.5m and petrographic evidence from Heij and Elmore (in press) suggests that such fabrics are associated with increased concentrations of ferroan dolomite. Among such fabrics, T values range from weakly oblate ( $T = 0.35$ ) to strongly prolate ( $T = -0.99$ ) (mean  $T = -0.61$ ) with low degrees of anisotropy (mean  $P_j = 1.009$ ).

The ChRM in the reoriented core displays northerly declinations and moderate down inclinations ( $Dec = 345.1^\circ$ ;  $Inc = 44.4^\circ$ ;  $\kappa = 16.84$ ;  $\alpha_{95} = 6.1$ ;  $D_p = 4.7$ ;  $D_m = 7.4$ ) which are revealed from 30/40mT to 120 mT during alternating field (AF) demagnetization (Figure 3A, 4B). From 0-40 mT specimens exhibit a DIRM (e.g. Figure 3A) with only a few specimens revealing a modern VRM. Thermal demagnetization was not performed on samples from Core 1 because AF demagnetization resulted in sufficient decay of the NRM (75-92%) (e.g. Figure 3B). The ChRM was acquired during the late Jurassic based on its pole position on the APWP, however, a lesser

portion of the 95% confidence ellipse overlaps with mid-Eocene and early Oligocene segment of the APWP (Figure 4C). A non-uniform distribution of inclinations are observed although there appears to be no relationship with depth or facies to explain this distribution (Figure 5). There are however, anomalously shallow inclinations (0-11.4°, Fig. 3b) associated with diagenetically altered MTCs and fractured concretions unblocked from 40-120mT (Figure 8A, 8B). These data were excluded from pole calculations and, due to a low number of specimens (n=4), a statistically valid pole position could not be determined. Based on inclination only calculations, the age of these diagenetically altered specimens would range from late Permian through the end of the Triassic.

On average, SIRM/ $K_{lf}$  values in Core 1 are greater than those observed in other, deeper cores with 25% of samples showing values  $> 10 \text{ kA/m}^{-1}$  (Figure 5). Similarly, GRMs are more frequently observed although, there is no relationship between the presence of a GRM and elevated SIRM/ $K_{lf}$  values.

### ***Core 2***

Like Core 1, Core 2 displays a moderate, steep down component unblocked from 40 to 120mT or from 60 to 375°C (Figure 3C, 3D). The degree of AF demagnetization varies widely from 30.5% to 92% (mean = 56.3%) and median destructive fields (MDFs) were, on average, lower (mean = 32.7mT) than Core 1 and 3. Reorientation of paleomagnetic specimens to geographic coordinates for this core was problematic for two reasons: 1) specimen sites located in close proximity to sub vertical fractures often displayed strong DIRM overprints (e.g. 2050-2072m) (Figure 6) and; 2) significantly fewer fractures were detected by FMI logs (n=6) which likely increased error related to mechanical rotation between fracture and specimen sites. The presence of DIRMs have no direct bearing on AMS data and therefore, AMS data was corrected

based on FMI fracture orientations. In certain cases, Core 2's AMS data is in good agreement with AMS orientations from Core 1, particularly from 1955m-1965m and 2039m-2084m, however, several intervals show N-S or NW-SE lineations (e.g. 1980m-1999m; 2000m-2009.5m) and therefore could indicate mechanical rotation. Core 2 contains widespread occurrences of vertical to sub-vertical AMS fabrics which, in several cases trend NW-SE. T and Pj values are similar to observed values in Core 1 (mean T = -0.62; mean Pj = 1.012).

Due to the problems with obtaining reliable geographic corrections, only paleomagnetic inclinations were considered. These were plotted against expected inclinations calculated for the APWP in order to determine their age. A mean inclination of  $42.1^\circ$  was computed ( $\kappa = 22.42$ ,  $\theta_{63} = 17.13$  and  $\alpha_{95} = 4.54$ ) and corresponds to a Jurassic age ( $165 \pm 15$ Ma) (Figure 4D). These ages are remarkably similar to those observed in Core 1. Another similarity is the presence of anomalously shallow inclinations ( $n = 3$ ) residing exclusively in diagenetically altered MTCs ( $-2.2$  to  $12.6^\circ$ ) (Figure 3E, 8C, 8D) and, like Core 2, fall within the late Permian through Triassic periods. These specimens, like shallow component in Core 1 are unblocked from 40-120mT (Figure 8E). The presence of shallow inclinations associated with diagenetically altered carbonate-rich facies in both Core 1 and Core 2 suggests that these inclinations are not mere outliers but in fact point to an early remagnetization.

SIRM/ $K_{lf}$  ratios are similar to, but slightly less than Core 1 (mean =  $8.3 \text{ kA/m}^{-1}$ ). GRMs occur across the entire core but are concentrated between 2008m - 2036m. SIRM/ $K_{lf}$  ratios have a positive correlation with  $k_{fd}$  ( $R^2 = 0.48$ ) (Figure 9B) and suggests that the concentration of SP grains influence the magnitude of SIRM/ $K_{lf}$  values.

### **Core 3**

A stable ChRM (moderate to steep down component) is generally revealed between 40mT and 120mT or from 50°C to 375°C (Figure 3F, 3G). AF demagnetization resulted in 23.5 to 88.1% (mean = 60.87%) decay of the NRM across all specimens and MDFs range from 85mT to 25Mt (mean = 46.5mT). Like the other cores, specimens acquired a GRM starting at 80-100mT AF demagnetization steps (Figure 3H) and specimens displaying a GRM were confined to discrete intervals (Figure 7). FMI logs were not available for this core and geographic corrections could not be applied, however, 74% of declinations were grouped between Dec = 320° and Dec = 60° which suggests that mechanical rotation between specimen sites was minimal. A nonuniform distribution of inclinations are observed with progressively increasing inclinations from 2962m to 2950 whereas at greater depths, little variation is observed (2966m – 2994m) (Figure 7). Overall, Core 3 has a mean inclination of 33.7° ( $\kappa = 18.7$ ,  $\theta_{63} = 18.77$  and  $\alpha_{95} = 6.36$ ) and corresponds to a Jurassic (170Ma±15) magnetization. SIRM/ $K_{lf}$  ratios are generally <5 kA/m<sup>-1</sup> with certain intervals showings values >20 kA/m<sup>-1</sup> (Figure 7). Overall, bulk magnetic susceptibility in Core 3 (Avg. = 7.6\*10<sup>-8</sup> m<sup>3</sup>/kg) is significantly greater than both Core 1 (Avg. = 3.8\*10<sup>-8</sup> m<sup>3</sup>/kg) and Core 2 (4.8\*10<sup>-8</sup> m<sup>3</sup>/kg). Finally, a remarkably consistent AMS fabric is observed in Core 3, with well constrained K1 confidence ellipses. Core 3 has a negligible concentration of sub-vertical AMS fabrics and is dominated by normal AMS fabrics. T and Pj values for normal AMS fabrics in Core 3 are also significantly greater than Core 1 and 2 (Core 3 mean T = 0.9 ; mean Pj = 1.067 ; Core 2 mean T =0.87; mean Pj = 1.048; Core 1 mean T =0.836; mean Pj = 1.025).

### ***Drilling induced remanent magnetizations (Core 1-3)***

Overall, ~20 % of specimens that underwent AF or thermal demagnetization produced invalid data owing to a strong drilling induced component or demagnetization vectors with

significant curvature that could not be fit using PCA (examples in Appendices). Such specimens generally exhibited lower MDFs (<20mT) than stable, ancient components. In general, specimens with MDFs <20mT are likely to carry low coercivity minerals which are prone to remagnetization by fields generated by the drill string during coring (e.g. Audunsson and Levi, 1989 and references therein). Among specimens with MDFs >20-25mT a DIRM is confined to low fields (0-40mT) (e.g. Figure 3A, 3B, 3C, 3G, 3H).

### ***Triaxial thermal decay, IRM acquisition and Hysteresis data Core 1-3***

During IRM acquisition, samples reached magnetic saturation at relatively low fields (300 – 450mT) and curves display smooth, concave downward shapes (n=12, 4 from each core) (Figure 9A). IRM unmixing models suggest that the coercivity spectrum is best represented by a single component with mean coercivities ranging from 55-75mT (Figure 9A inset). This range is consistent with reported values of magnetite (e.g. Egli, 2003). Unmixing of backfield demagnetization also indicates a single component with a similar range of mean coercivities.

Triaxial thermal demagnetization plots (Figure 10A, 10B, 10C) display unblocking temperatures along the Z-axis (1.2T) of 350°C to 425°C across all cores and are consistent with magnetite. Among all specimens measured, the X (0.12T) and Y (0.5T) fail to decay completely (75-80%) and magnetizations begin increasing rapidly from 300°C. This increase probably represents the oxidation of iron sulfides such as pyrite and marcasite. Rapid decay of the X axis and Y-axis does occur between 200°C and 300°C in several samples and may be indicative of ferrimagnetic iron sulfides (e.g. Figure 10C).

Unprocessed hysteresis data shows a large paramagnetic component (2 to 3 orders of magnitude greater than the ferromagnetic component) in all specimens measured (Figure 11A, 11D, 11G). Q values for processed loops range from 1.49 to 1.75 and suggests some deviation

from inversion symmetry, however, these values do fall within an acceptable range to compute meaningful hysteresis loop parameters (Jackson and Solheid, 2010). Root mean squared (RMS) noise of unprocessed (yellow) and processed (black) loops are shown in Figure 11C, 11F, 11I. A substantial reduction in signal noise was achieved after applying the corrections outlined in the Methods section. Hysteresis parameters and corresponding SIRM/ $k_{If}$  ratios are shown in Table 1. Processed and fitted hysteresis loops display a single magnetic component with the exception of Core 2 which shows a subtle wasp-waistedness which may be indicative of SP/SD assemblages (Tauxe et al., 1996). Based on Mr/Ms and Bcr/Bc ratios for magnetite (Day et al., 1977; Dunlop, 2002), pseudo single-domain (PSD) magnetic grain sizes occur in Core 1 and SD grain sizes carry the magnetic remanence in Core 2 and 3 (Table 1). S-ratios ranging from 0.92-0.98 also affirm that ferrimagnetic minerals dominate the magnetic mineralogy.

### ***SEM and EDS of magnetic extracts Core 1-3***

SEM analysis of magnetic extracts were primarily comprised of chlorite with dispersed magnetite spherules (Figure 12A). EDS spectra suggests Fe-rich chlorite with trace concentrations of Ni and Cr (Figure 12A). Chlorite is paramagnetic however, it is plausible that these silicate grains contain submicron magnetic inclusions that probably fall within the SD to SP grain size. This is supported by elevated atomic iron percentages that are substantially greater than those observed in chlorite alone. Spherules range from 20 $\mu$ m to >5 $\mu$ m in diameter and occur as smoothed spheres or aggregated crystals with some crystal habits similar to pyrite framboids observed in thin section (Figure 12A, 12B, 13D). EDS spectra of spherules have elemental concentrations consistent with magnetite and occasionally contain trace amounts of Cr and Al. Amorphous aggregates with thin organic matter films were also observed in the extract (Figure 12C). Organic-

rich masses with dispersed Ni/Cr-rich chlorite and magnetite with spinel-like crystal habits are observed in the magnetic extract (Figure 12D).

Although rarely observed, magnetic sulfides were also detected in the extract. These grains are generally  $>1\mu\text{m}$  and therefore, reliable EDS spectra were difficult to obtain because the interaction volume of the electron beam is greater than the individual crystal(s) measured. Despite this, elemental ratios obtained from these scans were markedly different than those obtained from EDS spectra of pyrite (e.g. Figure 13E). After normalization, iron and sulfur percentages ranged from 41.1-48% and 58.8 to 52%, respectively. These percentages fall within the stoichiometric percentages of both greigite and pyrrhotite.

### ***Microtextural observations from thin sections Core 1-3***

SEM analysis reveals iron sulfides residing within mica sheets (Figure 13A) of samples exhibiting a GRM in Core 3 (e.g. 2987m). Greigite can reside within mica sheets (e.g. Jiang et al., 2001), however, EDS analysis proved inconclusive for positive identification of greigite in this case. EDS spectra of several chlorite aggregates from the magnetic extract contain no sulfur associated with chlorite. Figure 13B shows barite with a “fish-tail” crystal habit and chlorite encapsulating the margins of the barite crystal. This association is common across all cores. Pyrite framboids have extensive overgrowths, with the overgrowths replacing both barite and ferroan dolomite (Figure 13B). Chlorite is also associated with authigenic albite however, it exhibits compositional and textural differences relative to chlorite associated with barite. Specifically, this chlorite tends to have higher Fe/Mg ratios and manifest as fine-grained intergrown masses (Figure 13C). Pyrite framboids show a variety of forms such as those with overgrown margins, disarticulated clusters and more equilibrated textures (Figure 13B, 13D). Disarticulated pyrite clusters resemble previously reported greigite microtextures (e.g. Roberts 2011), however, EDS

analysis indicates no detectable quantities of preserved greigite. In addition to pyrite framboids, cubic pyrite occurs individually or as aggregates within fractures, allochems and the matrix. Inclusions of barite, sphalerite and possible pyrrhotite/greigite occur within several cubic pyrite grains (Figure 13E). Furthermore, unusual textural transitions from predominately cubic to more elongated crystal habits are a feature in many specimens and suggests marcasite or pyrrhotite crystal growth (Figure 13F).

### ***1D Basin Modeling***

Figure 14A presents a 1D basin model with major tectonic events, age of magnetizations from each core, proposed timing for AMS lineation and relative timing of certain diagenetic minerals based on textural association with chlorite. Basin modeling suggests that peak burial temperatures in the Wolfcamp Formation (ranging from 105 to 130°C) occurred between 270 and 200 Ma shortly following a period of rapid subsidence. Following the Triassic, burial temperatures were sustained at 100 – 120°C until the late Cenozoic (Figure 14A). Three modeled maturity profiles are shown against the measured Ro data with each profile depicting 300m (dotted line), 800m (solid line) and 2000m (dashed line) of Cenozoic uplift (Figure 14B). The 800m maturity profile shows the best fit to the measured Ro whereas the 2000m and 300m maturity profiles overestimate and underestimate the measured Ro respectively.

Basin modeling also provided estimates of sedimentation rates. The majority of sedimentation occurred from ~320Ma to 265Ma with peak sedimentation rates reaching up to ~650m/Ma during this period (Appendix).

## DISCUSSION

### *Magnetic Fabrics and Fracture Orientations*

AMS fabrics showing bedding parallel K1 tensors are primarily carried by paramagnetic Fe-rich clays (documented by Heij and Elmore, in press). Furthermore a strong paramagnetic behavior is evident from hysteresis data and thus, further supports a paramagnetically dominated magnetic assemblage.

The consistency of K1 directions and subtle girdle of K3 tensors in both geographically corrected and specimen coordinates points to a tectonically influenced fabric produced by layer-parallel shortening (LPS) (e.g. Weil and Yonkee, 2009; Almquist and Koyi, 2018). The NE-SW magnetic lineation observed in Core 1 and reliably oriented specimens in Core 2 suggests a regional NW-SE shortening direction. Given the consistent fabric observed in Core 3, a similar stress regime was likely operating in the central part of the Midland Basin. The NE-SW fracture trend observed in Core 1 and Core 2 is also consistent with natural fracture trends reported by Lorentz et al. (2002) in the overlying Spraberry Formation (within the Leonardian sequence) in Midland County which lies due west of Core 3. Two distinct periods of tectonic shortening were known to be operating in the Midland Basin and therefore, the AMS lineation probably formed either at the embryonic development of the foreland basin (during Marathon-Ouachita thrusting) or, much later, in response to Laramide far-field stresses. A lineation related to Basin and Range Extension is considered unlikely given the paucity of Basin and Range structural features in the eastern Permian Basin. We tentatively attribute the presence of the magnetic lineation to Laramide deformation because field evidence of NE-SW layer-parallel compression has been documented by Anderson and Kirkland (1970) in Ochoan aged sediments in the Guadalupian Mountains. These deformation features post-date the period in which Marathon-Ouachita thrusting was active,

however, additional studies such as an AARM based study could provide further insight to better delineate which period of compression is responsible for the magnetic fabric.

Vertical/sub-vertical K1 tensors suggests that inverse AMS fabrics are present in Core 1 and 2. Inverse AMS fabrics can be carried by minerals such siderite, ferroan dolomite or SD magnetite and result from an inverse relationship between magnetic axes and shape/crystallographic axes (e.g. Rochette, 1988; Ihmle et al., 1989; Rochette, 1999). Core 1 and 2 show evidence for both ferroan dolomite (e.g. Figure 13B) and SD magnetite (Table 1), however, a study of AMS carrier minerals by Heij and Elmore (in press) suggest that ferromagnetic minerals do not significantly impact AMS fabrics in these rocks. Several intervals show inverse fabrics trending toward the NW-SE shortening direction (e.g. Figure 5, 1783m-1817m) and suggests that such fabrics record LPS in conjunction with normal AMS fabrics. This type of tectonic fabric has been previously reported in Alpine Jurassic metasediments with interbedded carbonate and shale units (Rochette, 1988). If Laramide stresses are indeed responsible for this fabric, it can be safely asserted that most of the ferroan dolomite in Core 1 and 2 formed before the Late Cretaceous (Figure 14A). This assertion is further supported by textural relationships that clearly indicate early dolomitization such as clays wrapping around euhedral ferroan dolomite rhombs (Heij and Elmore, in press). There are however, instances where inverse AMS fabrics do not lie parallel to a NW-SE shortening direction (Figure 6, 2055m-2085m). These instances can be explained by one or a combination of three processes: 1) partial replacement of ferroan dolomite by iron sulfides (Figure 13B); 2) partial dissolution of ferroan dolomite (Heij and Elmore, in press); 3) competing inverse and normal AMS carrier minerals forming an intermediate AMS fabric (Ferré, 2002).

### ***Magnetic Remanence Carrier(s) and the Nature of CRMs***

Rock magnetic experiments including SIRM/ $k_{lf}$  ratios, IRM acquisition, hysteresis and triaxial IRM decay all suggest the remanent magnetization resides primarily in magnetite although the presence of a widespread GRM brings into question whether greigite forms part of the magnetic assemblage. SEM analysis shows microtextural characteristics (e.g. Figure 13A, Figure 13D) consistent with previously documented occurrences of greigite (Roberts, 2011; Fu et al., 2008), however, EDS analysis fails to provide convincing evidence of elemental concentrations consistent with greigite. Favorable conditions for greigite formation such as organic carbon supply, sulfide production, reactive iron and anoxia were probably available during early diagenesis (Roberts, 2011, 2015), however, given the extended period of burial, metastable greigite would have probably completely converted to pyrite (Roberts, 2011). Alternatively, if greigite is indeed present, a stable magnetization may be inhibited by its magnetic granulometry (i.e. multi-domain MD or SP). Direct evidence for ferrimagnetic sulfides was observed in magnetic extracts, however a qualitative estimate suggest that they only make up ~1% of the total extracted material.

The presence of pyrrhotite/greigite as inclusions in cubic pyrite may suggest that ferrimagnetic sulfide formation occurred contemporaneously with thermochemical sulfate reduction (TSR) (Machel et al., 1995; Machel, 2001; Manning and Elmore, 2015). SIRM/ $k_{lf}$  ratios greater than  $20\text{kA/m}^{-1}$  are also consistent with the presence of pyrrhotite in certain intervals (Maher, 2007). Pyrrhotite may also occur within the textural transition from cubic pyrite to a more bladed crystal habits that reside in samples showing high SIRM/ $k_{lf}$  ratios (Figure 13F). We ascribe these textures to changes in pH during TSR because marcasite, a major constituent of these transitions, tends to prefer lower pH conditions (Taylor and Maquaker, 2000; Schieber, 2011).

The majority of magnetic extracts consisted of Fe-rich chlorite which suggests that ferrimagnetic minerals are probably incorporated within the matrix or on the surface of these clays (Figure 12A). The absence of sulfur peaks from the EDS data and pronounced oxygen and iron peaks indicate that magnetite likely occurs associated with these clays (Figure 12A). We attribute the Jurassic aged ChRM for all three cores to be a CRM primarily related to the neoformation of magnetite within the matrix of chlorite/illite sheets during chloritization/illitization (e.g. Hirt et al. 1993; Katz et al., 2000; Gill et al. 2002; Blumstein et al. 2004; Moreau et al. 2005; Tohver et al. 2008). Chloritization during clastic diagenesis is generally considered to be a solid-state transformation that occurs at temperatures from 40°C to 120°C (e.g. Shau and Peacor, 1992; Beaufort et al., 2015). This temperature range stands consistent with modeled burial temperatures (Figure 14A). Chloritization generally occurs concurrently with illitization of smectite which releases clay-bound water and cations such as iron, creating conditions suitable for magnetite authigenesis (Elmore et al., 2012). Textural associations of chlorite with albite (another common byproduct of illitization) further supports that chloritization was coeval with illitization (Lynch, 1997) (Figure 14A). Another interesting textural association emerges with chlorite and barite. Figure 13B shows chlorite growth approximately normal to the margins of a barite crystal. This texture may suggest that chloritization in this case resulted from a dissolution-crystallization mechanism where, fluids migrated along the margins of the barite crystal. Similar textural relationships are reported by Wickard et al. (in press) and suggests that barite predates chloritization (Figure 14A).

Regardless of whether chlorite formed via solid-state transformation or dissolution-crystallization, nucleation and magnetite growth within chlorite can be expected to produce nanoparticle populations with size distributions (i.e. SP-SD) controlled by factors such as element

availability, diffusion rates, reactivity, temperature and time (Jackson and Hysell, 2012). SP and SD grain size distributions in the Wolfcamp are confirmed by frequency-dependent susceptibility and hysteresis data. We postulate that PSD grain sizes (Table 1) can potentially be reached if favorable conditions persist through burial. Favorable conditions in the Wolfcamp would represent the sustained burial temperatures (100-120°C) during most of its burial history, increased supply of iron-bearing minerals to the basin (Heij and Elmore, in press) and maturation of organic material which can enhance illitization rates by increasing the Gibbs free energy of the reaction (Berger et al., 1997).

In addition to a remanence carried by neoformed magnetite hosted by chlorite, magnetic spherules also represent a possible magnetic carrier mineral. Magnetite spherules and amorphous aggregates closely resemble textures reported several authors (e.g. MaCabe et al., 1987; Elmore et al., 1987). Previous rock magnetic studies of individual magnetite spheroids and framboids indicate that these crystal forms contribute very little to the total NRM which is likely due to their MD grain size (Halgedahl and Suk, 1992; Xu et al., 1994). This stands consistent with the observation of Saffer and McCabe (1992) who found that the relative abundance of framboids are uncorrelated with degree of remagnetization. Proposed ideas for the formation of spherules in sedimentary rocks include oxidation of pyrite framboids and/or magnetite authigenesis promoted by hydrocarbon migration or maturation of organic matter (MaCbe et al., 1987; Suk et al., 1990, 1993a; Lu et al., 1990; Elmore et al., 1993; Banerjee et al., 1998). 1D Basin modeling confirms that both are viable mechanisms considering that the Wolfcamp was situated in the oil-window during the acquisition of the Jurassic CRM (Figure 14A). Sinclair's (2007) basin modeling reports similar results, suggesting that peak hydrocarbon generation was during the Cretaceous in cores located in deeper sections of the Midland Basin.

The main CRM acquisition across all three cores appears to follow a diachronous trend from the Lower Wolfcamp to the Upper Wolfcamp with older ages in the former (Figure 14A). The burial history model, which is predicated on data from Core 1 and 2, shows isotherms with a shallow gradient during this period. We postulate the slight diachroneity across these cores to be consistent with a slow, progressive subsidence rate as depicted by the model (Figure 14A). In contrast, if rapid subsidence was occurring during the Jurassic, the upper and lower Wolfcamp would probably reach the same thermal conditions within a narrower timeframe and likely acquire a CRM with the same age across both Core 1 and Core 2. Basin modeling also aids in determining the likelihood of a thermoviscous remanent magnetization (TVRM). Prolonged temperature exposure from the Jurassic until the end of the Cretaceous at 100°C-120°C suggests that the development of a TVRM is unlikely.

The anomalously shallow inclinations residing in fractured concretions and diagenetically altered MTCs suggests a facies-dependent remagnetization mechanism related to early diagenetic processes, however, given that only 7 specimens were recovered, interpretations for the origin of this component are mostly speculative. The age of the inclinations from these (~270Ma-200Ma) correspond to two key events: 1) Rapid flexural subsidence and 2) elevated burial temperatures (~110-130°C). Fluid migration related to dewatering would be pronounced during this period due to rapid sedimentation rates (Appendix). Septarian-like fissures comprised of barite and pyrite residing in the carbonate concretions are thought to form by shrinkage or dehydration during sulfate reduction (Figure 8A, 8B) (Raiswell and Fisher, 2000). The altered MTCs show similar diagenetic minerals to those observed in concretions and may have undergone similar fluid expulsion processes (Wickard et al., in press). In the altered MTCs large detrital carbonate lithoclasts may have been able to retain more fluids than the surrounding matrix during burial and

only expel fluids at greater depths/temperatures. These conditions may have been favorable for early CRM development (i.e. fluid migration and increased temperatures) (e.g. Jackson and Hysell, 2012), however, it is not clear why these “early CRMs” were preserved. One possibility could be an early cementation event(s) (i.e. chertification) following the CRM which buffered later fluid interactions. Overall, the underlying mechanism(s) for the early CRM residing in these facies are purely speculative and additional sampling is required to confirm the presence of this early magnetization.

## CONCLUSIONS

Combining paleomagnetic, rock magnetic and SEM analysis with basin modeling can provide a new integrative framework to decipher the spatial and temporal boundaries of tectonic and diagenetic processes operating in sedimentary basins. Results from this study demonstrate the following key burial events in the Wolfcamp Shale:

- 1) Chloritization via solid-state transformation or dissolution-crystallization is interpreted to be coeval with a Jurassic remagnetization. The magnetization resides primarily in SD magnetite hosted within chlorite based on SEM and rock magnetic data. Modeled temperatures for this period also stand consistent with reported temperature ranges for illitization and chloritization. In addition to chloritization the CRM may have also formed due to maturation of organic matter/migration of hydrocarbons.
- 2) The presence of GRMs suggests that greigite does form part of the magnetic mineralogy, however, it appears to carry an unstable magnetization in the Wolfcamp. Ferrimagnetic sulfides such as greigite or pyrrhotite likely reside

within cubic pyrite or within the textural transitions from cubic pyrite to bladed crystal habits.

- 3) Normal and inverse AMS fabrics show trends consistent with NW-SE LPS and likely correspond to Laramide-aged tectonic shortening. Normal AMS fabrics are dominantly carried by clays whereas inverse AMS fabrics are carried by ferroan dolomite.
- 4) Gradual subsidence rates during the Mesozoic are consistent with a slight diachroneity observed in the Jurassic CRMs residing in Core 1 and 2. Uplift during the Cenozoic in the Midland Basin was at least half of that occurring in the Delaware basin based on 1D Basin modeling.

### Chapter 3 Figures

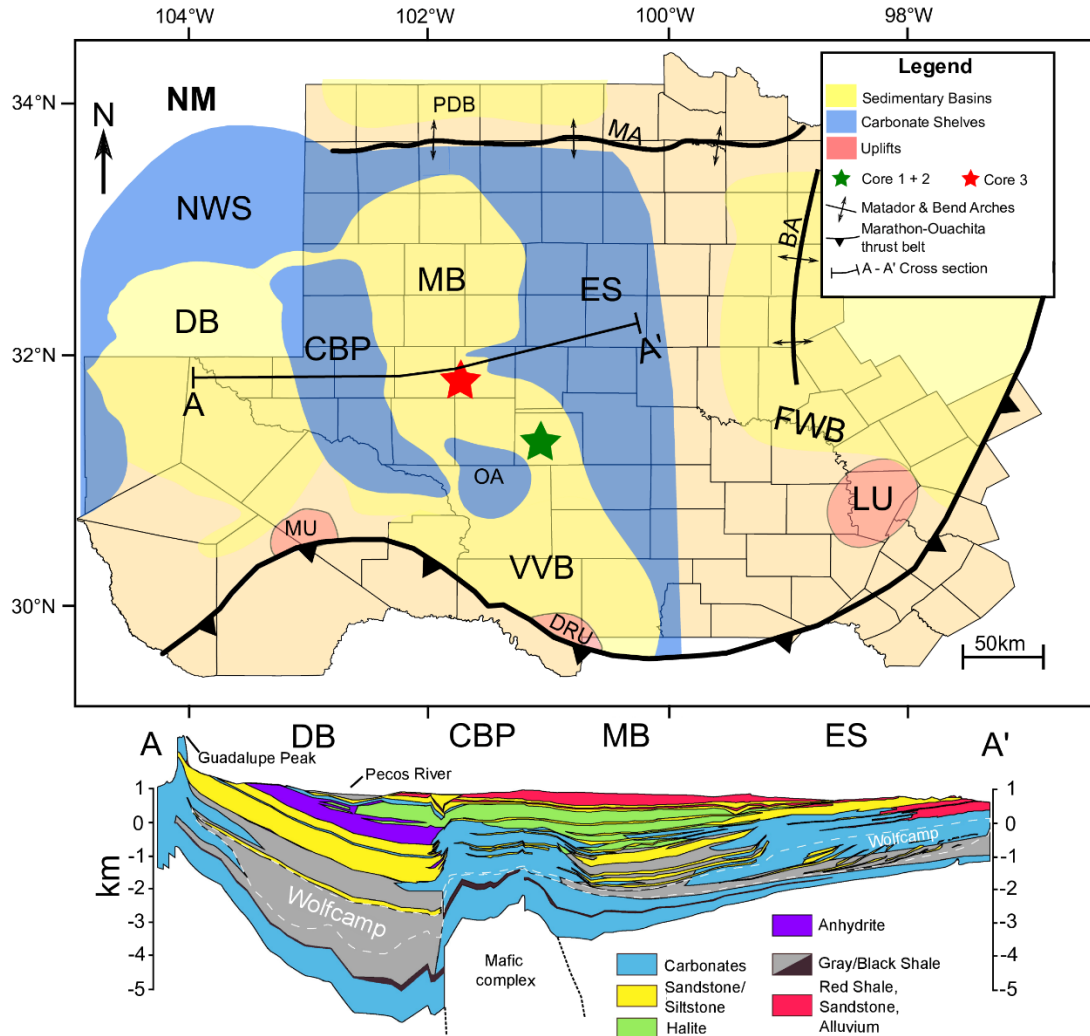


**Figure 1.** (A) Map of Permian Basin in West Texas with major structural features and core locations. Modified from Flawn et al. (1961). Green Star = Core 1 and 2; Red Star = Core 3; BA – Bend Arch; CBP – Central Basin Platform; DB – Delaware Basin; DRU – Devil Rivers Uplift; ES – East Shelf; FWB – Fort Worth Basin; LU – Llano Uplift; MA – Matador Arch; MB – Midland Basin; MU – Marathon Uplift; NM – New Mexico; NWS – North West Shelf; OA – Ozona Arch; PDB – Palo Duro Basin; VVB – Val Verde Basin. A generalized cross section (A-A') of the Permian Basin with stratigraphic boundaries of the Wolfcamp shown by dashed lines. Modified from Matchus and Jones (1984) and Engle et al. (2016).

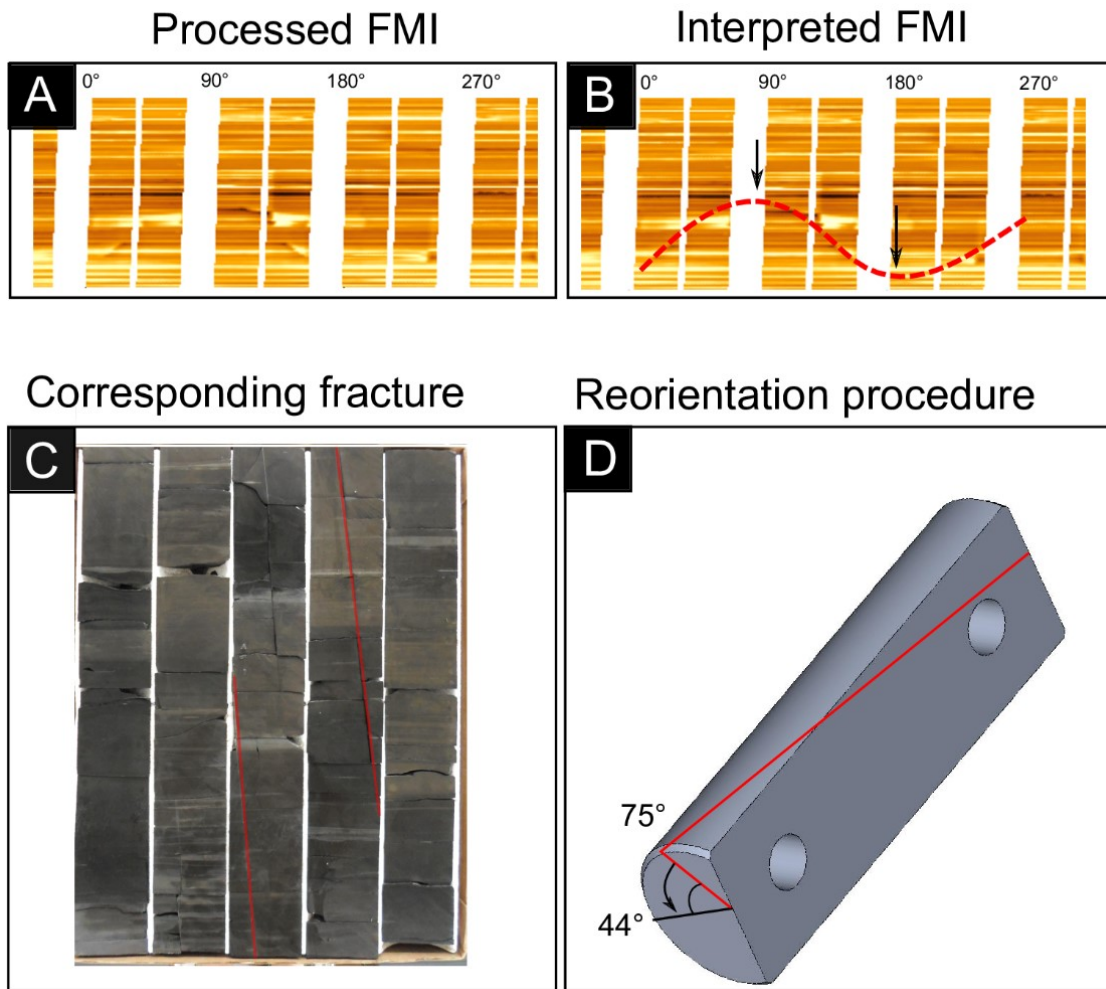


**Figure 2.** (A-D) Workflow for applying geographical corrections to unoriented core. (A) Processed FMI log showing horizontal bedding and sub-vertical fracture that manifests as a sinusoidal feature. (B) Interpreted FMI image with arrows showing fracture trend. (C) Photograph of core slab with fracture (red) corresponding to FMI image in (B). (D) Schematic representation of drilled core slab. Solid black line represents sampling datum or specimen coordinate system and red line presents the sub-vertical fracture. Geographic coordinates for specimens were determined by measuring the angle between the fracture orientation and the plug site(s).

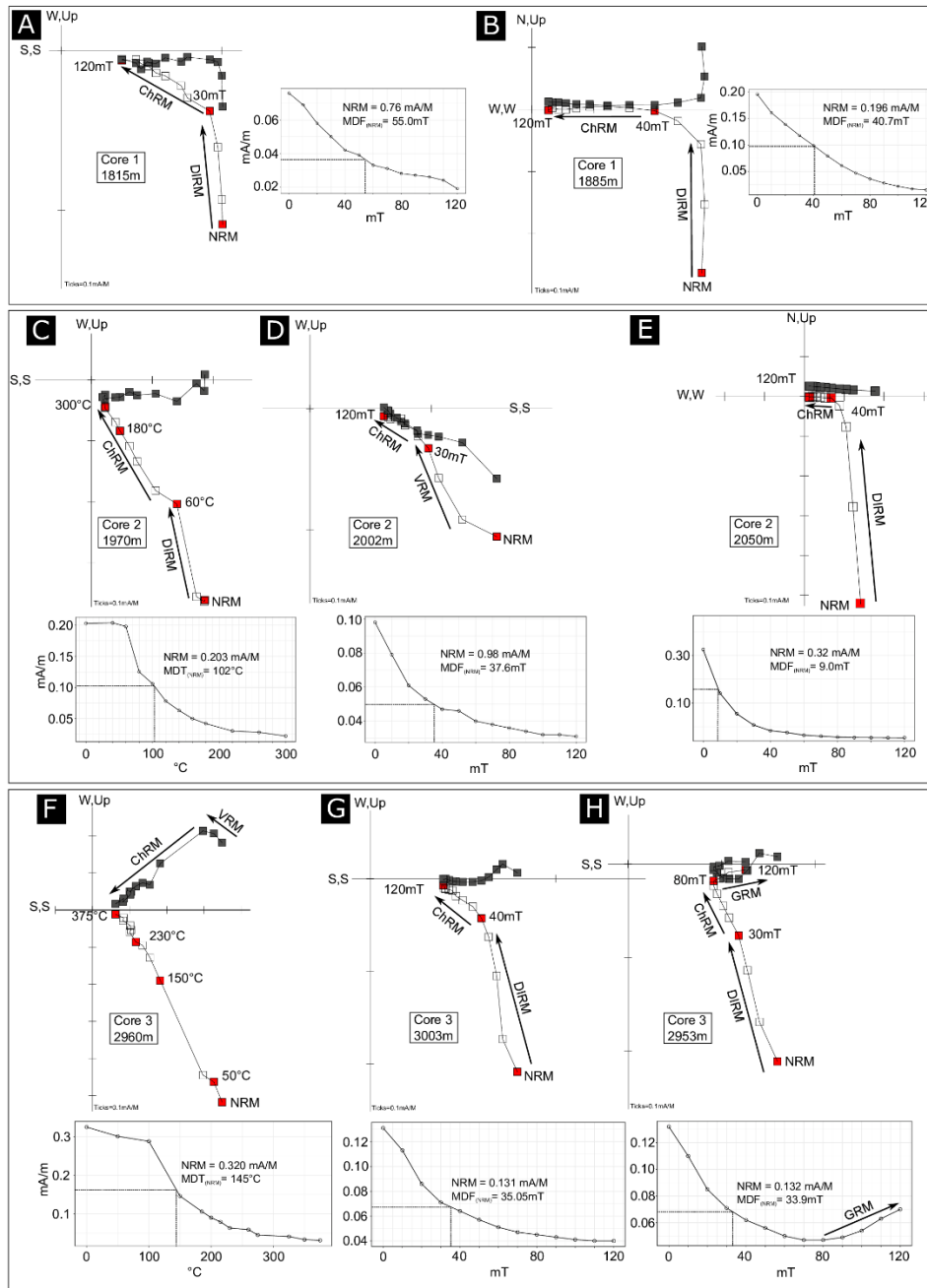


**Figure 3.** (A-H) Zijderveld diagrams (specimen coordinates) and demagnetization data for AF and thermal demagnetization experiments from Core 1 – 3. Note the presence of a DIRM in most specimens. Black squares = declinations, open squares = inclinations and red squares denote labeled demagnetization steps in mT or °C. (A-B) Zijderveld diagrams and AF demagnetization data from Core 1 showing a representative (A) mudrock and (B) carbonate concretion specimen. (C-E) Zijderveld diagrams and demagnetization data from Core 2 with representative (C) thermal decay of a mudrock specimen, (D) AF demagnetization of a carbonate and (E) diagenetically altered carbonate specimen. (F-H) Thermal and AF demagnetization of mudrock facies from Core 3. Note pronounced GRM development in (H) starting at 80mT.

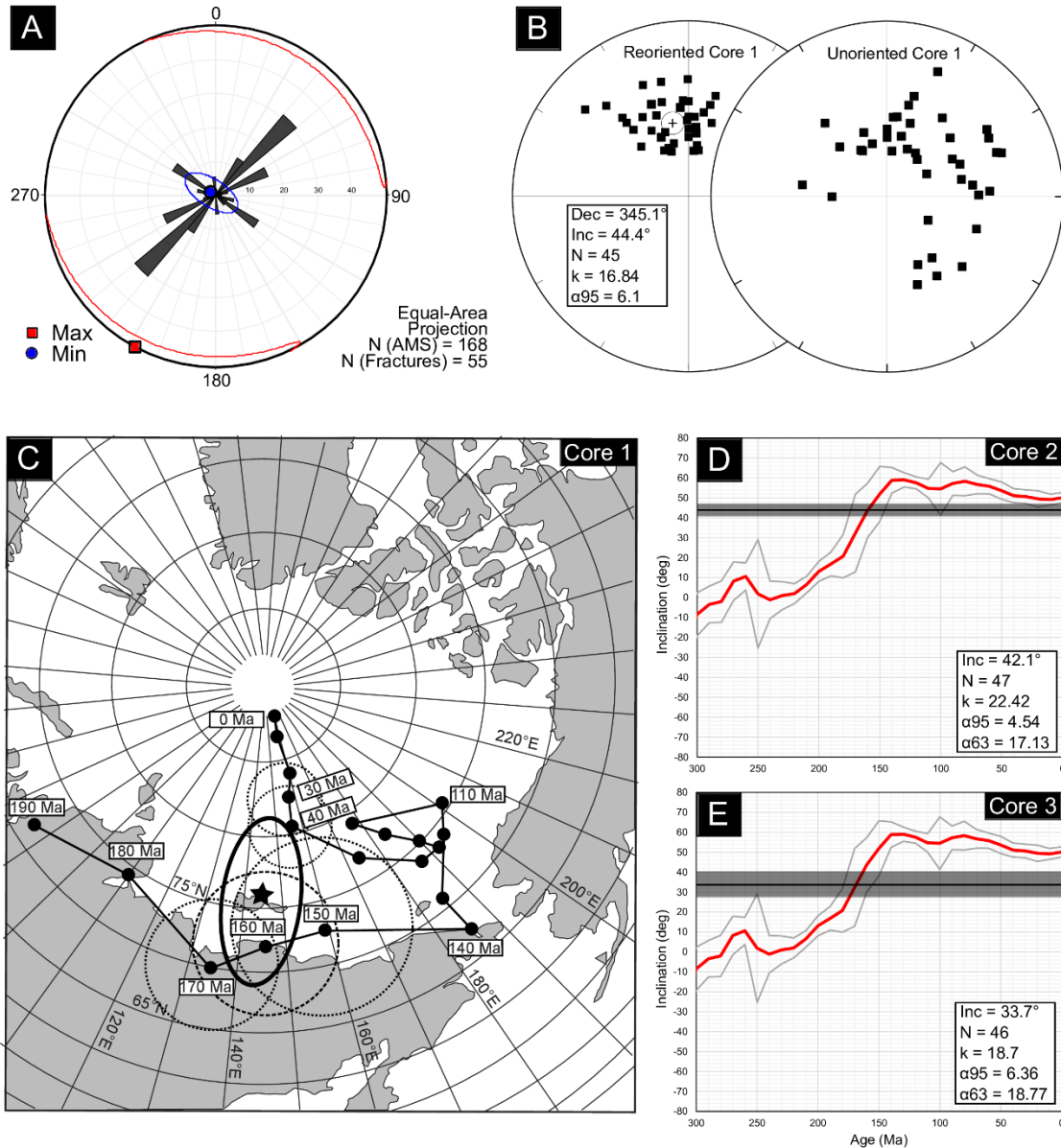


**Figure 4.** (A) Rose plot of fracture orientations from FMI logs overlaid onto the equal-area projection of mean K1 and K3 AMS tensors with 95% confidence ellipses (geographically corrected) from Core 1. (B) Equal-area projection of corrected (Reoriented Core 1) ChRM directions with crosshair denoting VGP and uncorrected ChRM directions (Unoriented Core 1) (C) APWP for North America (Torsvik et al., 2012) from 190Ma through 0Ma. Black star indicates VGP for Core 1 with corresponding  $\alpha_{95}$  confidence ellipse in solid black. Dashed ellipses represent  $\alpha_{95}$  confidence ellipses for ages intersecting the VGP. (D-E) Expected inclination plots for North America. Red line = expected inclination (Torsvik et al., 2012); gray lines =  $\alpha_{95}$  confidence limits for expected inclinations (Torsvik et al., 2012); black line and translucent area = mean inclination with  $\alpha_{95}$  confidence limits. (D) Inclination only plot Core 2 (E) Inclination only plot Core 3.

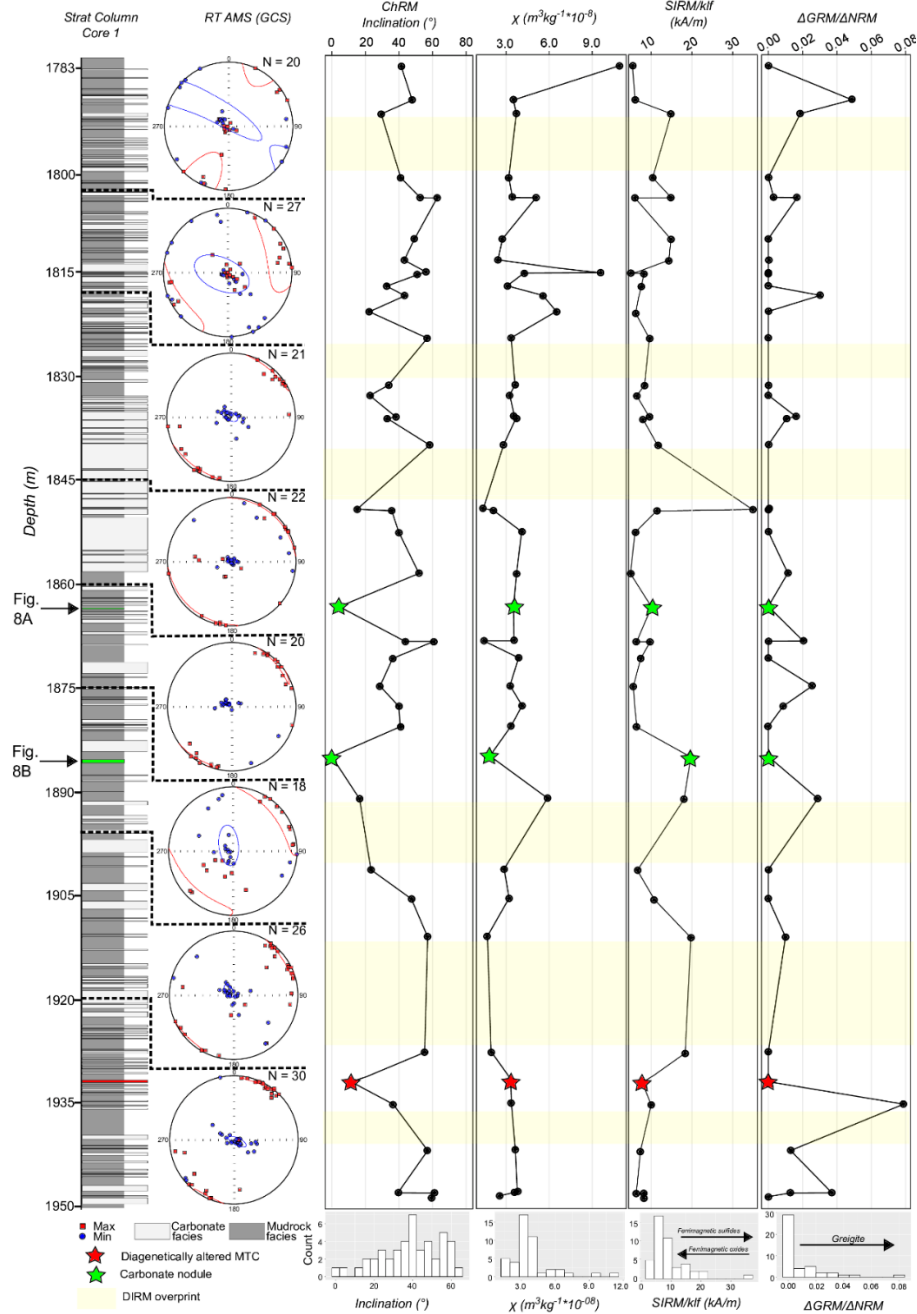


**Figure 5.** Core 1: (left to right) Simplified stratigraphic column with mudrock facies displayed in dark gray, MTCs in light gray, carbonate nodules in green and diagenetically altered MTC in red. Equal-area stereonet for AMS data displayed in a geographic coordinate system (GCS). Dashed lines delineate boundaries in core from which the AMS data was collected whereas the adjacent data tracks correspond to depth. Data tracks show, from left to right ChRM inclinations ( $^{\circ}$ ), mass-normalized magnetic susceptibility ( $\chi$ ), SIRM/ $k_{IF}$  values and  $\Delta GRM/\Delta NRM$  ratios. Shallow inclinations and their data are depicted by stars (green = carbonate concretions, red = diagenetically altered MTCs). Frequency distributions of each parameter is displayed directly below its corresponding track. Light yellow areas of the plot represent complete drilling overprint of the ChRM.

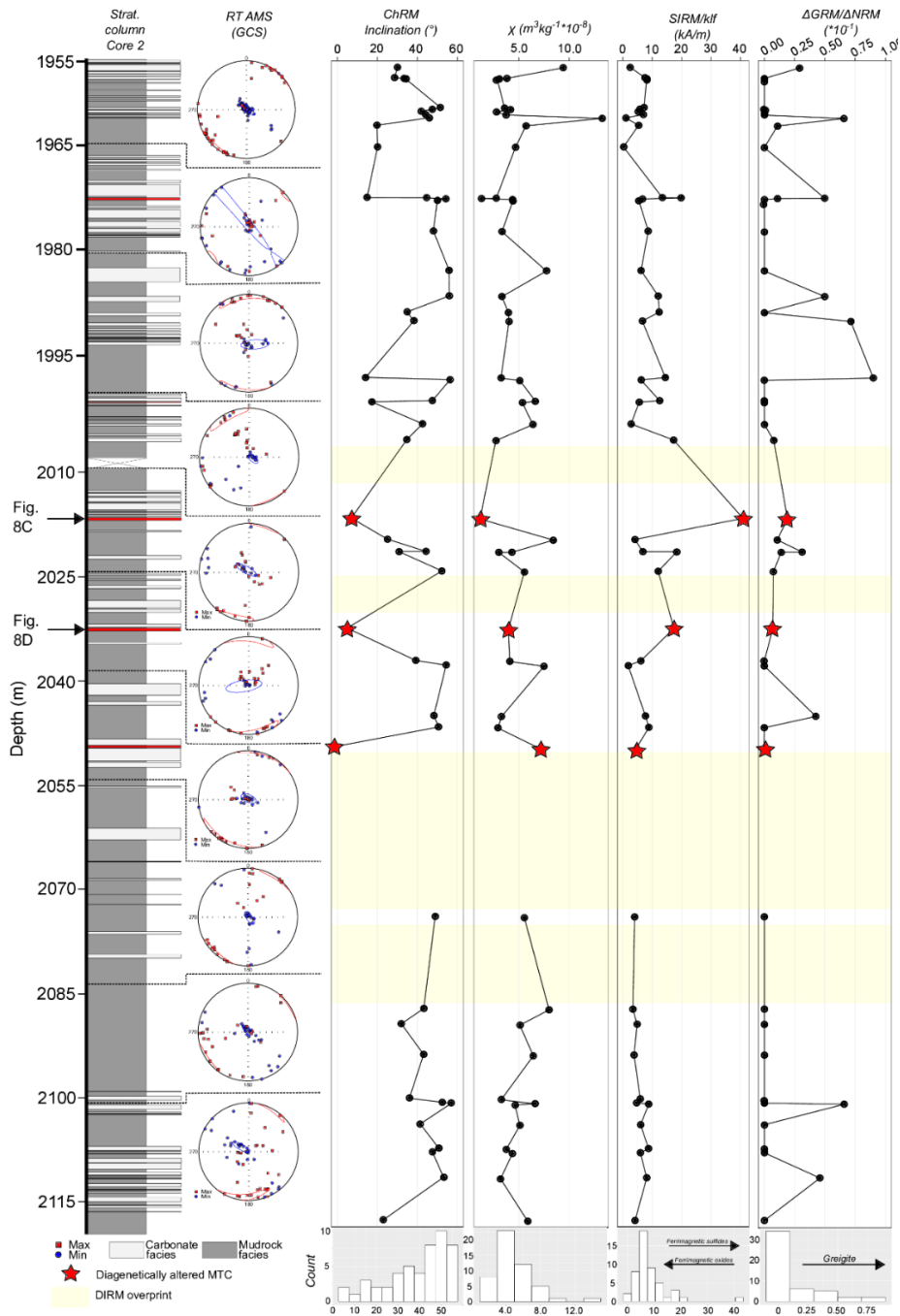


**Figure 6.** Core 2: (left to right) Simplified stratigraphic column with mudrock facies displayed in dark gray, MTCs in light gray and diagenetically altered MTCs in red. Equal-area stereonets for AMS data displayed in a geographic coordinate system (GCS). Dashed lines delineate boundaries of respective AMS data whereas the adjacent data tracks correspond to depth. Data tracks show, from left to right, ChRM inclinations ( $^{\circ}$ ), mass-normalized magnetic susceptibility ( $\chi$ ), SIRM/klf values and  $\Delta\text{GRM}/\Delta\text{NRM}$  ratios. Shallow inclinations and their data are depicted by stars. Frequency distributions of each parameter is displayed directly below its corresponding track. Light yellow areas of the plot represents total drilling overprint of the ChRM.

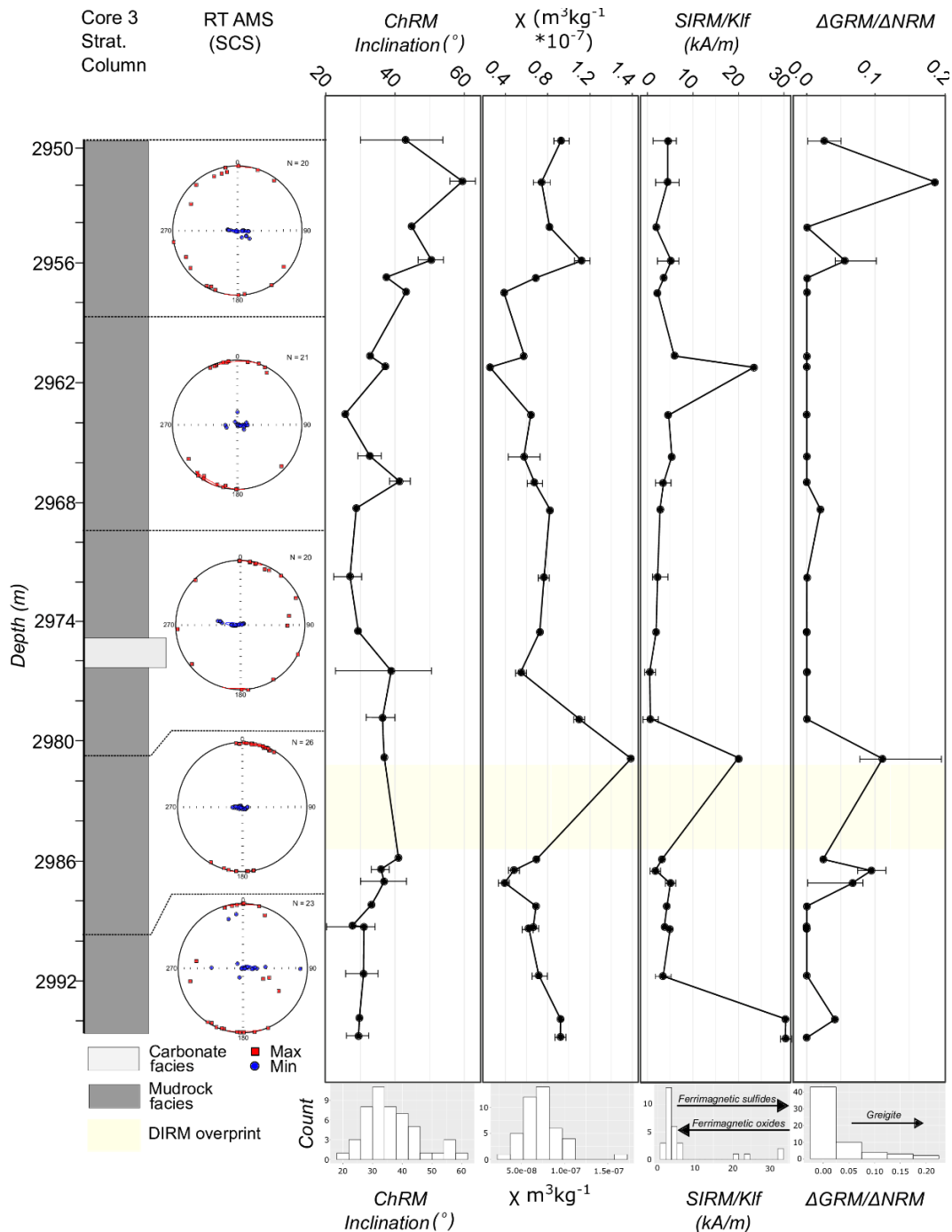


**Figure 7.** Core 3: (left to right) Stratigraphic column with mudrock facies displayed in dark gray a single MTC in light gray. Equal-area plots for AMS data displayed in a specimen coordinate system (SCS). Dashed lines delineate boundaries of AMS data whereas the adjacent data tracks correspond to depth. Data tracks show, from left to right, ChRM inclinations ( $^{\circ}$ ), mass-normalized magnetic susceptibility ( $\chi$ ), SIRM/klf values and  $\Delta\text{GRM}/\Delta\text{NRM}$  ratios. Frequency distributions of each parameter is displayed directly below its corresponding track. Light yellow area of the plot represent complete drilling overprint of the ChRM. Note gradual inclination shallowing from 2950m to 2964m.

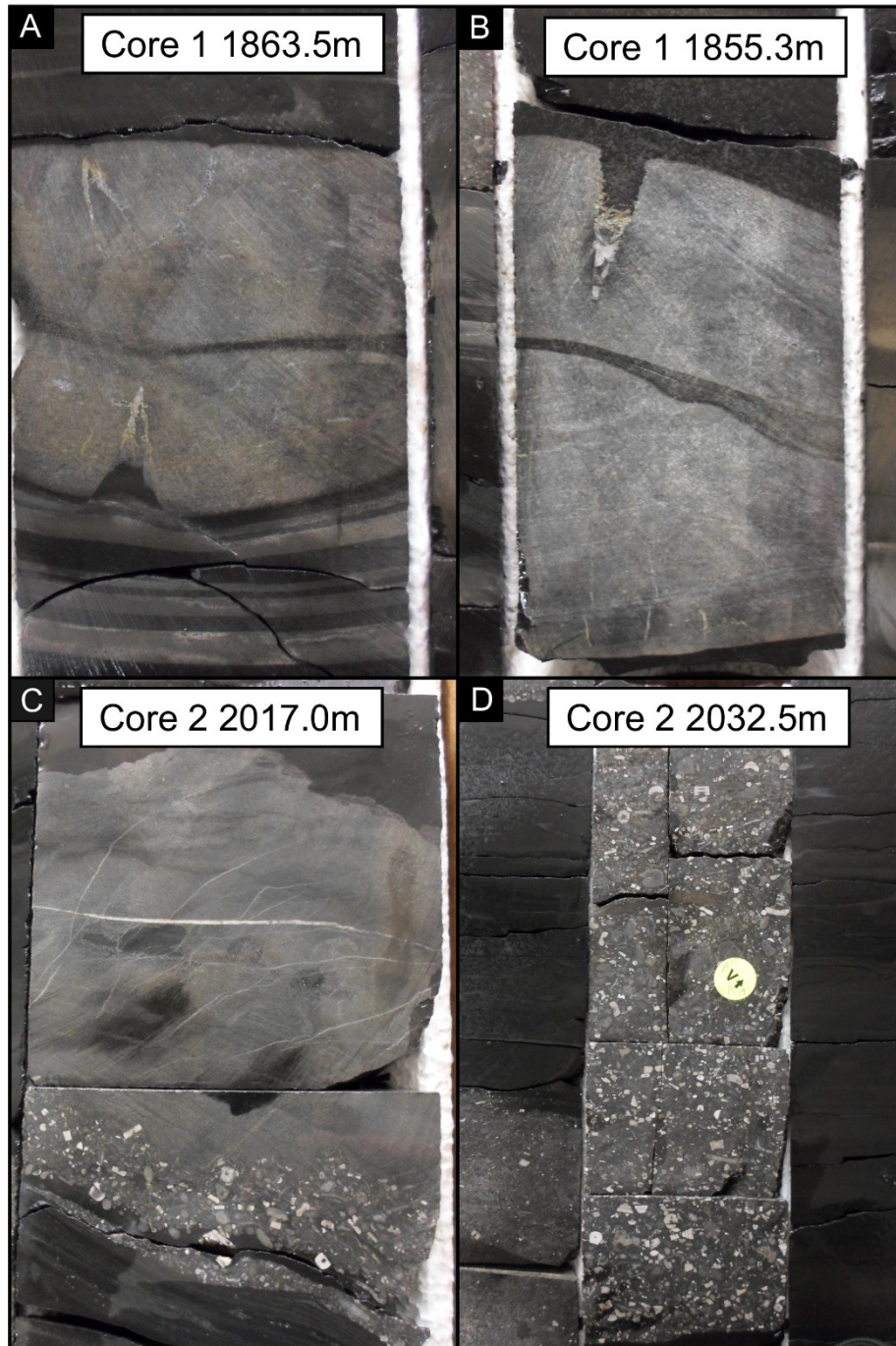


**Figure 8.** Core 1: (A-B) Concretions with septarian-like fissures that likely formed by shrinkage or dehydration owing to rapid burial. Note warped laminations underlying the concretion in (A). Fracture-fill is mainly comprised of barite and pyrite. Core 2 (C) Turbidite showing fining-up sequence with complex fracture arrays. Arrow indicates patchy chert replacement with pyrite “halo”. Horizontal fracture consistent with early overpressuring related to rapid burial. Sub-vertical tensile fractures appear to have formed later, perhaps during tectonic shortening? (D) Mud-supported debrite with abundant allochems and chert replaced clasts.

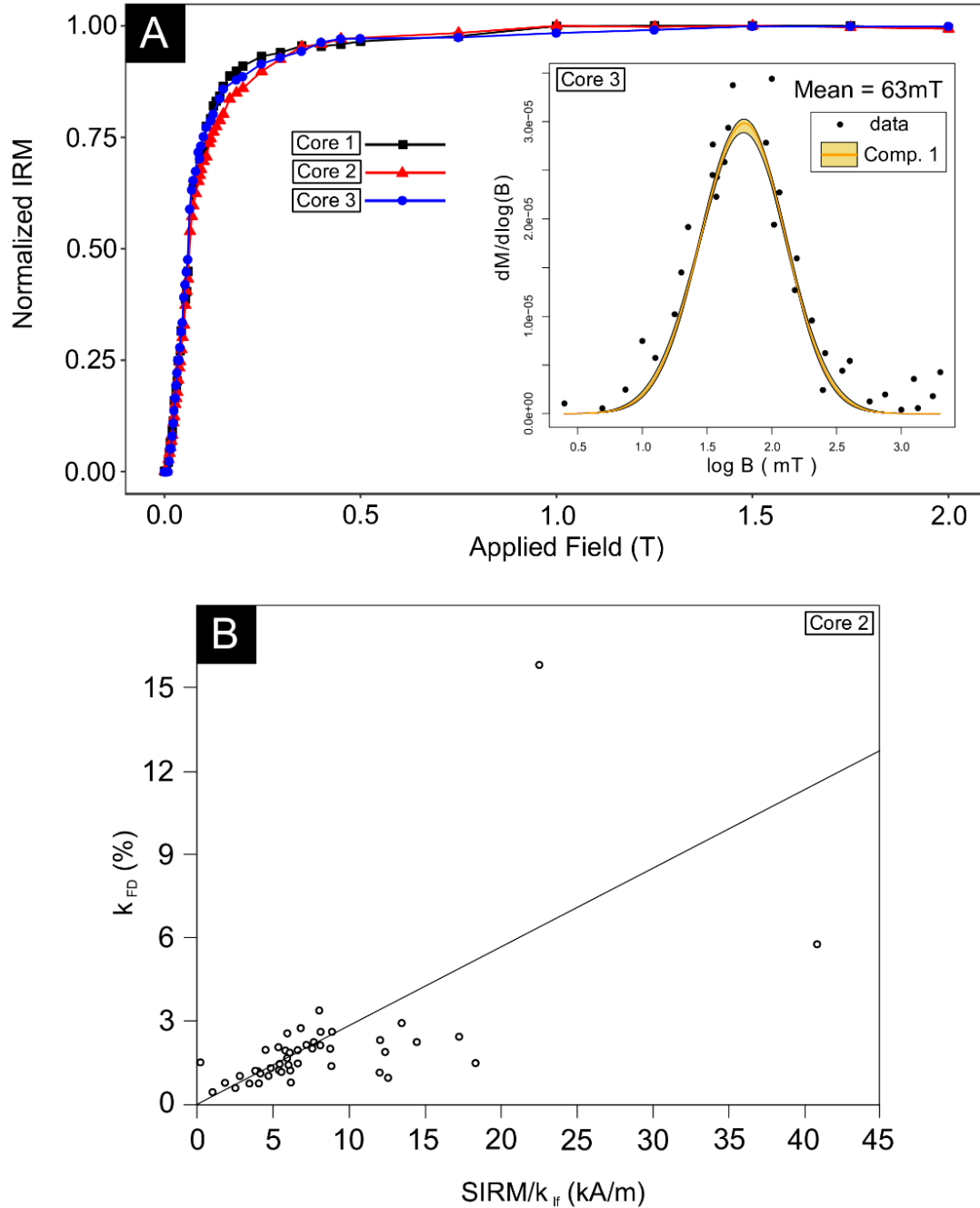


**Figure 9.** (A) Representative IRM acquisition curves from each core. Note single component, smooth concave down shape reaching saturation at 300-450mT. Inset shows a representative unmixed IRM acquisition curve and affirms that a single component best represents the coercivity spectrum. (B) Cross plot of  $k_{FD}$  vs.  $SIRM/k_{Hf}$  suggests that SP grains influence  $SIRM/k_{Hf}$  ratios in Core 2. Similar linear relationships are observed in Core 1 and 3.

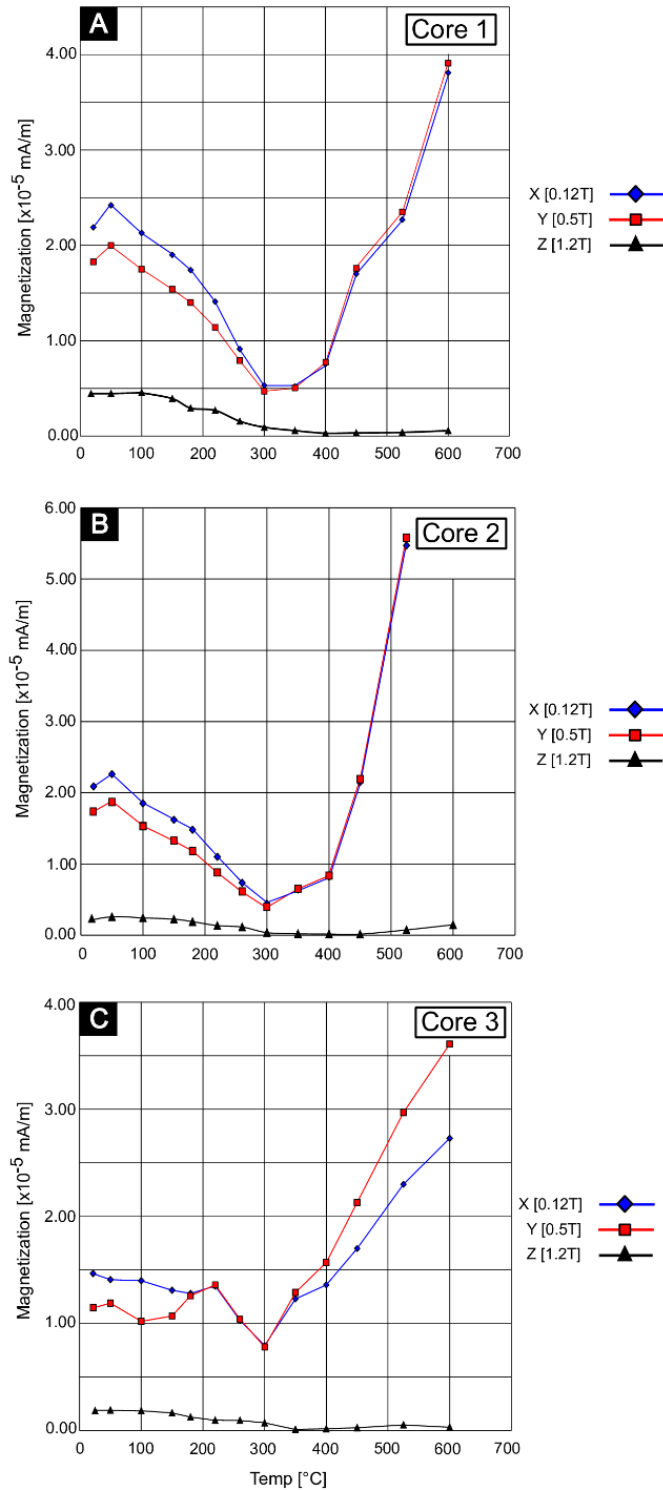


**Figure 10.** (A-C) Representative triaxial thermal demagnetization plots from each core. Note incomplete decay of X and Y axis likely owing to oxidation of iron-sulfides. Rapid decay of the X and Y-axis does occur between 200°C and 300°C in several samples and may be indicative of ferrimagnetic iron sulfides. Unblocking temperatures for the Z axis range from 350°C to 400°C.

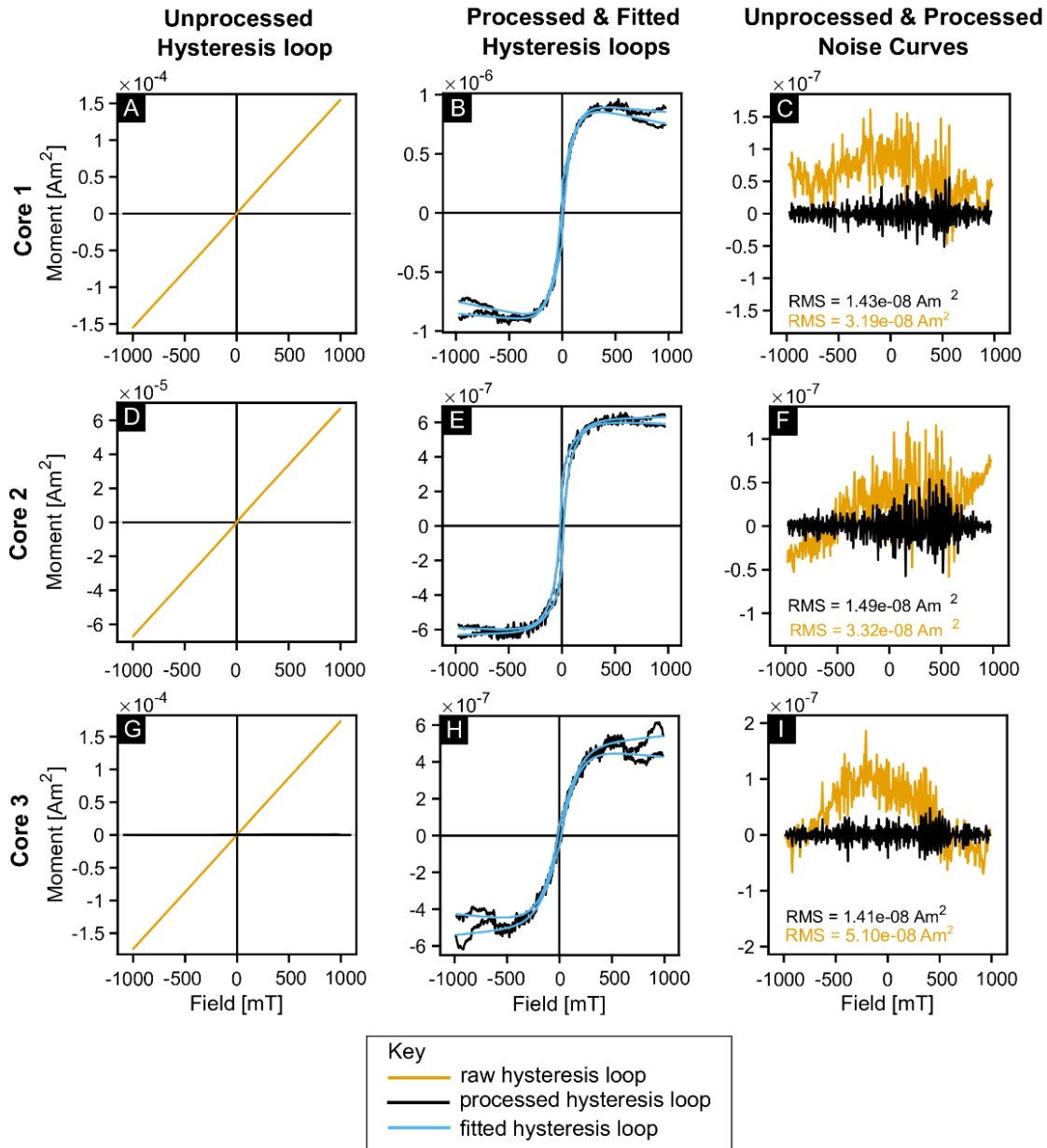


**Figure 11.** (A-I) Unprocessed, processed and fitted hysteresis loops with noise curves for both unprocessed and processed loops for one specimen from each core. Note strong paramagnetic component in all samples. Pole drift artifact present in all measurements. Overall, processed and fitted hysteresis loops display a single magnetic component (i.e. B, H) with the exception of Core 2 which shows a subtle wasp-waistedness (E) that may indicate SP/SD assemblages.

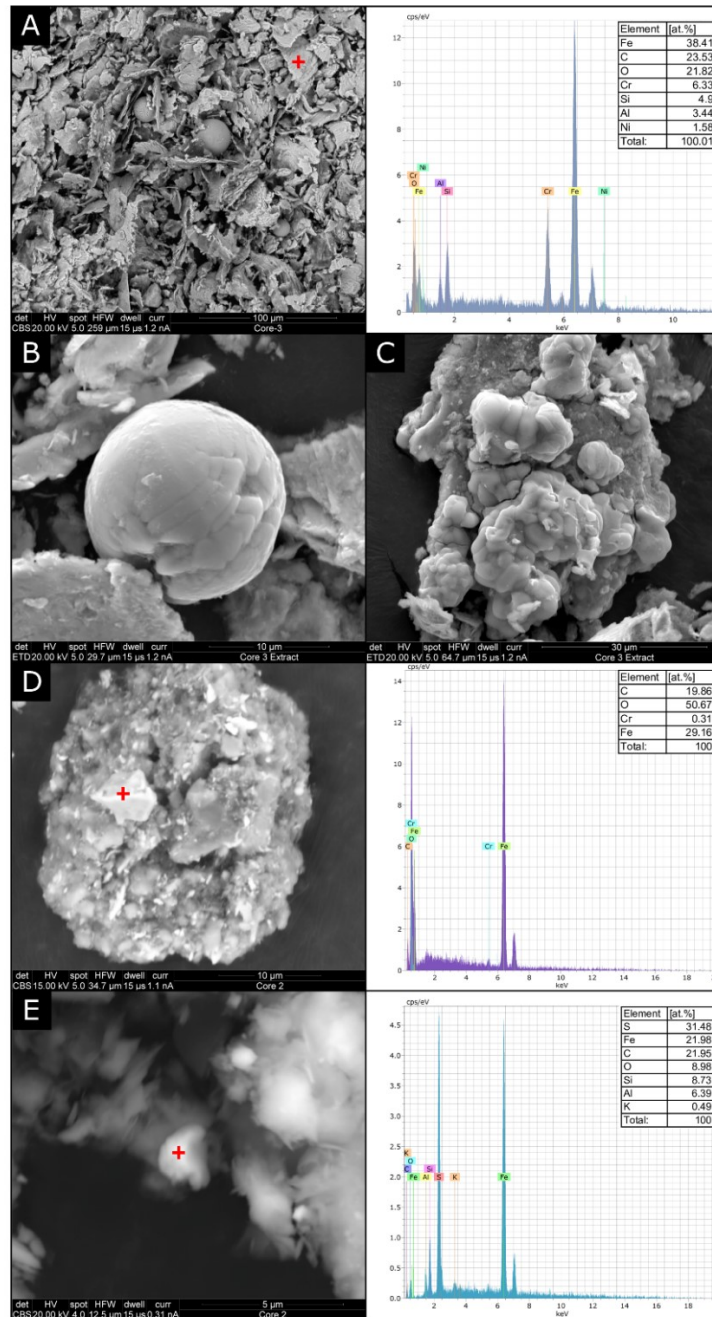


**Figure 12.** (A-D) Backscatter (CBS), secondary electron (ETD) and EDS spectra from magnetic extracts. (A) Predominately chlorite extract with some dispersed magnetite spherules showing both smoothed and textured surfaces. Black cross in top right represents EDS target. Its corresponding spectrum shows atomic percentages of Fe greater than that of chlorite alone, suggesting that magnetite resides within chlorite. (B) Example of textured, stoichiometric magnetite spherule, crystal shapes are consistent with pyrite framboids or spinel crystal habits. (C) Amorphous magnetite mass with some organic material. (D) Organic-rich extract with magnetite showing possible spinel crystal habit and fine grained chlorite/Fe-rich smectite. EDS scan shows trace amount of Cr in magnetite. (E) Rare ferrimagnetic sulfide that corresponds to either greigite or pyrrhotite.

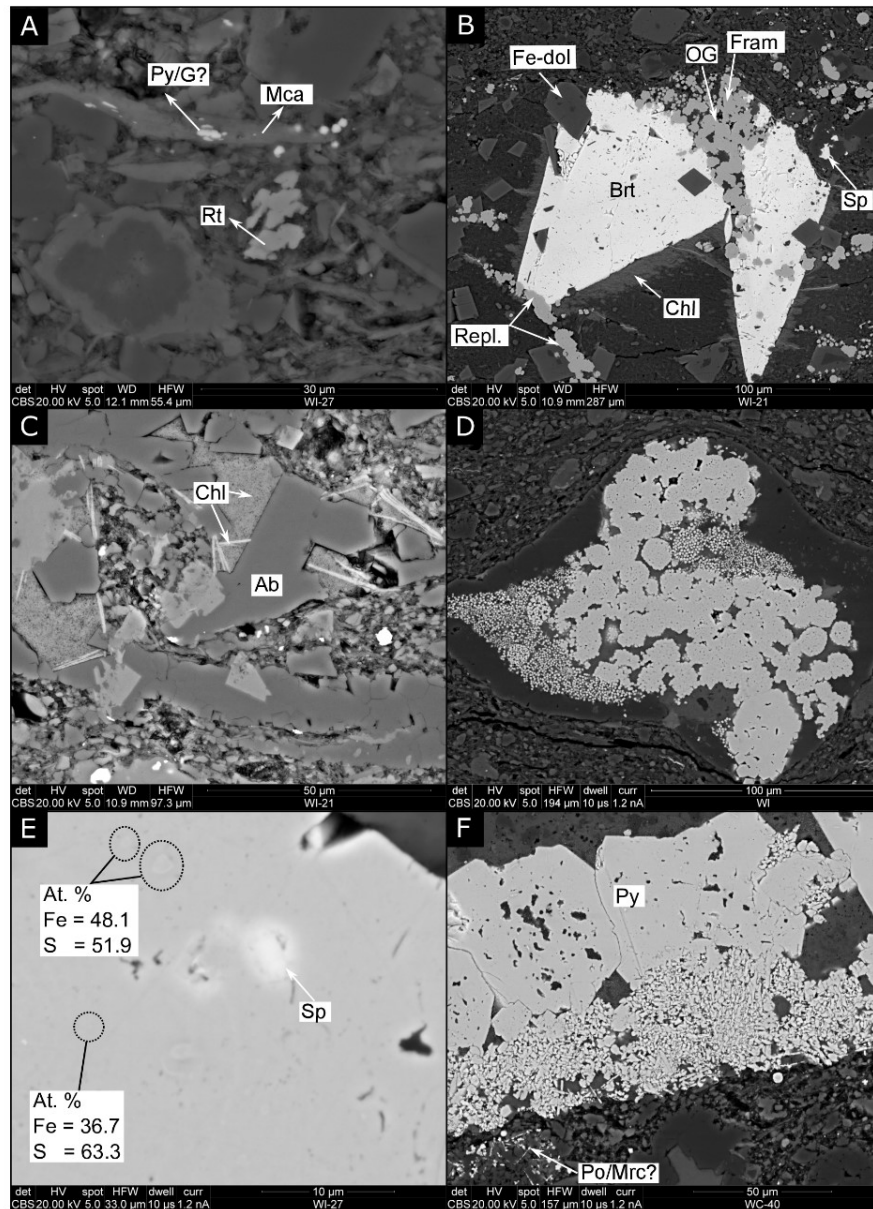


**Figure 13.** Backscatter images from siliceous mudrocks (A-E) and MTC (F). (A) Detrital rutile and mica with iron sulfide growth within sheets (pyrite (Py) or greigite (G)?). (B) Large barite (Brt) crystal with “fish-tail” habit rimmed with chlorite and replaced by pyrite overgrowths (OG) on framboids (Fram). Note replacement of ferroan dolomite (Fe-dol) by pyrite overgrowths. Isolated sphalerite cement. (C) Authigenic chlorite with increased concentration of iron (high electron density) and ultrafine-grained intergrown chlorite along with authigenic albite (Ab) with tabular habit. (D) Polyframboid within an allochem showing a variety of textures. (E) Cubic pyrite crystal hosting inclusions of sphalerite (barite is also commonly observed) and possible inclusions of ferrimagnetic sulfides. EDS scans on areas with higher electron densities (circled top left) show elemental concentrations other than pyrite (circled middle left). (F) Textural transition from cubic pyrite to bladed crystal habit may correspond to a compositional change to pyrrhotite (Po) and/or marcasite (Mrc).

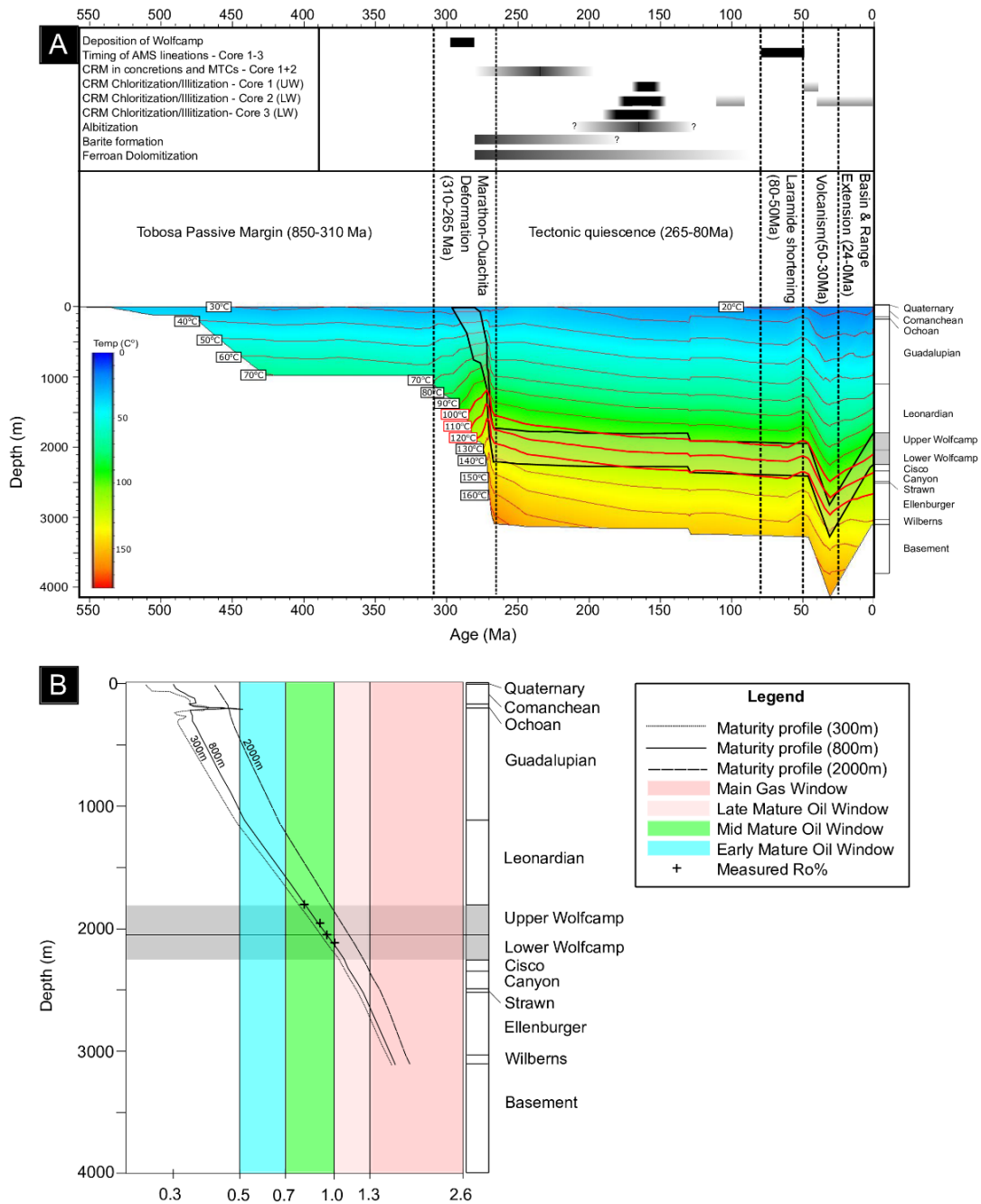


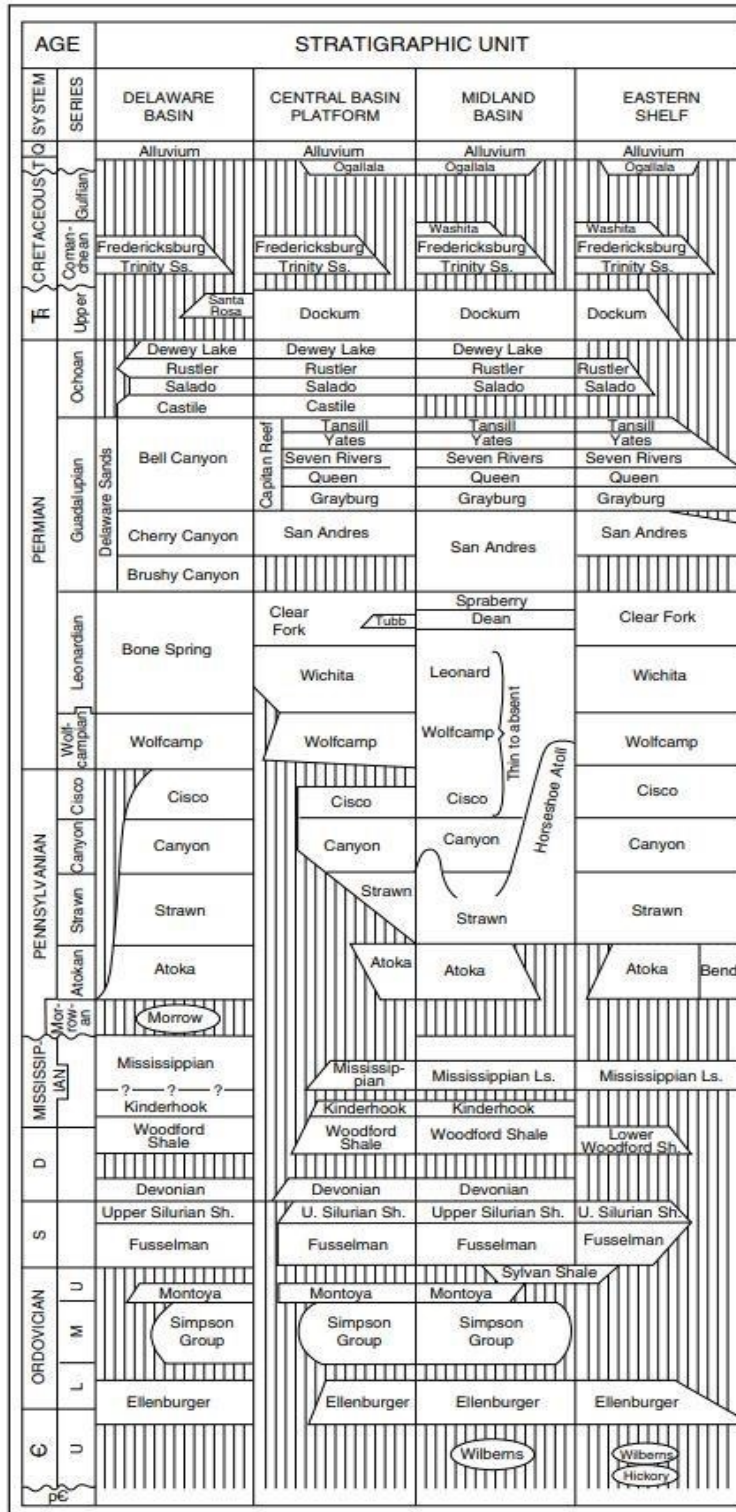
**Figure 14.** (A) 1D basin model with isotherms for Irion County. The approximate boundaries of major tectonic phases are denoted by dashed lines. The absolute and relative timing of burial events are depicted as a paragenetic sequence and are premised on AMS, paleomagnetic and textural relationships observed through SEM analysis. Solid bars in the sequence are considered to be well constrained events, faded bars of the CRMs correspond to the  $\alpha 95$  range of paleomagnetic ages and faded bars with question marks represent that the start or end of an event is poorly constrained. (B) Thermal profile predicted by the model for three iterations of Cenozoic uplift (2000m, 800m, 300m) plotted along with Ro data. Note the best fit solution obtained using 800m of Cenozoic uplift and erosion.

### Chapter 3 Tables

Core #	B <sub>c</sub> [mT]	B <sub>cr</sub> [mT]	M <sub>s</sub> [Am <sup>2</sup> x 10 <sup>-7</sup> ]	M <sub>r</sub> [Am <sup>2</sup> x 10 <sup>-7</sup> ]	M <sub>r</sub> /M <sub>s</sub>	B <sub>cr</sub> /B <sub>c</sub>	SIRM/k <sub>lf</sub>	S-ratio
1 processed	10.3	43	8.05	1.23	0.15	4.17	5.5	0.96
1 fitted loop	12.0		9.82	1.37	0.14	3.58	-	-
2 processed	16.3	28	6.31	2.00	0.32	1.72	17.3	0.92
2 fitted loop	15.4		5.79	1.89	0.33	1.82	-	-
3 processed	20	31	4.82	0.43	0.09	1.55	13.1	0.98
3 fitted loop	16.9		5.14	0.55	0.11	1.83	-	-

**Table 1.** Hysteresis data from processed and fitted loops. Corresponding SIRM/k<sub>lf</sub> ratios and S-ratios also shown.

# APPENDIX



Chronostratigraphy used for Basin Model from (Ball, 1995)

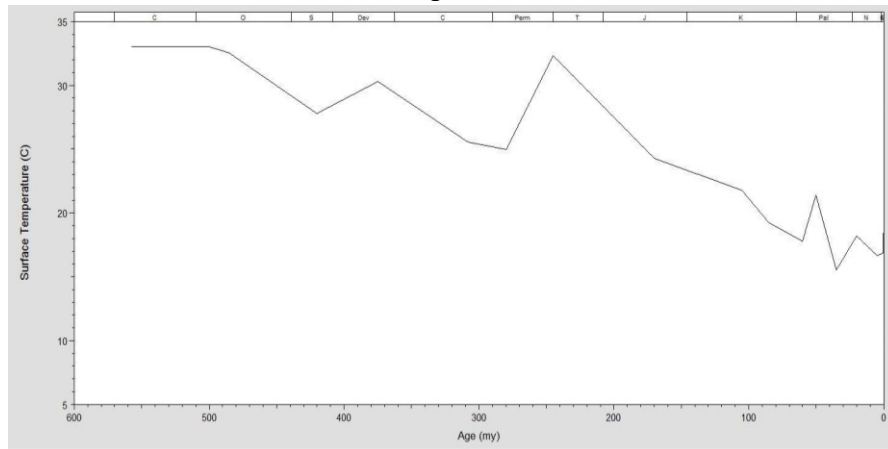
## Lithological Mixes used for Basin Model

Lithology Name	Lithology Color	Lithology Pattern	% Sandstone	% Siltstone	% Shale	% Limestone	% Dolomite	% Evaporite	% Kerogen	% Igneous	% User Lith1	% User Lith2	% User Lith3	Total %
Sandstone	Yellow	Sandstone	100	0	0	0	0	0	0	0	0	0	0	100
Siltstone	Green	Siltstone	0	100	0	0	0	0	0	0	0	0	0	100
Shale	Green	Shale	0	0	100	0	0	0	0	0	0	0	0	100
Limestone	Blue	Limestone	0	0	0	100	0	0	0	0	0	0	0	100
Dolomite	Blue	Dolomite	0	0	0	0	100	0	0	0	0	0	0	100
Evaporite	Magenta	Evaporite	0	0	0	0	0	100	0	0	0	0	0	100
Coal	Black	Coal	0	0	0	0	0	0	100	0	0	0	0	100
Igneous	Red	Igneous	0	0	0	0	0	0	0	100	0	0	0	100
Wilberns	Yellow	Solid Background	55	0	0	45	0	0	0	0	0	0	0	100
Quaternary	Light Gray	Solid Background	100	0	0	0	0	0	0	0	0	0	0	100
Washita	Light Blue	Solid Background	0	0	40	60	0	0	0	0	0	0	0	100
Fredericksburg	Light Blue	Solid Background	0	0	50	50	0	0	0	0	0	0	0	100
Trinity	Yellow	Solid Background	80	0	20	0	0	0	0	0	0	0	0	100
Dockum	Brown	Solid Background	40	20	40	0	0	0	0	0	0	0	0	100
Yates	Light Aqua	Solid Background	13	0	22.4	14.2	0	50.4	0	0	0	0	0	100
Queen	Light Aqua	Solid Background	41.5	0	10.9	0	4.9	42.7	0	0	0	0	0	100
Grayburg	Dark Gray	Solid Background	9.4	0	36.8	0	34.4	19.4	0	0	0	0	0	100
San Andres	Yellow	Solid Background	53.5	0	3.5	28	15	0	0	0	0	0	0	100
Upper Sprayberry	Dark Gray	Solid Background	11.8	0	76	4.9	7.3	0	0	0	0	0	0	100
Lower Sprayberry	Dark Gray	Solid Background	5.6	8.8	78.7	6.9	0	0	0	0	0	0	0	100
Dean	Light Gray	Solid Background	19.8	20	60.2	0	0	0	0	0	0	0	0	100
Upper Wolfcamp	Green	Solid Background	0	11.1	75.2	13.7	0	0	0	0	0	0	0	100
Lower Wolfcamp	Green	Solid Background	0	0	75.3	24.7	0	0	0	0	0	0	0	100
Cisco	Yellow	Solid Background	50	0	26.2	23.8	0	0	0	0	0	0	0	100
Canyon	Green	Solid Background	17.5	3.2	77.6	1.7	0	0	0	0	0	0	0	100
Strawn	Light Blue	Solid Background	0	0	50	50	0	0	0	0	0	0	0	100
Ellenburger	Blue	Solid Background	0	0	1.5	11.9	85.1	0	0	0	1.5	0	0	100
Basement	Red	Solid Background	0	0	0	0	0	0	0	100	0	0	0	100

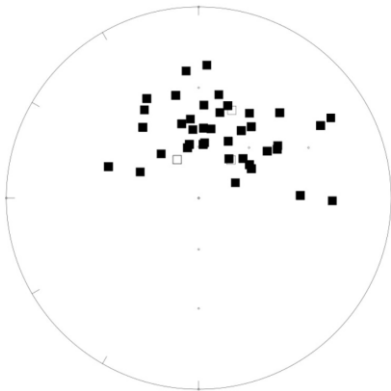
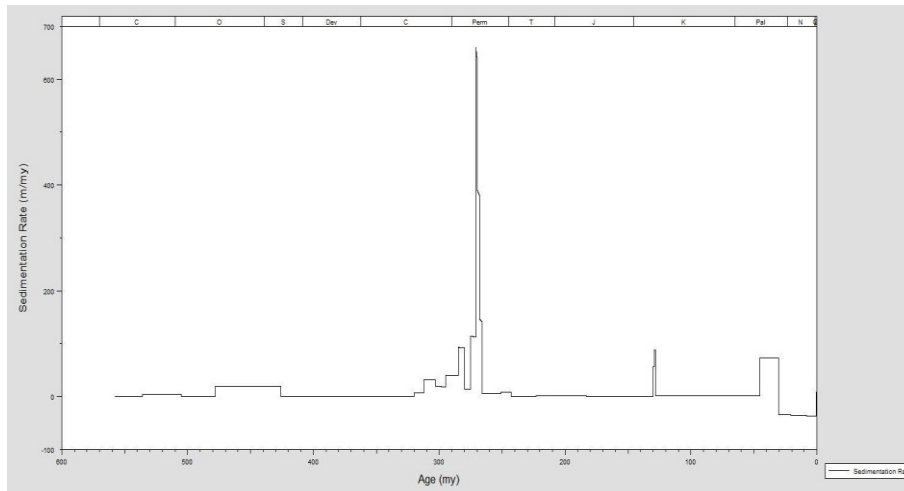
## Borehole temperatures used for Basin Model

Depth (m)	Temp (C)
70.1	30.65
170	31.77
270	32.89
370	34.56
470	36.24
570	37.92
670	39.6
770	41.27
870	43.23
970	45.47
1070	47.71
1170	49.66
1270	51.90
1370	53.30
1470	55.54
1570	57.21
1670	59.73
1770	62.25
1870	65.32
1970	68.68
2070	72.87
2170	75.95
2270	78.74

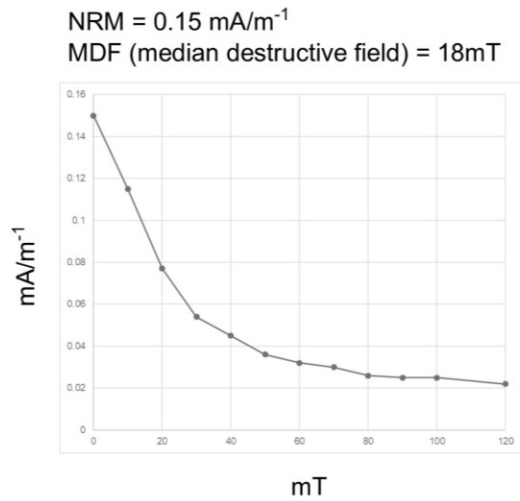
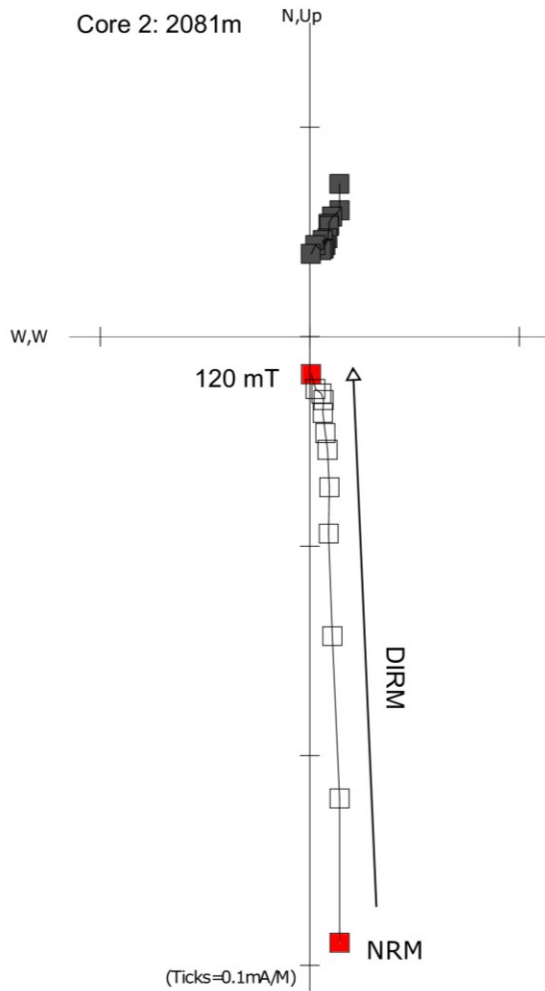
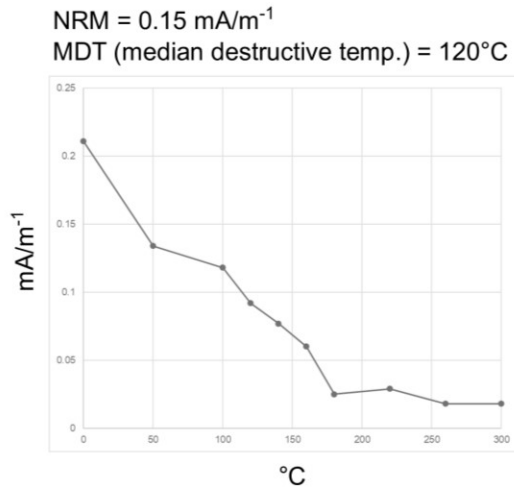
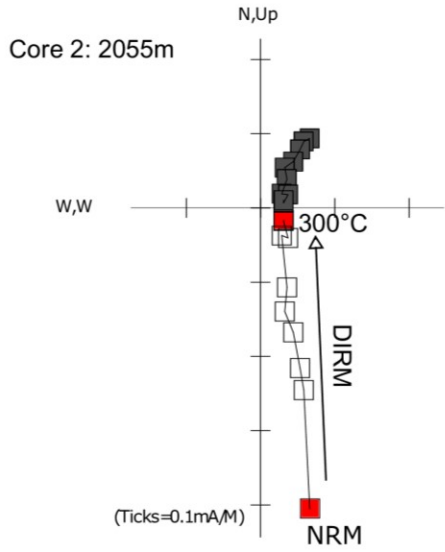
Calculated surface temperatures used for Basin Model



Sedimentation Rates – Basin Model



Unoriented paleomagnetic data for Core



Examples of DIRMs observed in Core 2

## REFERENCES

- Almqvist, B.S. and Koyi, H., 2018, Bulk strain in orogenic wedges based on insights from magnetic fabrics in sandbox models. *Geology*, 46(6), pp.483-486.
- Aubourg, C., Rochette, P., and Vialon, P., 1991, Subtle stretching lineation revealed by magnetic fabric of Callovian-Oxfordian black shales (French Alps). *Tectonophysics*, 185(3-4), 211-223.
- Audunsson, H. and Levi, S., 1989, Drilling-induced remanent magnetization in basalt drill cores. *Geophysical Journal International*, 98(3), pp.613-622.
- Arason, P. and Levi, S., 2010, Maximum likelihood solution for inclination-only data in paleomagnetism. *Geophysical Journal International*, 182(2), pp.753-771.
- Baldwin, B. and Butler, C.O., 1985, Compaction curves. *AAPG bulletin*, 69(4), pp.622-626.
- Ball, M., 1995, Permian Basin Province (044). In National assessment of United States oil and gas resources--Results, methodology, and supporting data: US Geological Survey Digital Data Series DDS-30, Release 2, [CD-ROM].
- Banerjee, S., Elmore, R.D. and Engel, M.H., 1997, Chemical remagnetization and burial diagenesis: testing the hypothesis in the Pennsylvanian Belden Formation, Colorado. *Journal of Geophysical Research: Solid Earth*, 102(B11), pp.24825-24842.
- Barnes, V.E., Bell, W.C., 1977, The Moore Hollow Group of central Texas. *Texas Bur. Econ. Geol., Rep. Invest.* 88, 169.
- Beaufort, D., Rigault, C., Billon, S., Billault, V., Inoue, A., Inoue, S., and Patrier, P. 2015, Chlorite and chloritization processes through mixed-layer mineral series in low-temperature geological systems—a review. *Clay Minerals*, 50(4), 497-523.
- Berger, G., Lacharpagne, J.C., Velde, B., Beaufort, D. and Lanson, B., 1997, Kinetic constraints on illitization reactions and the effects of organic diagenesis in sandstone/shale sequences. *Applied Geochemistry*, 12(1), pp.23-35.
- Blackwell, David, M. Richards, Z. Frone, J. Batir, A. Ruzo, R. Dingwall, and M. Williams 2011, Temperature at depth maps for the conterminous US and geothermal resource estimates, *GRC Transactions*, 35 (GRC1029452).
- Blakey, R.C., 2008, Gondwana paleogeography from assembly to breakup—A 500 my odyssey. Resolving the late paleozoic ice age in time and space: geological society of America Special Paper, 441, pp.1-28.
- Blumstein, A.M., Elmore, R.D., Engel, M.H., Elliot, C. and Basu, A., 2004, Paleomagnetic dating of burial diagenesis in Mississippian carbonates, Utah. *Journal of Geophysical Research: Solid Earth*, 109, B04101, [http://dx. doi.org/10.1029/2003JB002698](http://dx.doi.org/10.1029/2003JB002698)

- Borradaile, G. J., 1988, Magnetic susceptibility, petrofabrics and strain. *Tectonophysics*, 156(1-2), 1-20.
- Brown, L.F., Solís-Iriarte, R.F. and Johns, D.A., 1990, Regional depositional systems tracts, paleogeography, and sequence stratigraphy, upper Pennsylvanian and lower Permian strata, North-and-West-Central Texas: Texas Bureau of Economic Geology, Reports of Investigations 197, 116 p.
- Butler, R.F., 1998, Paleomagnetism: Magnetic domains to geologic terranes. Electronic edition, 23.
- Corrigan, J., Cervany, P. F., Donelick, R., and Bergman, S. C., 1998, Postorogenic denudation along the late Paleozoic Ouachita trend, south central United States of America: magnitude and timing constraints from apatite fission track data. *Tectonics*, 17(4), 587-603.
- Chadima, M., and Jelinék, V., 2009, Anisoft 4.2: anisotropy data browser for windows. Agico. Inc, Brno. <https://www.agico.com/text/software/anisoft/anisoft.php>
- Chadima, M., Pruner, P., Šlechta, S., Grygar, T., and Hirt, A. M., 2006, Magnetic fabric variations in Mesozoic black shales, Northern Siberia, Russia: Possible paleomagnetic implications. *Tectonophysics*, 418(1-2), 145-162.
- Craig, L.C., Connor, C.W., Armstrong, A.K., Varnes, K.L., Mast, C.A. and Kiteley, L.W., 1979, Paleotectonic investigations of the Mississippian System in the United States(No. 1010). Dept. of the Interior, Geological Survey.
- Day, R., Fuller, M. and Schmidt, V.A., 1977, Hysteresis properties of titanomagnetites: grain-size and compositional dependence. *Physics of the Earth and planetary interiors*, 13(4), pp.260-267.
- Dearing, J.A., Dann, R.J.L., Hay, K., Lees, J.A., Loveland, P.J., Maher, B.A. and O'grady, K., 1996, Frequency-dependent susceptibility measurements of environmental materials. *Geophysical Journal International*, 124(1), pp.228-240.
- Dennie, D., Elmore, R.D., Deng, J., Manning, E. and Pannalal, J., 2012, Palaeomagnetism of the Mississippian Barnett Shale, Fort Worth Basin, Texas. Geological Society, London, Special Publications, 371, pp.SP371-10.
- DeConto, R.M., 2009, Plate tectonics and climate change. In *Encyclopedia of paleoclimatology and ancient environments* (pp. 784-798). Springer, Dordrecht.
- Dunlop, D.J., 2002, Theory and application of the Day plot (Mrs/Ms versus Hcr/Hc) 1. Theoretical curves and tests using titanomagnetite data. *Journal of Geophysical Research: Solid Earth*, 107(B3), pp.EPM-4.
- Elmore, R.D., Engel, M.H., Crawford, L., Nick, K., Imbus, S. and Sofer, Z., 1987, Evidence for a relationship between hydrocarbons and authigenic magnetite. *Nature*, 325(6103), p.428.

- Elmore, R.D., London, D., Bagley, D., Fruit, D. and Gao, G., 1993, Remagnetization by basinal fluids: testing the hypothesis in the Viola Limestone, southern Oklahoma. *Journal of Geophysical Research: Solid Earth*, 98(B4), pp.6237-6254.
- Elmore, R.D., Muxworthy, A.R. and Aldana, M., 2012, Remagnetization and chemical alteration of sedimentary rocks. Geological Society, London, Special Publications, 371, pp.SP371-15.
- Falvey, D.A. and Middleton, M.F., 1981, Passive continental margins: evidence for a prebreakup deep crustal metamorphic subsidence mechanism. In: Blanchet R, Montadert L (eds) *Geology of continental margins*. *Oceanol Acta Proc 26th Int Geol Congr. C 3*: 103-114.
- Ferré, E.C., 2002, Theoretical models of intermediate and inverse AMS fabrics. *Geophysical Research Letters*, 29(7), pp.31-1.
- Flawn, P. T., Goldstein, A. J., King, P. B., and Weaver, C. E., 1961, The Ouachita System. University of Texas, Bureau of Economic Geology, Report 6120, 401 p., 6 sheets.
- Fisher, R.A., 1953, Dispersion on a sphere, *Proc. R. Soc. A*, 217, 295–305
- Frakes, L.A., Francis, J.E. and Syktus, J.I., 2005, *Climate modes of the Phanerozoic*. Cambridge University Press.
- Frenzel, H. N., Bloomer, R. R., Cline, R. B., Cys, J. M., Galley, J. E., Gibson, W. R., ... and Thompson III, S., 1988, The Permian basin region. Sedimentary cover—North American craton: US: Boulder, Colorado, Geological Society of America, *The Geology of North America*, 2, 261-306.
- Fu, Y., Von Dobeneck, T., Franke, C., Heslop, D. and Kasten, S., 2008, Rock magnetic identification and geochemical process models of greigite formation in Quaternary marine sediments from the Gulf of Mexico (IODP Hole U1319A). *Earth and Planetary Science Letters*, 275(3), pp.233-245.
- Galley, J.E., 1958, Oil and geology in the Permian basin of Texas and New Mexico, in L. G. Weeks, ed., *Habitat of oil: AAPG Special Publication*, p. 395–446.
- Gaswirth, S.B., Marra, K.R., Lillis, P.G., Mercier, T.J., Leathers-Miller, H.M., Schenk, C.J., Klett, T.R., Le, P.A., Tennyson, M.E., Hawkins, S.J., Brownfield, M.E., Pitman, J.K., and Finn, T.M., 2016, Assessment of undiscovered continuous oil resources in the Wolfcamp shale of the Midland Basin, Permian Basin Province, Texas, 2016: U.S. Geological Survey Fact Sheet 2016–3092, 4 p., <https://doi.org/10.3133/fs20163092>
- Gill, J.D., Elmore, R.D. and Engel, M.H., 2002, Chemical remagnetization and clay diagenesis: testing the hypothesis in the Cretaceous sedimentary rocks of northwestern Montana. *Physics and Chemistry of the Earth, Parts A/B/C*, 27(25-31), pp.1131-1139.
- Hamlin, H.S., Baumgardner, R.W., 2012, Wolfberry (Wolfcampian-Leonardian) Deep-water Depositional Systems in the Midland Basin: Stratigraphy, Lithofacies, Reservoirs, and

Source Rocks (No. Report of Investigations 277). Texas Bureau of Economic Geology.

- Halgedahl, S., Suk, D., 1992, On the carriers of remanence in Paleozoic platform carbonates of North America, 11.: Demagnetization characteristics of magnetite spherules vs. whole-rock specimens from the Onondaga Formation. *Eos Trans. AGU*, 73, p.154.
- Haq, B. U., and Schutter, S. R., 2008, A chronology of Paleozoic sea-level changes. *Science*, 322(5898), 64-68.
- Heij, G. W. and Elmore, R.D., in press, The Magnetic Fabric of the Wolfcamp Shale, Midland Basin: Understanding Petrofabric variability, Hydrocarbon distribution and Iron enrichment. *AAPG Bulletin*
- Hillier, S., 1993, Origin, diagenesis, and mineralogy of chlorite minerals in Devonian lacustrine mudrocks, Orcadian Basin, Scotland. *Clays and Clay Minerals*, 41, 240-240.
- Hirt, A., A. Banin and A. Gehring, 1993, Thermal generation of ferromagnetic minerals from iron-enriched smectites. *Geophys. J. Int.*, 115: 1161–1168.
- Horak, R.L., 1985, Tectonic and hydrocarbon maturation history in the Permian Basin: *Oil and Gas Journal*, v. 83, p. 124-129.
- Ihmlé, P.F., Hirt, A.M., Lowrie, W. and Dietrich, D., 1989, Inverse magnetic fabric in deformed limestones of the Morcles Nappe, Switzerland. *Geophysical Research Letters*, 16(12), pp.1383-1386.
- Jackson, M. and Solheid, P., 2010, On the quantitative analysis and evaluation of magnetic hysteresis data. *Geochem. Geophys. Geosyst.*, 11, Q04Z15, doi:10.1029/2009GC002932.
- Jackson, M. and Swanson-Hysell, N.L., 2012, Remagnetization and chemical alteration of sedimentary rocks: *Geological Society of London Special Publication 371*, 229 – 2551.
- Jelinek, V., 1981, Characterization of the magnetic fabric of rocks. *Tectonophysics*, 79(3-4), pp.T63-T67.
- Kargi, H. and Barnes, C.G., 1995, A Grenville-age layered intrusion in the subsurface of west Texas: Petrology, petrography, and possible tectonic setting. *Canadian Journal of Earth Sciences*, 32(12), pp.2159-2166.
- Katz, B., Elmore, R.D., Cogoini, M., Engel, M.H. and Ferry, S., 2000, Associations between burial diagenesis of smectite, chemical remagnetization, and magnetite authigenesis in the Vocontian trough, SE France. *Journal of Geophysical Research: Solid Earth*, 105(B1), pp.851-868.
- Katz, B., Elmore, R. D., Cogoini, M., Engel, M. H., and Ferry, S., 2000, Associations between burial diagenesis of smectite, chemical remagnetization, and magnetite authigenesis in the Vocontian trough, SE France. *Journal of Geophysical Research: Solid Earth*, 105(B1), 851-868.

- Keller, G.R., Hills, J.M., Baker, M.R. and Wallin, E.T., 1989, Geophysical and geochronological constraints on the extent and age of mafic intrusions in the basement of west Texas and eastern New Mexico. *Geology*, 17(11), pp.1049-1052.
- Lu, G., Marshak, S. and Kent, D.V., 1990, Characteristics of magnetic carriers responsible for Late Paleozoic remagnetization in carbonate strata of the mid-continent, USA. *Earth and Planetary Science Letters*, 99(4), pp.351-361.
- Kirkland, D.W. and Anderson, R.Y., 1970, Microfolding in the Castile and Todilto evaporites, Texas and New Mexico. *Geological Society of America Bulletin*, 81(11), pp.3259-3282.
- Kirschvink, J.L., 1980, The least-squares line and plane and the analysis of palaeomagnetic data. *Geophysical Journal International*, 62(3), pp.699-718.
- Liu, Q., Roberts, A.P., Torrent, J., Horng, C.S. and Larrasoana, J.C., 2007, What do the HIRM and S-ratio really measure in environmental magnetism?. *Geochemistry, Geophysics, Geosystems*, 8(9).
- Lynch, F.L., 1997, Frio shale mineralogy and the stoichiometry of the smectite-to-illite reaction: the most important reaction in clastic sedimentary diagenesis. *Clays and Clay Minerals*, 45(5), pp.618-631.
- Machel, H. G., Krouse, H. R., and Sassen, R., 1995, Products and distinguishing criteria of bacterial and thermochemical sulfate reduction. *Applied geochemistry*, 10(4), 373-389.
- Machel, H.G., 2001, Bacterial and thermochemical sulfate reduction in diagenetic settings—old and new insights. *Sedimentary Geology*, 140(1-2), pp.143-175.
- Magoon, L.B. and Dow, W.G., 1994, The petroleum system: chapter 1: Part I. Introduction. *AAPG Memoir* 60, p. 3-24.
- Maher, B.A., 2007, Environmental magnetism and climate change. *Contemporary Physics*, 48(5), pp.247-274.
- Manning, E.B. and Elmore, R.D., 2015, An integrated paleomagnetic, rock magnetic, and geochemical study of the Marcellus shale in the Valley and Ridge province in Pennsylvania and West Virginia. *Journal of Geophysical Research: Solid Earth*, 120(2), pp.705-724.
- Maxbauer, D.P., Feinberg, J.M. and Fox, D.L., 2016, MAX UnMix: A web application for unmixing magnetic coercivity distributions. *Computers and Geosciences*, 95, pp.140-145.
- Mazzullo, S. J., and Reid, A. M., 1989, Lower Permian platform and basin depositional systems, northern Midland Basin, Texas. In: P.D. Crevello, J.L. Wilson, J.F. Sarg and J.F. Read (Editors), *Controls on Carbonate Platform and Basin Development*. Soc. Econ. Paleontol. Mineral., Spec. Publ., 44: 305—320.
- MacLeod, C.J., Parson, L.M. and Sager, W.W., 1994, Reorientation of cores using the Formation MicroScanner and Borehole Televiewer: application to structural and paleomagnetic

- studies with the Ocean Drilling Program. In Proceedings of the Ocean Drilling Program. Scientific Results (Vol. 135, pp. 301-312). Ocean Drilling Program. McCabe, C., Sassen, R. and Saffer, B., 1987. Occurrence of secondary magnetite within biodegraded oil. *Geology*, 15(1), pp.7-10.
- McCabe, C. and Elmore, R.D., 1989, The occurrence and origin of late Paleozoic remagnetization in the sedimentary rocks of North America. *Reviews of Geophysics*, 27(4), pp.471-494.
- McGowen, J.H., Granata, G.E. and Seni, S.J., 1977, Depositional Framework of the Lower Dockum Group (Triassic), Texas Panhandle. *Gulf Coast Association of Geological Societies Transactions* Vol. 27, pp. 246-246
- Metwalli, F.I. and Pigott, J.D., 2005, Analysis of petroleum system criticals of the Matruh–Shushan Basin, Western Desert, Egypt. *Petroleum Geoscience*, 11(2), pp.157-178.
- Moreau, M.G., Ader, M. and Enkin, R.J., 2005, The magnetization of clay-rich rocks in sedimentary basins: low-temperature experimental formation of magnetic carriers in natural samples. *Earth and Planetary Science Letters*, 230(1-2), pp.193-210.
- Parés, J. M., and Van der Pluijm, B. A., 2004, Correlating magnetic fabrics with finite strain: Comparing results from mudrocks in the Variscan and Appalachian Orogens. *Geologica Acta: an international earth science journal*, 2(3), pp.213-220.
- Paterson, G.A., Zhao, X., Jackson, M. and Heslop, D., 2018, Measuring, processing, and analyzing hysteresis data. *Geochemistry, Geophysics, Geosystems* 19(7), <https://doi.org/10.1029/2018GC007620>
- Pawlewicz, M. J., Barker, C. E., and McDonald, S., 2005, Vitrinite reflectance data for the Permian Basin, west Texas and southeast New Mexico. U.S. Geological Survey Open-File Report 2005-1171, 25 p.
- Peters, C. and Dekkers, M.J., 2003, Selected room temperature magnetic parameters as a function of mineralogy, concentration and grain size. *Physics and Chemistry of the Earth, Parts A/B/C*, 28(16-19), pp.659-667.
- Raiswell, R. and Fisher, Q.J., 2000, Mudrock-hosted carbonate concretions: a review of growth mechanisms and their influence on chemical and isotopic composition. *Journal of the Geological Society*, 157(1), pp.239-251.
- Reynolds, R.L., Sweetkind, D.S., and Axford, Yarrow, 2001, An inexpensive magnetic mineral separator for fine-grained sediment: U.S. Geological Survey Open-File Report 01-281, 7 p.
- Roberts, A.P., Chang, L., Rowan, C.J., Horng, C.S. and Florindo, F., 2011, Magnetic properties of sedimentary greigite (Fe<sub>3</sub>S<sub>4</sub>): An update. *Reviews of Geophysics*, 49(1).
- Roberts, A.P., 2015, Magnetic mineral diagenesis. *Earth-Science Reviews*, 151, pp.1-47.

- Roberts, J.M. and Elmore, R.D., 2017, A diagenetic study of the Woodford Shale in the southeastern Anadarko Basin, Oklahoma, USA: Evidence for hydrothermal alteration in mineralized fractures. *Interpretation*, 6(1), pp.SC1-SC13.
- Rochette, P., 1988, Inverse magnetic fabric in carbonate-bearing rocks. *Earth and Planetary Science Letters*, 90(2), pp.229-237.
- Rochette, P., Aubourg, C. and Perrin, M., 1999, Is this magnetic fabric normal? A review and case studies in volcanic formations. *Tectonophysics*, 307(1-2), pp.219-234.
- Rolph, T.C., Shaw, J., Harper, T.R. and Hagan, J.T., 1995, Viscous remanent magnetization: a tool for orientation of drill cores. Geological Society, London, Special Publications, 98(1), pp.239-243.
- Rose, P.R., 2016, Late Cretaceous and Tertiary Burial History, Central Texas. *GCAGS Journal*, 5, pp.141-179.
- Ross, C. A., 1986, Paleozoic evolution of southern margin of Permian basin. *Geological Society of America Bulletin*, 97(5), 536-554.
- Saffer, B. and McCabe, C., 1992, Further studies of carbonate remagnetization in the northern Appalachian basin. *Journal of Geophysical Research: Solid Earth*, 97(B4), pp.4331-4348.
- San Angelo Geological Society. Stratigraphic Committee. Central Irion County, Texas: Composite electric log, columnar section, subsurface formations 1957.
- Shau, Y.H. and Peacor, D.R., 1992, Phyllosilicates in hydrothermally altered basalts from DSDP Hole 504B, Leg 83—a TEM and AEM study. *Contributions to Mineralogy and Petrology*, 112(1), pp.119-133.
- Schieber, J., 2011, Marcasite in black shales—a mineral proxy for oxygenated bottom waters and intermittent oxidation of carbonaceous muds. *Journal of Sedimentary Research*, 81(7), 447-458.
- Schieber, J., and Ellwood, B. B., 1993, Determination of basinwide paleocurrent patterns in a shale succession from anisotropy of magnetic susceptibility (AMS): a case study of the mid-Proterozoic Newland formation, Montana. *Journal of Sedimentary Research*, 63(5).
- Schwehr, K., Tauxe, L., Driscoll, N. and Lee, H., 2006, Detecting compaction disequilibrium with anisotropy of magnetic susceptibility. *Geochemistry, Geophysics, Geosystems*, 7(11).
- Sinclair, T.D., 2007, The generation and continued existence of overpressure in the Delaware Basin, Texas (Doctoral dissertation, Durham University).
- Snowball, I.F., 1997, Gyroremanent magnetization and the magnetic properties of greigite-bearing clays in southern Sweden. *Geophysical Journal International*, 129(3), pp.624-636.
- Suk, D., Peacor, D.R. and Van der Voo, R., 1990, Replacement of pyrite framboids by magnetite

- in limestone and implications for palaeomagnetism. *Nature*, 345(6276), p.611.
- Suk, D., Van Der Voo, R. and Peacor, D.R., 1993, Origin of magnetite responsible for remagnetization of early Paleozoic limestones of New York State. *Journal of Geophysical Research: Solid Earth*, 98(B1), pp.419-434.
- Stoner, J.S., Channell, J.E. and Hillaire-Marcel, C., 1996, The magnetic signature of rapidly deposited detrital layers from the deep Labrador Sea: Relationship to North Atlantic Heinrich layers. *Paleoceanography and Paleoclimatology*, 11(3), pp.309-325.
- Tarling, D., and Hrouda, F. (Eds.), 1993, *Magnetic anisotropy of rocks*. Chapman and Hall, London, 217 pp.
- Taylor, K. G., and Macquaker, J. H. S., 2000, Early diagenetic pyrite morphology in a mudstone-dominated succession: the Lower Jurassic Cleveland Ironstone Formation, eastern England. *Sedimentary Geology*, 131(1-2), 77-86.
- Tohver, E., Weil, A.B., Solum, J.G. and Hall, C.M., 2008, Direct dating of carbonate remagnetization by  $^{40}\text{Ar}/^{39}\text{Ar}$  analysis of the smectite–illite transformation. *Earth and Planetary Science Letters*, 274(3-4), pp.524-530.
- Torsvik, T.H., 2000, Super-IAPD. <http://www.geodynamics.no/software.htm>.
- Torsvik, T.H., Van der Voo, R., Preeden, U., Mac Niocaill, C., Steinberger, B., Doubrovine, P.V., van Hinsbergen, D.J., Domeier, M., Gaina, C., Tohver, E. and Meert, J.G., 2012, Phanerozoic polar wander, palaeogeography and dynamics. *Earth-Science Reviews*, 114(3-4), pp.325-368.
- Weil, A.B. and Yonkee, A., 2009, Anisotropy of magnetic susceptibility in weakly deformed red beds from the Wyoming salient, Sevier thrust belt: Relations to layer-parallel shortening and orogenic curvature. *Lithosphere*, 1(4), pp.235-256.
- Wickard, A.K., Elmore, R.D, and Heij, G.W, in press, A Diagenetic study of the Wolfcamp Shale in the Southeast Midland Basin, West Texas: A Petrographic and SEM study of two cores. AAPG, Memior.
- Xu, W., Van der Voo, R. and Peacor, D.R., 1994, Are magnetite spherules capable of carrying stable magnetizations?. *Geophysical research letters*, 21(7), pp.517-520.
- Yang, K. M., and Dorobek, S. L., 1995, The Permian basin of west Texas and New Mexico: tectonic history of a " composite" foreland basin and its effects on stratigraphic development. *Stratigraphic evolution of foreland basins: SEPM Special Publication*, 52, 149-174.
- Zijderveld, J.D.A., 1967. AC demagnetization of rocks: Analysis of results, *Methods in Paleomagnetism* DW Collinson, KM Creer, SK Runcorn, 254–286.

## CHAPTER 4

# UNRAVELING THE COMPLEX BURIAL HISTORY OF THE ANTRIM FORMATION IN MICHIGAN BASIN USING PALEOMAGNETISM, ROCK MAGNETISM AND GEOCHEMISTRY

### ABSTRACT

This paper presents the first integrated paleomagnetic, rock magnetic and geochemical study of the Devonian Antrim shale in the Michigan Basin. The Antrim may be characterized as an organic-rich, fractured siliceous mudrock which has been divided, based on organic richness and log-character into three members including the Lachine, Paxton and Norwood at its base. Specimens were obtained from two unoriented vertical cores (named St. Chester and Krocker) and sampled relative to a master specimen orientation line. The St. Chester core is located in the northern part of the basin where natural gas formation is predominantly biogenic in origin. The Krocker core is located in the central part of the basin, near the eastern arm of the midcontinent rift where thermogenic gas formation predominates. Alternating field (AF) demagnetization experiments isolated a lower coercivity (LC), formation-wide component from 0 to ~60mT in the Krocker core and corresponds to a Jurassic ( $170\text{Ma} \pm 25$ ) magnetization. Higher coercivity components (HC) in the Krocker core are unblocked from ~60 to 120 mT and unlike LC components, occasionally exhibit stable unblocking temperature ranges (e.g. 150 to 450°C) and higher AF demagnetization ranges (~60 to 120mT). HC components in the Krocker core are unique to certain members with a poorly resolved Middle Permian/Late Triassic magnetization in the Paxton member and Late Pennsylvanian ( $305\text{Ma} \pm 10$ ) component in the Norwood. The St. Chester well was less densely sampled, however, exhibited a LC component among all specimens similar to but, slightly older ( $205\text{Ma} \pm 10$ ) than the Krocker core. A small number of specimens collected

from the St. Chester well prevented delineating age differences between members based on their HC magnetization ages, however, on average the HC magnetizations are older ( $315\text{Ma} \pm 20$ ) than their counterparts in the Krocke core. Maximum unblocking temperatures and rock magnetic parameters indicate the magnetization resides in magnetite. Hysteresis data indicate mainly pseudo-single domain (PSD) behavior which likely stems from mixed single-domain (SD) and multi-domain (MD) or mixed SD/PSD grains suggested by back-field coercivity spectrum modeling. Overall, the magnetizations are interpreted to be chemical remanent magnetizations (CRMs) with the HC component residing in SD magnetite which formed during hydrothermal activity in both cores. The LC component likely resides in PSD/MD magnetite and is interpreted to have formed in response to fluid flow associated with tectonic uplift and/or hydrocarbon migration, however, due to unsuccessful thermal demagnetization experiments, a thermoviscous remanent magnetization cannot be excluded. Petrographic observations indicate mineral assemblages consistent with hydrothermal mineralization (e.g. baroque dolomite, euhedral quartz and sphalerite). Depleted  $\delta^{18}\text{O}$  data from carbonate fractures are consistent with hydrothermal fluids. Consistent anisotropy of magnetic susceptibility (AMS) lineations indicates either a long-lived paleocurrent direction or far-field tectonic shortening originating from the neighboring Acadian orogeny. Inorganic geochemistry, low temperature (LT) magnetic susceptibility and LT AMS indicate that paramagnetic Fe-rich clays carry the AMS signal. Lastly, an evaluation of the origin of chalcopyrite and monazite is performed through provenance analysis. These minerals are attributed to hydrothermal analysis however, strong evidence suggests that some population of these grains were sourced from the Michigan Peninsula and delivered to the basin by hyperpycnal flows.

## INTRODUCTION

Paleomagnetic studies of Devonian shales in North America have provided key insights regarding the timing of paleofluid activity in sedimentary basins (e.g. Dennie and Elmore, 2012; Manning and Elmore, 2015; Roberts and Elmore, 2017). The Antrim Formation represents one such shale deposited within the vast eastern interior seaway which separated the North American craton. However, unlike the Woodford or Marcellus shales, the Antrim resides in an intracratonic basin which underwent comparatively less intense tectonic episodes. Major regional tectonic events in the Michigan basin are limited to pulses of late Paleozoic subsidence, hydrothermal activity related to reactivation of the eastern limb of the midcontinent rift and post-Permian uplift (Howell and van der Pluijm, 1990; Crowley, 1991; Girard and Barnes, 1995; Ma et al., 2009; Apotria et al., 1994). The thermal maturity of the Antrim also provides clues to its burial history because, burial alone does not account for vitrinite reflectance values observed and therefore must indicate one or some combination of processes including tectonic uplift, elevated geothermal gradients or hydrothermal fluids (Crowley, 1991; Apotria et al., 1994; Luczaj et al., 2006). Petrographic and geochemical evidence of hydrothermal activity has been reported in underlying rocks such as Ordovician carbonates and middle Devonian dolomites (Coniglio and Sherlock, 1994; Luczaj et al., 2006), however, the presence of hydrothermal fluids in the Antrim has not been documented. Integrated paleomagnetic investigations buttressed by geochemical and observational evidence are well suited for determining the timing of hydrothermal activity and can potentially shed light on whether hydrothermal activity extended to the Antrim. Constraining whether or not hydrothermal activity extended to the Antrim is important for several reasons. For example, hydrothermal fluids can impact catagenesis of organic material (e.g. Simoneit et al. 1992)

and may constructively or destructively influence reservoir properties (e.g. Saller and Dickson, 2011).

In addition to testing for hydrothermal activity, the two cores utilized in this study offer a unique opportunity to investigate the differences, if any, between thermogenic and biogenically mediated (i.e. bacterial methanogenesis) natural gas formation on magnetic properties and diagenesis. Gas production in the northern St. Chester well is dominated by biogenically produced gas, evidenced by chemical and isotopic compositions of produced water (Martini et al., 1996) whereas the deeper, Krockel well from the middle of the basin is characterized by predominantly thermogenic gas which is self-sourced or migrated from underlying Silurian shales (East et al., 2005). According to Martini et al. (1998) the origin of biogenic gas stems from episodes of Pleistocene glaciation over northern Michigan where thick ice sheets provided hydraulic head that enhanced dilation of pre-existing fractures and caused influx of meteoric water which in turn, promoted microbial methanogenesis. If magnetotactic bacteria were active during this period, magnetite produced by such organisms could be recorded by paleomagnetic and rock magnetic methods (e.g. Chang et al., 1987; Moskowitz et al., 1993).

Lastly, there are unresolved questions regarding the role of paleostresses operating in the Michigan Basin. For example, fractures in the Antrim have been attributed to natural hydraulic fracturing (Apotria et al., 1994) and far-field tectonic stresses (Craddock and van der Pluijm, 1989; Versical, 1991). A petrofabric study can serve as an independent means to evaluate which hypothesis is more likely. Room temperature and low temperature anisotropy of magnetic susceptibility (AMS) are well-established petrofabric tools that have been used to successfully detect tectonic shortening and these tools are particularly sensitive to subtle strain recorded by clay-rich sediments (e.g. Pares, 2004; Pares and van der Pluijm, 2004). If consistent AMS

lineations are present, it could provide support for a tectonically driven fracture network in the Antrim Shale.

## **GEOLOGIC BACKGROUND**

The Michigan Basin is an oval, yoked intracratonic basin occupying an area of over 200,000 km<sup>2</sup> (e.g. Gutschick, 1987) (Figure 1). The basin is underlain by the eastern segment of the midcontinent rift system (MCRS) which formed during the Proterozoic. The incipient development of the Michigan Basin is attributed to fault controlled subsidence followed by thermal subsidence (Klein and Hsui, 1987). During the late Cambrian, minor subsidence occurred due to extension of the Reelfoot rift south of the Michigan basin (Sleep et al., 1980). Thereafter, episodic subsidence inferred from stratal geometries in the Michigan Basin occurred first during the middle Ordovician owing to the Taconic orogeny followed by another period of subsidence related to the Acadian orogeny (Howell and van der Pluijm, 1990). Subsurface structural expressions such as anticlines and synclines are interpreted as shear folds that formed in response to Appalachian tectonics (Figure 1) (Prouty, 1988; Versical, 1991). These features are thought to be thick-skinned tectonic features caused by inversion of extensional structures in basement rocks during the Late Mississippian (Prouty, 1988; Versical, 1991; Curran and Hurley, 1992).

In terms of lithostratigraphy, Paleozoic through Mesozoic sedimentary rocks in the Michigan Basin are primarily composed of evaporites, carbonates, shale, and sandstone underneath a thick layer of Pleistocene glacial deposits. As with other intracratonic basins, strata progressively thin towards the margins of the basin and occasionally show evidence of “yoking” where strata spill over into the neighboring basin.

### ***Hydrothermal activity in the Michigan Basin***

Ma (2009) reported depleted noble gas concentrations from deep brines of eight formations, including the Antrim which can result from boiling and steam separation in hydrothermal systems (e.g. Winckler et al., 2000). Based on these findings, Ma (2009) postulates an ancient thermal event in the basin, during which hydrothermal fluids migrated from deeper portions of the basin along major faults and fractured zones. The underlying mechanism for hydrothermal activity has been attributed to the reactivation of the MCRS during the Late Devonian–Mississippian (370–323 Ma) period based K-Ar dating of authigenic illite and fluid inclusion data from the underlying Ordovician St. Peter sandstone (Girard and Barnes, 1995; Luczaj et al., 2006).

### ***The Antrim Formation***

The Late Devonian Antrim Formation was deposited within the eastern interior seaway which covered large swaths of the North American Craton, including the Michigan Basin (Dellapenna, 1991). As a result, the Antrim is chronostratigraphically equivalent to other Devonian black shales in North America such as those within the neighboring Appalachian and Illinois basins (Mathews, 1983). Deposition of the Antrim occurred over a ~12Ma period and is broadly characterized by slow, hemipelagic basinal sedimentation in predominantly anoxic waters that were punctuated by prodeltaic complexes (Gutschick and Sandberg, 1991). Gutschick and Sandberg (1991) also report turbidite complexes extending to the central part of the basin.

Multiple orthogonal natural fracture sets occur across the Antrim, particularly in the northern Michigan Basin (e.g. Budai et al., 2002). The mechanism for fracture development is attributed to either natural hydraulic fracturing owing to hydrocarbon generation or far field paleostresses imposed by the Alleghenian Orogeny (Craddock and van der Pluijm, 1989; Apotria

et al., 1994). Burial and thermal history modeling by Aporia et al. (1994) suggest the Antrim shale reached its maximum burial temperature from 250-240Ma after-which, uplift since the Permian brought the Antrim to its present depth.

From a lithological standpoint, the Antrim Formation broadly consists of finely laminated, organic-rich and pyritic shales (Figure 2) that are intermittently interbedded with gray and green shales and carbonate units (Gutschick and Sandberg, 1991; Martini et al., 1998; Over, 2002). The Antrim formation ranges from 100ft to 600ft in thickness and is divided into three members that include the Norwood, Paxton and Lachine. The Norwood Member consists of black fissile pyritic shales with thin fossiliferous limestone beds, carbonate concretions, and cyclical greenish gray and black shales that show evidence of bioturbation (Gutschick and Sandberg, 1991) (Figure 2A, 2D). This member is also distinguished by its unusually high total organic carbon (TOC), which can range from 10 to 24 weight percent (Matthews, 1993). The Paxton Member is an interbedded light gray argillaceous calcareous greenish gray with significantly lower total organic carbon relative to the other members (Gutschick, 1987; Dellapena, 1991; Martini et al., 1998) (Figure 2B). Finally, the Lachine Member is a black shale punctuated by greenish-gray shales and carbonate concretions (Gutschick and Sandberg, 1991) with the Frasnian-Famennian boundary identified at its base (Figure 2C). Underlying the Antrim formation, the Squaw Bay, which forms part of the Traverse Group is a gray limestone/shaley limestone interbedded with gray and black shales. Although not, strictly part of the Antrim Formation, this unit is considered to be a transitional unit and is included in this study.

## **METHODS**

Two vertical cores were sampled at the Michigan Geological Repository for Research and Education (MGRRE) in Kalamazoo, MI (Figure 1). Drilling reports indicate no deviation from

vertical orientations in either well and dip-meter data confirm horizontal bedding. A total of 21 specimens were retrieved from the St. Chester well (Norwood (n = 9, 1597.1-1616.5ft); Paxton (n = 6, 1502-1555.5ft); Squaw Bay Limestone (n=6, 1670.5-1673.7ft). Additional sampling from the Lachine and other members were not possible because of the overall fissile and unconsolidated nature of the slabbed core. For the Krockler well, a total of 116 specimens were extracted (Norwood (n = 30, 3406.7-3443.9ft); Paxton (n = 57, 3350.1-3402.3ft); Lachine (n = 29, 3261.5-3332.7ft); Squaw Bay Limestone; (n = 12, 3460.3-3481.5ft)). Samples were drilled from slabs relative to a master orientation line and full-length plugs were cut to standard paleomagnetic specimen dimensions (25 mm diameter x 22 mm height) that yielded 2-3 plugs per sampling interval. All specimens were oriented with respect to the stratigraphic up direction. Thin sections were prepared from representative specimens and mineralized carbonate-filled fractures from both cores were sampled using a microdremel for carbon and oxygen stable isotope analysis.

### ***Magnetic experimental methods***

Paleomagnetic measurements were performed using a 2G Enterprise cryogenic magnetometer with DC superconducting quantum interference devices (SQUIDS) within a magnetically shielded room at the University of Oklahoma. One specimen from each depth interval underwent thermal demagnetization from 0°C to 500°C at 50°C increments and the remaining specimens were subjected to alternating field (AF) demagnetization at field increments of 10mT from 0mT to 120mT. Characteristic remanent magnetization (ChRM) were determined from principal component analysis (Kirsvinck, 1980) of demagnetization data plotted on Zijderveld diagrams. Maximum angular deviations (MAD) values for magnetic components were generally <10°, however, in a few instances reached up to 15°. ChRM inclinations were processed using the statistical routine proposed by Arason and Levi (2010) in order to correct for shallow-inclination

bias and plotted against the expected inclinations obtained from the North American APWP (Torsvik et al., 2012).

Magnetic hysteresis measurements were performed on representative specimens using a Princeton Measurements vibrating sample magnetometer (VSM) 3900-04 housed at Southern Illinois University Carbondale in order to constrain magnetic mineral type(s) and their granulometry. Specimens were subjected to an applied field ranging from 0.5 to 1T at a field step of 5.0 mT and averaging time of 500ms. Data processing was performed using HystLab, a MATLAB based software written by Paterson et al. (2018). Standard processing of hysteresis loops included linear high-field slope corrections, loop centering and paramagnetic drift corrections (Jackson and Solheid, 2010; Paterson et al., 2018). Hysteresis parameters, which include (remanent magnetization ( $M_{rs}$ ), saturation magnetization ( $M_s$ ) and coercivity ( $B_c$ )) were computed from processed loops and data quality was assessed using the Q-factor parameter (Jackson and Solheid, 2010). Back-field demagnetization curves were measured in order to obtain remanent coercivity ( $B_{cr}$ ) and were processed using the Max Unmix program (Maxbauer et al., 2016) in order to reveal the coercivity spectrums of representative specimens from each core. Saturation isothermal remanent magnetization (SIRM) were measured after applying a field of 1.5T on specimens following AF demagnetization. The ratio of SIRM and low-field magnetic susceptibility ( $k_{lf}$ ) was used to detect changes in magnetic mineralogy (e.g. Stoner et al., 1996; Peters and Dekers, 2003; Maher, 2007). Stepwise thermal demagnetization of triaxial isothermal remanent magnetizations ( $x = 120\text{mT}$   $y = 500\text{mT}$   $z = 1200\text{mT}$ ) imparted on AF demagnetized samples were performed in order identify magnetic carrier minerals based on unblocking temperatures of low (x), intermediate (y) and high (z) coercivity minerals.

Anisotropy of magnetic susceptibility (AMS) and magnetic susceptibility ( $k_{lf}$ ) were measured at both room temperature ( $\sim 297\text{K}$ ) and low temperature ( $\sim 77\text{K}$ ) using a MFK1-FA Kappabridge magnetic susceptimeter in order to quantify magnetic petrofabrics, enhance the paramagnetic contribution to AMS fabrics and constrain magnetic mineralogy respectively (e.g. Rochette et al., 1987; Pares and van der Pluijm, 2002). Low temperature AMS (LT-AMS) measurements were performed using a slightly modified approach originally described by Issachar et al. (2016) and consecutive  $k_{lf}$  measurements from 77K to 297K were conducted using the methodology of Richter and van der Pluijm (1994). Anisoft V4.2 was used to process AMS data and calculate the orientation of principal magnetic axes (K1, K2 and K3) and scalar parameters including the corrected degree of magnetic anisotropy ( $P_j$ ) and shape of the AMS ellipsoid ( $T$ ) (Jelinek, 1981).

### ***Geochemistry and Petrography***

Stable carbon and oxygen isotopic signatures were obtained from carbonate-filled fractures and carbonate matrix material in both cores. Aliquots of carbonate material (200-300 $\mu\text{g}$ ) were placed in a borosilicate exetainer vials and sealed with butyl rubber caps. Vials were then placed in a thermostated sample tray, heated to  $50^\circ\text{C}$  and flushed with He for 360 seconds to remove air. Then 0.4ml of 100% phosphoric acid ( $\text{H}_3\text{PO}_4$ ) was injected into each vial at  $50^\circ\text{C}$  for 2 hours (McCrea, 1950; Swart et al., 1991). Gas from this reaction was then analyzed for both carbon and oxygen isotope abundance using a Thermo Delta V Plus isotope mass spectrometer. The data is reported relative to the PeeDee Belemnite (PDB) and Vienna Standard Mean Ocean Water (SMOW) standards (Coplen, 2011).

Hand-held X-ray fluorescence measurements were performed on each plug using the Bruker Tracer III-V HH-ED-XRF Spectrometer. Plugs were analyzed for major (Al, Si, S, Ca, Ti,

and Fe) and trace (Cu, Zr, Nb) elements for 90 and 60 seconds respectively. Calibration of the raw X-ray spectra were performed using mudstone specific calibration reference materials compiled by Rowe et al. (2012) and data are reported in parts per million (ppm). Elemental abundances and ratios were used as proxies to infer mineralogical compositions, magnetic mineralogy, redox conditions and provenance lithotypes. Fe concentrations were used to evaluate the contribution of iron-bearing minerals to the  $k_{IF}$ , Al is used as a proxy for clay concentration, Cu as a proxy for copper-bearing minerals, Zr as a terrestrial source and textural maturity indicator, Si/Al for quartz concentration and Ti/Nb as a provenance lithotype indicator (i.e. basic vs quartzofeldspathic) (e.g. Tribovillard et al., 2006; Bonjour and Dabard, 1991).

Principal observations were conducted using transmitted and reflected light microscopy on polished thin sections using a Zeiss AxioImager.Z1m petrographic microscope. In addition, backscatter (BSE) and secondary electron (SE) images were collected using a FEI Quantum 250 field emission scanning electron microscope (SEM) with an attached Bruker X-ray detector for energy dispersive analysis (EDS).

## RESULTS

### *Paleomagnetism*

AF and thermal demagnetization resulted in 30 to 97.7% decay of the NRM (mean = 70.0%, Stdev. = 16.3%) among Krockers specimens whereas St. Chester specimens ranged from 16 to 68.7% decay (mean = 49.8%, Stdev = 19.35%). Median destructive fields (MDF) show no relation with depth or facies in the Krockers (mean = 38.3 mT, Stdev. = 24.4mT) or St. Chester (mean = 58.3 mT, Stdev. = 41.6mT) specimens. A lower coercivity (LC) (0~60mT) and higher coercivity (HC) component (~60-120mT) was revealed in all members with the exception of the Squaw Bay which only showed a stable, low coercivity component. Thermal demagnetization did

not yield interpretable unblocking temperatures for the LC component and, therefore, the possibility of a thermoviscous magnetization (TVRM) cannot be excluded.

The Lachine member's magnetizations in the Krocker are generally unblocked at low fields (0-60mT) (n = 11) with the exception of a single stable, higher temperature component unblocked from 100°C to 450°C sampled at 3322.1 ft. (Figure 3A). The remaining thermal demagnetization data for this member were unsuitable for PCA. AF demagnetization commonly produced laboratory induced, gyro-remanent magnetizations (GRM) starting at 40 to 60mT. LC inclinations are fairly well constrained and show a component with moderate, down inclinations ranging from 30° to 45° (Figure 3B, 5). NRM intensities in the Lachine display little variability and range between 0.07 and 0.09 mA/m (Figure 5). Similarly, SIRM/k<sub>lf</sub> ratios show little variability with values <10kA/m (Figure 5).

The more densely sampled Paxton shows an equal contribution of LC and HC components revealed by AF demagnetization experiments (Figure 5). Like the Lachine, thermal demagnetization yielded significantly fewer stable components in the Krocker core (n = 5) and only higher temperature components could be fit with PCA (Figure 3C). Stable components were unblocked between 200°C and 350°C, after which magnetic intensities rose sharply. Anomalously steep inclinations from 50°C to 200°C appeared in several specimens and likely correspond to a drilling induced remanent magnetization (DIRM) (Figure 3C). The LC data from the Paxton in the Krocker core show moderate inclinations ranging from 30° to 55° (n = 12) and from 20° to 40° (n=4) in the St. Chester core (Figure 3D, 3E, 5, 6). Its HC components are comparatively shallower and range from 0 to 30° (n =26) in the Krocker core (Figure 3D, 5) and from -35° to 1° (n=4) in the St. Chester (Figure 3E, 6). The mean inclination, statistics and age for the HC component in the Paxton (Krocker core only) are displayed in Figure 4 and Table 1. The mean inclination yields

a non-unique age due to multiple intersections with the predicted inclination plot (270Ma, 250Ma and 230Ma) and is therefore, broadly referred to as a Middle Permian/Late Triassic magnetization (Figure 4A). Like the Lachine, NRM intensities are typically  $<0.1\text{mAm}^{-1}$  and SIRM/ $k_{\text{IF}}$  ratios range from 18 to 3  $\text{kAm}^{-1}$  (mean =  $8.6\text{kAm}^{-1}$ ) (Figure 5).

Thermal demagnetization of Norwood specimens from the Krocker core reveal a high temperature, shallow up inclination that is unblocked from  $150^{\circ}\text{C}$  to  $450^{\circ}\text{C}$  ( $n=3$ ) (Figure 3F). AF demagnetization reveals a similar HC component in both the Krocker and St. Chester wells (Figure 3G, 3H). Inclinations for the HC component in the Krocker core range from  $-11^{\circ}$  to  $18^{\circ}$  (mean =  $-2.48^{\circ}$ ,  $n=15$ ) (Figure 4A, Table 1). The HC mean inclination indicate a Late Pennsylvanian age ( $305\text{Ma} \pm 10$ ) (Table 1, Figure 4A). LC components in the Norwood ( $n = 6$ ) show significant variability relative to the other members and range from  $8^{\circ}$  to  $55^{\circ}$ . The Norwood has the highest NRM intensities in both cores (mean =  $0.35\text{mAm}^{-1}$ ) and NRM values are up to 5 times greater than those observed in other units (Figure 5, 6). SIRM/ $k_{\text{IF}}$  ratios are broadly consistent with other units however, outlier values exceeding  $20\text{kAm}^{-1}$  are confined to the Norwood in both cores (Figures 5, 6)

A total of 11 specimens were obtained from the Squaw Bay, (Krocker = 7; St. Chester = 4) with all specimens revealing a single, LC component during AF demagnetization with inclinations ranging from  $30^{\circ}$  to  $55^{\circ}$  (Krocker) and  $16^{\circ}$  to  $36^{\circ}$  (St. Chester) (Figure 3I, 3J, 5, 6). Thermal demagnetization experiments produced data that could not be fit with PCA. NRM intensities and SIRM/ $k_{\text{IF}}$  ratios are consistent with values observed in the Lachine and Paxton members (Figures 5, 6).

Given the normal distribution observed in the histogram in Figure 5 of LC inclinations in the Krocker core, we interpret these magnetizations to be cogenetic. Under this assumption, mean

inclinations indicate a Jurassic ( $170\text{Ma} \pm 25$ ) magnetization (Table 1, Figure 4A). For the St. Chester, significantly less samples precludes the determination of a robust age, however, based on the available data, the age of the LC component is slightly older compared to the Krocker ( $205\text{Ma} \pm 10$ ) (Table 1, Figure 4B). Considerable overlap exists between LC magnetizations in both cores and therefore it is plausible that these magnetizations are also cogenetic.

The HC components residing in the Norwood and Paxton members ( $n=10$ ) in the St. Chester also preclude the determination of a robust age for these units. It is unclear whether the Norwood has a different age than the Paxton in the St. Chester core (as observed in the Krocker well), however, the available data does indicate, on average, older magnetizations ( $315\text{Ma} \pm 20$ ) residing in both the Norwood and the Paxton members (Table 1, Figure 4B)

### ***Rock Magnetism***

Triaxial thermal decay experiments reveals that the magnetization resides predominately in a higher coercivity mineral unblocked between  $450^{\circ}\text{C}$  and  $500^{\circ}\text{C}$  in the Norwood and Paxton members (Figure 7A). The normalized magnetization curves, show an increase in magnetization of the subordinate lower coercivity component starting at  $350^{\circ}\text{C}$  in the Paxton and Norwood (Figure 7B). In contrast, the magnetization in the Lachine and Squaw bay, resides in a lower coercivity mineral, however, sharp rises in magnetization starting a  $300\text{-}350^{\circ}\text{C}$  preclude precise determination of an unblocking temperature (Figure 7C). The subordinate higher coercivity component in the Lachine and Squaw Bay appears to be unblocked at  $\sim 400^{\circ}\text{C}$  (Figure 7D). Overall, all triaxial thermal decay experiments indicate unblocking temperatures consistent with magnetite.

Representative hysteresis loops are displayed in Figure 8. Processed hysteresis loops have excellent Q-values ranging from 2.93 to 3.43 and suggest good symmetry between upper and lower

branches. Pole drift artifacts are observed in specimens with weaker magnetizations however, the fidelity of hysteresis parameters are unaffected. Overall, two main behaviors are observed across all hysteresis loops 1) Clear wasp-waistedness in several Paxton and Norwood members (Krocker) indicative of mixed magnetic behaviors and 2) Smooth symmetrical hysteresis loops in the Lachine, Squaw Bay and St. Chester core specimens. Hysteresis parameters were plotted on a Day-plot and indicate pseudo-single-domain behavior among Paxton and Norwood specimens (Krocker) (Figure 9A). The proximity of these specimens to the SD-MD mixing curve (Dunlop 2002) suggests the PSD behavior results from a mixture of SD and MD grains. Unmixing of back-field curves show that the coercivity spectrum can be modeled with 2 components with coercivities consistent with SD and MD magnetite (Table 2, Figure 9C). The Lachine, Squaw bay and Paxton (St. Chester) hysteresis data plot closer to the SP-SD mixing curve and are also best modeled with two components, with essentially identical coercivity spectrums (Table 2, Figure 9B).

### ***Room Temperature AMS***

A consistent lineation of K1 tensors emerges across all members in the Krocker core, although there is some disparity in the consistency of groupings between members (Figure 5). For example, K1 confidence ellipses in the Lachine and Squaw Bay are better constrained than those observed in the Paxton and Norwood members. Frequency-distributions for K1 declinations and K3 declinations confirm a consistent lineation, however, a clear bimodal distribution of K3 tensors emerges (Figure 5). Significantly fewer K3 tensors plot in the lower hemisphere of the equal-area (i.e.  $90^\circ$  and  $270^\circ$ ) relative to data in the upper hemisphere and signifies a slight imbrication of the AMS fabric. Like the Krocker core, a consistent lineation among K1 tensors occurs in the St. Chester core (Figure 6) however, K3 tensors show a streaked distribution.

### ***Low Temperature AMS***

Low temperature AMS measurements were performed on mudrock facies and compared to their room temperature counterparts (Figure 10). K1 and K3 AMS orientations show no significant change from room temperature (RT) to low temperature (LT) among Lachine specimens (Figure 10A). P<sub>j</sub> values show significant increases and shape factors either remain constant or increase in oblateness (Figure 10A). Linear correlation coefficients for normalized reciprocal magnetic susceptibility ( $k_0/k$ ) vs. temperature suggest that 90 to 91% of the magnetic susceptibility is carried by paramagnetic minerals (Figure 10B). Among Paxton specimens, K1 orientations also show little variation, with the exception of specimen C (Figure 10C). Aside from specimen A, both B and C specimens exhibit changes in their K3 orientations (Figure 10C). P<sub>j</sub> values increase from RT to LT, however, this increase is less pronounced than what is observed in Figure 10A (Figure 10C). T values become more positive (toward the oblate domain) with the exception of specimen C which transitions from mildly oblate to strongly prolate (Figure 10C). The magnetic susceptibility of Paxton specimens are also dominated by paramagnetic minerals however, specimen C does exhibit a slightly lower (87%) paramagnetic contribution. Norwood specimens display the greatest disparities between RT and LT AMS orientations (Figure 10E). Shape factors move toward the prolate domain from RT to LT in specimens B and C and in specimen A, P<sub>j</sub> values decrease significantly (Figure 10E). Paramagnetic contributions are diminished in the Norwood with specimens exhibiting as little as 60% (Figure 10F). Much like the Lachine, very little change in AMS orientations are observed in the Squaw Bay (Figure 10G). P<sub>j</sub> values increase overall but, to differing degrees and T values remain more or less constant (Figure 10G). Overall, the highest paramagnetic contributions to susceptibility occur in the Squaw Bay (up to 96%).

### ***Magnetic Susceptibility and XRF***

Bulk magnetic susceptibility shows a positive correlation with Fe in low S-bearing (<15,000 ppm) specimens (Figure 11A). Interestingly, S-rich (>15,000 ppm) specimens which occur predominantly in the Lachine, tend to depart from the regression line. A positive correlation also emerges between Al and  $k_{lf}$  (Figure 11B). Additionally, Fe concentrations increase concurrently with Al and  $k_{lf}$  (Figure 11B)

### ***Microscopy***

Reflected light photomicrographs show evidence of preferential oxidation in iron sulfides occurring throughout the Antrim and the Squaw Bay (Figure 12A). Surficial oxidation of pyrite is a common artifact that forms during or after the thin section making process, however, such artifacts usually appear as splotches which do not occur in our thin sections. BSE imaging of pyrite also reveals oxidized margins and intergrown oxidized marcasite identified by its spearhead crystal habits (Figure 12B). EDS analysis confirms the presence of oxygen along with iron and sulfur in these oxidized zones and thereby indicates partial replacement by magnetite (Appendix 1). Cubic, octahedral and pyritohedral pyrite occur throughout the Antrim (Figure 12C). Closer examination reveals that the nucleus of many pyrite crystals show textures consistent with pyrite framboids (inset Figure 12C). Sphalerite is also commonly associated with dense pyrite clusters (Figure 12C). Certain pyrite crystals in the St. Chester well contain trace amounts of Ni (2-3 at%) based on EDS spectra (Appendix 1). EDS spectra of clays from both cores show Fe-rich clays that likely correspond to chlorite (Figure 12E). Patches of celestine with streaks of barite cement occur in the Paxton member (Figure 12F). Euhedral quartz crystals occur within the celestine/barite cements (Figure 12F). Within the Lachine, monazite and chalcopyrite occur within carbonate grains (Figure 12G, 12H). These minerals are found in the matrix, unassociated with fractures and often occur

together. Both rounded and euhedral chalcopyrite crystal habits are observed (Figure 12H) (Appendix 1).

### ***Provenance***

The Ti/Nb vs. Zr plot was used in order to differentiate provenance materials delivered to the Antrim (Figure 13). Four distinct groups emerge from the data: 1) a Cu-rich, mixed quartzofeldspathic/volcanic source generally confined to the Lachine member; 2) Cu-rich, quartzofeldspathic source restricted to certain specimens from the Paxton; 3) Cu-poor, quartzofeldspathic source among a few Paxton specimens and; 4) Cu-poor, dominantly intrabasinal sourced specimens residing in the Paxton, Norwood and Lachine. Group 4 specimens generally contain the highest concentrations of quartz relative to groups. The presence of chalcopyrite in the Lachine further corroborates the increased Cu concentrations detected by HHXRF.

### ***Stable Isotopes***

Carbonate-rich matrix material and mineralized fractures from the Paxton member in the Krock and St. Chester wells were sampled for stable oxygen and carbon isotopic analysis (Figure 14A).  $\delta^{13}\text{C}$  values in this study range from -7.44 to -13.11 ‰ (PDB) (mean = -10.3 ‰ (PDB)).  $\delta^{13}\text{C}$  values for calcite veins from Osego county in the Lachine member (Budai et al., 2002) are substantially greater than those observed in this study. Budai et al. (2002) attributes high  $\delta^{13}\text{C}$  values to bacterial methanogenesis whereas data from this study indicate abiotic methane oxidation (Budai et al., 2002).  $\delta^{18}\text{O}$  values from vein specimens in both cores show depleted values ranging from -9.5 to -11.8 ‰ (PDB) (19.1-21.9 ‰ (SMOW)).  $\delta^{18}\text{O}$  values from the adjacent matrix exhibit significantly less depleted values (-4.8, -4.9 ‰ (PDB); 25.9, 25.8 ‰ (SMOW)). The locations of matrix and vein sampling sites are shown in Figure 14B). Vuggy porosity commonly occurs within

such fractures and curved crystal habits consistent with baroque dolomite are observed (Figure 14C). Optical microscopy reveals baroque dolomite characterized by coarsely crystalline mosaics of anhedral to subhedral crystals with undulose extinction, curved crystal faces (Figure 14D). Large calcite crystals with occasional patches of anhydrite occur intergrown with baroque dolomite (Figure 14D).

## DISCUSSION

### *Paleomagnetic interpretations, remanence-carrying minerals and petrography*

Rock magnetic experiments suggest the magnetizations in the Antrim and Squaw Bay reside primarily in SD and PSD/MD magnetite (Figures 7-9) with the LC component most likely residing in PSD/MD magnetite and HC component residing in SD magnetite. The SD component is interpreted to be a chemical remanent magnetization (CRM) based on three lines of evidence discussed below. Burial temperatures (inferred from vitrinite reflectance and fluid inclusion homogenization temperatures of (Luczaj et al., 2006)) and unblocking temperatures (e.g. 450°C) of the HC component were evaluated against a TVRM nomogram for SD magnetite and indicate that the HC component is not a TVRM.

- 1) *Baroque dolomite occurring in fractures within the Paxton member exhibit depleted  $\delta^{18}O$  values consistent with previous data collected from hydrothermal baroque dolomite and calcite in the middle Devonian Dundee formation (Luczaj et al., 2006) (Figure 14).* Furthermore Luczaj et al. (2006) also report fluid inclusion data of aqueous inclusions in saddle dolomite and calcite with homogenization temperatures from 120°C - 150°C. This temperature range cannot be explained by burial heating alone unless an additional 3000m of overburden were present (Luczaj et al., 2006) and no evidence exists for an uplift event of such magnitude.

- 2) *Minerals associated with hydrothermal activity such as barite, celestine, sphalerite, nickel-bearing pyrite, monazite, chalcopyrite and euhedral megaquartz occur, although not uniformly across the Antrim and Squaw Bay (Cambell and Ethier, 1984; Rusk, 2012)(Figure 12, 14). Of course, many of these minerals can form independent of hydrothermal activity via burial diagenesis or may originate from extrabasinal sources (e.g. Kesler and Jones, 1980; Totten et al., 2000, Berner et al., 2013), however, the confluence of these minerals does support a hydrothermal origin. With the exception of baroque dolomite occurring in fractures, these minerals occur as individual constituents in the matrix (sphalerite, monazite, and chalcopyrite) (Figure 12C, 12G, 12H) or as isolated cemented patches (celestine, barite, euhedral quartz) (Figure 12F). This brings into question the mechanism by which fluids migrated through the Antrim and Squaw Bay. We speculate that hydrothermal mineralization in the matrix would have likely occurred during early burial, while sediments are undercompacted and geopressure regimes allow for mass transfer of fluids (Magara, 1978). HC CRM development most likely occurred via illitization initiated by hydrothermal fluids which can produce authigenic magnetite (McCabe and Elmore, 1989; Hirt et al., 1993; Katz et al., 2000). This may have been the case in the Norwood which contains hydrothermal minerals in the matrix and virtually no mineralized fractures. A separate hydrothermal event likely migrated through the Paxton via fractures also causing a CRM by a similar remagnetization mechanism. Additional evidence supporting two unique CRMs for the Norwood and Paxton include the starkly disparate NRM intensities (Figures 5, 6).*
- 3) *Paleomagnetic ages and their geographical differences overlap with radiometric ages determined by Girard and Barnes (1995). An older magnetization (315Ma ±15) carried by*

SD magnetite in the St. Chester core compared to younger magnetizations in the Krocker (Paxton –Middle Permian/Late Triassic; Norwood – 305Ma  $\pm$ 10) is consistent with regional age discrepancies recorded by K-Ar dating. Girard and Barnes (1995) recognized that shallower (1-1.5km) Ordovician rocks toward the Northern margin of the Michigan Basin recorded older K-Ar ages (355Ma-380Ma) relative to specimens collected above the MCR (318-365Ma) in the central and deepest part (2.1-3.1km) of the basin. Perhaps similar conduits facilitating hydrothermal activity resulting in illitization of Ordovician rocks also acted as conduits for hydrothermal fluids reaching the Antrim. These conduits most likely originate in the basement which is thought to have well-developed patterns of jointing and faulting, analogous to the highly fractured neighboring Canadian Shield outcrop (Sanford et al., 1985, Fisher et al., 1988). These conduits may have been similar but probably not identical due to the slight age discrepancy between HC components in the Krocker core and K-Ar ages. Perhaps paleoplumbing in the central section of the basin precluded early migration of hydrothermal fluids beyond Ordovician rocks and only later, instigated by a far-field orogenic pulse from the Appalachians, conduits for hydrothermal fluid migration to the Antrim became active. K-Ar dating on Antrim specimens would provide much needed clarification to further reconcile these age discrepancies.

The origin of LC components (Krocker – 170Ma $\pm$ 25) and (St. Chester - 205Ma $\pm$ 10) are more difficult to decipher however, some preliminary ideas will be discussed. Thermal demagnetization did not yield interpretable unblocking temperatures for the LC component and, therefore, the possibility of a thermoviscous magnetization (TVRM) cannot be excluded. LC components may reside in PSD/MD magnetite that has replaced iron sulfides which occur in each member and both cores (Figure 12A, 12B, 12C), however, mechanisms for oxidizing fluids moving through each

unit are unknown. Interestingly, LC magnetizations appear to be broadly coeval with apatite fission track ages obtained from basement specimens. Apatite fission track data indicate heating events culminating by the Triassic followed by cooling during the Mesozoic (Crowley, 1991). Cooling ages are interpreted to correspond to uplift and removal of Permian and Pennsylvanian sediments which presumably covered the Michigan Basin (Crowley, 1995). Given the microtextural evidence and interpretations from Crowley (1991), two hypothesis are put forth: 1) A CRM related to an additional pulse of regional hydrothermal fluids migrating through the Antrim and Squaw Bay or 2) a CRM related to fluid migration caused by overpressuring due to tectonic uplift which forced oxidizing fluids through the Antrim and Squaw Bay. Numerical and burial history modeling by Aportria et al. (1994) suggest peak thermogenic hydrocarbon generation occurred from 240-250 Ma followed by natural hydraulic fracturing. These conditions would favor hydrocarbon migration as a mechanism for CRM development in the Antrim and Squaw Bay (e.g. Kilgore and Elmore, 1989; Elmore and Leach, 1990)

#### ***Magnetic/Diagenetic differences owing to biogenic vs thermogenic gas production***

The available data do not indicate significant differences with respect to magnetic mineralogy, mineral authigenesis or stable isotopes, however, this could reflect sampling bias due to the lack of samples retrieved from the St. Chester core. For example, from a stable isotope standpoint  $\delta^{13}\text{C}$  values fall within similar ranges in Paxton members in both cores and suggest similar fractionation processes were at play (i.e. abiotic methane oxidation) (Figure 14). This does not necessarily indicate that no microbial processes were active in the Lachine which, previous studies have shown to exhibit strong evidence of microbial methanogenesis (Budai et al., 2002). Petrographically, no differences emerge in terms of authigenic minerals with the exception of Ni-bearing pyrite which is only observed in St. Chester core which has no obvious connection to

microbial methanogenesis. Paleomagnetic data also indicate no evidence of a modern or post-Pleistocene magnetization in the St. Chester well and suggests microbial methanogenesis does not result in the formation of remanence-bearing minerals. Future studies should focus on retrieving specimens from the Lachine member, which may have been the member most affected by infiltrated Pleistocene glacial waters.

### ***Magnetic fabrics – Depositional or tectonically driven?***

As with the majority of AMS studies on shales (e.g. Pares, 2015), bedding parallel K1 orientations observed in the Antrim and Squaw Bay are due to mechanical compaction, however, the origin of the consistent lineation is more ambiguous. A slight imbrication of K3 tensors (i.e. deviation from the vertical plane) in the Krocker core suggests a hydrodynamically influenced magnetic fabric (Figure 5) (e.g. Schieber and Ellwood, 1988). Such ellipsoid configurations have been attributed to moderate current velocities that produce an upstream imbrication of grains (e.g. Pares et al., 2007, Ellwood et al., 1979; Liu et al., 2001). In this study, no evidence of reworked sediments were found, therefore, current velocities were probably low to moderate. Consistent AMS lineations are generally confined to massive, featureless facies, cross-laminated or wavy discontinuously laminated facies. If paleocurrents are indeed responsible for AMS lineations in the Antrim, paleocurrent directions probably remained relatively constant throughout the Late Devonian. The preservation of a hydrodynamically shaped fabric is a function many factors including an unchanging basin configuration, sediment supply and sea-level variability (e.g. Schieber, 1994). Structure maps on the base of the Antrim Shale indicate a concentric depocenter and show little evidence of major basin reconfiguration during the Late Devonian (Gutschick and Sandberg, 1991). However, changes in sediment supply (i.e. contribution from Catskill delta and

eastward prograding Ellsworth deltaic sediments) along with gradually falling sea-levels could have inhibited preservation of paleocurrent lineations (Gutschick and Sandberg, 1991).

Subtle tectonic shortening is an alternative and equally plausible explanation for the origin of consistent AMS lineations in the Antrim. Versical (1990) among others suggest far-field tectonic shortening during the Late Mississippian evidenced by anticlinal features. The Krocker core is located within the crest of one such anticline (Figure 1). Furthermore, AMS tensors in the St. Chester core show hallmarks of a composite sedimentary/tectonic fabric (i.e. streaked K3 directions) (Weil and Yonkee, 2012) (Figure 6). Discrimination between weak tectonic and hydrodynamic AMS fabrics can be problematic when there are insufficient independent evidence of these processes (e.g. fracture orientations or bedforms). Preliminary experimental work by Heij et al. (2018) on compacted illite and quartz mixtures suggest that vertical axis rotation of clays is possible at low confining pressures and therefore brings the preservation potential of current-induced AMS fabrics into question. Diamagnetic framework mineral reorganization during incipient compaction can alter primary depositional clay orientations when framework minerals are in high abundance (40-80%) (Heij et al., 2018). Additional experimental work is required to test the stability of depositional clay orientations during compaction and understand the criterion for their preservation.

The AMS lineation observed at room temperature (RT) remains essentially unchanged at low temperature (LT) (Figure 10A, 10G), however, several anomalously oriented AMS tensors exhibit substantial changes from RT to LT. We attribute these changes to an increased contribution from ferrimagnetic minerals based on the behavior observed in the  $K/K_0$  vs. temperature plot (E.g. Figure 10F). Furthermore, increased ferrimagnetic contributions tend to coincide with elevated NRM intensities, especially in the Norwood member (Figure 5, 10F). Changes in scalar AMS

parameters from RT to LT can reflect the presence of phyllosilicates and clay subfabrics (Pares and van der Pluijm, 2002). Several specimens exhibit an increase in Pj and the AMS ellipsoid remains oblate, both of which are consistent with a phyllosilicate dominated AMS fabric (e.g. Biedermann et al., 2014). Along with correlations among  $k_{lf}$ , Fe and Al, AMS fabrics are dominantly carried by iron-rich clays. Transitions from oblate to prolate AMS ellipsoids are also observed and could be indicative of increased Fe-bearing carbonates. Schmidt et al. (2007) report a change from oblate to prolate AMS in calcite, magnesite and dolomite due to high-Fe concentrations at 77K. In addition to ferrimagnetic minerals causing anomalous fabrics, paramagnetic carbonates likely contribute to some of the anomalous AMS directions.

#### ***Origin of exotic minerals in the Antrim – hydrothermal or extrabasinal?***

Minerals such as baroque dolomite and associated stable isotopic compositions are often considered incontrovertible forms of evidence for hydrothermal activity (e.g. Qing and Mountjoy, 1994; Machel and Lonnee, 2002) (Figure 14), however, given the regional geology, it is worth considering whether a subset of the aforementioned hydrothermal minerals are in fact detrital. A case can be made that monazite and chalcopyrite were sourced from the Michigan peninsula which host significant monazite-bearing and copper-bearing Proterozoic rocks (Figure 1). Monazite occurs in economic quantities in the Paleoproterozoic Goodrich quartz and chalcopyrite is reported in a variety of pre-Devonian rocks within the Michigan peninsula such as the Nonesuch Shale, Copper Harbor Formation and Portage Lake volcanics (Bornhorst and Barron, 2011). In addition to the proximity of these deposits to the Michigan basin, compelling evidence from trace-element geochemistry also suggest these minerals were detrital. Increased concentrations of copper are largely confined to the Lachine (Group 1) and part of the Paxton (Group 2) member (Figure 13) (also confirmed by SEM analysis). These groups also contain the highest concentrations of Zr

which is a robust indicator of terrestrial provenance (e.g. Tribovillard et al., 2006). Group 1 could indicate a mixed quartzofeldspathic/volcanic origin whereas Group 2 could correspond to a dominantly quartzofeldspathic source (Figure 13). Textural evidence for a detrital origin of chalcopyrite and monazite are mixed. For example, these minerals are often accompanied by rutile, a common detrital constituent and often occur within by clasts (Figure 12G, 12H). Counter-evidence to a detrital origin include the well-defined crystal habits observed and the relatively large crystal sizes which show no evidence of transport particularly among certain chalcopyrite grains. If monazite and chalcopyrite are in fact detrital, it ties in fairly well with the transition from Catskill prodeltaic influx in the lower Antrim to a more westerly/north westerly prodeltaic input in the Upper Antrim. Chalcopyrite and monazite have higher densities relative to most detrital minerals therefore, a high energy transport mechanism must be invoked to support a detrital origin. Gutschick and Sandberg (1991) report upper Antrim/Ellsworth turbidite complexes extending far into the basin which could have been responsible for transporting these minerals into the Michigan Basin. A possible implication of establishing the origin of these minerals would be furthering our understanding of the Michigan Peninsula. If these minerals are detrital, it would indicate that Proterozoic rocks were exposed during the Late Devonian which could improve our understanding of the structural evolution of the Michigan Peninsula.

## **CONCLUSIONS**

Data from this study are consistent with a growing body of evidence for significant thermochemical activity in midcontinent North America during the late Paleozoic and the Mesozoic (McCabe and Elmore, 1989; Lu et al., 1990; Roberts and Elmore, 2017). Despite having undergone relatively quiescent tectonic episodes relative to other sedimentary basins in North America,

complex thermochemical activity took place in the Michigan basin. The following main conclusions can be drawn from this study:

1. Remagnetizations (HC) carried by SD magnetite occurred during the late Paleozoic and are most likely a result of hydrothermal fluids. This interpretation is buttressed by petrographic and isotopic evidence. Geographical variability of paleomagnetic ages and their timing relate to previous radiometric dating of Ordovician rocks (Girard and Barnes, 1991) and may indicate a complex paleoplumbing network in the Michigan basin.
2. A younger, widespread magnetization residing in PSD/MD magnetite occurred predominately during the Mesozoic. Petrographic evidence suggests this magnetization results from oxidation of metastable iron sulfides and the age coincides with regional uplift and hydrocarbon migration. Additional hypotheses should be explored to explain the nature of this magnetization (i.e TVRM).
3. AMS fabrics are predominantly carried by paramagnetic Fe-rich clays. The lineation observed in AMS data are consistent with hydrodynamic forces or subtle tectonic shortening.
4. A case can be made that chalcopyrite and monazite in the Antrim were sourced from the Northern Michigan Peninsula although a hydrothermal origin cannot be ruled out. It is also possible that populations of detrital chalcopyrite and monazite grains exist along with neofomed grains that formed during hydrothermal activity. Radiometric dating on monazite grains could provide valuable insight into this conundrum.

This study demonstrates that the integration of paleomagnetism, rock magnetism and geochemistry have wide reaching implications that can serve to better define the burial, tectonic

and depositional history of shales. The differences between thermogenic and biogenically gas systems require additional work to understand any associated magnetic and diagenetic mineral authigenesis.

## Chapter 4 Figures

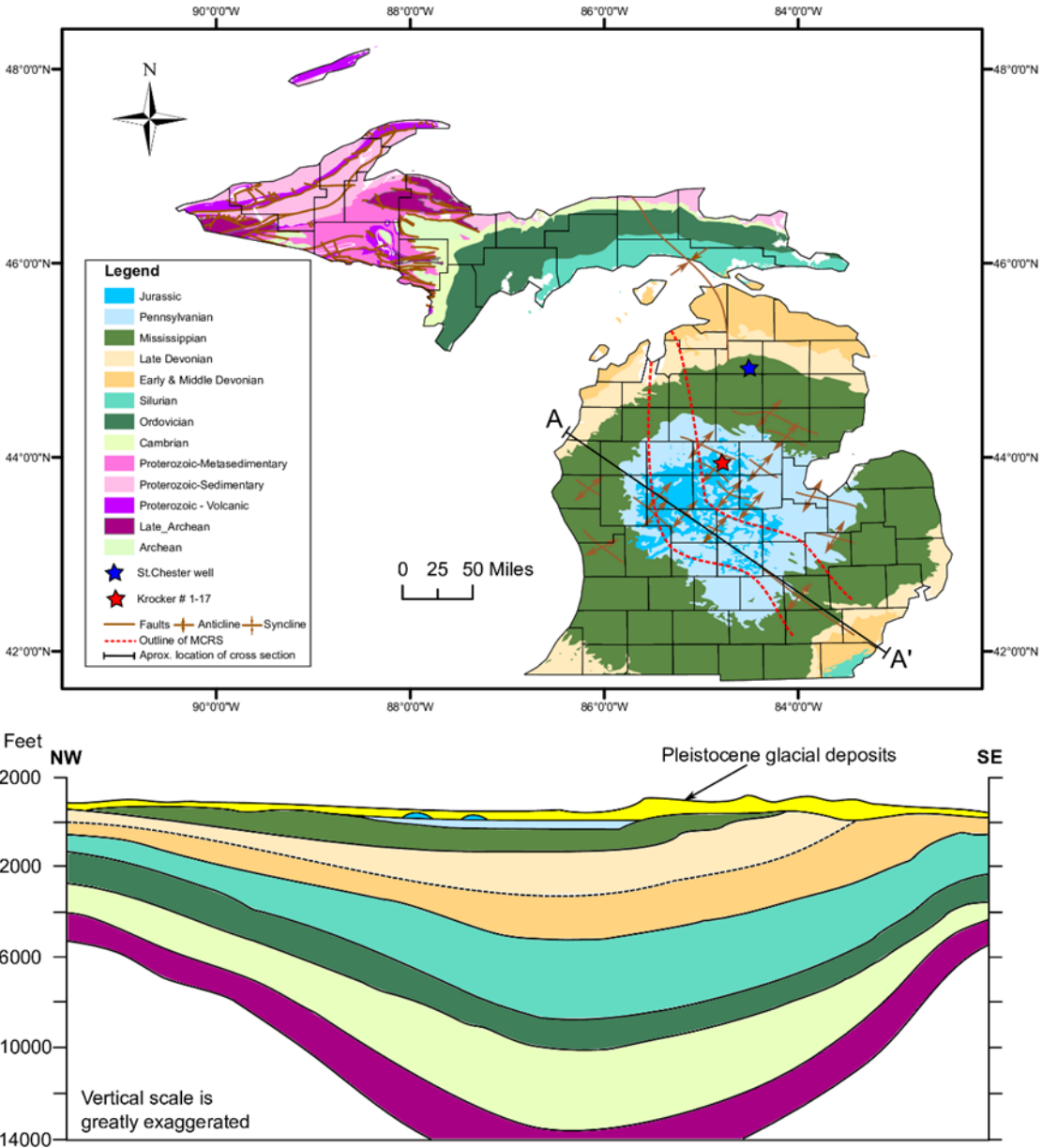


**Figure 1.** Geologic Map of Michigan modified from Dicken et al. (2004) and East et al. (2005). Schematic cross-section modified from Ma et al. (2009). Core locations denoted by stars. MCRS = Midcontinent rift system

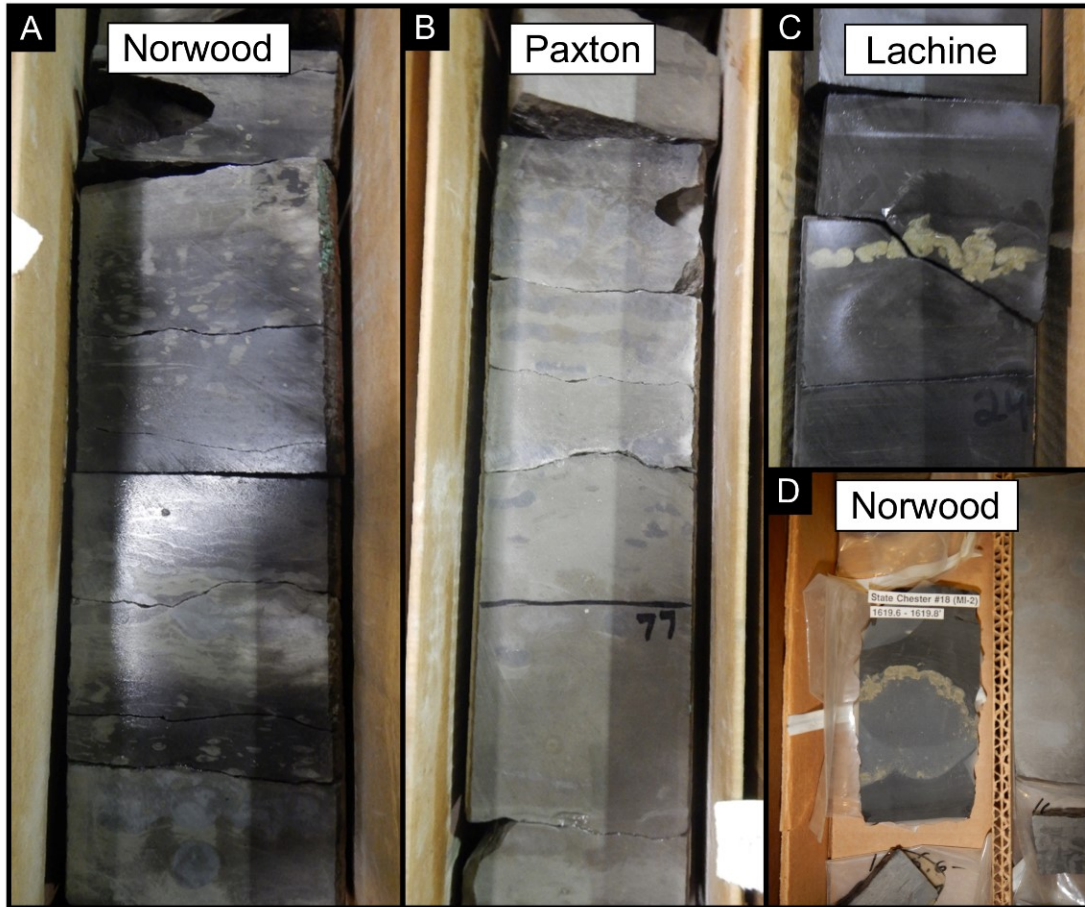


**Figure 2.** Representative lithofacies from each member in the Krocker core (A) – Norwood (B) – Paxton and (C) – Lachine. Similar facies characteristics are observed in the St. Chester core. (D) Carbonate concretion with pyritized margin in the St. Chester core.

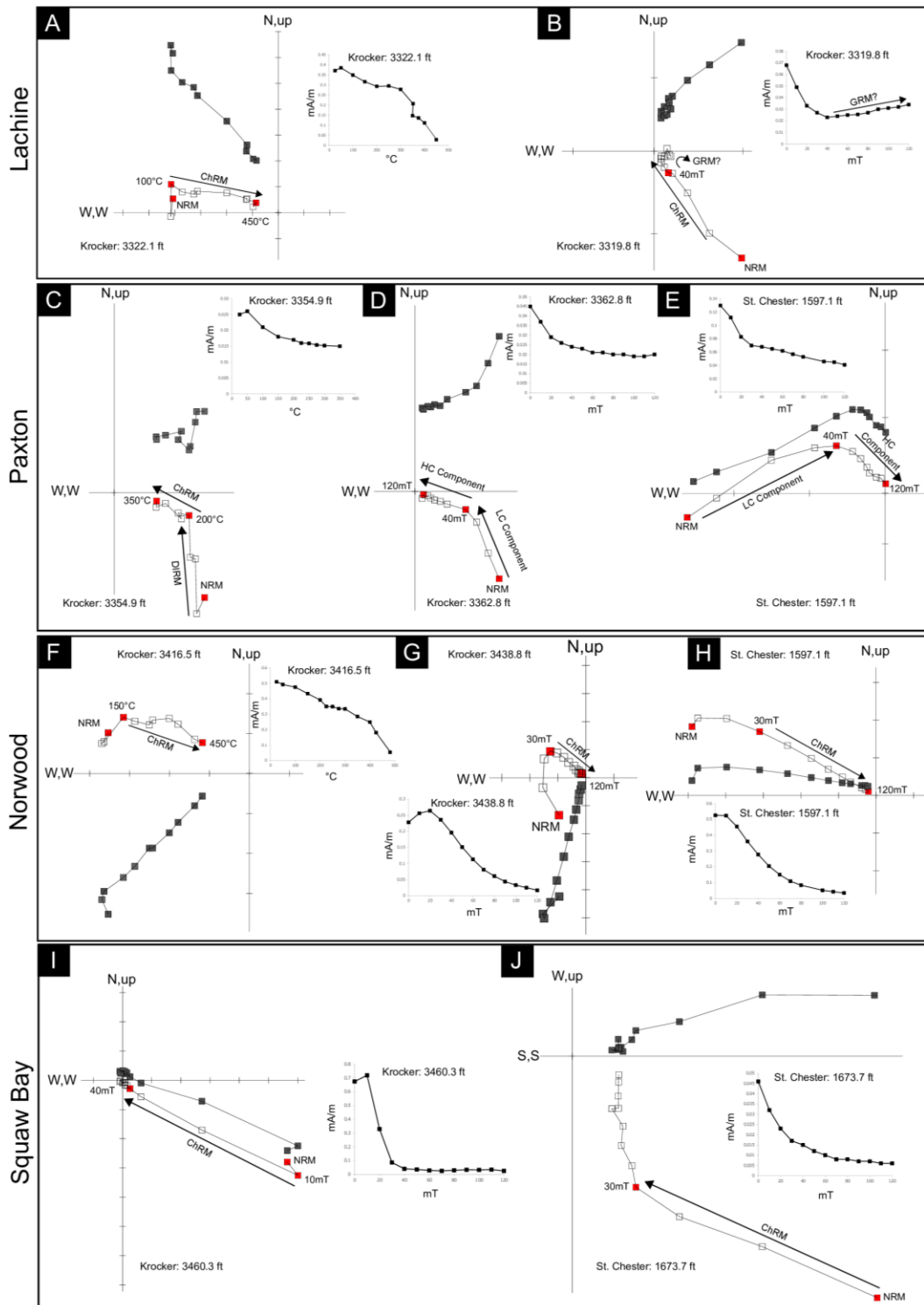


**Figure 3.** Representative Zijderveld diagrams and associated demagnetization curves from the Lachine, Paxton, Norwood and Squaw Bay. Note HC components only residing with Paxton and Norwood members. Stable LC components reside in the Lachine and Squaw Bay with the exception of one stable thermal demagnetization experiment from a Lachine specimen.

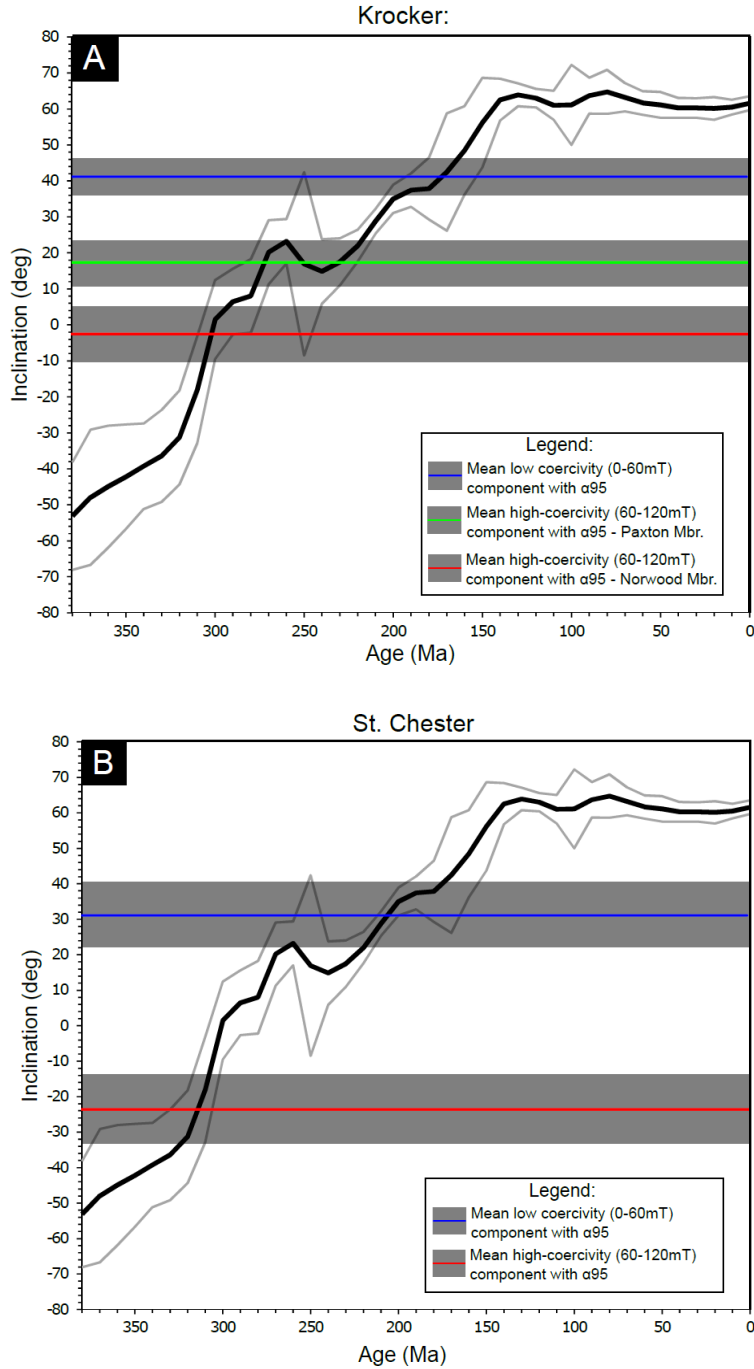


**Figure 4 .** Inclination only plots derived from the North American apparent polar wander path (Torsvik et al., 2012). (A) Mean inclinations with  $\alpha_{95}$  for various components – Krocker core. (B) Mean inclinations with  $\alpha_{95}$  for various components – St. Chester core. Solid black line indicates mean inclination and light-gray lines denote its  $\alpha_{95}$ .

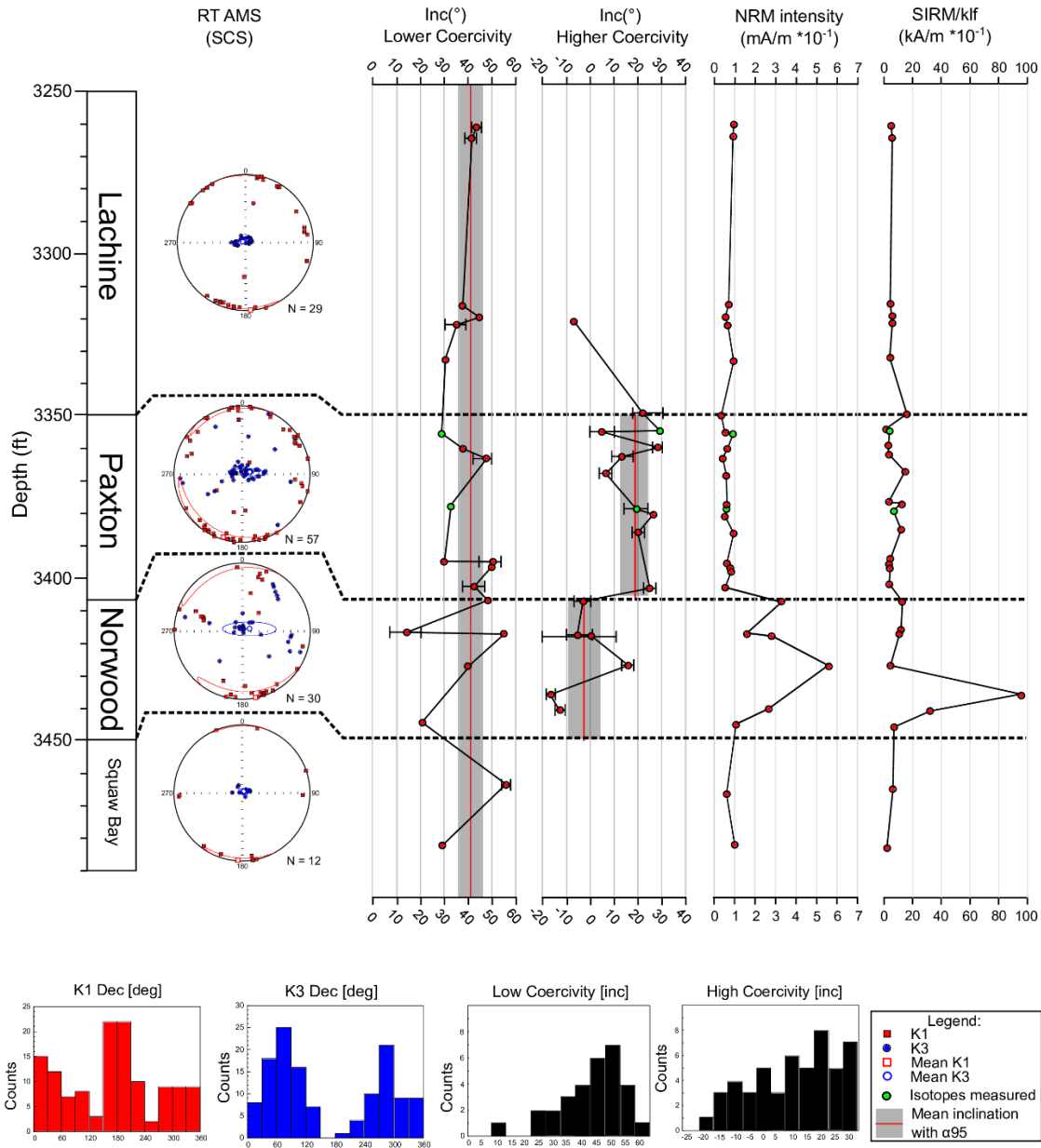


**Figure 5.** From left to right. AMS equal-area stereonet in specimen coordinate system and confidence ellipses for K1 and K3 tensors. LC and HC coercivity data with range of values per sampling depth indicated by error bars and mean inclination depicted by solid red line with  $\alpha_{95}$ . If no error bars are present, error bars were too small to plot. NRM and SIRM values, error bars are too small to be depicted. Bottom – from left to right, frequency distribution histograms for K1, K3, LC and HC components. Bottom left – legend.

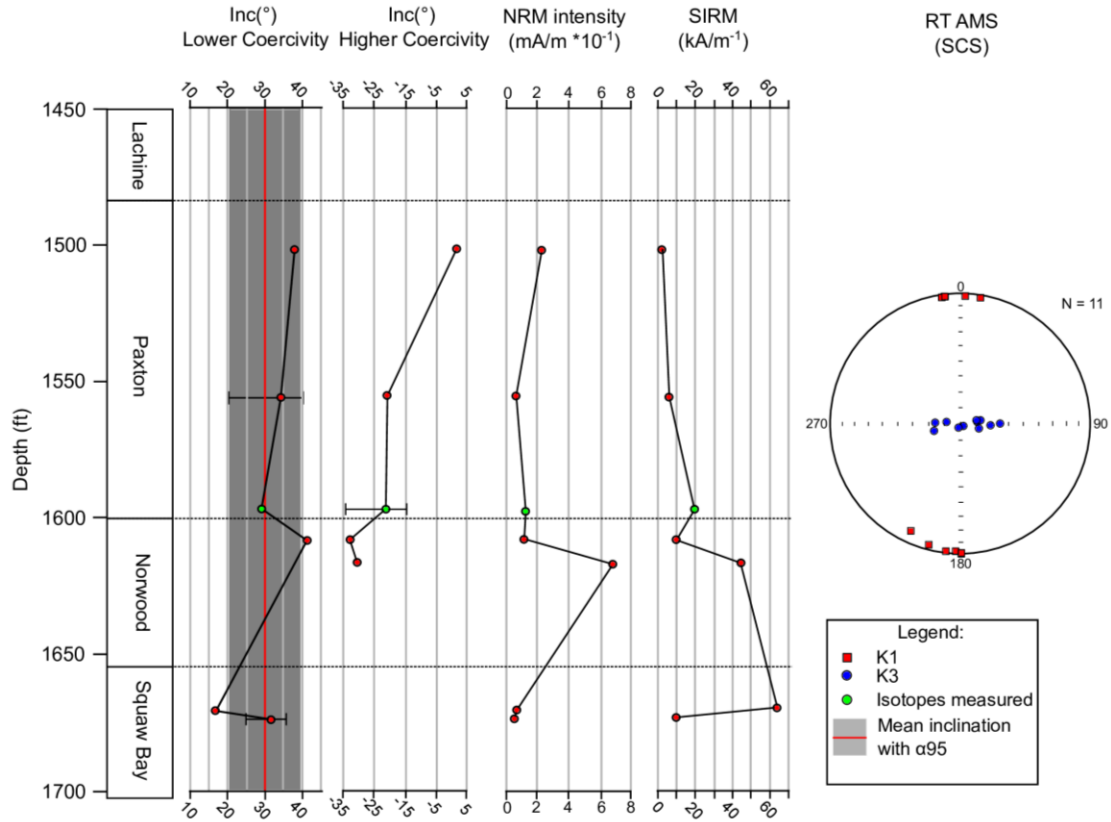


**Figure 6.** From left to right. LC coercivity and HC coercivity data with range of values per sampling depth indicated by error bars. If no error bars are present, only one specimen was measured or error bars were too small to plot. Mean inclination depicted by solid red line with  $\alpha_{95}$  in gray for LC components. For mean NRM and SIRM values, error bars are too small to be depicted. Far right – AMS Equal-area stereonet. Note streaked K3 tensors.

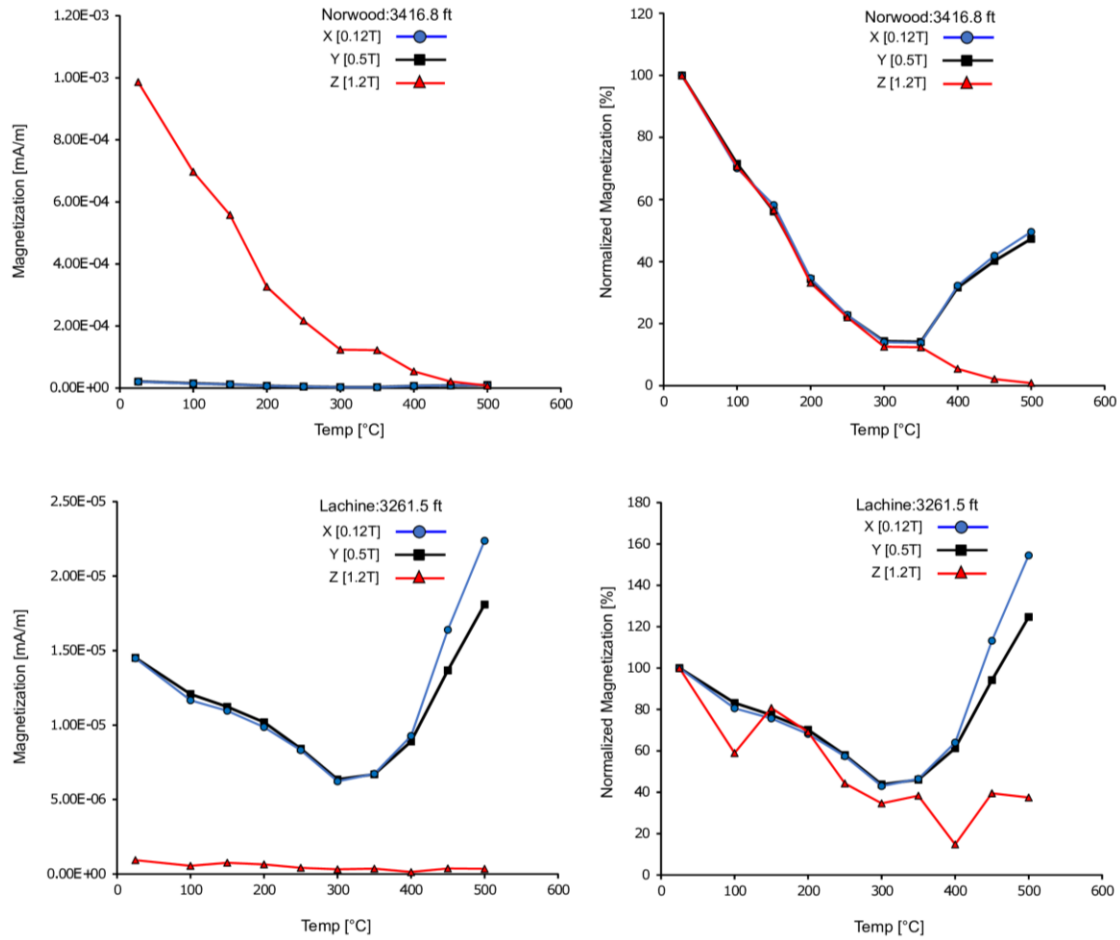


**Figure 7.** Representative triaxial thermal decay plots with low coercivity in blue, medium coercivity in black and high coercivity in red. Norwood and Paxton exhibit similar decay patterns in both cores. Similarly, Lachine and Squaw Bay display similar decay with magnetization residing mostly in low-coercivity minerals. Note sharp increase occurring at 300-350°C owing to oxidation of pyrite.

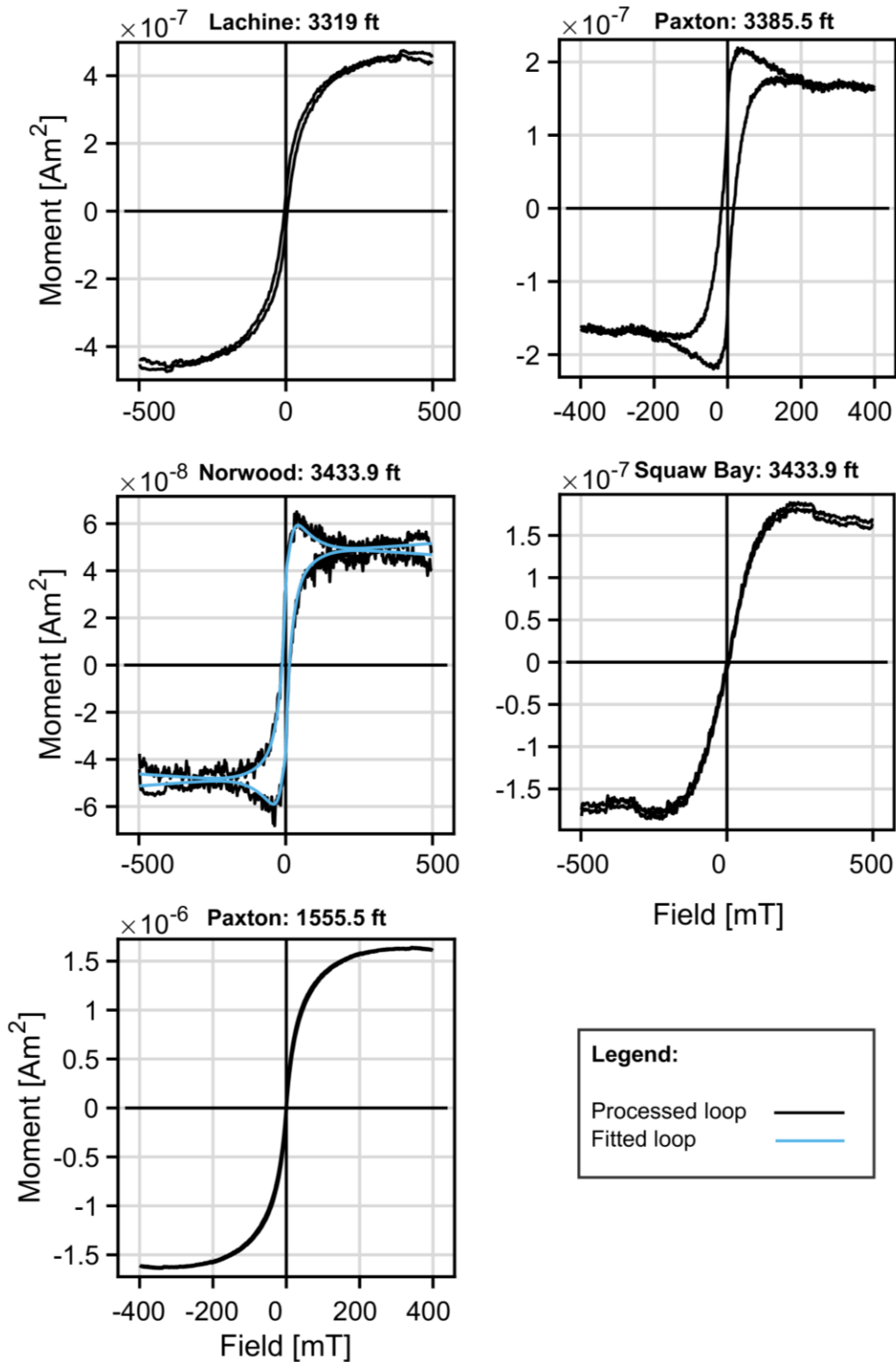


**Figure 8.** Representative processed hysteresis loops of Antrim and Squaw Bay specimens. Note wasp-waisted shapes among Norwood and Paxton specimens in the Krocker well. Pole drift artifacts occur in certain specimens however, loop closure is achieved in all specimens.

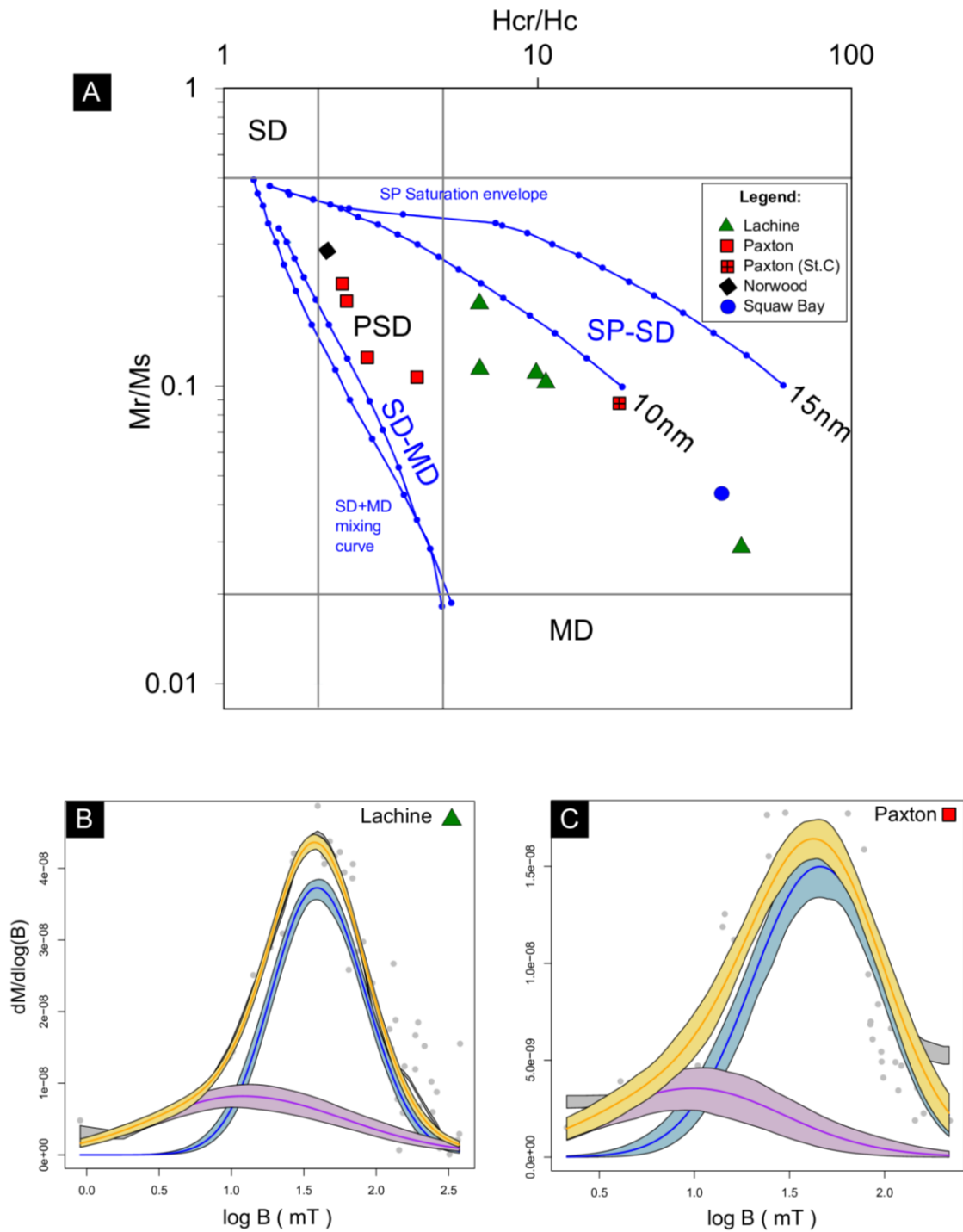


**Figure 9.** (A) Day plot of Antrim and Squaw Bay specimens. The horizontal and vertical lines delimitate the theoretical area for single (SD), pseudo-single (PSD) and multi domain (MD) magnetite grains. These lines and the mixing reference curves are from Dunlop (2002a, 2002b). (B) and (C) Representative coercivity spectrum modeling. Gray curve = spline fit of data. Blue line – high coercivity component with  $\alpha_{95}$ , purple line – low coercivity component, orange line – cumulative Gaussian curves (high + low coercivity components)

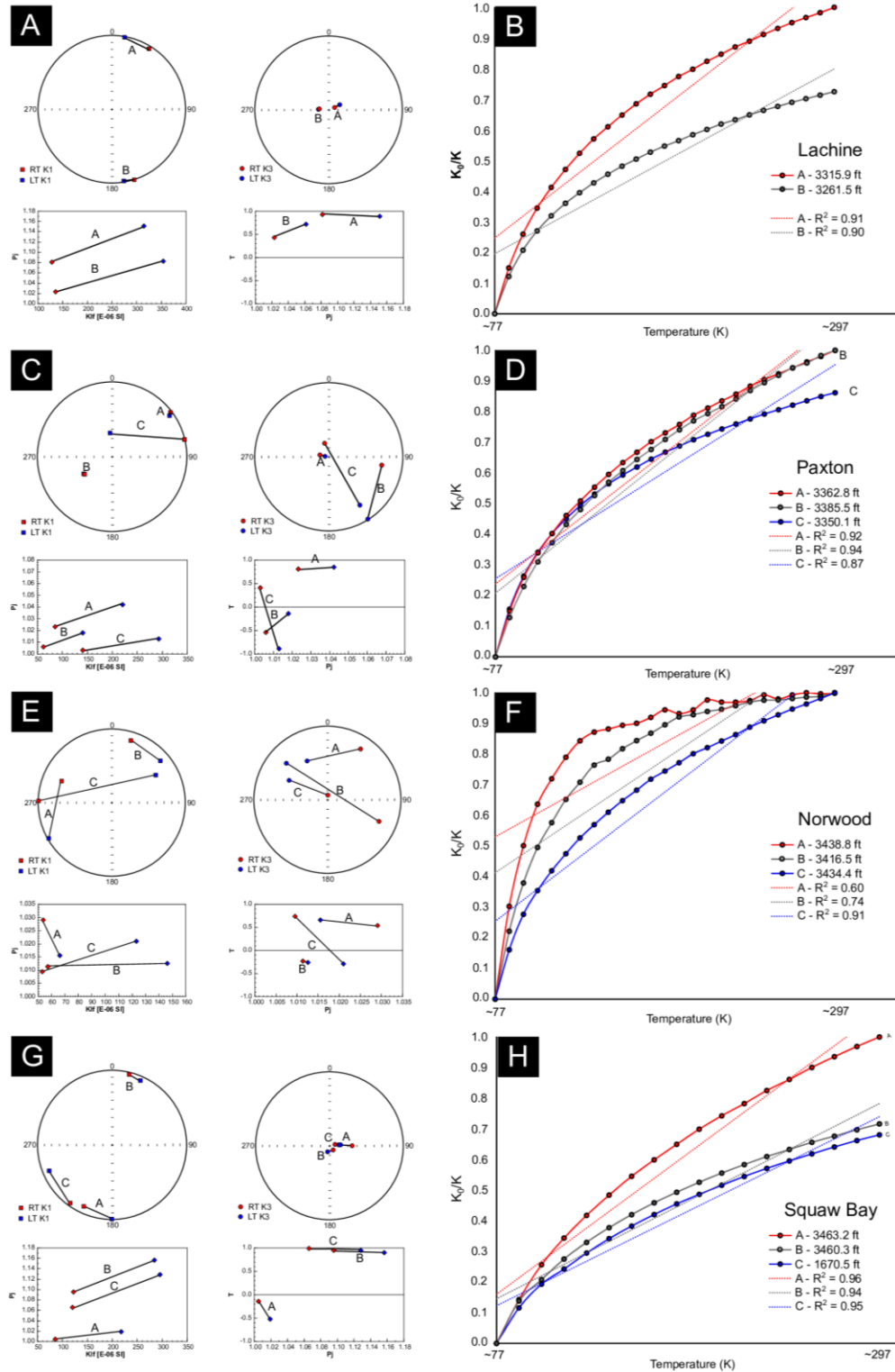


**Figure 10.** A, C, E, G: Room temperature (RT) and low temperature (LT) AMS data of representative specimens from each member with corresponding  $K_{lf}$  (bulk susceptibility) vs.  $P_j$  (corrected degree of magnetic anisotropy) and  $P_j$  vs.  $T$  (shape factor). B, D, F, H: Normalized reciprocal magnetic susceptibility ( $k_0/k$ ) vs. temperature of corresponding specimens.

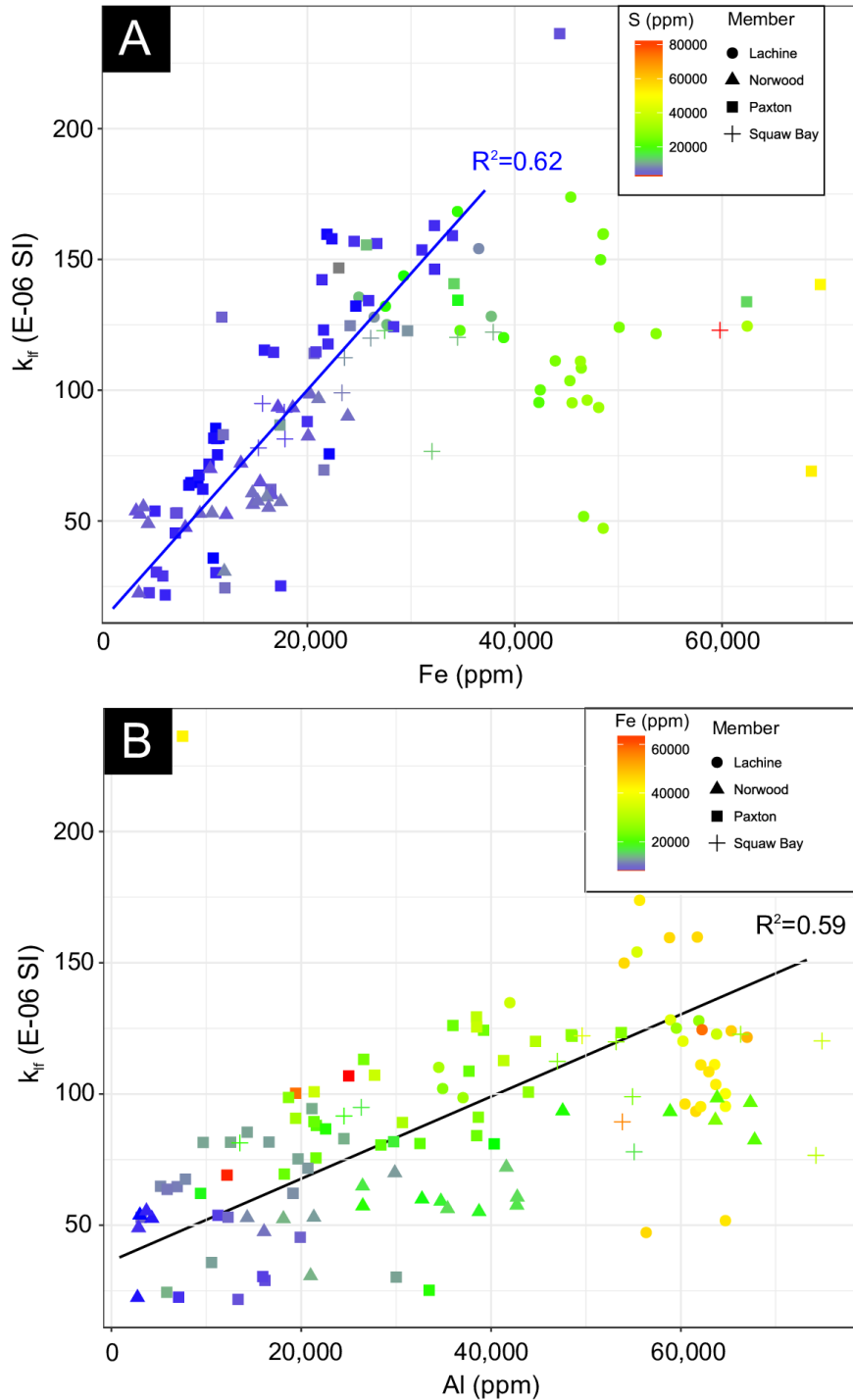


**Figure 11.** (A) Magnetic susceptibility ( $k_{if}$ ) vs. Fe cross plot with data points colored by sulfur (ppm). Magnetic susceptibility controlled by iron-bearing minerals when sulfur concentrations are low. With increasing sulfur no relationship is observed particularly in the Lachine member. Perhaps iron in the Lachine is mostly bound to pyrite and chalcopyrite which have lower magnetic susceptibilities than illite. (B) Positive correlation between Al and  $k_{if}$  suggests clays control the magnetic susceptibility and its anisotropy.

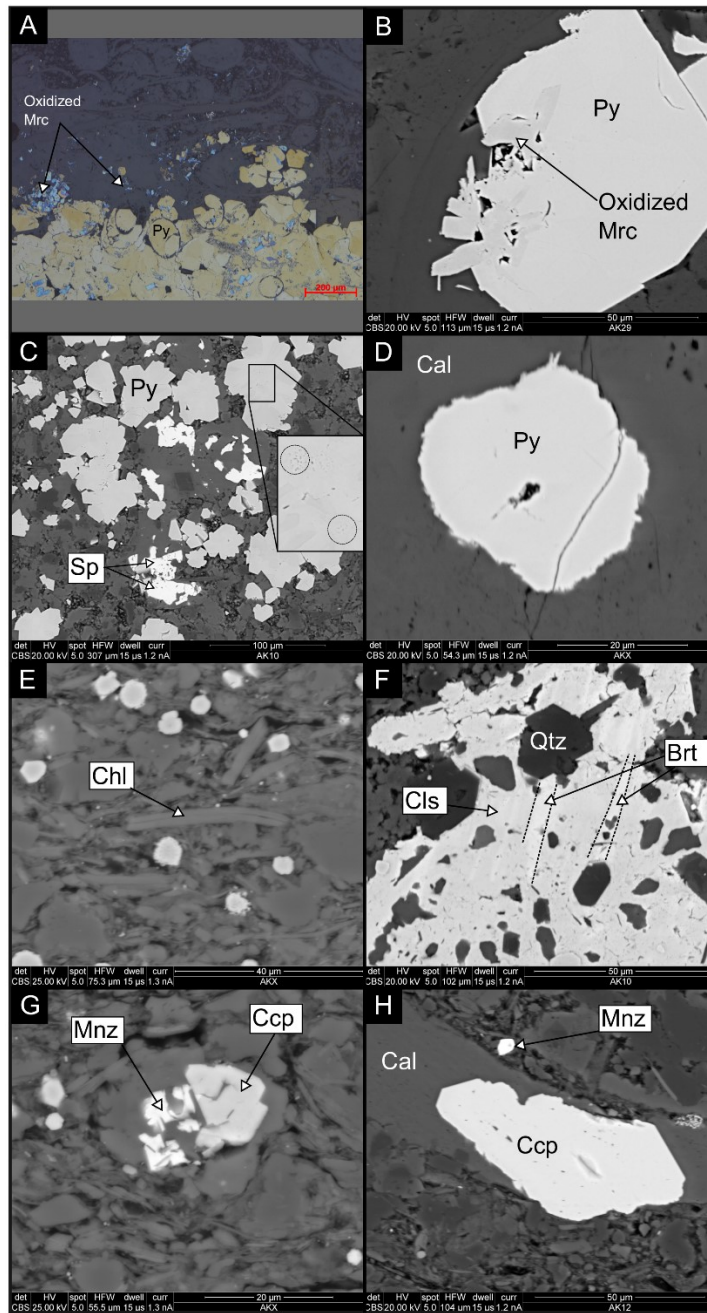


**Figure 12.** (A) Reflected light image of pyritized bed in the Paxton – Krocker core. (Py – pyrite) Note preferential oxidation of iron sulfides. (B) Cubic pyrite with oxidized intergrown marcasite in the Lachine – Krocker Core (See Appendix 1 for EDS spectra). (C) Pyrite and sphalerite (Sp) in the Paxton the note relic framboids at the nucleus of several pyrite grains – Krocker core. (D) Nickel-bearing pyrite surrounded by calcite (Ca) in the Paxton – St. Chester Core. (E) Siliceous mudrock with chlorite (Chl) in the Norwood – St. Chester. (F) Patch of barite (Brt) and celestine (Cls) cement with euhedral and double terminated quartz (Qtz) in the Paxton – Krocker core. (G) Monazite and chalcopyrite (Ccp) in the Lachine member – Krocker core. (H) Euhedral chalcopyrite grain within calcite in the Lachine member – Krocker core.

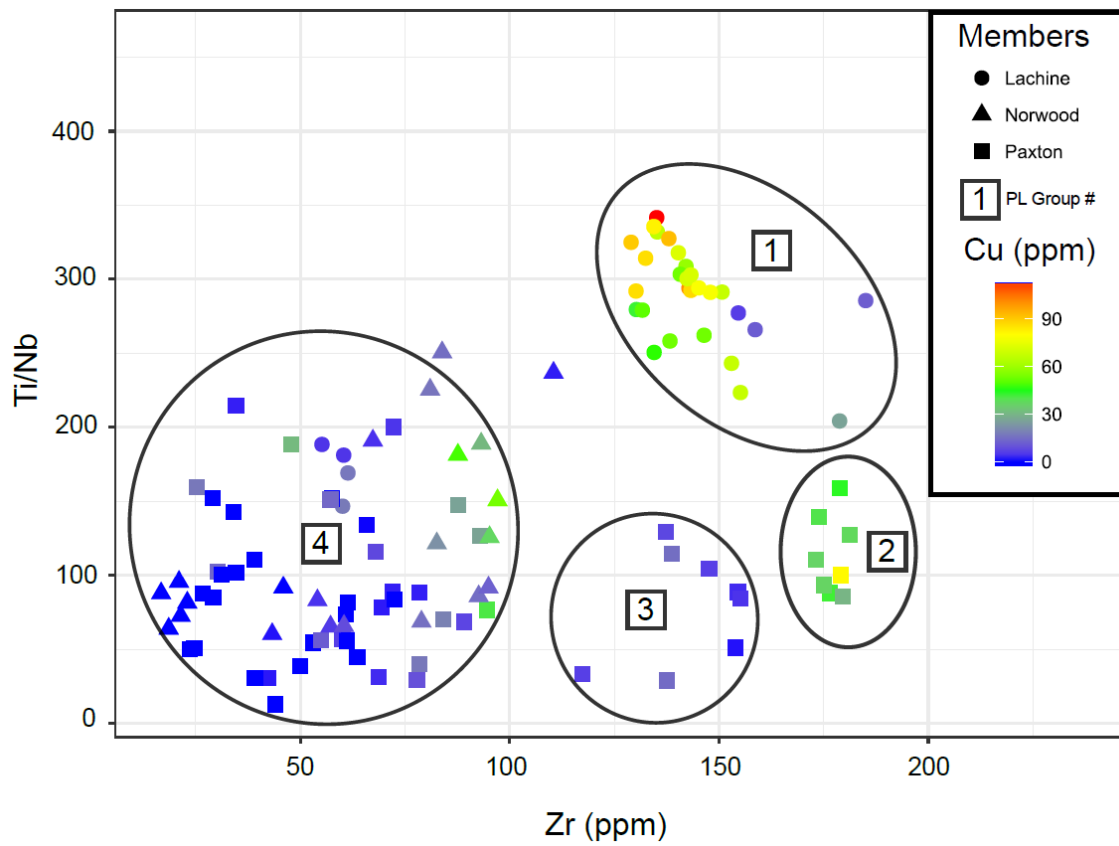


**Figure 13.** Ti/Nb vs Zr plot with data points colored by their copper concentration. Group 1 - 4 delimited by ellipses

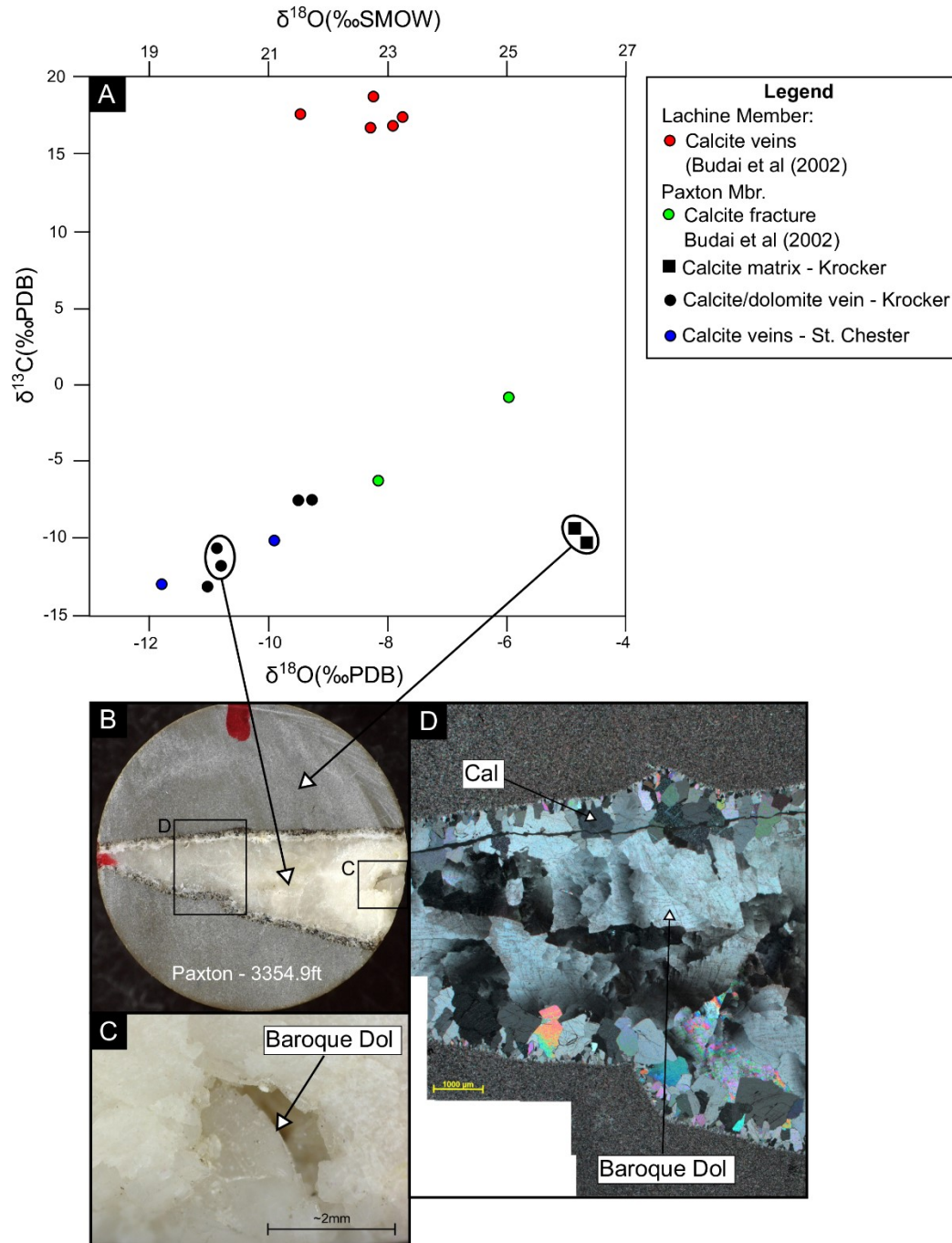


**Figure 14.** (A) Carbon and oxygen stable isotope data from this study and from Budai et al. (2002). Vein specimens display depleted  $\delta^{18}\text{O}$  whereas matrix specimens show more standard values. Budai et al. (2002) attributes high  $\delta^{13}\text{C}$  values to bacterial methanogenesis whereas data from this study indicate abiotic methane oxidation (Budai et al., 2002). (B) Sampling sites for isotopic analysis. (C) Vuggy porosity in fracture with curved crystal habit indicative of baroque dolomite. Cross polar photomicrograph of vein fill with calcite (Cal) and coarsely crystalline mosaics of anhedral to subhedral baroque dolomite with undulose extinction

**Chapter 4 Tables**

Well	Formations/Member(s)	Component	n	I (°)	$\kappa$	$\alpha_{63}$	$\alpha_{95}$	Mean Age (Ma)
Krocker	Antrim & SB	LC	30	40.95	26.68	15.69	5.18	170±25
Krocker	Paxton	HC	26	19.2	21.45	17.51	6.27	230-270±10
Krocker	Norwood	HC	15	-2.48	19.7	18.28	8.83	305±10
St. Chester	Paxton, Norwood & SB	LC	8	31.42	41.34	12.59	8.72	315±10
St. Chester	Paxton & Norwood	HC	10	-22.82	26.84	15.65	9.5	205±10

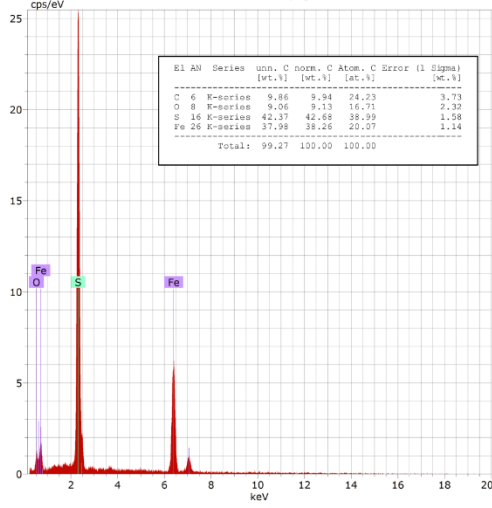
**Table 1.** Statistics for magnetic components. SB – Squaw Bay, LC – lower coercivity component, HC – higher coercivity component

Specimen	Component	Bh(mT)	Bh.sd	DP	DP.sd	OC.mean	OC.sd	EC.mean	EC.sd
Norwood [Krocker]	1	44.74	1.04	2.25	1.05	0.76	0.05	0.76	0.05
	2	9.55	1.16	3.09	1.13	0.24	0.11	0.24	0.11
Paxton [Krocker]	1	32.82	1.09	2.37	1.09	0.87	0.16	0.77	0.13
	2	8.20	1.21	2.16	1.14	0.13	0.08	0.23	0.14
Paxton [Krocker]	1	40.81	1.04	1.88	1.03	0.39	0.06	0.39	0.05
	2	23.09	1.06	3.93	1.06	0.61	0.07	0.61	0.06
Paxton [Krocker]	1	37.09	1.11	2.20	1.10	0.75	0.14	0.65	0.10
	2	11.65	1.24	2.70	1.14	0.25	0.10	0.35	0.15
Paxton [Krocker]	1	40.80	1.10	2.76	1.09	0.68	0.09	0.60	0.07
	2	7.66	1.18	3.43	1.13	0.32	0.11	0.40	0.13
Lachine [Krocker]	1	40.34	1.03	2.11	1.02	0.70	0.03	0.70	0.03
	2	14.11	1.10	4.66	1.09	0.30	0.08	0.30	0.08
Paxton [St.Chester]	1	36.36	1.10	4.21	1.08	1.00	0.00	1.00	0.00

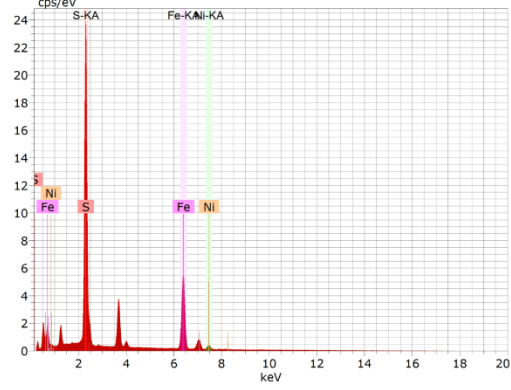
**Table 2.** Results from coercivity spectrum modeling or “unmixing”. Component 1 = HC; Component 2 = LC; Bh = mean coercivity; DP = dispersion parameter; OC = observed contribution; EC = extrapolated contribution.

# APPENDIX

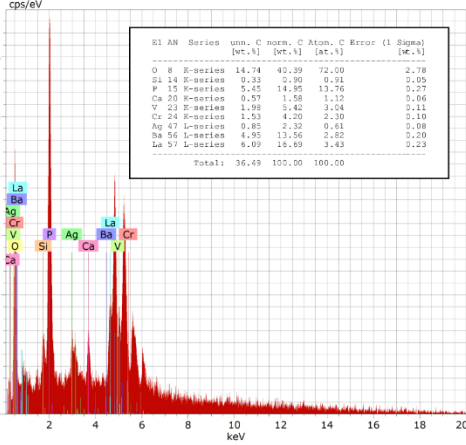
oxidized pyrite



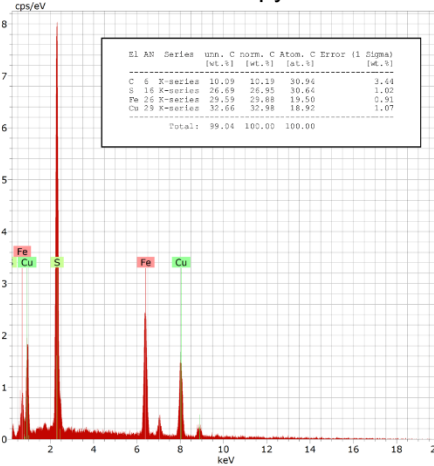
nickel-bearing pyrite



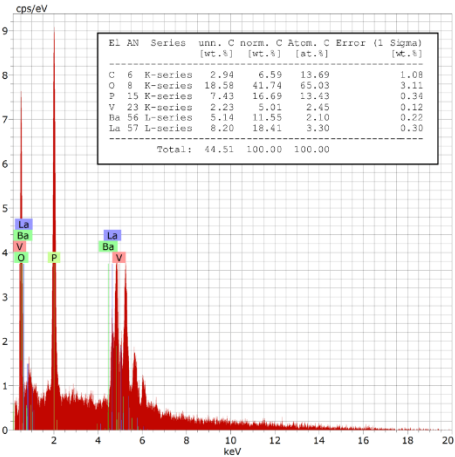
monazite



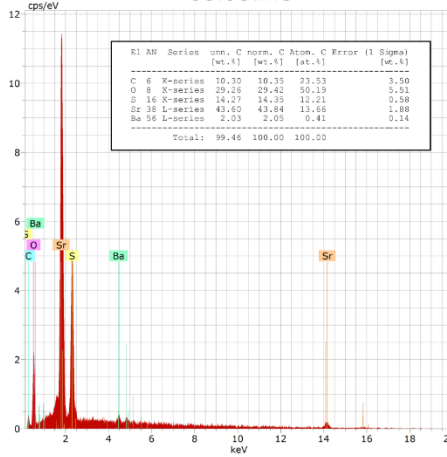
chalcopyrite



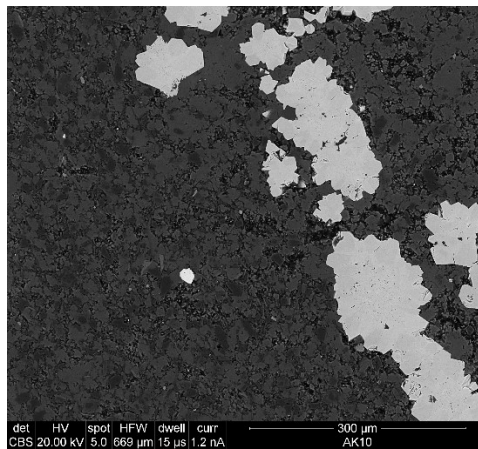
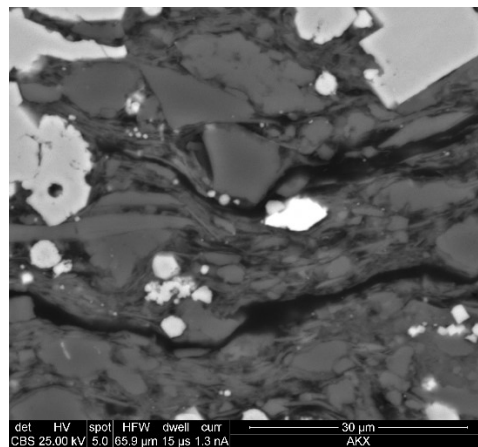
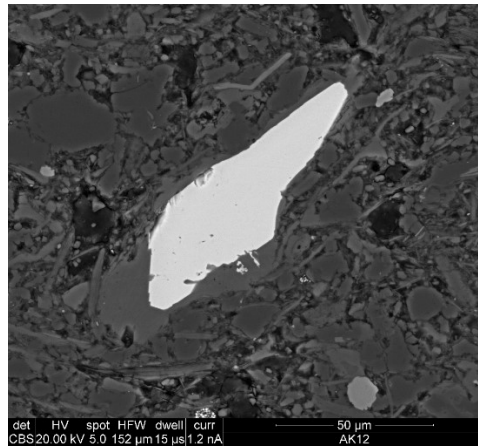
monazite



celestine



EDS Spectra for Figure 12.



(Top) Chalcopyrite grain with rutile in bottom right. (Middle) Monazite grain (center of image).

(Bottom) Oxidized pyrite. Bright grain is chalcopyrite

## REFERENCES

- Apotria TG, Kaiser CJ, Cain BA, 1994, Fracturing and stress history of the Devonian Antrim Shale, Michigan Basin. In: Rock Mechanics (eds Nelson, PP, Lauback, SE), pp. 809–16. Balkema, Rotterdam.
- Arason, P. and Levi, S., 2010, Maximum likelihood solution for inclination-only data in paleomagnetism. *Geophysical Journal International*, 182(2), pp.753-771.
- Berner, Z.A., Puchelt, H., Nöltner, T. and Kramar, U.T.Z., 2013, Pyrite geochemistry in the Toarcian Posidonia Shale of south-west Germany: Evidence for contrasting trace-element patterns of diagenetic and syngenetic pyrites. *Sedimentology*, 60(2), pp.548-573.
- Biedermann, A.R., Koch, C.B., Lorenz, W.E. and Hirt, A.M., 2014, Low-temperature magnetic anisotropy in micas and chlorite. *Tectonophysics*, 629, pp.63-74.
- Bonjour, J. L., and Dabard, M. P., 1991, Ti/Nb ratios of clastic terrigenous sediments used as an indicator of provenance. *Chemical Geology*, 91(3), 257-267.
- Bornhorst, T.J. and Barron, R.J., 2011, Copper deposits of the western Upper Peninsula of Michigan. *Geological Society of America Field Guide*, 24, pp.83-99.
- Budai, J.M., Martini, A.M., Walter, L.M. and Ku, T.C.W., 2002, Fracture-fill calcite as a record of microbial methanogenesis and fluid migration: a case study from the Devonian Antrim Shale, Michigan Basin. *Geofluids*, 2(3), pp.163-183.
- Campbell, F.A. and Ethier, V.G., 1984, Nickel and cobalt in pyrrhotite and pyrite from the Faro and Sullivan orebodies. *The Canadian Mineralogist*, 22(3), pp.503-506.
- Chadima, M., and Jelinék, V., 2009, Anisoft 4.2: anisotropy data browser for windows. Agico. Inc, Brno. <https://www.agico.com/text/software/anisoft/anisoft.php>
- Chang, S.B.R., Kirschvink, J.L. and Stolz, J.F., 1987, Biogenic magnetite as a primary remanence carrier in limestone deposits. *Physics of the Earth and Planetary Interiors*, 46(1-3), pp.289-303.
- Coplen, T.B., 2011, Guidelines and recommended terms for expression of stable-isotope-ratio and gas-ratio measurement results. *Rapid communications in mass spectrometry*, 25(17), pp.2538-2560.
- Craddock, J.P. and Pluijm, B.A.V.D., 1989, Late Paleozoic deformation of the cratonic carbonate cover of eastern North America. *Geology*, 17(5), pp.416-419.
- Crowley, K.D., 1991, Thermal history of Michigan Basin and Southern Canadian Shield from apatite fission track analysis. *Journal of Geophysical Research: Solid Earth*, 96(B1), pp.697-711.

- Coniglio, M., Sherlock, R., Williams-Jones, A.E., Middleton, K., Frape, S.K., Purser, B., Tucker, M. and Zenger, D., 1994, Burial and hydrothermal diagenesis of Ordovician carbonates from the Michigan Basin, Ontario, Canada. *Dolomites—A volume in honour of Dolomieu*. B. Purser, M. Tucker and D. Zenger (eds.). International Association of Sedimentologists, Special Publication, 21, pp.231-254.
- Curran, B.C. and Hurley, N.F., 1992, Geology of the Devonian Dundee Reservoir, West Branch Field, Michigan (1). *AAPG Bulletin*, 76(9), pp.1363-1383.
- Dellapenna, T. M., 1991, Sedimentological, Structural, and Organic Geochemical controls on Natural Gas occurrence in the Antrim Formation in Otsego County, Michigan: unpublished PhD dissertation, Western Michigan University, pg. 90
- Dicken, S.W.N.C.L. and Mueller, M.P.F.J.A., 2004, The Upper Midwest States: Minnesota, Wisconsin, Michigan, Illinois and Indiana-The State of Wisconsin. USGS Issue 2004-1355.
- Dunlop, D. J., 2002a, Theory and application of the Day plot (Mrs/Ms versus Hcr/Hc): 1. Theoretical curves and tests using titanomagnetite data, *J. Geophys. Res.*, 107(B3), 2056, doi:10.1029/2001JB000486.
- Dunlop, D. J., 2002b, Theory and application of the Day plot (Mrs/Ms versus Hcr/Hc): 2. Application to data for rocks, sediments, and soils, *J. Geophys. Res.*, 107(B3), 2057, doi:10.1029/2001JB000487.
- East, J.A., Swezey, C.S., Repetski, J.E., Hayba, D.O., 2012, Thermal maturity map of Devonian Shale in the Illinois, Michigan, and Appalachian Basins of North America. U. S. Geological Survey Scientific Investigations Map 3214. (1 pp.).
- Ellwood, B.B. and Ledbetter, M.T., 1979, Paleocurrent indicators in deep-sea sediment. *Science*, 203(4387), pp.1335-1337.
- Elmore, R.D. and Leach, M.C., 1990, Remagnetization of the Rush Springs Formation, Cement, Oklahoma: Implications for dating hydrocarbon migration and aeromagnetic exploration. *Geology*, 18(2), pp.124-127.
- Formolo, M.J., Riedinger, N. and Gill, B.C., 2014, Geochemical evidence for euxinia during the Late Devonian extinction events in the Michigan Basin (USA). *Palaeogeography, palaeoclimatology, palaeoecology*, 414, pp.146-154.
- Fisher, J.H., Barratt, M.W., Droste, J.B. and Shaver, R.H., 1988, Michigan basin. *The Geology of North America*, 2, pp.361-382.
- Girard, J.P. and Barnes, D.A., 1995, Illitization and paleothermal regimes in the Middle Ordovician St. Peter Sandstone, central Michigan basin: K-Ar, oxygen isotope, and fluid inclusion data. *AAPG bulletin*, 79(1), pp.49-69.
- Gutschick, R.C., 1987, Devonian shelf-basin, Michigan Basin, Alpena, Michigan. North-Central

- Section of the Geological Society of America, Boulder, Colorado, Geological Society of America, Centennial Field Guide, 3, pp.297-302.
- Gutschick, R.C. and Sandberg, C.A., 1991, Late Devonian history of Michigan basin. Early sedimentary evolution of the Michigan basin: Geological Society of America Special Paper, 256, pp.181-202.
- Hirt, A., A. Banin and A. Gehring, 1993, Thermal generation of ferromagnetic minerals from iron-enriched smectites. *Geophys. J. Int.*, 115: 1161–1168.
- Howell, P.D. and Pluijm, B.A.V.D., 1990, Early history of the Michigan basin: Subsidence and Appalachian tectonics. *Geology*, 18(12), pp.1195-1198.
- Hunt, J.M., 1990, Generation and migration of petroleum from abnormally pressured fluid compartments (1). *AAPG bulletin*, 74(1), pp.1-12.
- Issachar, R., Levi, T., Lyakhovsky, V., Marco, S. and Weinberger, R., 2016, Improving the method of low-temperature anisotropy of magnetic susceptibility (LT-AMS) measurements in air. *Geochemistry, Geophysics, Geosystems*, 17(7), pp.2940-2950.
- Jackson, M. and Solheid, P., 2010, On the quantitative analysis and evaluation of magnetic hysteresis data. *Geochemistry, Geophysics, Geosystems*, 11(4).
- Jelinek, V., 1981, Characterization of the magnetic fabric of rocks. *Tectonophysics*, 79(3-4), pp.T63-T67.
- Katz, B., Elmore, R.D., Cogoini, M., Engel, M.H. and Ferry, S., 2000, Associations between burial diagenesis of smectite, chemical remagnetization, and magnetite authigenesis in the Vocontian trough, SE France. *Journal of Geophysical Research: Solid Earth*, 105(B1), pp.851-868.
- Kennedy, M.J., Pevear, D.R. and Hill, R.J., 2002, Mineral surface control of organic carbon in black shale. *Science*, 295(5555), pp.657-660.
- Kesler, S.E. and Jones, L.M., 1980, Sulfur-and strontium-isotopic geochemistry of celestite, barite and gypsum from the Mesozoic basins of northeastern Mexico. *Chemical Geology*, 31, pp.211-224.
- Kilgore, B. and Elmore, R.D., 1989, A study of the relationship between hydrocarbon migration and the precipitation of authigenic magnetic minerals in the Triassic Chugwater Formation, southern Montana. *Geological Society of America Bulletin*, 101(10), pp.1280-1288.
- Klein, G.D. and Hsui, A.T., 1987, Origin of cratonic basins. *Geology*, 15(12), pp.1094-1098.
- Liu, B., Saito, Y., Yamazaki, T., Abdeldayem, A., Oda, H., Hori, K. and Zhao, Q., 2001, Paleocurrent analysis for the Late Pleistocene–Holocene incised-valley fill of the Yangtze delta, China by using anisotropy of magnetic susceptibility data. *Marine Geology*, 176(1-4), pp.175-189.

- Luczaj, J.A., Harrison III, W.B. and Williams, N.S., 2006, Fractured hydrothermal dolomite reservoirs in the Devonian Dundee Formation of the central Michigan Basin. *AAPG bulletin*, 90(11), pp.1787-1801.
- Ma, L., Castro, M.C. and Hall, C.M., 2009, Atmospheric noble gas signatures in deep Michigan Basin brines as indicators of a past thermal event. *Earth and Planetary Science Letters*, 277(1-2), pp.137-147.
- Machel, H.G. and Lonnee, J., 2002, Hydrothermal dolomite—A product of poor definition and imagination. *Sedimentary geology*, 152(3-4), pp.163-171.
- Magara, K., 1978, *Compaction and fluid migration*. Dev. Petrol. Sci. 9, Elsevier, New York.
- Maher, B.A., 2007, Environmental magnetism and climate change. *Contemporary Physics*, 48(5), pp.247-274.
- Manning, E.B. and Elmore, R.D., 2015, An integrated paleomagnetic, rock magnetic, and geochemical study of the Marcellus shale in the Valley and Ridge province in Pennsylvania and West Virginia. *Journal of Geophysical Research: Solid Earth*, 120(2), pp.705-724.
- Martini, A.M., Budai, J.M., Walter, L.M. and Schoell, M., 1996, Microbial generation of economic accumulations of methane within a shallow organic-rich shale. *Nature*, 383(6596), p.155.
- Martini, A.M., Walter, L.M., Budai, J.M., Ku, T.C.W., Kaiser, C.J. and Schoell, M., 1998, Genetic and temporal relations between formation waters and biogenic methane: Upper Devonian Antrim Shale, Michigan Basin, USA. *Geochimica et Cosmochimica Acta*, 62(10), pp.1699-1720.
- Matthews, D., 1983, April. The Devonian-Mississippian oil shale resource of the eastern United States. In Preprint of paper presented at 16th Oil Shale Symposium, Golden Colorado. Institute of Gas Technology, Chicago, Illinois (pp. 14-25).
- Matthews, R. D., 1993, Review and revision of the Devonian–Mississippian stratigraphy in the Michigan basin, in J. B. Roen and R. C. Kepferle, eds., *Petroleum geology of the Devonian and Mississippian black shale of eastern North America: U.S. Geological Survey Bulletin 1909*, p. D1–D85.
- Maxbauer, D.P., Feinberg, J.M. and Fox, D.L., 2016, MAX UnMix: A web application for unmixing magnetic coercivity distributions. *Computers and Geosciences*, 95, pp.140-145.
- McCabe, C. and Elmore, R.D., 1989, The occurrence and origin of late Paleozoic remagnetization in the sedimentary rocks of North America. *Reviews of Geophysics*, 27(4), pp.471-494.
- McCrea, J.M., 1950, On the isotopic chemistry of carbonates and a paleotemperature scale. *The Journal of Chemical Physics*, 18(6), pp.849-857.
- Moskowitz, B.M., Frankel, R.B. and Bazylinski, D.A., 1993, Rock magnetic criteria for the detection of biogenic magnetite. *Earth and Planetary Science Letters*, 120(3-4), pp.283-

- Over, D.J., 2002, The Frasnian/Famennian boundary in central and eastern United States. *Palaeogeography, Palaeoclimatology, Palaeoecology*, 181(1-3), pp.153-169.
- Parés, J.M. and van der Pluijm, B.A., 2002, Phyllosilicate fabric characterization by low-temperature anisotropy of magnetic susceptibility (LT-AMS). *Geophysical Research Letters*, 29(24).
- Parés, J.M., 2004, How deformed are weakly deformed mudrocks? Insights from magnetic anisotropy. Geological Society, London, Special Publications, 238(1), pp.191-203.
- Parés, J.M. and Van der Pluijm, B.A., 2004, Correlating magnetic fabrics with finite strain: Comparing results from mudrocks in the Variscan and Appalachian Orogens. *Geologica Acta: an international earth science journal*, 2(3), pp.213-220.
- Parés, J.M., Hassold, N.J.C., Rea, D.K. and Van der Pluijm, B.A., 2007, Paleocurrent directions from paleomagnetic reorientation of magnetic fabrics in deep-sea sediments at the Antarctic Peninsula Pacific margin (ODP Sites 1095, 1101). *Marine Geology*, 242(4), pp.261-269.
- Parés, J.M., 2015, Sixty years of anisotropy of magnetic susceptibility in deformed sedimentary rocks. *Frontiers in Earth Science*, 3, p.4.
- Paterson, G.A., Zhao, X., Jackson, M. and Heslop, D., 2018, Measuring, processing, and analyzing hysteresis data. *Geochemistry, Geophysics, Geosystems* 19(7), <https://doi.org/10.1029/2018GC007620>
- Peters, C. and Dekkers, M.J., 2003, Selected room temperature magnetic parameters as a function of mineralogy, concentration and grain size. *Physics and Chemistry of the Earth, Parts A/B/C*, 28(16-19), pp.659-667.
- Prouty, C.E., 1988, Fractured hydrocarbon reservoir models--Michigan Basin: Geological Association of Canada, Mineralogical Association of Canada and Canadian Society of Petroleum Geologists Annual Meeting, St. Johns, Newfoundland, Program with Abstracts, 13, p.101.
- Pullaiah, G., Irving, E., Buchan, K.L. and Dunlop, D.J., 1975, Magnetization changes caused by burial and uplift. *Earth and Planetary Science Letters*, 28(2), pp.133-143.
- Qing, H. and Mountjoy, E.W., 1994, Formation of coarsely crystalline, hydrothermal dolomite reservoirs in the Presqu'ile barrier, Western Canada sedimentary basin. *AAPG bulletin*, 78(1), pp.55-77.
- Reed, R.C., 1991, Economic geology and history of metallic minerals in the Northern Peninsula of Michigan. *Geological Society of America Special Papers*, 256, pp.13-52.
- Richter, C. and van der Pluijm, B.A., 1994, Separation of paramagnetic and ferrimagnetic

- susceptibilities using low temperature magnetic susceptibilities and comparison with high field methods. *Physics of the Earth and Planetary Interiors*, 82(2), pp.113-123.
- Roberts, J.M. and Elmore, R.D., 2017, A diagenetic study of the Woodford Shale in the southeastern Anadarko Basin, Oklahoma, USA: Evidence for hydrothermal alteration in mineralized fractures. *Interpretation*, 6(1), pp.SC1-SC13.
- Rochette, P., 1987, Magnetic susceptibility of the rock matrix related to magnetic fabric studies. *Journal of Structural Geology*, 9(8), pp.1015-1020.
- Rowe, H., Hughes, N. and Robinson, K., 2012, The quantification and application of handheld energy-dispersive x-ray fluorescence (ED-XRF) in mudrock chemostratigraphy and geochemistry. *Chemical Geology*, 324, pp.122-131.
- Rusk, B., 2012, Cathodoluminescent textures and trace elements in hydrothermal quartz. In *Quartz: Deposits, mineralogy and analytics*. Springer, Berlin, Heidelberg. (pp. 307-329).
- Saller, A.H. and Dickson, J.A.T.D., 2011, Partial dolomitization of a Pennsylvanian limestone buildup by hydrothermal fluids and its effect on reservoir quality and performance. *AAPG bulletin*, 95(10), pp.1745-1762.
- Sanford, B.V., Thompson, F.J. and McFall, G.H., 1985, Plate tectonics--a possible controlling mechanism in the development of hydrocarbon traps in southwestern Ontario. *Bulletin of Canadian Petroleum Geology*, 33(1), pp.52-71.
- Schieber, J. and Ellwood, B.B., 1988, The coincidence of macroscopic paleocurrent indicators and magnetic lineation in shales from the Precambrian Belt Basin. *Journal of Sedimentary Research*, 58(5), pp.830-835.
- Schieber, J., 1994c, Paleoflow patterns and macroscopic sedimentary features in the Late Devonian Chattanooga Shale of Tennessee; differences between the western and eastern Appalachian Basin. In: Embry, A.F., Beauchamp, B., Glass, D.J. (Eds.), *Pangea : global environments and resources: Canad. Soc. Petrol. Geol. Mem.*, vol. 17, pp. 763–772.
- Schmidt, V., Hirt, A.M., Rosselli, P. and Martín-Hernández, F., 2007, Separation of diamagnetic and paramagnetic anisotropy by high-field, low-temperature torque measurements. *Geophysical Journal International*, 168(1), pp.40-47.
- Simoneit, B.R.T., Goodfellow, W.D. and Franklin, J.M., 1992, Hydrothermal petroleum at the seafloor and organic matter alteration in sediments of Middle Valley, Northern Juan de Fuca Ridge. *Applied geochemistry*, 7(3), pp.257-264.
- Sleep, N.H., Nunn, J.A. and Chou, L., 1980, Platform basins. *Annual Review of Earth and Planetary Sciences*, 8(1), pp.17-34.
- Stoner, J.S., Channell, J.E. and Hillaire-Marcel, C., 1996, The magnetic signature of rapidly deposited detrital layers from the deep Labrador Sea: Relationship to North Atlantic Heinrich layers. *Paleoceanography and Paleoclimatology*, 11(3), pp.309-325.

- Swart, P.K., Burns, S.J. and Leder, J.J., 1991, Fractionation of the stable isotopes of oxygen and carbon in carbon dioxide during the reaction of calcite with phosphoric acid as a function of temperature and technique. *Chemical Geology: Isotope Geoscience section*, 86(2), pp.89-96.
- Torsvik, T.H., Van der Voo, R., Preeden, U., Mac Niocaill, C., Steinberger, B., Doubrovine, P.V., van Hinsbergen, D.J., Domeier, M., Gaina, C., Tohver, E. and Meert, J.G., 2012, Phanerozoic polar wander, palaeogeography and dynamics. *Earth-Science Reviews*, 114(3-4), pp.325-368.
- Totten, M.W., Hanan, M.A. and Weaver, B.L., 2000, Beyond whole-rock geochemistry of shales: the importance of assessing mineralogic controls for revealing tectonic discriminants of multiple sediment sources for the Ouachita Mountain flysch deposits. *Geological Society of America Bulletin*, 112(7), pp.1012-1022.
- Tribovillard, N., Algeo, T.J., Lyons, T. and Riboulleau, A., 2006, Trace metals as paleoredox and paleoproductivity proxies: an update. *Chemical Geology*, 232(1), pp.12-32.
- Versical, R. T., 1991, Basement control on the development of selected Michigan Basin oil fields as constrained by fabric elements in Paleozoic limestones. Masters Thesis. Western Michigan University, Western Michigan, p 98.
- Weil, A.B. and Yonkee, W.A., 2012, Layer-parallel shortening across the Sevier fold-thrust belt and Laramide foreland of Wyoming: spatial and temporal evolution of a complex geodynamic system. *Earth and Planetary Science Letters*, 357, pp.405-420.
- Winckler, G., Kipfer, R., Aeschbach-Hertig, W., Botz, R., Schmidt, M., Schuler, S. and Bayer, R., 2000, Sub sea floor boiling of Red Sea Brines: New indication from noble gas data. *Geochimica et Cosmochimica Acta*, 64(9), pp.1567-1575.

## CHAPTER 5

### SUMMARY OF CHAPTERS

Chapter 2, provides proof of concept for integrating scalar AMS parameters with inorganic geochemistry as a new petrofabric tool for unconventional reservoir characterization. This tool, coupled with organic geochemistry can be useful for determining whether clay-bound organic matter was delivered to the ocean floor. Chapter 2 also presents a new model explaining iron-enrichment in the Midland Basin. These findings highlight the importance of determining provenance lithotypes and how they are ultimately manifested as authigenic minerals. By integrating inorganic geochemistry with scalar AMS parameters, one can extract the concentration-dependent component from the microstructural component of magnetic anisotropy which can aid in future interpretations of AMS in mudrocks. Lastly, chapter 2 posits a petrofabric control on hydrocarbon migration based on released hydrocarbons associating with certain magnetic fabric types.

Chapter 3, integrates paleomagnetism, AMS, textural observations and basin modeling to identify the timing of illitization/chloritization, tectonic shortening, and mineral paragenesis and frame these events with respect to a burial history model. The timing of clay diagenesis, as established through paleomagnetism, is used as an anchor to establish the relative timing of albitization and barite formation based off their textural associations with chlorite. Normal and inverse magnetic fabrics are utilized to detect tectonic shortening and establish constraints on the timing of ferroan dolomite formation. Finally, new estimates of Cenozoic uplift are provided which further refines the geological history of the Permian Basin.

Chapter 4 presents the first paleomagnetic study of the Antrim shale in the Michigan Basin. Paleomagnetic, stable isotopes and textural observations are consistent with hydrothermal activity

sourced from the eastern segment of the mid-continent rift. Exotic minerals (i.e. chalcopyrite and monazite) in the Antrim probably formed due to hydrothermal activity, however, a subset of these minerals may have been derived from the Michigan Peninsula which could have implications for understanding the structural evolution of this region. Magnetic fabric analysis of the Antrim indicate somewhat paradoxical results and suggests either a hydrodynamically or tectonically influenced petrofabric.

### **SYNTHESIS**

The complex nature of diagenesis demands the use of integrated methodologies to extract which pre- and post-depositional variables shape the way mudrocks are manifested in the rock record. For example, in the Wolfcamp shale, the type of provenance material (i.e. mafic rocks) probably exerted some influence on the volume of organic material generated in the basin through supplying micronutrients to benthic organisms. A mafic provenance also clearly impacted mineral authigenesis, with widespread ferroan dolomite, iron-sulfides and iron-bearing clay formation from early through late burial. In terms of the temporal component of diagenesis, the paleomagnetic work on the Wolfcamp indicate a diachronous magnetization which suggests that illitization/chloritization occurred gradually over the course of millions of years when subsidence rates are subdued. In summation, provenance and tectonics probably represent two first-order controls on diagenesis in the Wolfcamp shale. In contrast, the diagenesis of the Antrim shale appears to be influenced primarily by external-fluids. This assertion is supported by paleomagnetic, isotopic and petrographic observations. In Chapter 1, diagenesis is described as a complex confluence of variables, however, this research demonstrates that it is possible to extract which variables exert more influence on mudrock diagenesis compared to others.